CENTRO INTERNACIONAL DE ESTUDOS
DE DOUTORAMENTO E AVANZADOS
DA USC (CIEDUS)

TESIS DE DOCTORADO

STUDIES ON THE COMPOSITION AND ENERGY OF SECONDARY COSMIC RAYS WITH THE TRAGALDABAS DETECTOR

Yanis Fontenla Barba

ESCUELA DE DOCTORADO INTERNACIONAL

PROGRAMA DE DOCTORADO EN FÍSICA NUCLEAR Y DE PARTÍCULAS

SANTIAGO DE COMPOSTELA

2019

USC
UNIVERSIDADE
DE SANTIAGO
DE COMPOSTELA

DECLARACIÓN DEL AUTOR DE LA TESIS

Studies on the composition and energy of secondary cosmic rays with the Tragaldabas detector

D. Yanis Fontenla Barba

Presento mi tesis, siguiendo el procedimiento adecuado al Reglamento, y declaro que:

1) *La tesis abarca los resultados de la elaboración de mi trabajo.*
2) *En su caso, en la tesis se hace referencia a las colaboraciones que tuvo este trabajo.*
3) *La tesis es la versión definitiva presentada para su defensa y coincide con la versión enviada en formato electrónico.*
4) *Confirmo que la tesis no incurre en ningún tipo de plagio de otros autores ni de trabajos presentados por mí para la obtención de otros títulos.*

En Santiago de Compostela, 12 de Septiembre de 2019

Fdo. Yanis Fontenla Barba

USC
UNIVERSIDADE
DE SANTIAGO
DE COMPOSTELA

AUTORIZACIÓN DEL DIRECTOR / TUTOR DE LA TESIS

Studies on the composition and energy of secondary cosmic rays with the Tragaldabas detector

D. Juan Antonio Garzón Heydt
D. Pablo Cabanelas Eiras

INFORMAN:

Que la presente tesis, corresponde con el trabajo realizado por D. Yanis Fontenla Barba , bajo mi dirección, y autorizo su presentación, considerando que reúne los requisitos exigidos en el Reglamento de Estudios de Doctorado de la USC, y que como director de ésta no incurre en las causas de abstención establecidas en Ley 40/2015.

En Santiago de Compostela, 12 de Septiembre de 2019

Fdo. Juan Antonio Garzón Heydt

Fdo. Pablo Cabanelas Eiras

USC
UNIVERSIDADE
DE SANTIAGO
DE COMPOSTELA

Agradecimientos

En primer lugar, deseo expresar mis agradecimientos a los directores de la tesis doctoral, Dr. Juan Antonio Garzón Heydt y Dr. Pablo Cabanelas Eiras, por el apoyo y dedicación que han aportado a este trabajo.

Gracias a Marcos Antonio Seco Miguélez por dedicarme su tiempo para que este trabajo pudiera seguir adelante.

Dar las gracias a mi familia por su apoyo en los momentos más dificiles.

Acknowledgements

Plan Galego de Investigación, Innovación e Crecemento (I2C) of Xunta de Galicia under projects POS-B/2016/015 and ED431C-2017/54.

Some results presented in this work were obtained thanks to the access granted to Galicia Supercomputing Center (CESGA) high performance computing resources.

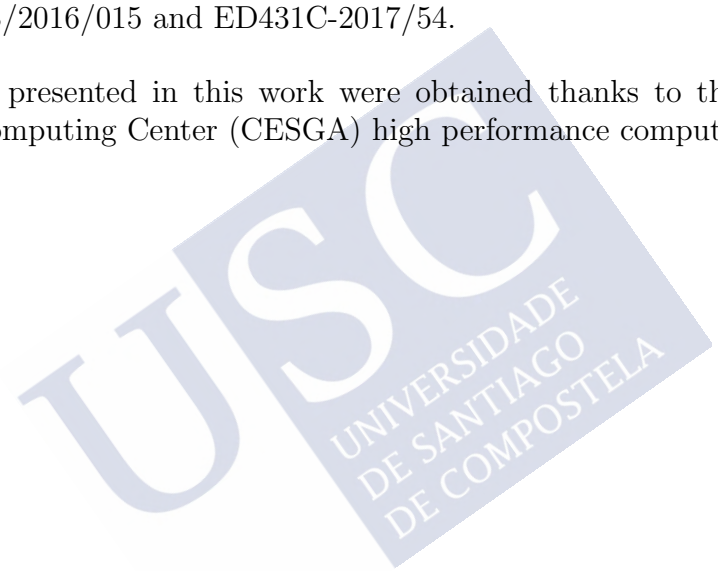

USC
UNIVERSIDADE
DE SANTIAGO
DE COMPOSTELA

Table of Contents

USC
UNIVERSIDADE
DE SANTIAGO
DE COMPOSTELA

List of Figures

USC
UNIVERSIDADE
DE SANTIAGO
DE COMPOSTELA

List of Tables

USC
UNIVERSIDADE
DE SANTIAGO
DE COMPOSTELA

USC
UNIVERSIDADE
DE SANTIAGO
DE COMPOSTELA

Introducción

Los rayos cósmicos son partículas subatómicas, protones y núcleos atómicos, de alta energía que provienen del espacio e inciden sobre la Tierra. Los rayos cósmicos fueron descubiertos por el científico austriaco Victor F. Hess por medio de viajes en globo entre 1911 y 1913. Los rayos cósmicos llegan a la Tierra, interaccionan con la atmósfera terrestre y se genera una cascada atmosférica. Las múltiples interacciones de fragmentos del cósmico con la atmósfera genera la cascada atmosférica. Parte de los rayos cósmicos se detectan en la parte alta de la atmósfera por medio de satélites y globos sonda, y otra parte, se detectan a nivel del suelo por medio de grandes redes de detectores y telescopios.

El detector TRAGALDABAS mide la tasa de partículas que llegan a la superficie terrestre. El sistema Tragaldabas está incluido en el *framework* EnsarRoot para el análisis y simulación por medio de su implementación geométrica. Además, un sofisticado código de reconstrucción de trayectorias de partículas TimTrack está implementado en EnsarRoot para el estudio y análisis del comportamiento de partículas y con ello poder realizar un estudio exhaustivo por medio del estadístico χ^2, entre otros. Con este trabajo se incrementa la investigación y desarrollo de detectores de tipo Trasgo para la identificación de muones y electrones procedentes de rayos cósmicos, y para la instalación de sistemas de detección y estudio de cascadas atmosféricas con distintas redes de detectores instalados en una amplia superficie de la Universidad de Santiago de Compostela (USC) y en otras localizaciones geográficas interesantes, como el continente Antártico. Para ello, varios sistemas Tragaldabas fueron implementados en EnsarRoot para la identificación de partículas, a la vez se implementó la geometría del edificio de la Facultad de Física y el programa de generación de eventos basado en datos CRY. Programas de análisis de datos y resultados fue realizado e incorporado en la rutina para el estudio de partículas a nivel del suelo procedente de cascadas atmosféricas. Este permite conocer la respuesta de detectores Trasgo tales que Tragaldabas, pudiendo así obtener un buen estimador de las propiedades del rayo cósmico incidente en la atmósfera. A su vez, permite estimar el tamaño de la red por medio del análisis de agrupamiento de partículas a nivel del suelo.

El documento comienza exponiendo una introducción sobre la naturaleza y el descubrimiento de los rayos cósmicos, la influencia de los campos magnéticos (e.j solar) y terrestre sobre los rayos cósmicos galácticos y extragalácticos que llegan a la Tierra, fórmulas básicas e históricas para la medida de dichos rayos cósmicos tanto primarios como secundarios sobre la superficie de la Tierra, y sus flujos de partículas medidas experimentalmente. También, se presenta un estudio detallado de la física de las cascadas atmosféricas y sus componentes handronica y electromagnética y, en general, también se estudia la interacción de las partículas neutras y cargadas de las cascadas electromagnéticas con la materia, con el

objetivo de poder conocer sus interacciones y utilizarlo en el diseño de detectores y montajes experimentales para medidas en Física de partículas, astropartículas, nuclear e incluso Física médica.

En el Capítulo 2 se expone con detalle la familia de Trasgos de detectores RPCs para el estudio y medida de rayos cósmicos y su influencia en la atmósfera, y en particular se describe con detalle el experimento Tragaldabas, un telescopio de rayos cósmicos de tipo Trasgo localizado en la Facultad de Física de la Universidad de Santiago de Compostela, y en base al cual he realizado la mayor parte de mi trabajo.

El Capítulo 3 recoge los diferentes programas informáticos (paquetes de *software*) utilizados para la simulación de eventos y análisis de datos. Se hace una introducción al método de Monte Carlo, comúnmente usado en programas de simulación hoy día, y se continúa con una descripción de los programas y entornos de análisis más usados en el ámbito de la física experimental. Se complementa el capítulo con una introducción al método *timtrack*, un algoritmo específico de reconstrucción de trayectorias en experimentos de partículas, el entorno de *software* EnsarRoot, dentro del cual está implementado *timtrack*, y así que una introducción al funcionamiento de los programas de generación de eventos de rayos cósmicos simulados Corsika y Cry.

En el Capítulo 4 se describen las simulaciones específicas realizadas sobre el detector Tragaldabas, la implementación de la geometría del edificio de la Facultad de Física de la USC, análisis del comportamiento de las prestaciones de Tragaldabas bajo cambios en su geometría y diseño, como la introducción de láminas de plomo de diferentes espesores entre sus planos de detección, mapas de aceptancia, y prestaciones del sistema en general. Siguientemente, se estudian todos los observables físicos relevantes para el caso general de un detector de tipo Trasgo con 4 planos de detección. El capítulo se complementa con la implementación de un programa sencillo de generación de eventos de rayos cósmicos sobre la superficie de la Tierra en EnsarRoot, basado en análisis exhaustivo de datos obtenidos con Cry.

El Capítulo 5 expone el desarrollo y los resultados de un algoritmo de identificación de partículas (PID) en detectores de tipo Trasgo basado en la fenomenología de los eventos: selección y análisis de observables para el estudio, método de generación de eventos, diagramas de flujo del algoritmo en sus diferentes variantes experimentales, y resultados finales. Estos resultados finales de precisión y probabilidad de acierto son altamente relevantes y significativos, proporcionando la bondad de la identificación de eventos reales sobre la superficie de la Tierra.

El Capítulo 6 describe el estudio de estructura de cascadas electromagnéticas sobre grandes áreas a nivel del suelo por medio de simulaciones con el programa Corsika. Este programa permite conocer la disposición de secundarios a nivel del suelo para diferentes núcleos primarios (H, He, C y Fe) interactuando en capas altas de la atmósfera. Se presenta el método de generación de eventos con el programa de simulación Corsika,

la estimación de primarios y secundarios, la distribución de función respuesta aplicada a detectores de tipo Trasgo, tanto para electrones ($e^{\pm}$) como muones ($\mu^{\pm}$), calculada en la USC y en la Base española de Livingstone, en la Antártida (BAE). Se presenta un estudio de distribución lateral y de agrupamiento de secundarios (*clusters*) a nivel del suelo, lo que permite estimar un área de acción óptima de detección, y conocer las características esenciales de la cascada a nivel del suelo con el fin de mejorar y optimizar la implementación de nuevos sistemas de detectores.

Finalmente, se presenta un pequeño capítulo de conclusiones, y un resumen global en castellano.

Las perspectivas de futuro de este trabajo son: un análisis de datos reales por medio del algoritmo de identificación de partículas integrado en EnsarRoot y, la instalación de una red de detectores por medio de los resultados de agrupamiento de partículas para la detección exhaustiva de secundarios a nivel del suelo por medio de las propiedades y características del primario con ayuda de los resultados de respuesta de los detectores Trasgo.

USC
UNIVERSIDADE
DE SANTIAGO
DE COMPOSTELA

Introduction

More than one hundred years after their discovery by V. Hess, cosmic rays are still a permanent source of unknowns. Although we have learn a lot about their properties and the energy they have, we don′t know yet the masses of those with higher energies, where and how are they produced or how do they reach the huge energies that some of them show when they arrive to the Earth′s surface.

Most of the cosmic rays are protons and light nuclei, although there is some contribution of medium and heavy elements, especially of the iron nuclei. Their energies range from almost the rest up to a few tens of Joules. The less energetic ones, below a few GeV, are produced in the Sun and they arrive to the Earth′s surface as a part of the solar wind. Sometimes, when the Sun produces a so called Coronal Mass Ejection (CME), the protons may reach energies up to a few GeV, being the rate of cosmic rays arriving to the top of the atmosphere around $10^3/\mathrm{m}^2\,s$. Above those energies, cosmic rays are produced either in our galaxy or in other galaxies, we classify both as galactic cosmic rays (GCR).

Up to energies of about 10^{14} eV cosmic rays are usually measured directly using detectors placed in satellites or stratospheric balloons. Also ground detectors, mainly neutron monitors or muon telescopes, are used all around the world for the regular monitoring of the primary cosmic rays by means of the secondary cosmic rays produced in the nuclear collisions taking place on top of the atmosphere. A very interesting effect is that the solar wind does interact with the galactic cosmic rays, modulating their arrival flux. Then, these on-ground detector are used for the indirect monitoring of the solar activity and for predicting the arrival of magnetic storms.

Taking into account the size of our galaxy and the mean value of the magnetic field, we may assume that cosmic rays below 10^{17} eV are not able to leave the galaxy and keep confined in it. Cosmic rays above that energy may only be explained as having an extragalactic origin.

Above an energy of about 10^{14} eV, the rate of cosmic rays at the top of the atmosphere is so small that their properties, mainly: mass, energy and arrival direction, have to be estimated indirectly at the Earth′s surface using huge arrays of detectors. These arrays, sometimes covering surfaces of several thousands of km^2, make a sampling of the billions of secondary cosmic rays arriving to the ground (mainly muons and electrons) and reconstruct the properties of the primary cosmic ray using the complementary information of Monte Carlo simulation codes. The problem is far to be easy because the energies involved in cosmic ray collisions may be up to one thousand times bigger than those

reached in particle accelerators and many of the cross sections of the reactions involved are not yet well known and their extrapolation is still doubtful.

A few of the inner properties of the cosmic ray showers were analyzed a few years ago by J. A. Garzón and G. Kornakov during the commissioning of the RPC (Resistive Plate Chambers) Time of Flight Wall, of the HADES Nuclear Physics experiment at the GSI (Darmstadt, Germany). For such purpose, two RPC detectors, of about 1.25 m^2 surface were stacked one on top of the other at a distance of ∼33 cm. Cosmic rays were measured making a trigger between coincidences of at least a hit in the upper and in the lower sector. Tracks were reconstructed matching hits in both detectors and asking for having a velocity compatible with the speed of light.

At the end, after five days of data taking with the detectors running in a very stable condition about 40 millions of events were chosen for a careful study of showers. The sample showed a joint resolution of a few cm^2 in position, a few hundreds of ps in the arrival time and a few degrees in the arrival direction. Those values had been never reached together by any cosmic ray detector at the Earth′s surface.

Although the results of the analysis were not conclusive from the point of view of the cosmic ray physics (there were any easy way of estimating neither the effect of the building in the sample or making the both the acceptance and efficiency corrections), they observe several interesting features: Although most of the events have multiplicity equal to one, sometimes multiplicities higher than 50 tracks or more were observed. In high multiplicity events most of times all the particles arrived in a time window of several ns, but some times isolated particles arrived 10 or 20 ns behind the main bundle of particles. Many events showed a high granularity with bundles of a few particles arriving in well defined space-time groups.
Sometimes the hit multiplicity in the first and the second detectors were very different showing either a very big increasing are very big decreasing or attenuation. Both cases could correspond, probably, to high energy and low energy electromagnetic showers, respectively. At high multiplicity events, the fastest particle were usually perpendicular to the plane defined by the arrival time of the rest of the particles. This result suggests that the arrival direction of the fastest particle is a good estimator or the local arrival direction of the front end of the cosmic ray shower.
All those results suggested several investigators of the University of Santiago the interest of continuing such line of research, developing a new family of specific detectors aimed to systematic study of the microstructure of cosmic ray showers of particles with improved performances. They proposed for such detectors the name of TRASGOs, an acronym corresponding to TRAck reconStructinG mOdule. Such kind of detectors would be also of interest for measuring the regular arrival of single cosmic rays or low multiplicity bundles of cosmic rays, opening an affordable and high resolution alternative to neutron monitors and muon telescopes for studies related with Solar Physics among others fields.
Together with the device design (mainly based on RPC chambers, the HADES Front End Electronics FEE and the TRB readout board designed by the GSI, another important goal

was to develop all the associated tools related with the simulation of the detector and their environment, the monitoring of the data taking, the track and event reconstruction and, finally, the analysis. The TRAGALDABAS detector, located in the building of the Faculty of Physics of the University of Santiago de Compostela (USC) is the first device designed and built according with the TRASGO philosophy. It was installed in a conditioned room an is taking data regularly since April 2015.

This document starts by introducing the nature and discovery of cosmic rays, the influence of solar and Earth magnetic fields on galactic and extragalactic CR that arrive to Earth, basic and historical formulae for measuring both primaries and secondaries[1] [1] CR on the Earth′s surface and the particle flux measured experimentally. Study of physics involving atmospheric showers and their hadronic and electromagnetic components, and in general, also interaction of neutral and charged particles of electromagnetic showers with matter, aiming to understand their interactions for the design of detectors and experimental montage for particle physics measurements, astroparticles, nuclear and even biomedical physics.

Chapter 2 exposes a through the Trasgo family [2] detectors of RPCs for the study and measurement of cosmic rays and their influence in the atmosphere and specifically it is described in detail the TRAGALDABAS [3] experiment, a Trasgo type of Cosmic ray telescope, localized at the Physics Faculty of the University of Santiago de Compostela and which is where most of my work come from.

Chapter 3 gathers the different computer programs (software packages) used for event simulation and data analysis. An introduction is done with the Monte Carlo method used in all simulation programs existing nowadays. It continues with a description of the analysis programs and frameworks used in most of the experimental physics domains. Complementing this, there is introduction to Timtrack method, a specific algorithm for particle trajectory reconstruction in particle experiments. Also the software framework EnsarRoot inside of which it is implemented Timtrack, and an introduction to the operation of simulated CR event generation simulation programs, CORSIKA and CRY.

Chapter 4 describes the specific simulations realized over Tragaldabas detector, the implementation of the geometry of the Physics Faculty building of USC, the behaviour analysis of Tragaldabas detector under changes of its geometry and layout, such as the introduction of lead layers of different thicknesses between its detection planes, acceptance maps, and general capabilities of the system. Then, all the physical observables relevant for the general case of a detector Trasgo-like with 4 detection planes are studied. This is complemented with the implementation of a simple program for CR events generation at ground level in EnsarRoot, based on a comprehensive analysis of data obtained with Cry.

[1] Primary cosmic rays are nuclei that interact with the top of the atmosphere and are originated outside the Earth. Secondary cosmic rays are fragments and particles of the primary interacting with the atmospheric particles or nulcei.

The Chapter 5 shows the development and results of an algorithm for particle identification (PID) in Trasgo-like detectors, based on the phenomenology of events: selection and observables analysis for the study, event generation method, flowcharts of the algorithm in its different experimental variants and the final results. This precise and right guess probability results are highly relevant and significant, providing the goodness of the identification of real events on the Earth′s surface.

Chapter 6 covers the study of the structure of the electromagnetic shower over vast areas at ground level using simulations with the program Corsika. It allows knowing the distribution of secondaries at ground level for different primary nuclei (H, He, C and Fe) interacting at the higher layers of the atmosphere. It is presented the method of event generation with the simulation program Corsika, the estimation of primaries and secondaries, the distribution of the response function applied to Trasgo-like detectors for both electrons ($e^{\pm}$) and muons ($\mu^{\pm}$), calculated in the USC and the Antarctic Spanish base in Livingstone (BAE). The study of lateral distribution and secondaries clustering (clusters) at ground level is also done, this allows to estimate an optimal detection action area and to know the essential characteristics of the showers at ground level with purpose of improving and optimizing the implementation of new detectors systems.

Finally, a short chapter for conclusions is presented and a global summary in Spanish.

The future perspectives of this work are an analysis of real data with the algorithm of identification particles implemented in EnsarRoot and, the installation of a array of Trasgo with the results of distribution clusters for the detection of secondary particles at ground level to know the characteristics of the primary cosmic rays with the response distributions of the Trasgo detectors.

USC
UNIVERSIDADE
DE SANTIAGO
DE COMPOSTELA

USC
UNIVERSIDADE
DE SANTIAGO
DE COMPOSTELA

1 Cosmic Rays and particles interacting with matter

The chapter presents in a logical and structured way the basic notions of cosmic rays study, the sources that generate them and the course of the charged nuclei until they arrive the Earth′s surface after interacting with the magnetic fields of the solar system and the atmosphere. A section of observables used in physics of cosmic rays [1] is implemented. sources and accelerators of cosmic rays [4, 5] are essential to understand where they come from and how the primaries that arrive at the Earth are generated. The interactions of particles with the material are implemented in the chapter to know the physical processes existing after the passage of cosmic rays particles through the detector.

1.1 The discovery of cosmic rays

The discovery of cosmic rays (CR) appears after the discovery of natural radioactivity. Some Earth elements are naturally radioactive. These elements are radon gas, uranium and so on. It was obvious to think that the ionization of a medium was caused by the radioactivity of the ground.
The discoveries began with Theodor Wulf, a German physicist. In 1909 he developed the electrometer[1] that allowed to take measurements on the rate of ions produced inside in a hermetically sealed container. He detected sources of natural radiation at ground level with his electrometer. He thought that if one moves away from the ground the rate of ions would decrease. In 1910 Wulf climbed to the top of the Eiffel Tower and discovered that the ionization decreased from $6{\cdot}10^6$ ions m^{-3} (ground level) to $3.5{\cdot}10^6$ ions m^{-3} (330 m height) [6]. A very small difference for such an increase in height. However, his article published in Physikalische Zeitschrift did not find wide acceptance. Domenico Pacini carried out a series of experiments between 1907 and 1911. A memoir was published in the New Cimento in 1912 [7]. Pacini observed simultaneous variations of the ionization rate on a Bracciano lake, in the marine waters of Livorno and at a depth of 3 meters below the surface. The intensity of the radiation decreased and was less than on the ground surface. Between 1911 and 1912 the Austrian physicist Victor Franz Hess did a some experiments going up to a hot air balloon. On one of his travels, he noticed that metal sheets were electrically charged. Victor F. Hess climbed back into a hot air balloon with a Wulf electrometer and noted that as he ascended the electroscope sheets tended to be

[1] An electrometer is an electroscope with a strip that allows measurements [ions m^{-3}]. The device consists of two thin sheets of metal enclosed in a glass jar with a lid. When the sheets are charged electrically, the sheets repel each other.

charged. On August 7th, 1912, along with a flight commander and a meteorologist, he did a six hour flight in which he rose to more than five thousand meters height. On April 17th, 1912, at the moment of an almost total solar eclipse, he did some measurements and ruled out the possibility radiation coming from the Sun. In November 1912, he publish the results in the German journal Physikalische Zeitschrift, concluding that there is a penetrating radiation in the atmosphere from above [8]. The Figure 1.1 shows Victor F. Hess boarded on a hot air balloon in Vienna, 1911 [9]. Victor F. Hess was awarded the Nobel Prize in Physics for the discovery of cosmic rays in 1936.

Figure 1.1: Victor F. Hess on a hot air balloon.

1.2 Influence of magnetic field on CRs

Two magnetic phenomena that create kinematic variations in cosmic rays with trajectories to Earth are existing. One is the interplanetary magnetic field (IMF) and the other is the Earth′s magnetic field. The **interplanetary magnetic field** is created by the Sun. The IMF is transported by the solar wind to the different planets of the solar system. The solar wind is a plasma and has magnetohydrodynamic plasma characteristics. The dynamic

pressure of the solar wind dominates the magnetic pressure so that the magnetic field forms a spiral named Parker′s [10]. The Figure 1.2 [11] represents the three-dimensional (3D) heliospheric current sheet (HCS) based on Parker′s heliospheric magnetic field. The HCS undulations for a radius of 10 AU can be seen. The Sun at the center of the spiral would create current fluctuations in the form of undulations subjecting all planets of the solar system to IMF. The spiral motion would be created by the change of polarity and the rotating motion of the Sun. The undulations would be directly related to the 11 years period polarity change of the solar magnetic field.

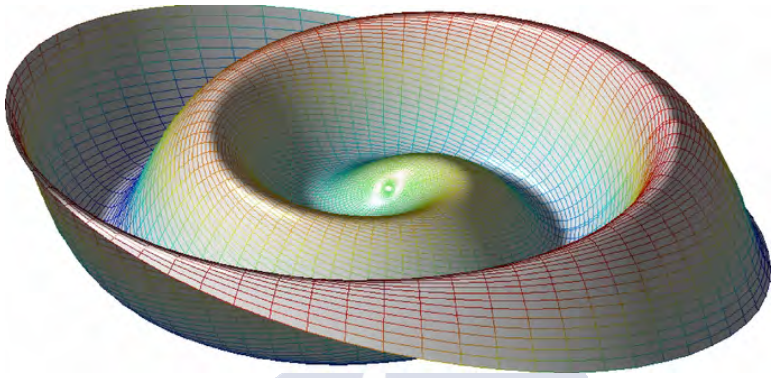

Figure 1.2: The 3D heliospheric current sheet.

Some observations say that the magnetic field of the Sun in Earth′s orbit is about $2{\cdot}10^{-9}$ T ($2{\cdot}10^{-5}$ G) [12]. The concept of HCS plays an important role in the solar modulation of CRs.

The **Earth′s magnetic field** or geomagnetic field is the sum of small magnetic fields that are on Earth. The geomagnetic field extends from the Earth′s inner core to the limit where it meets the solar wind. The Earth′s magnetic field is similar to a bar magnet tilted 11 degrees from the normal axis of the ecliptic. The geographic North pole is the magnetic South pole and vice versa. Today it is known that magnetic fields originate in the vicinity of electric currents located in the Earth′s core. The magnetic fields are caused by the looping movement of the circulating currents of the Earth′s liquid metal core. The value of the magnetic field measured at ground level is between 0.3 and 0.6 G. In the thirties, different experiments showed that cosmic rays are located at the poles of the Earth and their minimum intensity is at the equator.

The interaction of a magnetic field with a charged particle produces the deviation of its trajectory. The trajectory of a CR in the direction of the Earth is constantly deviating to a greater or lesser degree due to the Earth′s magnetic field and the IMF. The **trajectories of particles** are helical in regions where the intensity of the Earth′s magnetic field becomes relevant. The movement of a charged particle q and particle velocity $\vec{\mathrm{v}}$ is governed by the Lorentz force law with external force in the presence of a magnetic field $\vec{B}$: $m\,\mathrm{d}\vec{\mathrm{v}}/\mathrm{d}t = q\,(\vec{\mathrm{v}} \times \vec{B}) + \vec{F}_{\mathrm{ext}}$. The transverse component and the parallel component of particle velocity is the origin of the helical movement of particles. Some phenomena

related to the geomagnetic field can be manifested by implementing terms to Lorentz force law related to gravity, the electric field, the magnetic gradient or due to the curvature of the field.
The helical trajectories of the charged particles is confined in the vicinity of the magnetic field lines as a rule. Charged and high-energy particles are trapped in the magnetosphere moving along the magnetic field lines and rotating around the Earth. This phenomenon is called **geomagnetically trapped radiation**. The Figure 1.3 [13] shows the properties that characterize the geomagnetically trapped radiation and its different related phenomena. One can see the trajectory of particles (or trace) trapped in a flux tube where the particles follow the line of the magnetic field. The trajectories of trapped particle in the regions near the Earth come together and follow each other. The lines tend to separate as they move away from the Earth. The radius of curvature of the trace tends to grow as the particles move away from the Earth. The magnetic field is the cause of the radius of curvature size. The magnetic field is more intense in regions close to Earth.

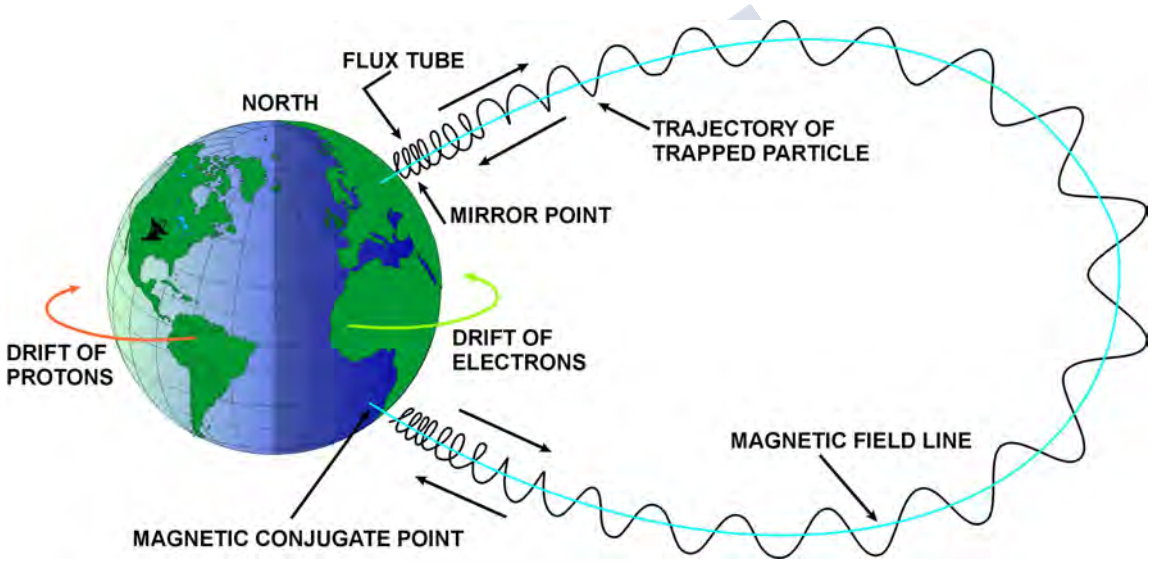

Figure 1.3: The geomagnetically trapped radiation.

The mirror point is well-located point where the trajectory of charged particles suffers rebounds. A lot of charged particles can be bouncing between points in the geomagnetic field. The magnetic conjugate point is the opposite ends of the magnetic field line. The supplementary terms that appear in the equations generate a drift. The drift is the tendency of the trajectories of the particles around the Earth, in the vicinity of the Earth surface. The drift to the West for protons and other nuclei, and to the East for electrons. This phenomenon is called **East-West effect**. The direction of the cosmic arrival directly affects the cuttoff rigidity. Positive CRs are more abundant if they enter from West and negative if from East.

The Earth′s magnetic field has a direct influence on the trajectory of the particles. The trajectories of charged cosmic ray particles are bent by the Earth′s magnetic field. The radius of a charged particle r_{L} in circular motion in the presence of a uniform magnetic

field B has been obtained by equating the Lorentz force with the centripetal force, $r_{\mathrm{L}} = p/(Z\,e\,B)$. If the cuttof rigidity P is defined as the gyroradius times the uniform magnetic field B and the light velocity c, the following relationship is obtained:

$$P = \frac{p\,c}{Z\,e}\ [\mathrm{GV}]\ , \tag{1.1}$$

where $p\,c$ is the kinetic energy [GV] of a relativistic particle, p being the momentum [GeV/c], Z is the atomic number, and e is the elementary charge of the electron.
The Figure 1.4 [14] shows the map of effective vertical cutoff rigidity calculated by a global network using the IGRF model for Epoch 2000.

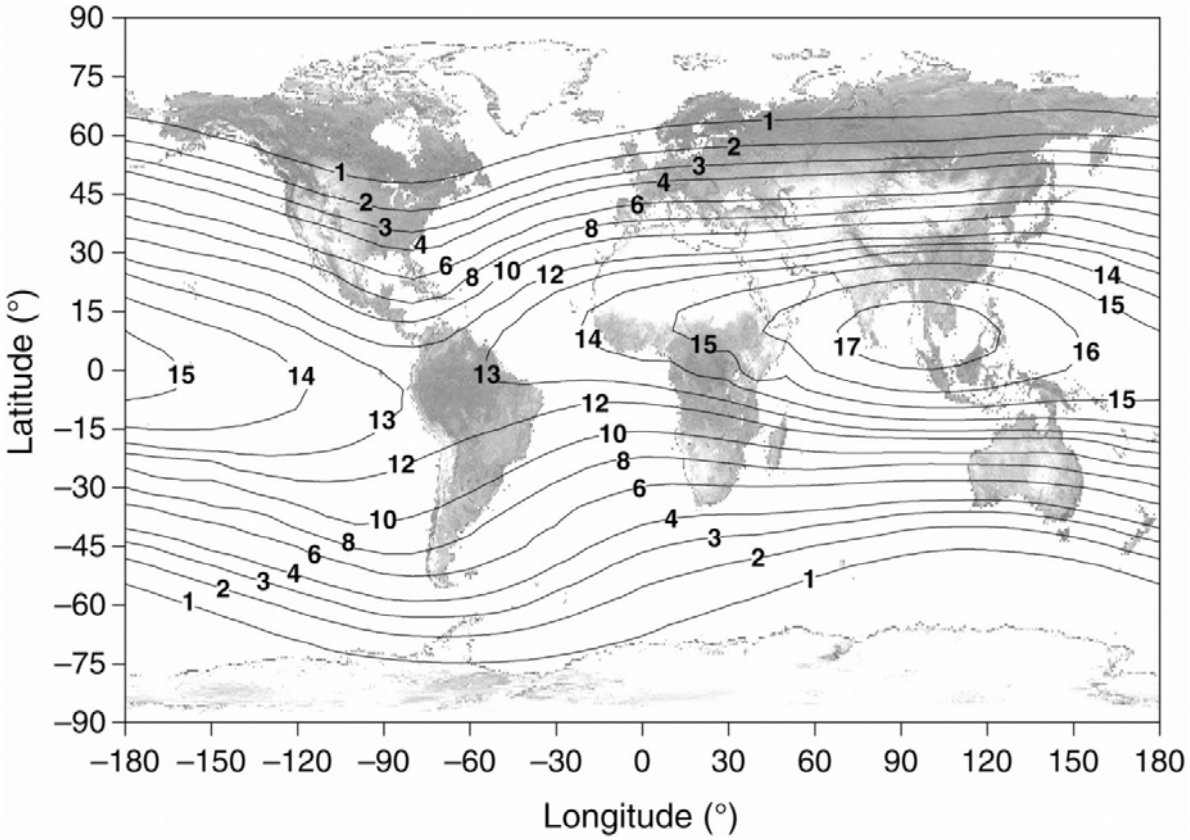

Figure 1.4: Vertical Geomagnetic Cuttof Rigidity [GV]. The rigidity is around 6 and 8 GV in the Iberian peninsula.

The lines of the map show the rigidity values [GV]. The rigidity values are from 1 GV close to the ± 75° to 17 GV in the Indonesian region (equatorial). Values at low rigidity are found at latitudes near to ±[50, 75]°. The maximum rigidity values have been in latitudes close to zero and longitudes near to 80° and 120°. The rigidity is 17 GV for an range in approximate longitude of [60,120]° and in approximate latitude of [0,15]°. In the vicinity of the poles, the rigidity is very near to zero. The rigidity is approximately between 5 and 9 GV in the peninsular Spain. Namely, the rigidity and lines of geomagnetic field lines may vary along the years.

Summarizing, a particle with momentum greater than the rigidity can overcome the force exerted by the geomagnetic field and therefore, the initial direction of the particle changes. The bombardment of cosmic particles near the poles will be greater than in the regions near the equator. The maximum deviation of the trajectory of charged particles is in southeast Asia.

1.3 The CR physics

In this section, essential magnitudes for the detection of cosmic rays are studied. The magnitudes reproduce the amount of cosmic rays that are detected from low Earth orbit (up to a few km below the Earth′s surface). The differential flux or directional intensity $I_i(\theta, \phi)$ of a particle i is written as:

$$I_i(\theta, \phi) = \frac{dN_i}{dA\, dt\, d\Omega} \quad [\mathrm{cm^{-2}\, s^{-1}\, sr^{-1}}] \ ,$$

where dN_i is the number of incident particles, dA is the area element, dt is the time and $d\omega$ is the solid angle element. The directional intensity is usually called intensity. The intensity depends on the zenith angle θ and the azimuth angle ϕ. In turn (θ, ϕ) depend on the energy E and on time at low energy. The total intensity is defined as the integrated intensity for all energies $I_i(\theta, \phi, \geq E, t)$. The differential current is the intensity at a fixed energy, $I_i(\theta, \phi, E, t)$. The vertical intensity is defined as the intensity at a zero zenital angle, $I_{V,i} = I_i(0°)$. The relationship between vertical intensity and $I_i(\theta)$ is as follows,

$$I_i(\theta) = I_i(0°)\, cos^{n_i}\theta \ .$$

The exponent n_i (n≈2 for muons) correlates with the atmospheric depth X [g/cm^2] and the energy E.

The flux represents the number of particles for i particles that cross an area element dA per unit of time dt. The formula that relates the flux and directional intensity is like that,

$$J_1 = \int_{\bigcap} I_i(\theta, \phi)\, cos\theta\, d\Omega \quad [\mathrm{cm^{-2}\, s^{-1}}] \ .$$

The symbol $\bigcap$ refers to the integral for the upper hemisphere ($\theta \leq \pi/2$). The integrated intensity or omnidirectionality intensity J_2 is a formula very similar to the previous ones. J_2 is obtained by integrating the directional intensity for any angle,

$$J_2 = \int I_i(\theta, \phi)\, d\Omega \ .$$

$d\Omega = sin\theta\, d\theta\, d\phi$, Omnidirectionality is integrated at ranges of $[0, \pi]$ in zenith angle and $[0, 2\pi]$ in azimuth angle. The resulting equation of the azimuthal angle integral is,

$$J_2 = 2\,\pi \int_{\theta=0}^{\theta=\pi} I(\theta) \sin\theta\, d\theta \ [\mathrm{cm^{-2}\, s^{-1}}] \ .$$

Generally, the omnidirectionality is always greater than or equal to the flux, $J_2 \geq J_1$.

One of the most important relationships that exist in cosmic ray physics is called as differential energy spectrum, $j(E)$. The differential energy spectrum is defined as the number of particles $dN(E)$, per unit area dA, per unit time dt, per unit of solid angle $d\Omega$ and per unit of range of energy dE,

$$j(E) = \frac{dN(E)}{dA\, d\Omega\, dE\, dt} \quad [\mathrm{cm^{-2}\, s^{-1}\, sr^{-1}\, GeV^{-1}}] \ .$$

Sometimes the differential energy spectrum is represented as a function of the spectrum moment $j(p)$ or as a function of the rigidity P (equation (1.1)). The spectrum associated with $j(p)$ is called Particle Spectrum. The integral energy spectrum $J(\geq E)$ is defined as the total of particles with an energy greater than E per unit area dA, per unit of solid angle $d\Omega$ and per unit of time dt. The formula that describes the integral energy spectrum is,

$$J(E) = \frac{dN(\geq E)}{dA\, d\Omega\, dt} \quad [\mathrm{cm^{-2}\, s^{-1}\, sr^{-1}}] \ .$$

The integral Spectrum is obtained directly by integrating the differential energy spectrum:

$$J(\geq E) = \int_E^\infty j(E)\, dE \ .$$

The differential energy spectrum is derived from the integral energy spectrum:¡

$$j(E) = -\frac{dJ(\geq E)}{dE} \ .$$

The energy spectrum follows an exponential law in almost all cases. It is usual to write the integral energy as $J(\leq E) = C\, E^{-\gamma}$, where C is a constant and γ the exponent of the potential law called differential spectral index. Deriving the previous relationship, write the following:

$$j(\leq E) = C\, \gamma\, E^{-(\gamma+1)} = A\, E^{-(\gamma+1)} \ , \tag{1.2}$$

where A is a constant. The exponent $(\gamma + 1)$ is approximately 2.7 and remains almost constant from about 100 GeV to 10^6 GeV (Knee region). $(\gamma + 1)$ is approximately 3.0 for values between 10^9 GeV and 10^{10} GeV (between the knee and the so-called ankle). After the ankle the value $(\gamma + 1)$ returns to approximately 2.7.

1.4 Terrestrial CRs

The flux of particles passes through nearby interstellar space at speeds close to light. The particles are composed mostly of protons and atomic nuclei with kinetic energy range 10^8 more than 10^{20} eV. The flux through the solar system is practically isotropic and immutable. The observed flux on Earth is variant due to several phenomena. One of the phenomena is the interplanetary magnetic fields. The kinematics of particles change given the existence of interplanetary magnetic fields. Therefore the intensity changes a few GeV. The geomagnetic field is another cause.

The Figure 1.5 [15] show the energy spectrum of primary cosmic rays. The spectrum represents the cosmic ray flux [$m^{-2}\,s^{-1}\,sr^{-1}\,eV^{-1}$] as a function of the energy of the primary cosmic ray [eV]. The graph also gives information about the altitude where the flux measurement of CR particles has been made. This information is given in units of [gr/cm^2], of [km] or in the form of different atmospheric strata. The altitude is represented by a logarithmic axis.

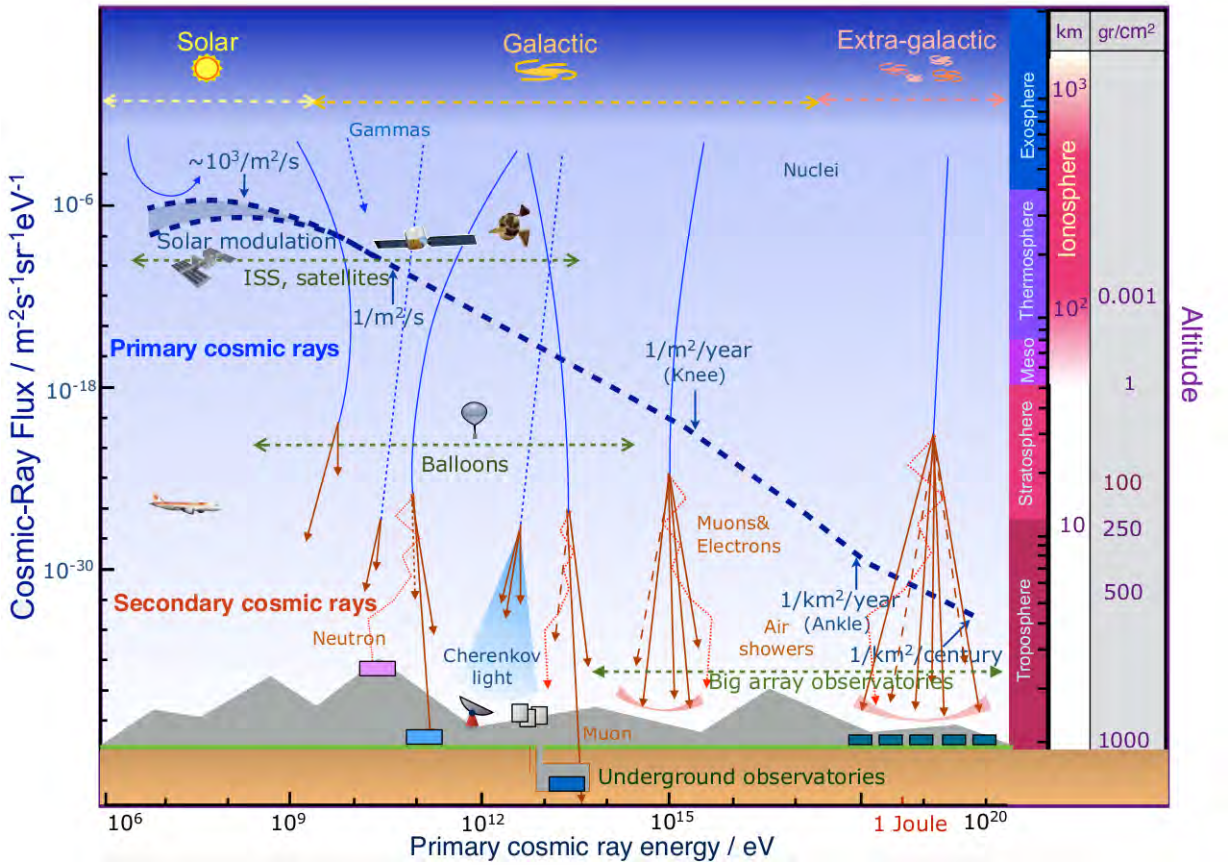

Figure 1.5: Cosmic ray energy spectrum.

The altitude range is from about 10^{-3} (few 10^3 km) to 10^3 gr/cm^2 (near to 0 km). The altitude range of different atmospheric layers are: from 7 to 20 km high for the troposphere, from about 10-15 km to 45-50 km high in the stratosphere, from 50 to 85 km in the mesosphere, from about 90 to 500-1000 km high it is the thermosphere, of about 500-1000 up to 10000 km for the exosphere. The thermosphere and a part of the exosphere from the so-called ionosphere. The stratum of the ionosphere has a depth of about 700 km. The energy spectrum extends by 14 orders of magnitude in energy and 24 orders of magnitude in flux. The flux decreases as the energy increases. The data follows a power law. The curve presents two irregularities. One at about 10^{15} eV called the Knee and another one at about 10^{18} eV called Ankle. There is a discrepancy in the values of the curve due to the modulation of the solar wind at lower energies. The cosmic rays rate

is $1/m^2\,s$ for an energy around 10^{11} eV, $1/m^2\,year$ around 10^{15} eV, $1/km^2\,year$ to 10^{18} eV and $1/km^2\,century$ to higher energies. The 14 orders of magnitude in energies can be divided into 3 sources of cosmic rays. The solar source provides evidences of flux in a energy range of [10^6,10^9] eV, the flux measured by galactic sources extends into an energy range of about [10^9,10^{18}] eV and the flux of extra-galactic source is in a range energy of 10^{18} a 10^{20} eV. The primary cosmic rays are detected in the top of the atmosphere and secondary in the bottom of the atmosphere. Primary CRs are usually protons and other atomic nuclei. So protons are detected essentially at low energies. It is suspected that the nuclei heavier than the proton come from galactic and extragalactic sources since these nuclei are detected at very high energies. Secondary cosmic rays have a flux of about $200/m^2/s$ at the Earth′s surface. These particles are usually composed of photons, electrons, muons, protons and neutrons.

Charged particles with an energy range of [10^6, 10^9] eV are strongly influenced by the geomagnetic field and for an energy of [10^8, 10^{11}] eV are greatly influenced by the IMF field. A large set of detectors is needed to collect information about the cosmic rays flux shown in Figure 1.5. The detection of primary CRs is done by satellites or detectors installed in the International Space Station (ISS). These detectors work in high atmosphere and collect much information of the flux of primary CRs. Energy range of the high atmosphere detectors is from 10^8 eV to about 10^{14} eV. The flux in stratosphere is measured by detectors in attached to balloons. The balloons collect the CR rate in an energy range of 10^{10} to 10^{14} eV (e.g. ATIC experiment). The flux of secondary CR is measured with big array observatories in the energy range from 10^{14} eV to 10^{20} eV. Some most important secondary CRs detectors are: Argo YBJ (Tibet) that works in a energy range of 10^{12} to 10^{15} eV, ICE CUBE-ICE TOP (Antarctica) with a energy range from 10^{14} to a few hundred 10^{17} eV, HAWC (Puebla, Mexico) with a energy between 100 GeV and 50 TeV, and Pierre Auger (Argentina) that works with energies from 10^{18} to 10^{12} eV. Other arrays observatories are: Volcano Ranch (Utah), HiRes (Utah), Telescope Array (Utah), HEGRA (Spain), HESS (Namibia), EAS-TOP (Italy), ANTARES (Mediteranean Sea), Tunka or now named TAIGA (Russian-Siberia). Obsolete experiments of cosmic rays study are KASKADE (Germany) with an energy range from 10^{14} up to a few hundred of 10^{16} eV, KASKADE-Grande (Germany) with energy range from [$5{\cdot}10^{15}$, 10^{18}] eV and MILAGRO (New Mexico).

The Figure 1.6 [16] represents the differential energy spectrum F(E) multiplied by $E^{2.6}$ [$GeV^{1.6}\,m^{-1}\,s^{-1}\,sr^{-1}$] as a function of the energy per nucleon [eV]. The secondary particles detected from air showers leads to the spectrum. The secondary were measured with such as Pierre Auger, Cherenkov telescope array, Kascade, Kascade Grande, Akeno, ... The variable $E^{2.6}$ near to the differential flux facilitates highlighting the breaks in the curve. Some artistic graphics resemble the curve with one leg. For this reason, one call the break of the curve like knee and 2nd knee, ankle and toe. The effects of propagation and acceleration of the nuclei create the breaks of the spectrum. The differential spectral index (equation (1.2)) takes different values at different energy ranges given the existence of these breaks. The knee of the spectrum is at $10^{15} - 10^{16}$ eV and the ankle is located at

$10^{18.5}$ eV. The maximum energies of nuclei from galactic accelerators such that supernova remnant (SNR) (see the Illustration I) may be the cause of the steepening of the Knee. The differential spectral index is 3 between the knee and the ankle. Another steepening can be found at $8{\cdot}10^{16}$ eV observed by Kaskade Grande. This steepening is probably produced by transitions to heavy primaries. Fluorescence techniques have been used to perform the measurements at energies above 10^{17} eV. Above the ankle range of energies ($3{\cdot}10^{19}$eV), there is the region of ultra high-energy nuclei, called toe. The standard deviation σ grows given the very little statistics of N events in this region. The standard deviation is about 90 ($\pm$45) from HiRes 1 experiment at $2{\cdot}10^{20}$ eV. If the standard deviation of values is 45, the square root of the number of events $\sigma \sim \sqrt{N}$ given a approximatelly value of 2025 events. Then, it is very difficult to do statistics calculation with these few hundred events.

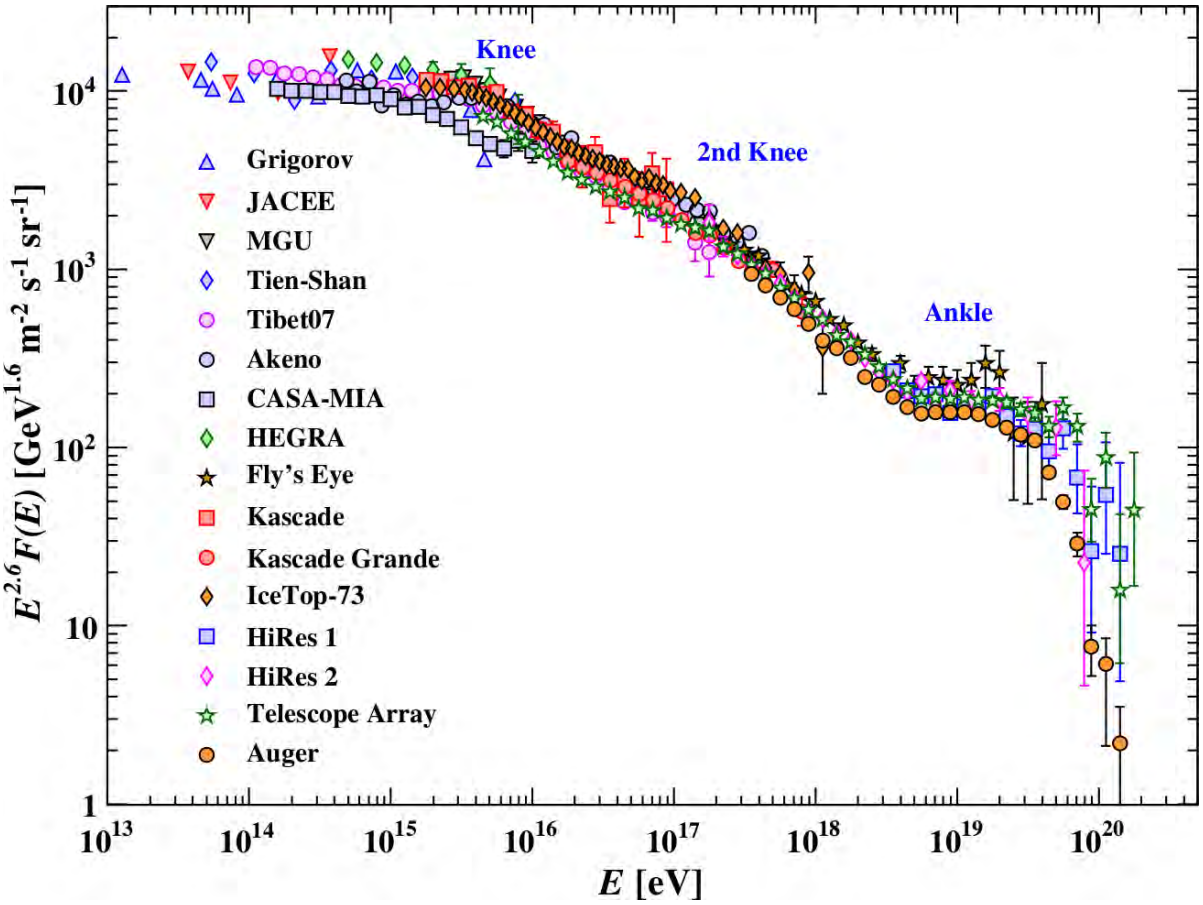

Figure 1.6: Differential spectrum energy of CRs multiplied by $E^{2.6}$. The different regions called knee, second knee and ankle are consistent with the origin of cosmic rays.

A cut in the detection of CR is existing in the data around 10^{20} eV, called Greisen-Zatsepin-Kuzmin limit (GZK limit). Kenneth Greisen [17], Georgiy Zatsepin and Vadim Kuzmin [18] were the authors of the theory of this limit, the theory that states that there is an upper limit to the energy of cosmic rays from distant sources. The authors predicted that CR with energies above the threshold of $5{\cdot}10^{19}$ eV interact with photons from the cosmic microwave background (CMB), this limit value is equivalent to approximately

8 Joules. It is assumed that a mixed of heavy nuclei interact with the atmosphere in this energetic region. The study of secondary CR flux at ground level is essential to understand the basic characteristics of air showers. The Figure 1.7 [16] show the vertical flux of the major CR components in the atmosphere in energy regions of greatest interest. The Graph represents the vertical flux [$m^{-2}s^{-1}\,sr^{-1}$] as a function of the altitude [km] or atmospheric thickness [$g\,cm^{-2}$]. The Graph represents the measures or observable as dots and the expected data as lines.

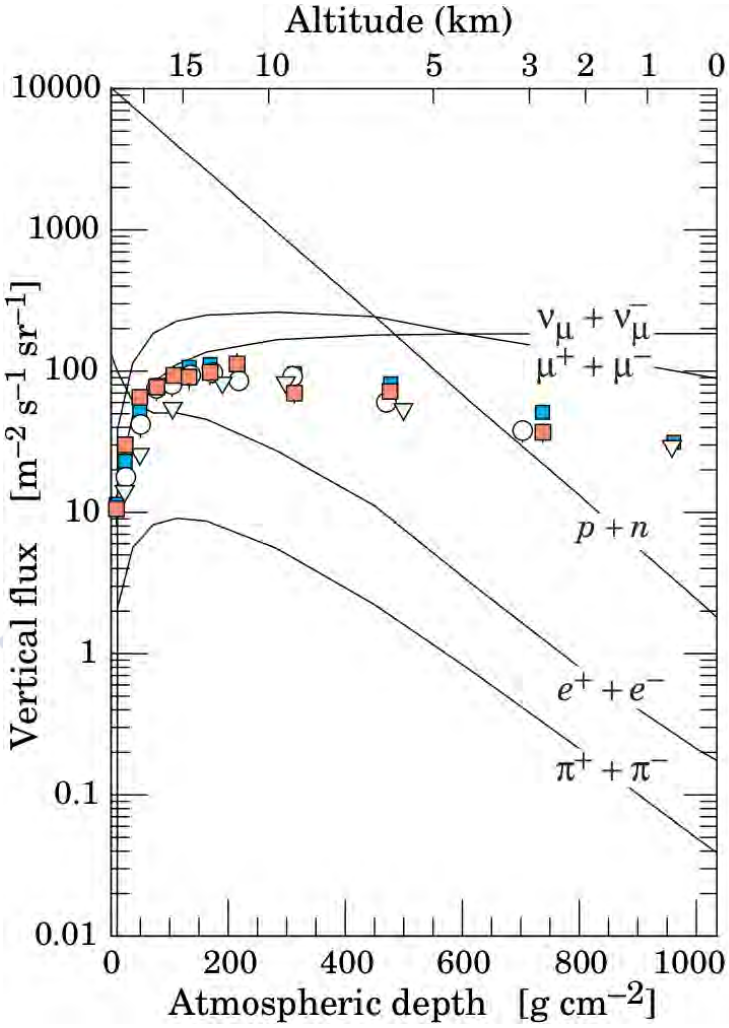

Figure 1.7: Vertical flux of secondary CR for a energy bigger than 1 GeV. The dots, squares, circles and triangles show the observable data and the lines represent the expected data. The muon flux is high and change little along the atmosphere layer, the electron flux increases strongly at high altitude.

The energy cutoff is E > 1GeV. The measurements were taken mainly at ground level, near the top of the atmosphere or by airplanes. The data show that the vertical flux of CR is very small for altitudes above 15 km and the flux has a fast growth until reaching 100 to 1000 g cm^{-2}. The measurements tend to decrease below the 15 km height and the flux decrease slowly until reaching a value close to 30 $m^{-2}\,s^{-1}\,sr^{-1}$ for about 1000 $g\,cm^{-2}$.

Apparently, the curves show the same trend as the curves (expected data) of muonic electronic channels. The measurements are adjusted to the expected data of the muonic and neutrino disintegration channels above the 15 km height. The measurements are adjusted to the curve of the neutrino decay channel between 13 and 15 km and these do not fit any curves below 10 km. The expected data say that the primary CRs $(p + n)$ dominate over 6.5 km. The electrons and pions have the same tendency as the primary CRs below 16 km. The flux of muons is dominant at sea level, then, muons can penetrate deep into the atmosphere. The flux of electrons and $p + n$ with energies greater than 1 GeV is 0.2 and 2 $m^{-2}\,s^{-1}\,sr^{-1}$ at sea level.
Next, the tabulated flux of KAYE&LABY from the national physical laboratory (NPL) are studied. The flux measurements reveal the rate of **cosmic radiation** at sea level. The flux of CR secondary particles is important if one wants to make a good analysis of particle physics applied to detectors. The Table 1.1 show the mean integral flux of cosmic rays at the sea level [$m^{-2}\,s^{-1}\,sr^{-1}$] for some threshold kinetic energy [GeV]. Show the total flux of muons, electrons (positrons), photons, protons and neutrons. The integral flux (IntFx.) and differential flux (DifFx.) are also shown for muons in percent. The 9 threshold are between 10^{-3} and 20 GeV. The flux was measured at geomagnetic latitudes $>\sim 40°$. The asterisk $(*)$ near to neutron value describes data calculated using theoretical models.

Table 1.1: Mean flux of cosmic rays from NPL.

E [GeV]	Muons			Electrons[1]	Photons	Protons	Neutrons
	Flux	InFx.[%]	DifFx. [%]				
0.001	100	$\ll 1$	$\ll 1$	60	130	2.1	30*
0.1	99	1	1	6.0	8	1.9	10*
0.2	97	3	2	3.0	3.5	1.5	-
0.5	86	14	11	1.0	1.1	0.9	1.5
1	69	31	17	0.4	0.4	0.5	0.7
2	46	54	23	0.1	0.1	0.25	*Estimated theoretical values
5	20	80	26	0.02	0.02	0.1	
10	9	91	11			0.03	– – ––
20	3	97	6				[1]Include positrons

The muon flux is 100 [$m^{-2}\,s^{-1}\,sr^{-1}$] to 10^{-3} GeV and decreases as the threshold increases. The muon flux is minimal (3 [$m^{-2}\,s^{-1}\,sr^{-1}$]) to 20 GeV. The trend is similar for other particles. The maximum flux of other particles is 60 (electrons), 130 (photons), 2.1 (protons) and 30 (neutrons) to 0.001 GeV. The minimum flux become 0.02 (electrons and photons) at 5 GeV, 0.03 (protons) at 10 GeV and 0.7 (neutrons) at 1 GeV. The tendency of the muon integral flux and muon differential flux is inverse to the flux described above. The muon integral flux grows as the threshold increases, the flux is less than 1% at 0.001 GeV and 97% at 20 GeV. The muon differential flux is less than 1 to 0.001 GeV, the flux increases as energy increases. The maximum flux of 26% is at 5 GeV and decreases to 6% at 20 GeV after the maximum.

Summary of table results, the abundance of muons is greater than the other particles

at sea level and the hierarchical abundance of particles is: muons, photons, electrons (positrons), neutrons and finally protons. Then, secondary muons are the most abundant according to the data in the Table 1.1 and Figure 1.7. The energy range of the maximum muon flux is [1,5] GeV.

1.5 CR sources and accelerator mechanisms

The study of the acceleration mechanisms and the CR sources is important to know the origin of the primary CR particles detected on Earth. The progress of knowledge in matter of emission and direction of the primary particle from the cosmic source is the essence of current research in astrophysics. Disturbing phenomena of the direction of the source and the production process of mass and charged particles exist. These phenomena can be: the magnetic fields (terrestrial, solar or cosmic background), cosmic interactions and so on. A very important finding of the Ice Cube collaboration was made in July 2018, the detection of a neutrino from the AGN 0506+056 was confirmed with more than 5σ [19]. The TXS 0506+056 is classified as Blazar[2].

The important point of this section is to know the **CR particle sources**. It is necessary to study the important nuclear phenomena of the Sun to know the **solar CRs** that come to Earth.

The Sun is a yellow dwarf of main sequence star[3]. This is about 700000 km radius and is composed mainly of hydrogen and helium. Also small amounts of other elements in plasma state are attributed to it. The Sun has a structure in layers of a spherical onion where the solar nucleus (core) is located in the center of the star. Thermonuclear reactions where the H is constantly transformed into He through the dominant *proton-proton chain reaction* occur in the core. The proton-proton reaction is:

$$
\begin{aligned}
{}^{1}\mathrm{H} \;+\; {}^{1}\mathrm{H} \;&\longrightarrow\; {}^{2}\mathrm{H} \;+\; e^{+} \;+\; \nu_e \\
{}^{2}\mathrm{H} \;+\; {}^{1}\mathrm{H} \;&\longrightarrow\; {}^{3}\mathrm{He} \;+\; \gamma \\
{}^{3}\mathrm{H} \;+\; {}^{3}\mathrm{H} \;&\longrightarrow\; {}^{4}\mathrm{He} \;+\; 2\,{}^{1}\mathrm{H}\ ,
\end{aligned}
$$

The chain transforms 4 ^{1}H into one of ^{4}He, exothermic energy of 26.21 MeV and two neutrinos. The reaction is given at a temperature of 10^7 kelvin, near at the radiative region beyond the core and the energy is transported by radiation out of the star. This region is about 0.713 solar radius from the core. The convective region is made by huge gas bubbles in motion. The photosphere is the last layer of the solar structure, it has a thickness of 500 km and an approximate temperature of 7000 K at the bottom and 4000k at the top. The Chromosphere with about 500 km of height on the base solar atmosphere begins after the Photosphere. The chromosphere can reach 6000k. The temperature is approximately 1 or 2 million kelvins about 2500 km above the photosphere, this region extends a few solar radius and is called Corona. Radiation and solar wind are produced

[2]A Blazar is simply a quasar with particle jets pointing directly at Earth.
[3]The main sequence is a plots of stellar color versus brightness called as Hertzprung-Russell diagram.

that detached from the Sun out of the solar system in the Corona. These phenomena are called Coronal Mass Ejections (CME) (see the Illustration II). The so-called solar flares or solar flares strongly are other phenomena that may exist on the surface of the Sun. A solar flare is a flash of brightness seen on the surface of the Sun that is interpreted as an energy release of up to $6{\cdot}10^{25}$ Joules. The clouds of solar plasma arrive on Earth one or two days after the phenomenon. Solar flares can produce streams of highly energetic particles in the solar wind called proton events (SPE), these can reach Earth within 15 to 60 minutes of big eruptions. Solar flares also produce for example X-rays.

Next, the source of **Galactic** CRs is studied, it is believed that supernovae and maybe kilonovas[4] are the source of galactic cosmic rays. The supernova is a stellar explosion, these are the most luminous objects in the galaxy and it′s classified according to intensity in brightness when they explode (Type Ia / IIn, Type Ian, Type IIa and Type IIan). The explosions of supernovae are the last evolutionary stages of the massive stars in main sequence. There are several shapes of evolutionary stages for a star to end in a supernova explosion. The core of the stars contract and their envelope expands developing He of high density (Branch of the giants) in the last stages of its evolution. The burning of He occurs in ideal conditions, this produces the expansion of the envelope of the star and its increase in temperature. Carbon burning occurs when helium is depleted, when the supernova explosions can become violent for stars with masses less than $9M_{\odot}$, being $M_{\odot}$ the solar mass. This becomes possible when carbon combustion occurs and there has been no loss of mass in the combustion of He. The explosion is so violent that the star explodes without leaving gravitationally bound objects. Two sequences in the final stages of a supernovae are existing: a planetary nebula with a white dwarf at its center ($M_{dwarf} < 1.4\ M_{\odot}$) is produced when the star has a mass in the range of $2.2M_{\odot} < M < 9M_{\odot}$ and a star can transfer mass to the white dwarf companion in binary systems. The combustion of carbon and oxygen is carried out when the mass exceeds the Chandrasekhar limit[5] of $1.4M_{\odot}$, the energy released will produce a supernova explosion and the disruption of all star. Evolved massive stars (e.g: pre-supernovae) have an onion-layered structure, the iron (^{56}Fe) is usually the compound of the star′s core. The other components are Silicon (^{56}Si), Carbon (^{12}C) and Oxygen (^{16}O), Helium (^{4}He) and Hydrogen (^{1}H) as one moves away from the core and crosses the different layers of the onion. All the matter that constitutes the star will be expelled by the galaxy if the stars explode without any object.

Finally, the sources of **Extragalactic** CRs are studied below. The scientific community thought that the accelerators of extragalactic particles were very varied. The Hillas criterium proposes to classify and get very specific candidates for particle accelerators CR.Hillas [21] predicted in 1984 that the particles of CR must be confined in a region of space in order to be accelerated at high energies. The radius of Larmor (or gyroradius)

[4] A kilonova is a merge phenomenon of compact binary systems given by neutron-neutron stars or neutron-black hole that generates strong electromagnetic radiation and short emission of gamma rays.

[5] The Chandrasekhar limit is the mass above which the electron degeneracy pressure in the star′s nucleus is insufficient and the gravitational collapse is imminent. The Chandrasekhar limit is about $1.4M_{\odot}$ [20]

r_g of the particle must be equal to or smaller than the size of the accelerator:

$$r_g \sim 1.08\,\mathrm{Mpc}\,Z^{-1}\left(\frac{E}{10^{18}\,\mathrm{eV}}\right)\left(\frac{B}{1\,\mathrm{nG}}\right)^{-1} \leq R\ , \tag{1.3}$$

where the length scale characterizing the motion of a particle of energy E, the electric charge Ze, the size of the region R and the strength of the magnetic field of the accelerator B. The inequation 1.3 called Criterion Hillas translates for the maximal energy in,

$$E \leq E_{max} \sim 10^{15}\,\mathrm{eV}\,Z\left(\frac{B}{1\,\mu\mathrm{G}}\right)\left(\frac{R}{1\,\mathrm{pc}}\right)\ . \tag{1.4}$$

The maximum energy to accelerate protons is 10^{15} eV given 1 μG of magnetic field, 1 pc of accelerator size and Z=1 (proton). The diagram with all the possible candidates to accelerate CR is achieved with the inequation 1.4. The Figure 1.8 shows the Hillas plot [22] which represents the magnetic field [G] as a function of the accelerators size [km].

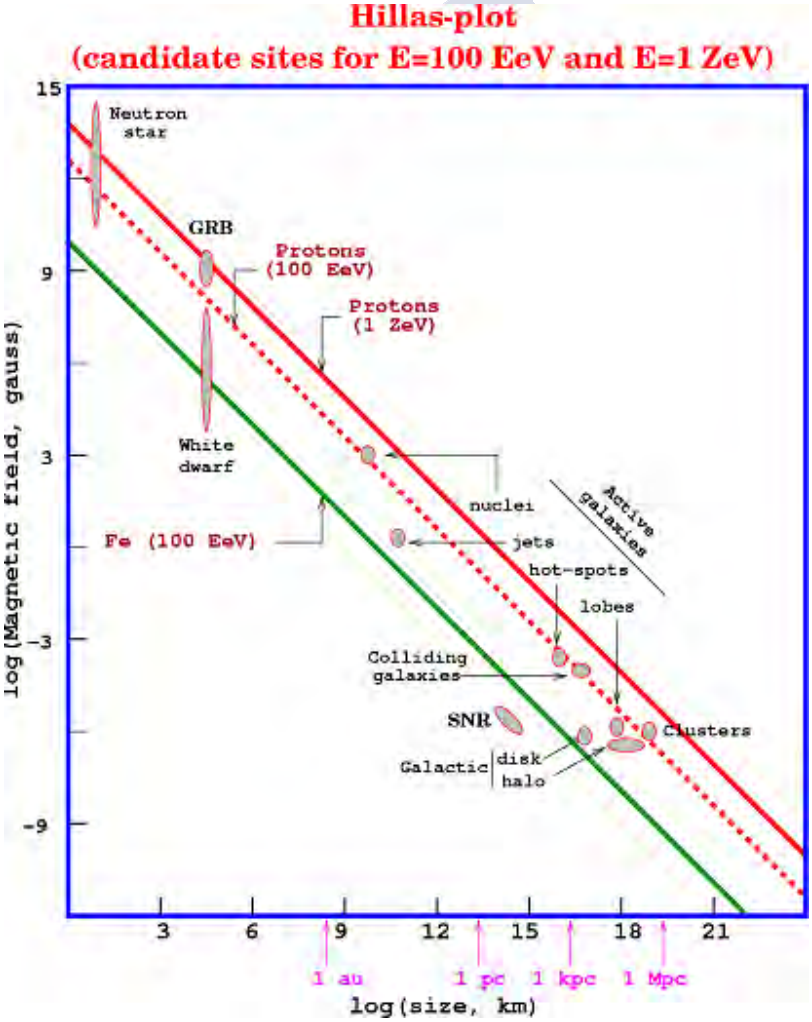

Figure 1.8: The Hillas Plot. Threshold energy cosmic rays of galactic and extragalactic accelerators.

Some values in astronomical units (AU[6]) and in parsecs (pc[7], kpc and Mpc) are implemented on the abscissa axis of the diagram. The solid curves correspond to different shock wave velocities. The solid curve of red color is the B(R) values for a power of maximum reach ($\beta \sim 1$). This equals 1 ZeV (10^{21} eV) in units of proton kinetic energy. The red and green dashed curves are B(R) values with lower reaches energies: 100 EeV ($100 \cdot 10^{18}$ eV) for protons (β=1/300) and 100 EeV for iron nuclei, respectively. The neutron stars dominate for intense magnetic field and small accelerator size. The objects such as neutron stars can accelerate protons with energies of 100 EeV or more than 1 ZeV. The gamma-ray bursts (GRBs) and white dwarfs appear for accelerator sizes smaller than neutron stars, these can accelerate protons up to 1 ZeV. The white dwarfs can accelerate iron up to 100 EeV or protons near to 100 EeV. The extragalactic nuclei are near to 10^3 G and greater than 1 au. The nuclei accelerate exclusively protons up to about 100 EeV. The jets (see the Illustration III) are below 1 pc, these can accelerate iron above 100 EeV and protons below 100 EeV. The extragalactic supernova remnant (SNR) can accelerate iron to energies well below 100 EeV. These are above 1 pc. Other phenomena exist called Active Galaxies (AGN) (see Illustration IV) located at greater than 1 pc and less than 1 Mpc, these phenomena are hot-spots, lobes colliding galaxies and Clusters (see the Illustration V). The active galaxies accelerate protons of about 100 EeV. The discs and galactic halos accelerate iron to energies above 100 EeV.

The cosmic particles are created and accelerated at high energies in the same sources. In general, the particles of cosmic rays are accelerated under the action of magnetic and gravitational fields. There are a wide variety of candidates for generation and acceleration of CRs as if we were before. These are the following: stellar interactions, supernovae explosions, electromagnetic interactions in neutron stars, active galactic nuclei and possible black holes. Other possible accelerators that are not highly massive may be magnetic clouds. The **accelerator mechanism** of particles [5] in the sources of known CRs are discussed below. **Cyclotron Mechanism** proposes the acceleration of charged particles in circular orbits generated by time-dependent magnetic fields. The charged particle moves along the lines of the magnetic field. The sunspots or star spots are the source of magnetic fields. The sunspots generate magnetic fields of up to 1T (10^3 Gauss) and has an extension of about 10^7 m. The solar magnetic fields are generated by movements of plasma (protons and electrons). The lifetime of sunspots is of several periods of Sun rotation. Some evidence reveals the existence of particle energies of few GeV from the Sun.

Sometimes, two sunspots with opposite magnetic polarities are near and an electric field perpendicular to the lines of the dipole is produced. High velocity particles move along the lines of the electric field, the phenomenon is called **Acceleration by Sunspot Pairs**. The magnetic sunspots can produce electric fields of 10 V/m, the relative velocity of the

[6]The astronomical unit is the fundamental unit used for the measurement of distance in astronomy. Equivalent to $1.49597870 \cdot 10^{11}$ m.

[7]Acronyme of parallax second. It′s defined as the distance from the Earth of an object that exhibits a parallax of 1 arcsecond. 1 pc=206265 au=3.26 light years=$3.086 \cdot 10^{16}$ m

particles is usually 10^7 m/day and the energy range of the particles are GeV. **Shoch Acceleration** is a phenomenon produced by a supernova explosion. The massive stars follow a process of burning the Hydrogen inside them. The star suffers a gravitational collapse after the burning of hydrogen. The temperature of the star increases until the process of burning the helium begins. The gravitational inflection process will continue until the star no longer contains Helium. Successive fusion processes begin after burning. The fusion processes will be stopped when the star is composed of heavy elements (iron, cobalt and nickel). The massive star imploses by expelling a part of its mass into space after the fusion processes. A neutron star is formed at the end of his stage. The star can get to eject all its mass to space in some binary systems. The star ejects its mass like an envelope after the implosion. The expulsion of the envelope represents a shock front due to the violence of the shoke-wave. The internal shock fronts of the star can have speeds of 20000 km/s. The external shock fronts are around 100 km/s at 1000 km/s.

A Fermi study involved the transfer of macroscopic kinetic energy from a moving plasma to individual particles (e.g: CR particles). The method consists of an iterative process of energy gain. The relative energy again to leading order in **Fermi Mechanism** is: $\Delta E/E = 2(u^2/v^2)$, where u and v are the parallel component of the particle speed and cloud gas respectively. The mechanism of acceleration of RC particles called **Pulsars** is described below. A pulsar is a magnetized neutron star produced after a supernova explosion. These stars have a radius of about 20 km and approximately nuclear densities ($\approx 6{\cdot}10^{13}$g/cm^3). The interaction process of a neutron star is: $p + e^- \rightarrow n + \nu_e$. The angular momentum of the star is conserved due to gravitational collapse. Therefore the rotational period of the star is very short. The phenomenon of collapse greatly amplifies the magnetic field. Assuming that the field lines before and after the collapse are equal is not wrong. The field lines being the massive star should be very similar to the neutron star now very small. The field lines are very tight. The magnetic field B of a magnetic pulsar is about 1000 Gauss ($2.5{\cdot}10^8$ T). The speed of rotation will be about $4{\cdot}10^6$ m/s and an electric field of about 10^{15} V/m assuming a period of rotation of the star is about 30 ms. So intense electric fields implies particles momentum of 1 PeV/m. The total acceleration energy of RC particles is $2.2{\cdot}10^{67}$ eV for an injection time press of $5{\cdot}10^9$ years. This values correspond to an energy density of CR of approximately 1 eV/cm^3.
Binaries is a system formed by a neutron star (or pulsar) and a star with normal characteristics. The neutron star carries matter from its partner. The existing electromagnetic fields are enormous since there is a drag of matter from a star to the neutron star. Therefore the particles are accelerated to very high energies. The Energy gains $\triangle$E around 70 MeV and speeds about $1.2{\cdot}10^8$ m/s in regions near to the accretion disk. The magnetic field is about 10^6 T and the particles path $\triangle$s of about 10^5 m if the velocity of the particles is comparable to the speed of light. The energy of the particles of $3{\cdot}10^{19}$ eV given these values of field and path. Higher energies could be reached in accretion disks formed by black holes or nuclei of active galaxies.

1.6 Elementary particle physics

Atomic, molecular and nuclear physics sensed the existence of a substructure after the classification of chemical elements in Mendeliev′s periodic table. Negative charged electrons orbit around a nucleus with equal and positive electrical charge. The nucleus is formed by nucleons: protons and neutrons. The neutrons stabilize heavy nuclei and contribute to strong attraction between nucleons. The protons have properties similar to neutrons but with charge. The chemical elements are atoms with a number of different electrons. The chemical isotopes are atoms with identical chemical properties (number Z of electrons and protons). The isotopes have masses different from each other since the number of neutrons is different. The electromagnetic interaction between electrons and atomic nuclei is responsible for the atomic structure. This interaction is governed by the laws of quantum mechanics. The matter can be easily defined with only 3 elementary particles (electron, proton and neutron) and the electromagnetic and the strong interactions. Dirac theoretically demonstrated the existence of antimatter in 1928 [23] The antimatter is constituted by antiparticles with identical properties that the particles but with opposite charge. The positron (the antielectron) was discovered with the study of cosmic rays at Earth level four years later. The antiproton and antineutrino was discovered with the first particle accelerators in the 1950s. Pauli predicted the existence of a third particle (the neutrino) in the decay β in 1930 [24]. The first observation of an antineutrino placing a detector next to a nuclear reactor occurred in the 1950s. The neutrons disintegrate and antineutrinos are produced (10^{13} $\bar{\nu}$ s/cm^2). A few antineutrinos are detected. The existence of 4 particles (electron, proton, neutron and neutrino) and their respective antiparticles were sufficient to describe the visible matter. Although, another level of substructure inside the nucleons exists.

The proton and neutron belong to the family of strongly interacting particles called hadrons. The pions were discovered in cosmic rays. A large number of these particles were produced in the particle accelerators. The structures of the hadrons are formed by three quarks (baryons), by three antiquarks (antibarions) or by a quark and an antiquark (mesons). Two quarks are discovered inside the nucleons: up (u) and down (d). The muon is the cousin of the electron and appears with the cosmic rays in the 1940s. The tau lepton (τ) was discovered at the Stanford accelerator in 1975. The muon and the tau are identical to the electron but much heavier: 200 (μ) and 3000 (τ) times more. These are unstable and decay to electrons. Each lepton has its neutrino: electronic neutrino (ν_e), muon neutrino (ν_μ) and tauonic neutrino (ν_τ). The first observation of neutrino or tauonic was obtained in 2000 in Femilab. The existence of other quarks are given: charm (c), top (t), strange (s) and bottom (b). The fermionic matter can be grouped into three families [25]. Three leptonic families and three families of quarks:

$$\begin{bmatrix} \nu_e & u \\ e^- & d \end{bmatrix} \quad ; \quad \begin{bmatrix} \nu_\mu & c \\ \mu^- & s \end{bmatrix} \quad ; \quad \begin{bmatrix} \nu_\tau & t \\ \tau^- & b \end{bmatrix}.$$

The elementary particles are grouped as leptonic doublets and quarks in each fermionic family. The behavior of physical interactions between particles is described by the Standard

Model (SM) [26] of physics. The interactions are governed by Gauge theories with group symmetry encompassing interactions:

$$SU(3)_C \otimes SU(2)_L \otimes U(1)_Y \ ,$$

where the symmetry $SU(3)_{\mathrm{C}}$ represents the strong interaction between quarks with a color subscript C and the symmetries $SU(2)_{\mathrm{L}} \otimes U(1)_{\mathrm{Y}}$ refer to the electroweak interactions between the leptons with left field subscripts L and weak hypercharge Y. The component $SU(2)_L \otimes U(1)_Y$ can be reduced to the symmetry of group $U(1)_{QED}$ through Spontaneous Symmetry Breaking (SSB):

$$SU(3)_C \otimes U(1)_{QED} \ .$$

The symmetry $SU(3)_C$ represents the strong interactions of the quarks governed by the laws of quantum chromodynamics (QCD). The gauge transformation in the color space with massless spin 1 mediators (gluons) gives rise to long-range interactions traveling at the speed of light c. The $U(1)_{QED}$ symmetry describes the electroweak interactions governed by Standard Electroweak Theory. The unification between electromagnetism and the weak interaction predicted by the theory is given with this symmetry. This symmetry fixes the properties of the electroweak interaction mediated by four particles of spin 1: the photon of the electromagnetic interaction (γ) and the bosons responsible for the weak force (Z^0 and $W^{\pm}$). The Table 1.2 presents the coupling constants that provide the amplitudes of the different interaction processes.

Table 1.2: **Fundamental interactions of particles**.

Interactions	Electromagnetic	Weak	Strong
Boson	Photon	$W^{\pm}, Z^0$	Gluons
Masses [GeV/c^2]	0	80.4, 91.2	0
Coupling constant	$\alpha(Q = m_e) \sim \frac{1}{137}$	$\mathrm{G_F} = 1.167 \cdot 10^{-5}\,\mathrm{GeV}^{-2}$	$\alpha_S(m_Z) \sim 0.1$
Strenght [cm]	∞	10^{-16}	10^{-13}

The fine structure coupling constant $\alpha(Q_e = m_e)$ has been calculated for an energy scale Q equal to the mass of the electron. The constant has an approximate value of 1/137 [27]. The value of the coupling constant of Fermi $\mathrm{G_F}$ was collected from the reference [28]. The coupling constant of the strong interaction $\alpha_s(m_Z)$ was calculated with the boson mass Z [29]. The constant has an approximate value of 0.1. Another fundamental interaction is defined as gravitational interaction. The particle that describes this gravitational interaction has not been yet. Therefore, gravitation has not been added to the other interactions described by the Standard Model. Theoretical models of quantum gravity and string theory propose the G graviton as a particle of gravitational interaction. Currently, the graviton has zero mass, zero electric charge, spin 2 and has an infinite interaction range [30, 31]. Something more is understood of gravitation after the gravitational wave findings of LIGO, Virgo and GEO600 collaborations [32]. The particle physics is not ready to discover a particle that describes gravitational interaction today.

1.7 Hadronic and electromagnetic components

The decay channels [16] of the most probable events that occur of EAS are studied in this section. An Air shower is composed of an electromagnetic component, a mesonic or muonic component and a nucleonic component. The nucleonic component is not studied in this work. The electromagnetic (e.m) shower are collected in the electromagnetic component of the air shower. The electromagnetic component comprises the decay channel of the neutral pion π^0. Another decay channel exists to produce an additional e.m component: the muon charged $\mu^{\pm}$. A large number of muons can arrive at ground level before decay (see section 1.8 "Development of a EAS in the Atmosphere") as relativity dictates. The muonic component comprises the disintegration channel of charged pions $\pi^{\pm}$ and charged kons $K^{\pm}$.

In general, pions have spin 0 and are composed of the first family of quarks. The neutral pion is the lightest meson. This has zero charge, a mass of 134.97 MeV, a lifetime of τ=8.52·10^{-17} s and $c\tau$=25.5 nm. The most probable decay of the neutral pion is $\pi^0 \longrightarrow \gamma\ \gamma$, with a Branching Ratio (BR) of 98.82%. The Figure 1.9 shows the Feynman diagram of this decay.

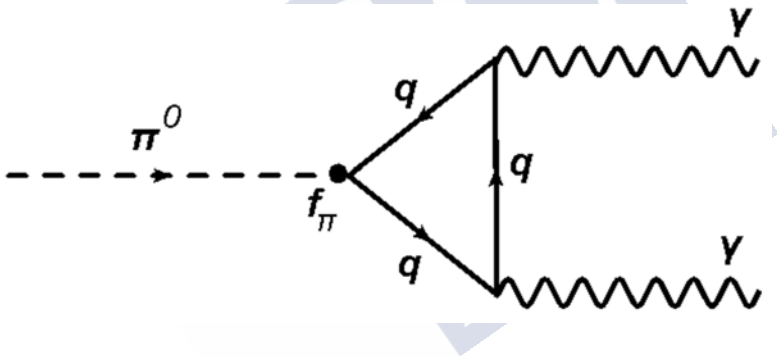

Figure 1.9: Neutral pion decay diagram.

The quantum state of the zero pion is written as: $|\pi^0\rangle = \frac{1}{\sqrt{2}}(|u\bar{u}\rangle - |d\bar{d}\rangle)$ (bra-ket notation). The π^0 is formed by two quarks states by equals according to the model quarks governed by Quantum Mechanics. A state consists of quark-antiquark u ($u\bar{u}$) and the other quark-antiquark d ($d\bar{d}$). The decay vertex is composed of a triangular loop-vertex and a disintegration constant of the pion f_π. The vertex provides anomalous terms to the identities of Ward associated with the theory that explains the decay of the zero pion. The constant f_π is a measure of the probability that the quark and the antiquark are at the origin. The theoretically calculated decay width is $\Gamma(\pi^0 \to \gamma\gamma)$=7.75 eV for a number of colors of N_C=3. The experimental value is $\Gamma(\pi^0 \to \gamma\gamma)$=7.86 ± 0.54 eV. The experimental result is consistent with the theoretical result. The charged pion $\pi^{\pm}$ has a mass of 139.57 MeV, a lifetime τ of 2.6·10^{-8} s and $c\tau$=7.8045 m. The π^+ is composed of quarks $u\bar{d}$ while its antiparticle π^- by the quarks $d\bar{u}$. The BR of pion decay channel $\pi^+ \to \mu^+\,\nu_\mu$ ($\pi^- \to \mu^-\,\bar{\nu}_\mu$) is 99.988%. Important relationship, $\Gamma(\pi \to \mu\,\nu_\mu) = 1/\tau$.

The Kaons have a spin 0 and are composed of the first and second family of quarks. The charged Kaon $K^{\pm}$ has a mass of 493.68 MeV, a lifetime of 1.2380·10^{-8}s and $c\tau$ of 3.712 m. The decay channel $\mu\ \nu_\mu$ has a BR of 63.55% The Figure 1.10 presents the decay Feynmann diagram of π^-. The Figure 1.11 shows the decay Feynmann diagram of K^-. The negative charge Boson W^- is the mediator of the interaction and is in both diagrams. The final leptonic state are identical. The vertex of the interaction are different. The pion vertex is $\frac{g_W}{\sqrt{2}}$ sin θ_C while the kaon vertex is $\frac{g_W}{\sqrt{2}}$ cos θ_C. The Cabibbo angle θ_C refers to the terms of the Cabibbo-Kobayashi-Maskawa matrix [16] (CKM Matrix).

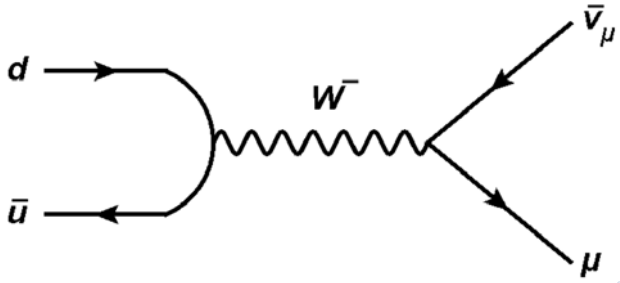

Figure 1.10: Pion decay diagram.

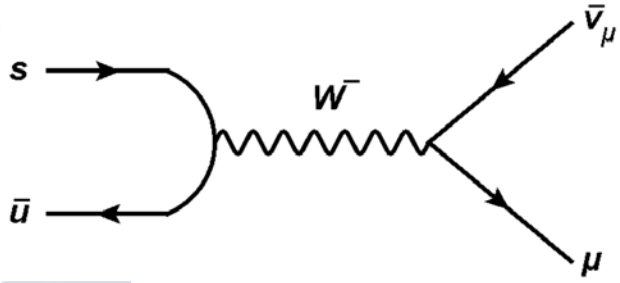

Figure 1.11: Kaon decay diagram.

The muon is an elementary particle with spin $\frac{1}{2}$. The muon has a positive or negative charge $\mu^{\pm}$, has a mass of 105.66 MeV, a lifetime of 2.1969·10^{-6} s and $c\tau$=658.638 m. The decay channel $\mu^- \rightarrow e^-\,\bar{\nu}_e\,\nu_\mu$ has a BR near to 100%. To know that $\Gamma(\mu^- \rightarrow e^-\,\bar{\nu}_e\,\nu_\mu)=1/\tau$. The Figure 1.12 presents the Tree-level[8] Feynman diagrams [33].

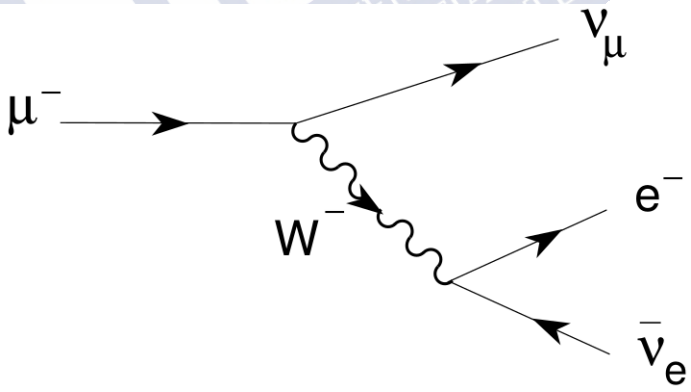

Figure 1.12: Muon decay diagram.

The μ^- produces 3 particles and the mediator of the interaction is a Boson W^-. The vertex of the interaction is $\frac{-ig}{\sqrt{2}}\gamma_\mu P_L$, where g is the SU(2) coupling constant which is related with the vacum expectation value v trough $g = \frac{2M_W}{v}$ ($v^2 = \sqrt{2}\,G_F$), γ_μ is the Dirac matrix and the left projector P_L is related with the γ_5 matrix as $P_L = \frac{1-\gamma_5}{2}$ [33].

[8]The Tree-level defines the lowest level in approach theory (order 0) of a Feynman diagram.

1.8 Development of a EAS in the atmosphere

The particles are classified as primary particles and secondary particles in Cosmic Ray Physics. The primary cosmic rays are composed of protons (H), Helium (He), Carbon (C), Iron (Fe), ... The secondary cosmic rays are the fragments of the successive interactions of primaries with the atmosphere generating mainly photons (γ), electrons ($e^{\pm}$) and muons ($\mu^{\pm}$) in a wide range of energies. The final states of mesonic decays are usually muons ($\mu^{\pm}$) and photons. The mesonic decays are mostly pions (π^0, $\pi^{\pm}$) and minority kaons ($K^{\pm}$). Namely, the atmosphere is usually composed of nitrogen (N_2), oxygen (O_2), argon (Ar), water vapor (H_2O) and carbon dioxide (CO_2). The probability of collision between primary CR and nuclei of N and O is very high, because 98% of these elements make up the atmosphere. Figure 1.13[9] represents the development of cosmic rays air showers. The primary cosmic ray approaches the top of the atmosphere, crosses it and interacts with atmospheric compounds. The interaction of the primary cosmic ray with this compounds breaks the cosmic and several light fragments are produced, hadrons.
The photons and electrons of the cascade forms the **electromagnetic component** of EAS. The muon decay generates electrons with a high probability. The neutral pion decay generate two photons: $\pi^0 \rightarrow \gamma + \gamma$. A simple explanation of this component in is given with the Heitler′s toy model [34] for electromagnetic cascade. The photons produce electrons by pair production $e^{-}e^{+}$ and the electron produce a photon by Bremsstrahlung effect. A threshold path of the electromagnetic component can be calculated simply with the splitting lenght $x = n\,X_0 \ln 2$ from de Heitler′s model, where n is the number of splitting lenghts, the radiation lenght for electron is 36.7 g/cm^2 and his critical energy is 85 MeV. Assuming a huge electron energy of 10^{20} eV, $n \ln 2 \approx 40$, the maximum reach of the cascade is about 1500 meters (1.5 km). The charged pion decay produce an electron (positron) with a negative charge (positive charge) and an antineutrino (neutrino): $\pi^{-} \rightarrow e^{-} + \bar{\nu}_e$ or $\pi^{+} \rightarrow e^{+} + \nu_e$. To know that the decays of pions to electrons have low BR. Therefore, this decay channel is not the ideal to generate electrons.

The **muonic component** is composed usually by charged pion decays or charged kaon decays to muons and neutrinos. The Kaon decay ($K^{\pm}$) gives a muon (antimuon) and antineutrino (neutrino): $K^{-} \rightarrow \mu^{-} + \bar{\nu}_e$ or $K^{+} \rightarrow \mu^{+} + \nu_e$. The decay channel of the Kaon ($\pi^{\pm}$) produces a muon (antimuon) and antineutrino (neutrino): $\pi^{-} \rightarrow \mu^{-} + \bar{\nu}_\mu$ or $\pi^{+} \rightarrow \mu^{+} + \nu_\mu$. The muons are of great interest in the study of cosmic rays air shower because most of these particles reach ground level. The muons have a lifetime around 2.1969 μs and a speed near to 0.978 c, this flies about 660 meters. The special relativity is the solution to calculate the lifetime and travel of the muon for an observer located at ground level. The muon does not take 2.1969 μs but 30.17 μs according to the dilation of time. Then, the muon to fly about 15 km before it decays. Many of the muons of EAS arrive at ground level assuming a first interaction with the top of the atmosphere is about 30 km[10] for protons and about 40 km for carbons.

[9] The following reference of an EAS picture is cited,[35].

[10] Some heights values of the first interaction for different nuclei (H, He and C) simulated with Corsika in units of g/cm^2 are included in tables of the Appendix "Data sheets from MF and RF study". More information

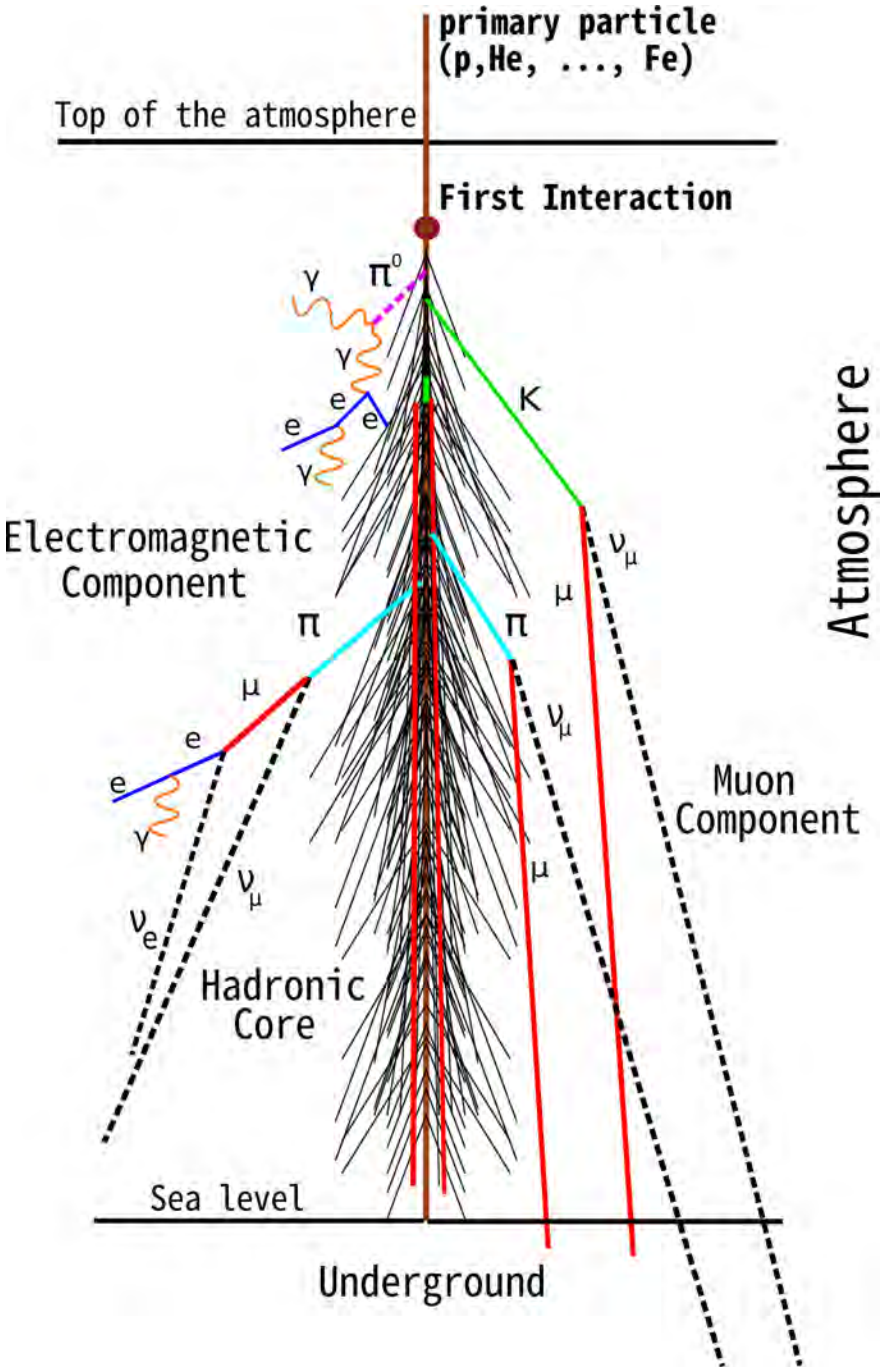

Figure 1.13: Cosmic rays air shower.

The hadronic processes of the shower located in the **hadronic core** are described by quantum chromodynamics. The production of subshowers will be higher to a higher nucleus mass according to the superposition principle. The shower depth of maximum X_{max}[11] decreases with the mass of the primary CR. The longer hadronic length is $X_{had} \sim$

values in reference [35].

[11]The depth corresponding to the maximum development of the shower X_{max} is a physic observable that determined the nature of primary CR.

$90 g/cm^2$. Then, the maximum depth of the shower in the atmosphere is approximately 0.8 km. Greater is the nucleus mass at the same energy of the primary CR, greater the height of the first interaction, smaller is X_{max} and greater the maximum number of particles at that point. The hadronic decays of the core produce vertical muons. Greater the mass of the primary nucleus at the same energy, greater the angular aperture of muons. The angular aperture of vertical muons is increasing as the mass of the primary nucleus increases. The shower arrive at ground level because the muon component is very penetrating in the atmosphere.

The Figure 1.14 [36] presents the relative chemical composition of cosmic rays from the solar system (CR solar system) and galactic cosmic rays (GCR).

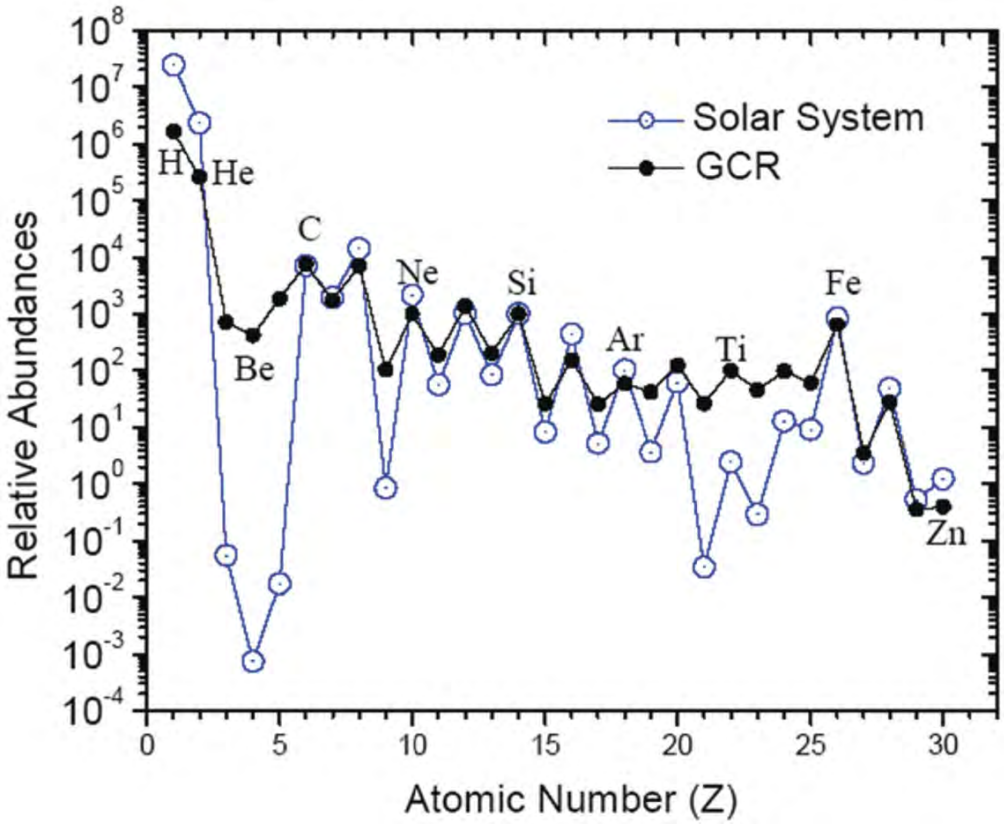

Figure 1.14: Cosmic ray relative abundances for nucleus with $1 \leqslant Z \leqslant 28$.

The chemical composition of CR solar system is similar with the elements of GCR in abundance. However, there are some very clear differences. The abundance of chemical elements decreases as the atomic number (Z) increases. The most abundant elements of primary cosmic rays are small Z. The hydrogen or proton is the most abundant chemical element with a relative value near to $2{\cdot}10^6$ for GCR and $3{\cdot}10^7$ for solar system sources. The abundance between GCR and CR solar system differs by a factor of 10. The helium (He) is the second most abundant chemical element. The relative abundance is lower than those of the proton. The discrepancy between GCR values and CR solar system

is also a factor of 10. The chemical composition is very different in abundance for the nuclei of Lition (Li), Beryllium (Be) and Boron (B). The values differ by a factor 10^4 (Li), 10^6 (Be) and 10^5 (B). The discrepancy for the Fluor (F) is also remarkable, about a factor of 20. These are secondary nuclei produced in the spallation[12] of heavier elements (C and Oxygen: O). The discrepancies are very small from Z=5 (C) to Z=20 (Calcium: Ca). The discrepancies grow from Z=21 (Scandium: Sc) to Z=25 (Manganese: Mn). The discrepancy factors are approximately 10^3 (Sc), 10^2 (Titanium: Ti and Vanadium: V) and 10 (Chromium: Cr and Mn). The discrepancy between values are again produced by the spallation of elements. These secondary nuclei come from the fragmentation of Fe. The values are not very discrepant for Fe, Nickel (Ni), Copper (Cu) and Zinc (Zn). The see-saw effect is due to the fact that the nuclei with Z (or/and A) have waker bounds and are less frequent products of thermonuclear reactions. Something important to remember from this graph is: the proton and the helium are the most abundant. The H and He of the solar system is more abundant. Around a factor 10 compared to GCRs. The C and O are the most abundant after the H and the He at small Z. A large Z dominates the Fe. Today, it is known that the protons arrived to the ground level are 74% and about 18% are heliums.

1.9 Study of EAS characteristics

The discovery of cosmic rays was the starting point of the development research of the extensive air showers. Sophisticated Monte Carlo simulation programs are used for the generation of the physical processes of EAS given the difficulty of calibrating the observatories for the study of primary CR from ground level. Corsika[13] is an example of a simulation program used for the study and development of EAS. The program is used in this thesis work for the analysis of data from EAS with different nucleus. The CRs are simply characterized by their direction, mass and energy. But, it is very difficult to associate shower with these 3 parameters that represent the primary CR. One method of analysis is to statistically study the average mass of the primary CR and associate it with a set of energetic observations and zenith angles. The astroparticle physics estimates several observables that define the space-time structure of the shower when it reaches ground level. The Figure 1.15 presents the evolution and structure of an EAS. This shows the lateral distribution of the primary CR and its characteristic properties (energy, direction and mass), the core and the front of the EAS. The front is the plane perpendicular to the EAS propagation. The air shower front encloses the time profile, the transverse component of particle, the arrival direction of the fastest particle, the density particles and clusters of particles. Some of the possible observables studied in EAS physics are: the maximum number of particles, shower depth of maximum X_{max}, the time profile, the direction of the front curvature, the particle density and the muon and electron profiles and others.

[12]The spallation is the phenomenon of fragmentation of heavy chemical elements produced by the impact of elements with highly energetic particles.

[13]See section 1.8 “CORSIKA: Extensive Air Shower Simulator”.

There are some important aspects when studying EAS. The high energy muons, electrons and gammas of low energies dominate at ground level. The temporal profile of the EAS is narrower near the nucleus when it reaches ground level. The density of particles in the shower decreases with distance to the core. The density of particles in the shower grows with the amount of particles generated in the collision region. The amount of particles generated in the collision is related to the energy and mass of primary CR. The electrons and muons are suitable for the study of EAS due to the abundance of these secondaries. The electrons/muons ratio grows with the mass of primary CR. The parameters and properties directly related to the physical observables of the EAS are defined below.

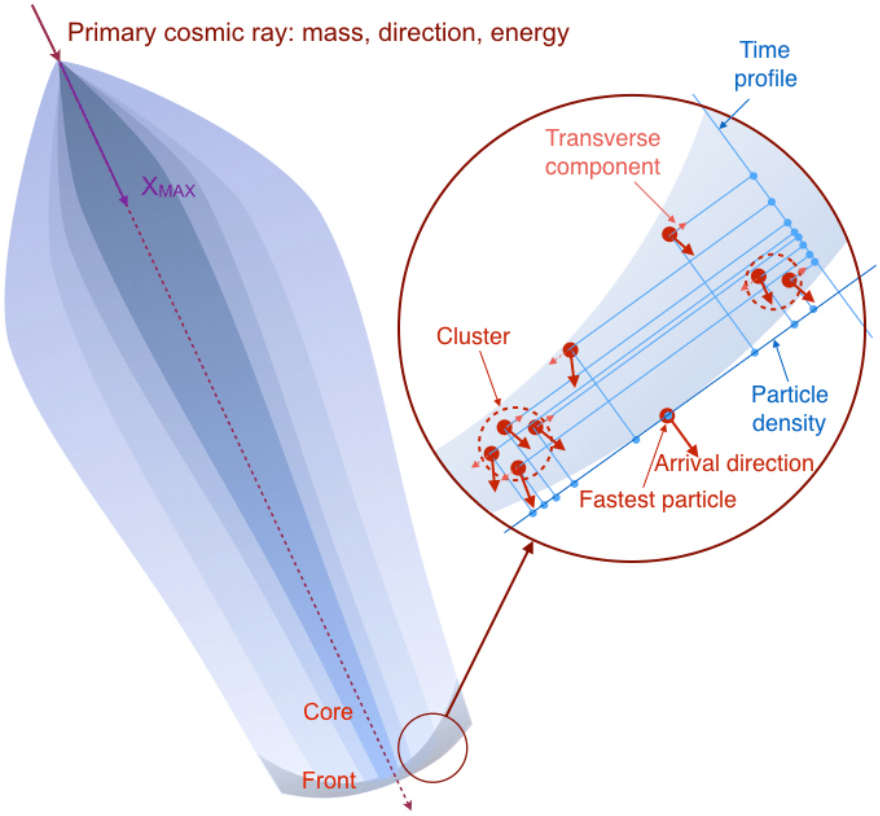

Figure 1.15: Characteristics of primary cosmic rays and possible observables to study in a EAS .

1.9.1 Motivation of EAS study

A systematic study of the main variables that characterize the EAS and their correlations are interesting for the development of detectors. The Trasgo detectors are suitable for the study of variables that characterize EAS. The behavior of different nuclei (H, He, C, Fe, ...) can be studied. The study should be done for different energy and different zenith angles. The variables of possible study are discussed below. The temporary profiles of the air shower as a function of the core distance. The arrival time of the first particle that travels at light speed from the front of the shower. The radial density, the distribution in energies and the average longitudinal-transversal components of usual particles (electrons and

muons). The clumpiness or clustering in the spatio-temporal distribution of the particles in front of the air shower[14]. The study of the response function[15] is complementary and interesting to obtain relevant information of the primary CR and its energy.

1.9.2 EAS physics

The EAS is characterized by shower size [35]. The size of an individual shower is determined by sampling the particle density distribution at ground level with an array of suitable detectors over the EAS action area. To compute the shower size N from the data sample the LDF (lateral "density" distribution function) of particles ρ is required to carry out integration over the entire shower impact area:

$$\mathrm{N} = 2\pi \int_0^\infty \rho(\mathrm{r})\, \mathrm{r}\, \mathrm{dr} \ .$$

The particle density ρ(r) represent the flux of shower particles integrated overt the event time t and solid angle Ω, at distance r from the shower axis. It include the full particle mix. The density distribution can be obtained experimentally from measurements or derived theoretically with the help of cascade theory. The original classical and theoretically is well founded and considers only the electromagnetic processes to describe the air shower. Then the density distribution is described simply. The **density of particles** or the LDF of particles ρ [m^{-2}] depends on the distance r and weakly depends on the shower size N_0 (number of particles) at a given distance to the core. The lateral density distribution is represented by:

$$\rho(\mathrm{r}, \mathrm{N}) = \epsilon \cdot \mathrm{N}_0 \cdot \mathrm{r}^{-\mathrm{n}} \ , \tag{1.5}$$

where both, ϵ and n, depend on the mass of the primary CR. For a proton ϵ=0.00053 and n=1.5. The empirical description of LDF defined is very simple but the equations can be more complex. The Table 1.3 presents some LDF equations: the Greisen equations of 1960 [37] for muons and electrons, the modified Nishimura-Kamata-Greisen (NKG) equation and others.

The secondary particles in an EAS are bunches that move at the speed of light toward the ground level with the direction of the primary particle. The bunches will hit the ground level at different times when they are not exactly parallel to the surface. The Figure 1.16 shows the time profile and density of two showers fronts. The particle density and the temporary width of the shower front changes with the distance to the center of the shower. The shower of high energy have a greater density of particles and a higher temporal profile than the shower of lower energy.

[14] See the study in section 6.3.3 "Cluster analysis".
[15] See section 6.2 "Estimating primary energy of CR with Trasgo detectors".

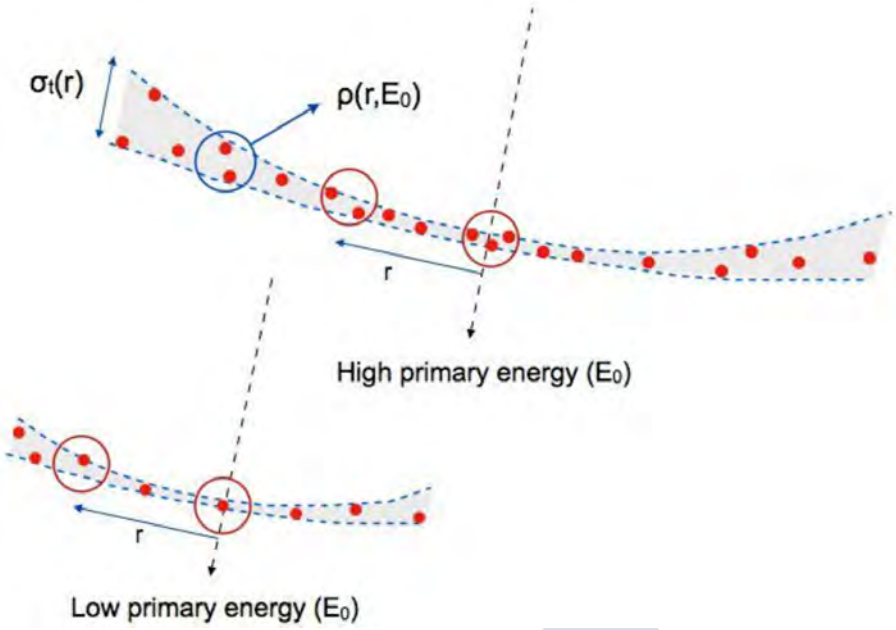

Figure 1.16: Time profile and density of showers at different energies of the same primary cosmic ray.

The **time width** or time spread σ_t [ns] of a shower increases significantly with the distance r [m] to the axis of the shower and is quite independent of the energy of the primary CR. This Behaviour was parametrised by J.Linsley [38] in the form:

$$\sigma(r) = \sigma_{t_0} \left(1 + \frac{r}{r_t}\right)^{\zeta} , \tag{1.6}$$

where σ_{t_0}=2.6 ns is the initial time dispersion, r_t=30 m is the distance to the shower axis and ζ=1.6 is an empirical parameter. The parameter r can be determined if σ_t measurements are known. The **energy** of the primary CR is closely related to the size of the shower by:

$$E_0(N_0) \simeq \kappa \cdot N_0^b , \tag{1.7}$$

where for protons $\kappa = 2.217 \cdot 10^{11}$ and b=0.798 [21]. The energy of primary CR as a function of the time width and the density of particles measured by a single detector can be found. A new equation can be found by substituting the distance of the shower r of the equation 1.6 in the equation 1.5 of density of particles and replacing it in the equation 1.7 of energy. The energy can be rewritten as:

$$E_0 = \kappa \left[\frac{\rho}{\epsilon}\left(r_t\left[\left(\frac{\sigma_t}{b}\right)^{\frac{1}{\zeta}}\right] - 1\right)^{n}\right]^{b} .$$

The study of temporal and density profiles can be very complex. Therefore, the data can be difficult to fit. Table 1.3 shows parametrization formulas used in several studies of temporary profiles and density of shower performed by different researchers and various research groups. On the one hand, the parametrization formulas are represented: LDF for electrons and muons, the total particles, number of muons ratio, time spread and others.

Table 1.3: **Parameterizations of observables studied in a EAS**.

Parametrization formula	Comments	Reference
E[R^{-1}]=2000 m, R_{min}=1300 m.	Experiment with 3 tanks with liquid scintillator and one PM RAC 5819.	[39]
$\rho_e(R) = C\left(\frac{R}{R_m}\right)^{-\alpha}\left(1+\frac{R}{R_m}\right)^{-\eta-\alpha}$ $R_{moliere}$=91.6 m $\rho_\mu(R) = C\left(\frac{R}{R_0}\right)^{-0.75}\left(1+\frac{R}{R_m}\right)^{-2.5}$ [200 m-1 km] R_0=280 m.	Akeno new array Ref. Greisen. AnRevNSci 10, 63 (1960).	[40]
$\rho(R) = 0.18\left(\frac{N}{R_0}^2\right)\left(\frac{R}{R_0}\right)^{-1.2}\left(1+\frac{R}{R_0}\right)^{-2.3}$, with R_0=100 m.	Analysis of one HE event.	[41]
K= $\left(\frac{N_\mu}{N}\right) = B\left(\frac{E}{A}\right)^{-q}$, with R_0=100 m.	- Analysis of data at $10^{17}-10^{18}$ eV - $\frac{\rho_\mu(obs)}{\rho_\mu(exp)}$ $\sim$ age of the shower.	[42]
K= $\left(\frac{N_\mu}{N}\right) = 0.061\left(\frac{R}{100}\right)^{0.74}$, with: 80 m<R<1000 m.	- Analysis of data at R in [200, 1500] m - $\frac{1}{2}$ of muons produced at h<320g cm^{-2} Heigth of first muons greater for inclined shower.	[43]
D(R)=(kN)R^{-n}, with: D=Energy loss density, kN=const.	- R in [200, 600] m: n=2.95 - D=$\frac{1}{600}$ E_{tot}s	[44]
t_m(R)=a+bR, with: t_m=median(t), a in [35, 56], b=[0.15, 0.20].	E$\sim 10^{18}$ eV.	[45]
d(t)=0.39 t^a e^{-bt} with: a$\sim$0.9, b$\sim$0.6.	- R in [4, 10] m, t<12 ns	[46]
$\rho(R)$=C$\left(\frac{N}{R_0^2}\right)\left(\frac{R}{R_m}\right)^{s-2}\left(1+\frac{R}{R_m}\right)^{s-4.5}$ with: N shower size, s age, R_m Moliere length.	C(s)= $\frac{\Gamma(4.5-s)}{2\pi\Gamma(s)\Gamma(4.5-s)}$.	[37, 47]
σ(t)=σ(t$_0$)$\left(1+\frac{R}{R_t}\right)^b$ with: σ(t$_0$)=2.6 ns, R_t=30 m, b=1.5.	Several interesting estimates about time and angular resolutions.	[48]
σ(t)=B R$^\beta$, B=0.0158 ns, β=1.5 ρ(R)=C N R^{-n}, C=853, n=3.8, N: size J(N)=D N$^{-\gamma}$, D=318, γ=1.7 E=A eV 10^{13} N$^{0.56}$, A=1.122.	- J.Linsley - T.Hara, R>1000 m - A.M.Hillas - B.N.Afanasiev, G.Array Yakutsh	[49]

On the other hand the information related to the parameterizations formula is given with comments. Finally, the bibliographical references are added. More information related to equations used in lateral distribution studies see references [35, 50].

1.10 Particle Interaction with matter

Particles lose energy as they interact with matter, ans such loses are far different depending on the nature and main properties of the given particle: electric charge, mass, kinetic energy. A deep understanding of all the processes of particle interaction with matter is mandatory for any development in radiation detectors.

In the following lines, a small description of a particle interactions with matter is given. First, *heavy* charged particles are discussed. All particles heavier than electrons are considered as *heavy* particles (that is, from pions, muons and on). Then, the case of photons and electrons is treated. Finally, a summary of a neutron interactions is given.

1.10.1 Energy loss by heavy particles

At intermediate energies, the mean rate of energy loss by moderately relativistic charged heavy particles is described by the Bethe equation:

$$\left\langle -\frac{dE}{dx} \right\rangle = K\, z^2\, \frac{Z}{A}\, \frac{1}{\beta} \left[\frac{1}{2} \ln \frac{2m_e c^2 \beta^2 \gamma^2 W_{max}}{I^2} - \beta^2 - \frac{\delta(\beta\gamma)}{2} \right] , \tag{1.8}$$

where:
$K = 4\pi\, N_A r_e^2 m_e c^2$,
z is the charge number of incident particle,
Z is the atomic number of incident absorber,
A is the atomic mass of absorber,
β is the particle speed,
γ is the lorentz factor,
I is the mean excitation energy,
$\delta(\beta\gamma)$ is the density effect correction to ionization energy loss.
The W_{max} is the maximum energy transfer in a single collision. W_{max} is described as follows:

$$W_{max} = \frac{2m_e c^2 \beta^2 \gamma^2}{1 + 2\gamma m_e/M + (m_e/M)^2} ,$$

where M is the mass of the particle. At low energies $2\gamma m_e \ll M$ so $W_{max} = 2m_e c^2 \beta^2 \gamma^2$. If $2\gamma m_e \gg M$, $W_{max} = Mc^2 \beta^2 \gamma$.

Equation (1.8) describes the mean rate of energy loss in the region $0.1 \simeq \beta\gamma \simeq 1000$ for intermediate-Z materials with an accuracy of a few percent. It can be showed either as *mass stopping power* in MeV g^{-1} cm^2 or as *linear stopping power* in MeV/cm (only the density factor of medium is the difference). The stopping power in several materials is computed in Figure 1.17. In general, particles with the same velocity have similar rates of energy loss in different materials. On the other hand, in practical cases, most relativistic particles, like the cosmic-ray muons, have mean energy loss rates close to the minimum They are minimum-ionizing particles, or MIPS. The concept of MIPS is important in detectors developments, since they lose the less, they are the less likely detected.

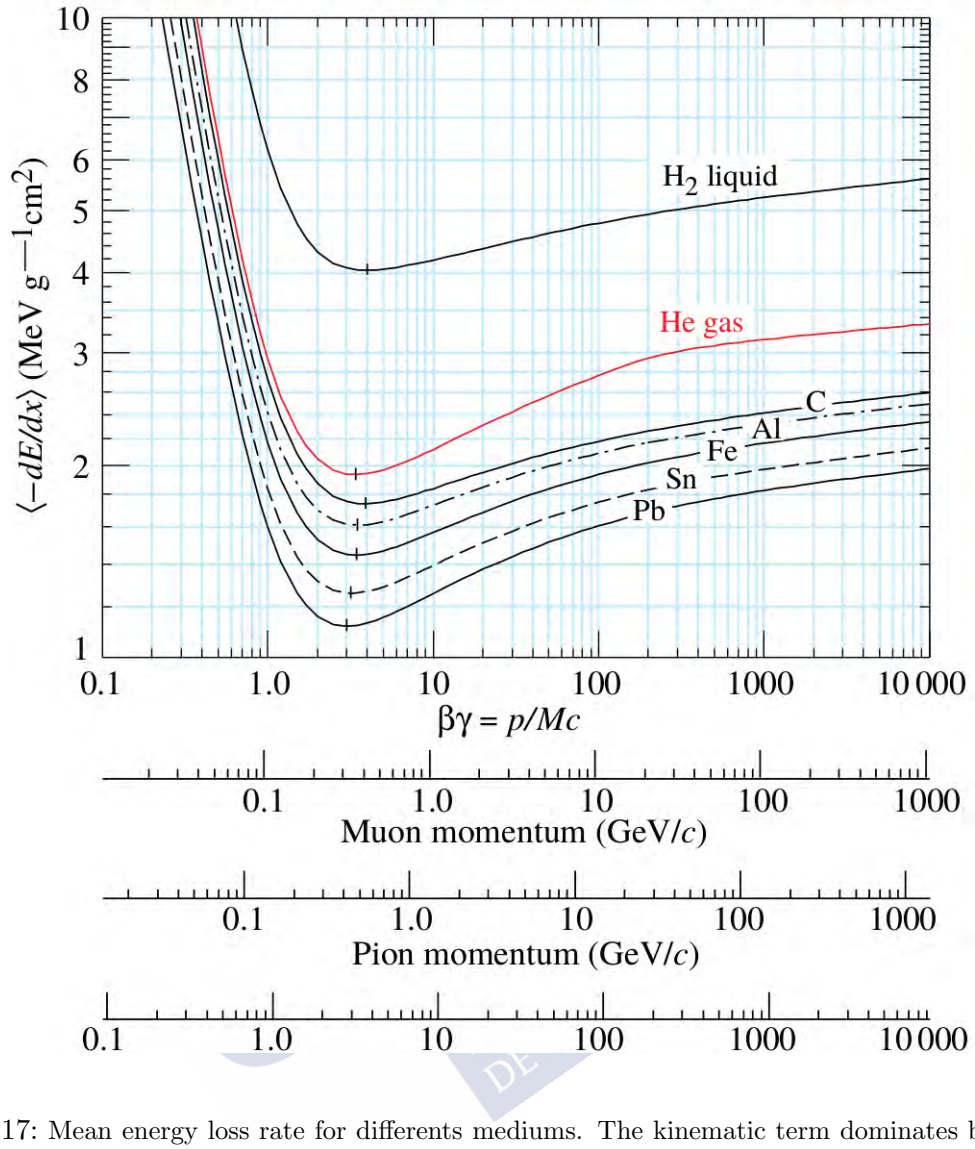

Figure 1.17: Mean energy loss rate for differents mediums. The kinematic term dominates by a factor of $1/\beta^2$ for low relativistic particles, in $\beta\gamma \approx 3.5$ there is minimal ionization particles for Z goes from 7 to 100 and the Fermi plateau for high relativistic particles appear.

At low energies, the atomic effects become important and inelastic collisions and projectile charge play a crucial role in the energy losses. The Bethe approximation is no longer valid and some corrections have to be added. For ultra-relativistic energies, another different approximations to the Bethe equation have to be considered as well. Figure 1.18 illustrates the mass stopping power of positive muons in copper over several order of magnitude in momentum. The vertical bands indicate boundaries between the different approximations.

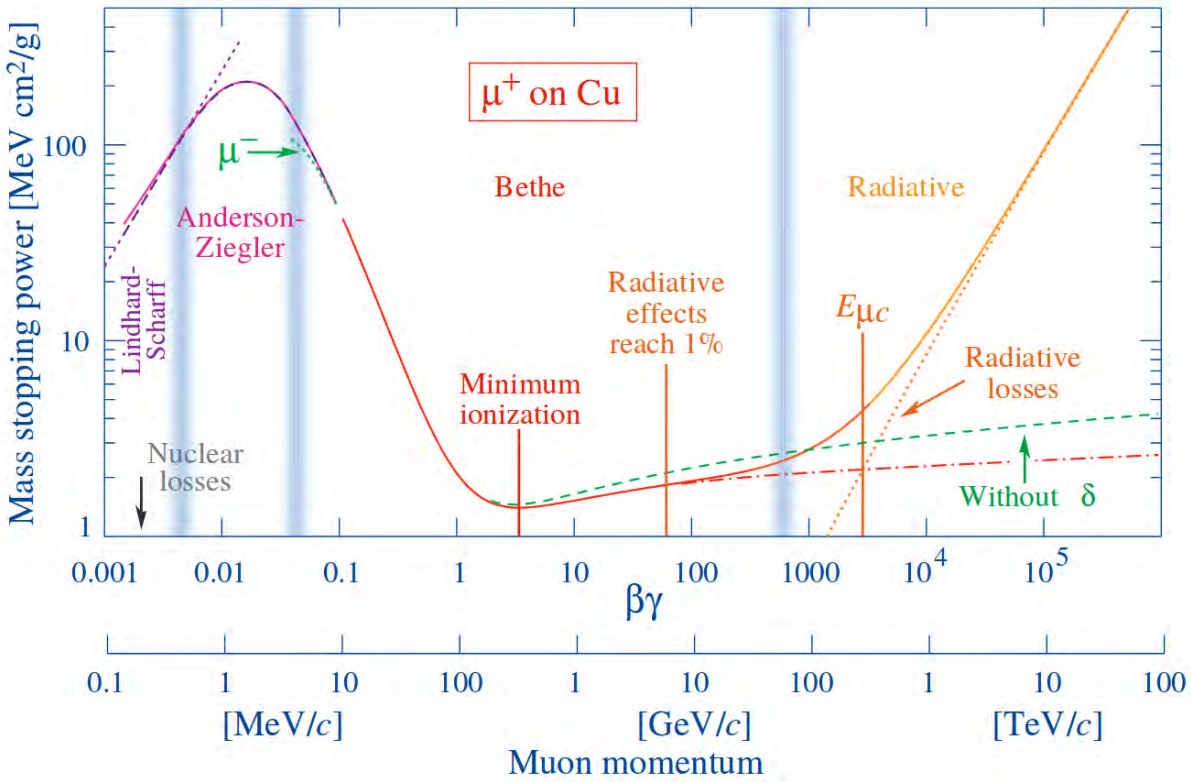

Figure 1.18: Mass stopping power diagram for positive muon in copper. At low relativistic particles, nuclear losses are significant below $\beta\gamma \approx 0.005$. Intermediate relativistic particles, the curve follows the Bethe-Bloch model, μ^+ can capture e^- below $\beta\gamma \approx 0.06$, the minimum ionization of the particles is given at $\beta\gamma \approx 3.5$ (independent of particle type and material), the radiative effects reaching 1% appears at $\beta\gamma \approx 80$ and the muon critical energy (ionization losses equal to radiation losses) appears at $\beta\gamma \approx 4000$. At high relativistic particles, radiative losses grow strongly.

1.10.2 Photon and electron interactions in matter

Photons interact with matter through three main processes: photoelectric effect, Compton scattering and pair production. Figure 1.19 shows the diagram of the three interactions. In the photoelectric effect, the gamma particle is absorbed in the inner shells of the atom and an electron is ejected; in the Compton scattering the photon interacts with the outermost electrons shells of the atom. An electron is detached from the atom and the photon is deflected with different energy; in the pair production, a photon is converted into an electron and a positron as it passes close to the nuclear field of the atom. Both, the electron and the positron are then emitted in opposite directions with high kinetic energy. The emitted positron suffers an e^+e^- annihilation a short time later. As a consequence, two opposite gamma rays of 511 keV each are emitted.

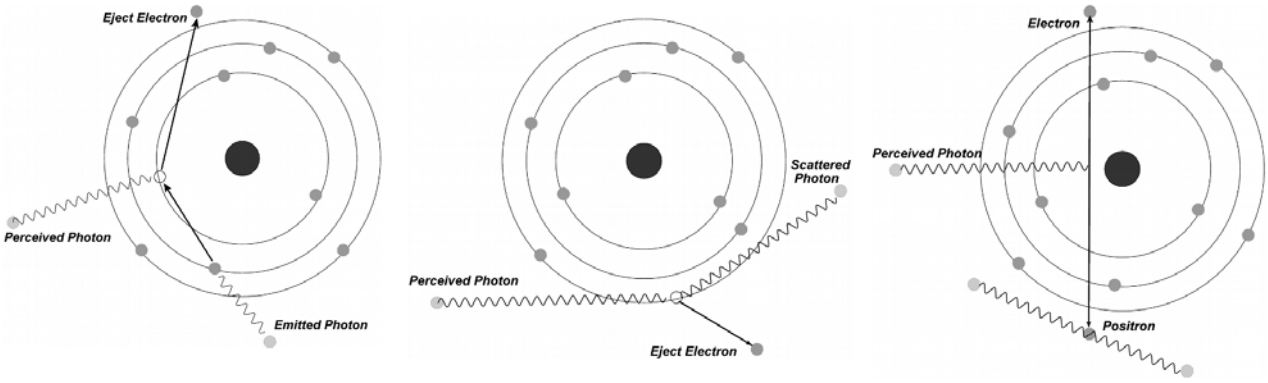

Figure 1.19: Diagrams of photoelectric effect (left): emission of a electron when a photon excited the electron in the inner shell and detach from the same. Compton scattering (center): scattering of a photon with the electron of the inner shell of the atom and detach the same electron, therefore the photon energy decreases. Pair production (right): interaction of a photon with the atomic nucleus and emission of pairs e^+e^-.

Figure 1.20 represents the total photon cross sections as a function of the energy in carbon (a diagram) and lead (b diagram).The circular dots show the experimental data of cross section. The straight and dashes curves show different processes calculated theoretically. At low energies it is seen that the photoelectric effect dominates, although Compton scattering, Rayleigh scattering and the photoelectric cross section is characterized by discontinuities (absorption edges) as thresholds for photo-ionization of various atomic levels are reached. At intermediate energies, the Compton scattering is dominant effect. And starting from the threshold energy of twice the mass of the electron (1022 keV), it is observed an increasing domination of pair production as the energy increases. The contribution of the different processes is shown below:
$\sigma_{\text{p.e}}$ is the atomic photoelectric effect,
$\sigma_{\text{Raylaeigh}}$ is the Rayleigh scattering-atom neither ionized nor excited,
σ_{Compton} is the incoherent scattering (Compton scattering off an electron),
κ_{nuc} is the pair production, nuclear field,
κ_e is the pair production, electron field,
$\sigma_{g.d.r}$ is the photonuclear interactions, most notably the Giant Dipole Resonance.

The electrons and positrons lose energy mainly by ionization at low energies, although other processes also contribute. Therefore, they have a random path through matter, driven by the multiple Coulomb scattering, before they either are ejected or stopped. The stopping power for electrons and positrons changes from stopping power to heavy particles. The change is due to the kinematics, the spin[16], the charge and the identity[17] of the electron incident with the electrons that it ionizes. The maximum energy transferred by a simple collision is $W_{max} = m_e c(\gamma - 1)$ but for identical particles the maximum is half $W_{max} = m_e c(\gamma - 1)/2$. The stopping power is calculated for the fastest electron of the two emerging electrons by convention. The moller′s equation describes the stopping

[16]The spin is a physical property of elementary particles with intrinsic angular momentum of fixed value.
[17]The identity of the particles can be defined as the symmetry of the mechano-quantum states after the exchange of physical properties of the particles.

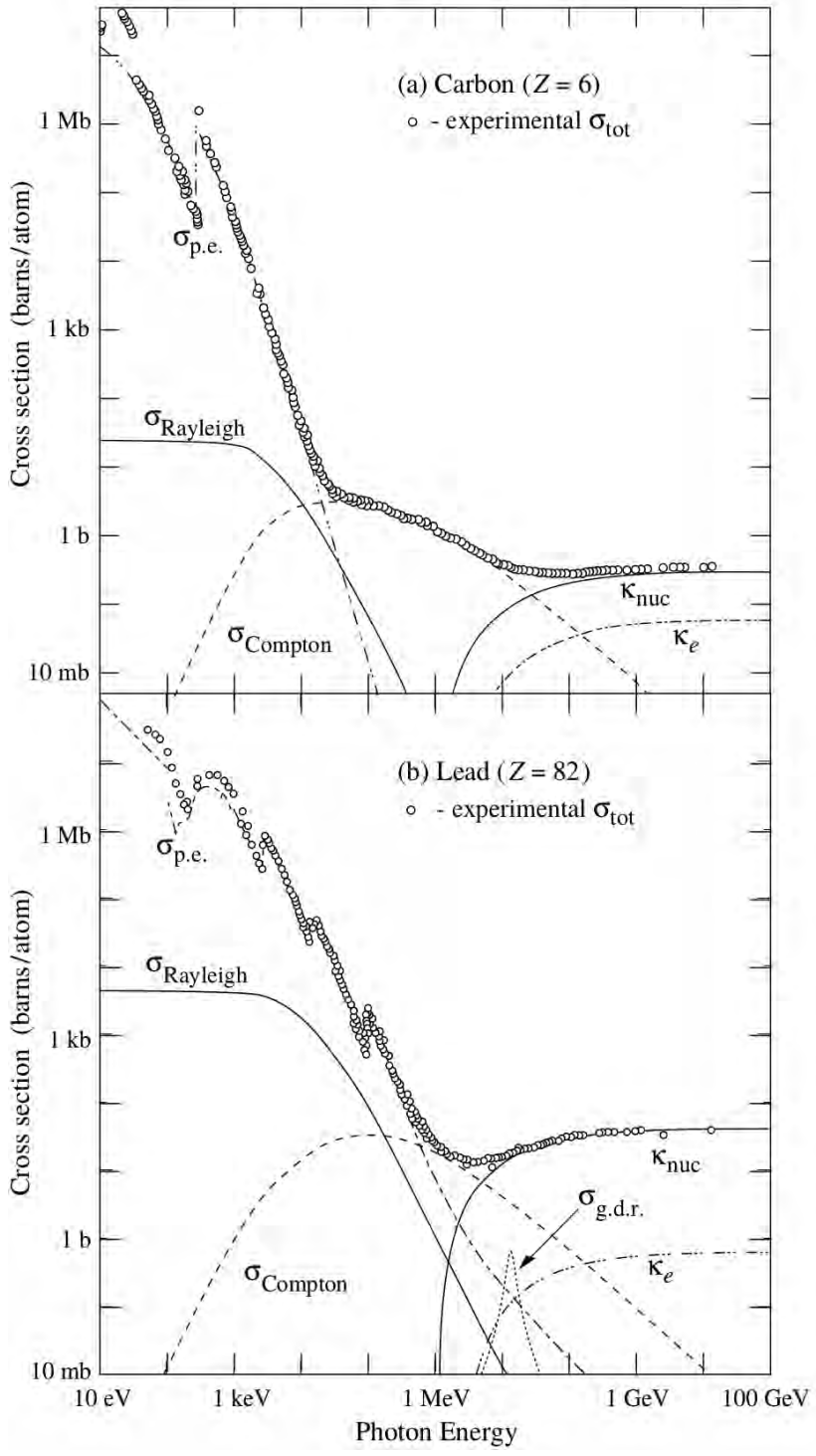

Figure 1.20: Total interaction cross section of photons in carbon (a) and lead (b). The photoelectric effect is dominant at low energies, Compton scattering is prevalent for intermediate energies (carbon phenomenon is accentuated) and pair production is the most importante at high energies.

power of electrons. The formula is written as follows:

$$\left\langle -\frac{dE}{dx} \right\rangle = \frac{1}{2} K \frac{Z}{A} \frac{1}{\beta} \left[\ln \frac{m_e c^2 \beta^2 \gamma^2 \left[m_e c^2 \left(\gamma - 1 \right) / 2 \right]}{I^2} + \left(1 - \beta^2 \right) - \frac{2\gamma - 1}{\gamma^2} \ln 2 + \frac{1}{8} \left(\frac{\gamma - 1}{\gamma} \right)^2 \right] . \tag{1.9}$$

The Bhabha equation describes the stopping power of electron-positron. The Bhabha equation is complex. The equation has terms of correction to the effect of density $\delta(\beta\gamma)$ in addition to having included the first term of the equation (1.9). The Figure 1.21 represents the fractional energy loss per radiation length in lead as a function of electrons or positron energy. The scale at losses has a size of 1.4 cm^2/g. The energy scale is extended

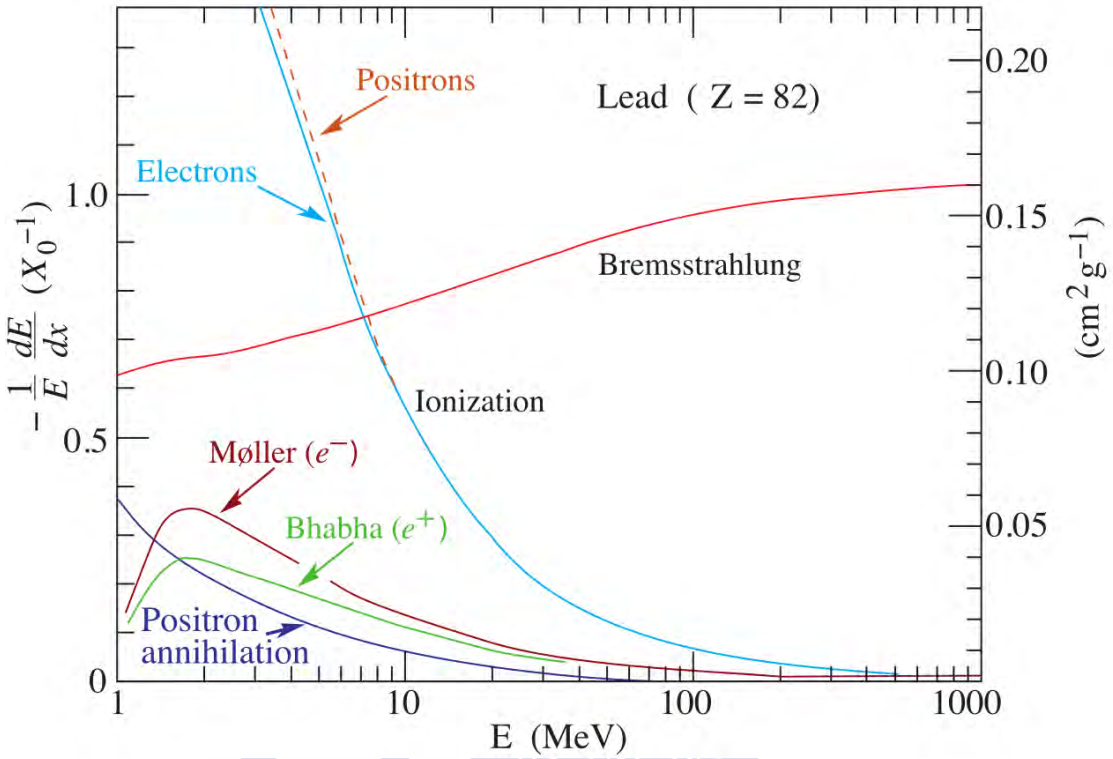

Figure 1.21: Diagram of fractional energy loss per radiation length in lead ($Z = 82$). The ionization loss of electrons and positrons are dominante at low energies, the bremsstraling loss are the most important at hight energies, and, the coexistence between phenomena is about 10 MeV.

by 3 orders of magnitude E $\in$ [1, 1000] MeV. The losses by dispersion Moller, dispersion Bhabha and annihilation e^+ are very small. The Moller and Bhabha distributions are centered at approximately 2 MeV and the maxima are 0.35 and 0.25 cm^2/g respectively. The positron annihilation curve slowly decreases to a zero value for about 60 MeV. The losses by ionization and Bremsstrahlung are higher than the previous ones. The ionization loss of electrons and positrons rapidly decreases and becomes zero at about 500 MeV. The ionization loss of electrons (blue straight) and positrons (orange dashes) have a very small change below 10 MeV. The Bremsstrahlung curve slowly increased from 0.6 cm^2/g at 1 MeV to about 1 cm^2/g at 1 TeV.

An important parameter to be considered is the radiation length, X_0. The radiation length of a material is the mean length [cm] to reduce the energy of an electron by the factor $1/e$. The X_0 can also be defined as 7/9 of the mean free path for pair production by a high energy photon λ_{pair}. The high energy electrons lose essentially energy by Bremsstrahlung and the high energy photons by the pair production e^+e^-. The radiation

length is also used as a scale to describe high-energy electromagnetic shower in a medium. X_0 is mathematically defined as:

$$\frac{1}{X_0} = 4\alpha r_e^2 \frac{N_A}{A} \left[Z^2 [L_{\text{rad}} - f(Z)] + Z\, L'_{\text{rad}} \right] \ , \tag{1.10}$$

where A=1 g mol^{-1}, $4\alpha r_e^2 N_A/A$=(716.408 gcm^{-2})$^{-1}$, α is the fine structure constant and r_e is the classical electron radius. L_{rad} and L'_{rad} have tabulated values in reference [16]. The function $f(Z)$ is an infinite sum. $f(Z)$ for the elements until the uranium is written as:

$$f(Z) = a^2 \left[(1+a^2)^{-1} + 0.20206 - 0.0369a^2 + 0.0083a^4 - 0.002a^6 \right] \ ,$$

where $a = \alpha Z$. For $Z > 4$ and a first order of $f(Z)$:

$$X_0 = \frac{716.4\, A}{Z(Z+1)\ln(287/\sqrt{Z})} \ \ [\text{g cm}^{-2}] \ .$$

X_0 for mixed materials is obtained with the following equation:

$$\frac{1}{X_0} = \sum_j \frac{w_j}{X_{0,j}} \ ,$$

where w is the weight fraction and $X_{0,j}$ is the radiation length for the jth element.

1.10.3 Neutron interactions

Neutrons are neutral particles, therefore they travel in straight lines, deviating from their path only when they actually collide with a nucleus to be scattered into a new direction or absorbed. Neither the electrons surrounding a nucleus nor the electric field caused by a positively charged nucleus affect a neutron′s flight. In short, neutrons collide with nuclei, not with atoms. Because of small size of the nucleus in relation to the atom, neutrons have very low probability of interaction. They have very long travelling distances in matter and also long life times. Thus, they are hardly detected in most detector devices.

A very descriptive feature of the transmission of neutrons through bulk matter is the mean free path length, λ, which is the mean distance a neutron travels between interactions. It can be estimated by the inverse of the cross section for all the nuclear processes which a neutron with a given energy can suffer interacting with a given medium. Elastic and inelastic scattering, capture and fission absorption processes, and transfer reactions, are the neutron-nucleus interactions that contribute to the cross section.

USC
UNIVERSIDADE
DE SANTIAGO
DE COMPOSTELA

USC
UNIVERSIDADE
DE SANTIAGO
DE COMPOSTELA

2 RPC detectors and the TRAGALDABAS experiment

Tragaldabas is the Trasgo-like detector for Cosmic Ray measurements at the University of Santiago de Compostela. The so-called Trasgo family is a set of different particle detectors, based on the resistive plate chamber (RPC) technology, and devoted to the study of Cosmic Rays. This chapter introduces first the RPC technology and the Trasgo project, and then, the Tragaldabas Cosmic Ray telescope extensively presented.

2.1 The TRASGO project

The TRASGO, or Trasgo, project (TRAck reconStructinG mOdule) started at the University of Santiago de Compostela a few years ago: it consists of the development of innovative detectors for Cosmic Rays Physics, based on RPCs, in modular configurations, with timing tracking capabilities. The very good temporal resolution contributes to achieve good arrival times and arrival direction resolutions. It also allows to achieve better efficiencies in rate reconstruction and rejection capacity of outliers. A Trasgo is designed to operate autonomously and offers the ability to arrange several of the detectors to build larger structures by assembling or overlapping them. Figure 2.1 [2] show several representations of Trasgos. The simplest model shows a single Trasgo with one RPC detector plane above the other (a). The simplest configuration can be arranged covering a larger area (b) or can be stacked one on top of the other as a column to increase efficiency and resolution (c). The conceptual design of the Trasgo-like detectors is based on the low angle TOF wall of the HADES collaboration at GSI (Gessellschaft für SchwerIonen forschung) Institute in Dramstadt (Germany) [51] which has been proved to be suitable also for Cosmic Rays measurements [52]. The simplified detector allows to analyze the internal structure of an EAS with arrival time resolution of 100 ps and angle resolution of 0.04 rad s. The efficiency is greater than 90% for shower densities of 100 particules/m^2 on an active surface of 0.8×0.8 m^2 inside an approximate volume of 0.9×0.9×0.9 m^3 [53].

The development of Trasgos also opens a wide variety of future subprojects: improvement of RPC detectors simplifying and cheapening them, development of sealed RPCs to eliminate bulky systems, search for gas to work in a wider range of temperatures and pressures, improvement of input electronics (FEE[1]) to optimize energy consumption, or improve the performance and energy consumption of a future version of the acquisition board (TRB), among others. Figure 2.1 shows some examples of different layouts that can

[1]The Front-End Electronic is defined in the section 2.4.2 “Front-End and Read-out electronics”.

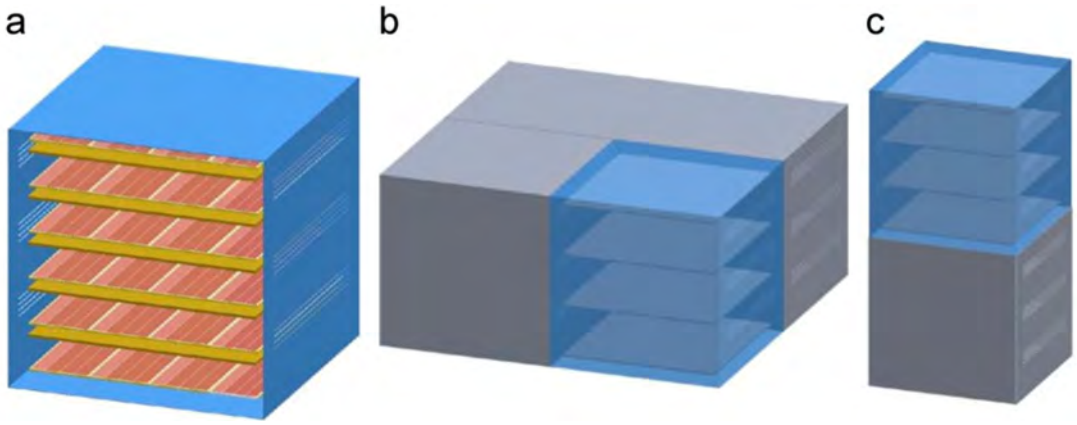

Figure 2.1: Many configuration of simplest model shows a Trasgo with some RPC detector planes arranged one over the other inside the main box (a), cover larger area than the original (b) and one on top of the other as a column to increase the detection efficiency (c). Picture from [2].

be arranged using Trasgo detectors for covering bigger surfaces or improving the angular resolution.

2.2 Resistive Plate Chamber devices

The first Resistive Plate Chamber [54] was developed in 1981 by Santonico and Cardarelli [55]. It is a variant of the widely distributed spark chambers of parallel plates developed in 1951. Between plates, a homogeneous electric field is applied through two parallel that enclose. Particles passing through the gap ionise the gas and an electron avalanche is created and therefore produce a detectable signal in the electrodes. 1956 M.V Babykin et all. [56] reduced the distance between the electrodes down to 0.2 mm and applied a mixture of argon and ether to the camera. The timing resolution resolution of the spark chamber improved at the level of ns. In 1970 V.V Parkhomchuck et al [57] improved the design by introducing a very high resistivity material limiting the progress of sparks in the detector. This improved the counting rate and the size of the device. Then, after that, Santonico and Cardarelli developed and RPC device with 97% detection efficiency, timing resolution of 1.2 ns and working at atmospheric gas pressure. The space between plates was 1.5 mm and the applied electrid field between electrods was 60 kV/cm. The device was simple and cheap compared to other detectors with similar characteristics. The gas mixture used was 50% Argon and 50% isobutane. In the year 2000, P. Fonte et al. developed the timing RPC [58]. The last device is the timing RPCs developed in 2000 by P.Fonte et al [58]. The detector is capable of providing a time accuracy of 120 ps and an efficiency of approximately 98% for MIPs. The design consists of plates with 10^{-12} Ω cm resistivity and metallized ceramic electrodes. The gas mixture was freon with isobutane as inhibitor and sulfur hexafluoride (SF_6). The now called standard mixture is Freon R134a/iButane/SF6 at 96.7/3/0.3 %, respectively. Currently, RPCs have been used with success in experiments and collaborations such as: ATLAS [59] (A Toroidal

LHC ApparatuS), ALICE [60] (A Large Ion Collider Experiment), HADES [61] (High Acceptance Di-Electron Spectrometer) and others (CMS, STAR, HARP, FOPI, ...).

ATLAS RPC system is located in the Muon Spectrometer. The Muon Spectrometer is submerged under a toroidal magnetic field and measures the signal from high-energy muon traces. The RPCs provide the first-level muon trigger and the measurement of the coordinate. The Figure 2.2 [59] shows the disposition of the RPCs by the detector. The system is composed of 3 concentric layers of RPC doublets. Each layer is organized in 16 sectors along the azimuth coordinate of the detector. There is a total of 3714 RPC gas volumes covering an area of approximately 4000 m^2.

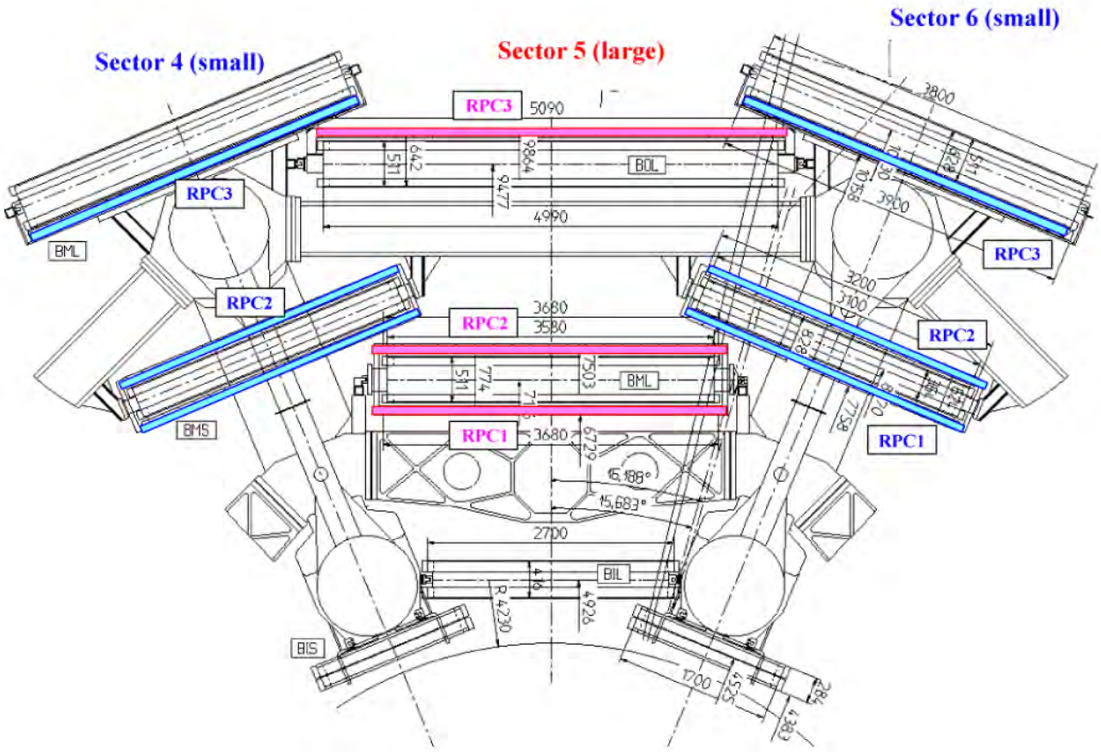

Figure 2.2: Layout of the RPC ATLAS system. RPCs is located in the muon spectrometer of this large detector and provide the tracking of muons with a first-level trigger.

ALICE has been designed to investigate the properties of matter that interact strongly at very high temperatures and densities. The design of ALICE is determined by the very high multiplicity of high energy ion collision events. The Figure 2.3 shows the schematic drawing of one TOF supermodule. The supermodule comes from the external zone of the cylindrical design of the detector. The detector is segmented into 1593 multiple-space RPC symmetric modules (MPRC).

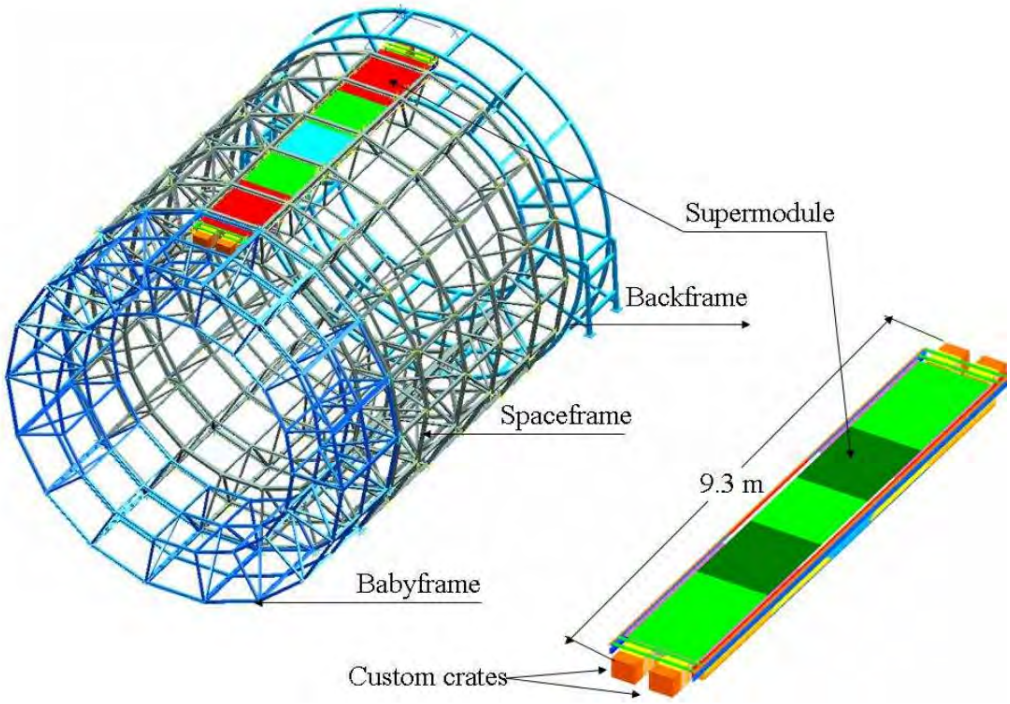

Figure 2.3: The TOF ALICE system. RPC detectors provide the muons trigger of the experiment, the devices are located in the out region of the experiment and have a total area of about m^2.

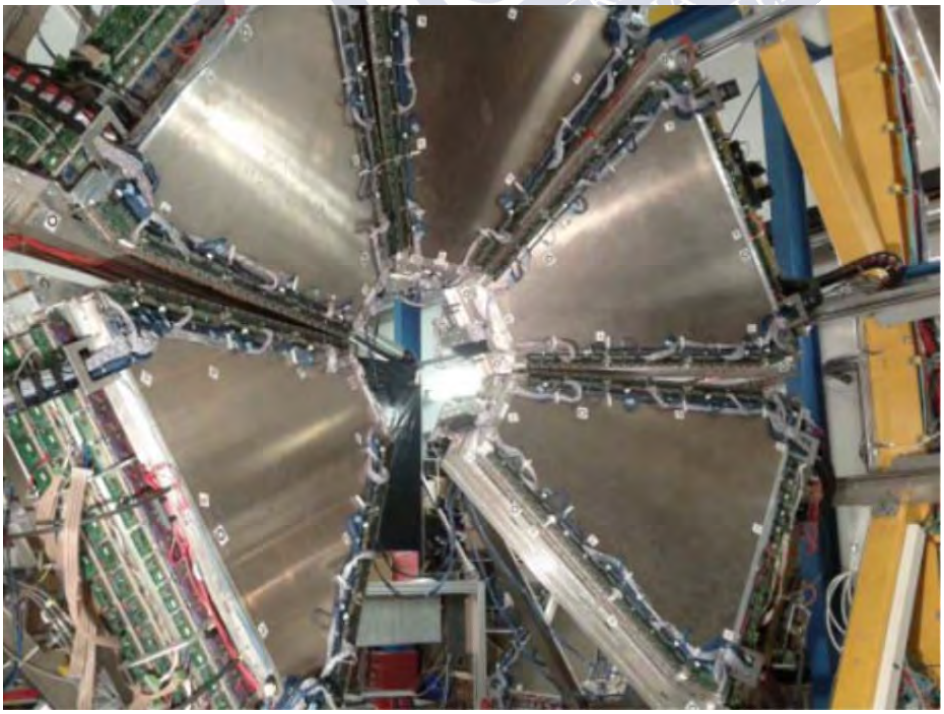

Figure 2.4: Photograph of the HADES RPC wall. The system consists on 6 sectors of 4-gap timing RPCs of around 1 m^2 each, covering the low polar angle region of the HADES experiment.

HADES is a detector for the precise spectroscopy of dielectron pairs (e^+e^-) and charged hadrons produced by collisions of pions, protons and heavy ions in the kinetic energy range of [1,3.5] GeV. The main objective of the HADES experiment is to investigate the properties of dense nuclear material cured by strong ion collisions and to learn intrinsic properties of hadrons such as masses or decay widths. Figure 2.4 shows the HADES RPC TOF wall detector. The wall is divided into 6 trapezoidal sectors that cover a total area of approximately $8m^2$. It is composed of 1116 timing-RPC cells, of four gas gaps of 0.3 mm, in a symmetric configutration and achivied a time resolutions of about 80 ps and position resolution of a few mm.

2.3 Electrons avalanches in RPC gas

The electric avalanche [62] is produced in the gas gap located between conductive layers. Such gap has a thickness of from hundred microns to a few millimeters and is defined as gas gap. A voltage is applied between the electrodesgenerating an electric field. A charged particle passing through the gas gap ionizes the gas atoms. The electrons and ions released are accelerated by the electric field and interact with the gas molecules. The applied voltage must be high enough to avoid the recombination of positive ions and electrons. This effect would give a false indication of the velocity of ion formation and charge. The charge induced by the electrons in the electrodes is the collected signal. In timing RPCs, amplifiers are needed. The modus operandi is to use the fast electron signal. For this, the time constant $\tau = RC$ (measurement time) must be greater than the rise time of the signal induced by the electrons but less than that of the ion. The electrons gain enough energy to ionize other gas atoms if the external applied voltage is high enough. Typically, voltages or more than 50 kV/cm are needed. This process is repeated until the electrons are collected at the anode. This phenomenon is called an avalanche of electrons. John Sealy Townsend observed and studied Electron avalanche multiplication phenomena in gases between 1897 and 1901 [63]. The total charge Q generated by the multiplication process is:

$$Q = n_0\, e\, M \ ,$$

where n_0 is the number of ion pairs produced, e is the electron charge and M is the multiplication factor. The process of gas multiplication takes the form of a Townsend avalanche where each free electron created in the gas can create more free electrons by the same process. The Towsend equation provides the fractional increase in the number of electrons per unit path length:

$$\frac{dn}{n} = \alpha\, dx\,,$$

where α is the first Townsend coefficient and increases with electric field. By integrating the equation 2.3, one obtaind the next expression:

$$n(x) = n(0)e^{\alpha\, x} \ ,$$

where x is the distance to the anode. The electron density grows exponentially towards the anode.

2.4 The TRAGALDABAS telescope detector

2.4.1 Introduction to the experiment

The TRAGALDABAS or Tragaldabas detector (TRAsGo for the AnaLysis of the nuclear matter Decay, the Atmosphere, the earth B-Field And the Solar activity) [3] is a Cosmic Ray telescope of the Trasgo family. Tragaldabas is located in the labCAF research laboratory. The laboratory is devoted to the development of radiation detectors, instrumentation and associated analysis techniques. The facilities are inside the building of the Faculty of Physics of the University of Santiago de Compostela (USC), Galicia (Spain). The detector is located at the geographic coordinates of N 42° 52′ 34″ and W 8° 33′ 37″and at about of 260 m above sea level. Figure 2.5 show the exact location of the detector inside the building. The detector is represented as a gray rectangle on the image. The arrangement of the detector inside the laboratory is shown as well. The x-axis of the detector is oriented to 301.5° North (N) and corresponds with the largest dimension of the detector.

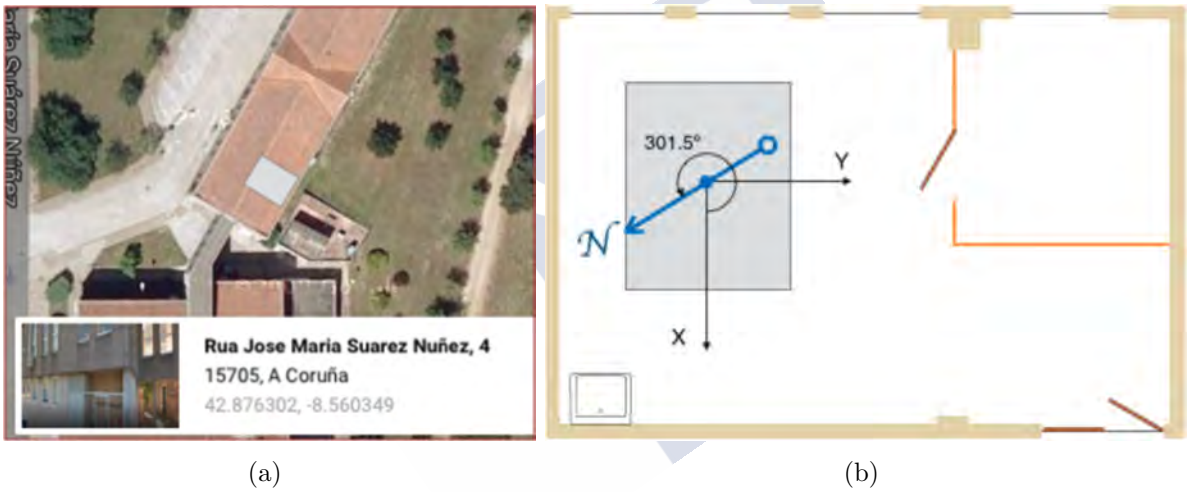

(a) (b)

Figure 2.5: Tragaldabas situation in USC physic building (a) and Tragaldabas emplacement in laboratory labCAF and coordinates disposition of experiment (b).

The Figure 2.6 shows the start-up of the Tragaldabas detector. The device has 4 planes on a scaffolding structure with a height of 1.8 m. Each RPC plane has dimensions of 1650×1285×26 mm^3 and a weight of ∼90 kg. Each RPC plane houses 120 rectangular RPC cells of 111×116 mm^2 separated by 10 mm. The RPC cells is composed by 2 gaps of 1 mm where it lodges R134a commercial freon gas. The planes are placed at a height of 187 cm (T1), 135 cm (T3), 97 cm (T3) and at ground level (T4). The trigger[2] signal can be produced by using a coincidence signal between whatever two planes. Actually 3 planes are in continuous operation and taking data regularly since April 2015 from air showers. The detector collects ∼7 million of events per day, equivalent to a particle

[2]The trigger can be definded as procedural that is automatically executed in response to certain signal or event in a particular database. The trigger is mostly used for maintaining the integrity of the information on the database.

rate of about 80 Hz. The detector has an angular resolution better than 3°. The time resolution provided by the detector-acquisition electronics chain is approximately 280 ps. The spatial resolution of the detector is approximately 3 cm, the speed resolution of the particle is 5% of the speed of light and the Hit efficiency of each plane is around 90% for MIPs. Many of the charged particles that reach the ground can be identified with this Trasgo detector: muons, protons and electrons.

Figure 2.6: The Tragaldabas experiment inside the Laboratory of Carmen Fernández.

The next future perspectives of the system are the connection of the 4 planes, collect data of a 4-planes trigger signal and to place a lead layer of 1-2 cm of thickness after the T3 plane in order to increase the calorimetric capacity of the detector. These supplements to the apparatus will provide a substantial improvement in the detection, tracking and identification capabilities of Tragaldabas.

The **RPC cells of Tragaldabas** are are enclosed in an aluminum box, holding a sandwich structure, as it is shown in Figure 2.7. The copper layer collects the electrical signal after

the passage of a charged particle and the signal is sent to the FEE[3]. The same layer of Cu has a guard strip that attenuates any small parasite signal caused by electrical induction. Other visible components are the conductive coating, the metacrilate box and the glass plates, which act as the high resistivity material.

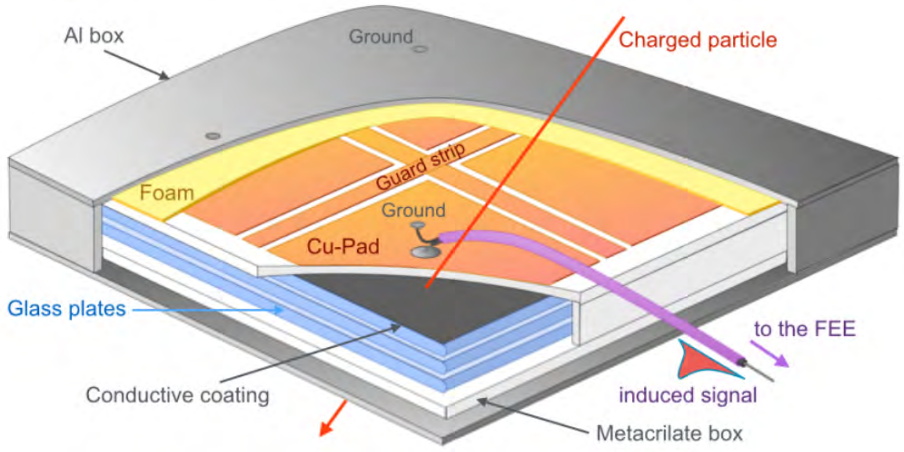

Figure 2.7: Components in a plane of the detector. The cross section of the plane show the aluminum case, different layers of the pads, guard strips between pads and the signal taking electrode situated in the center of the pad (ground).

The Figure 2.8 shows the diagram of double gap RPC cell. There are 3 layers of Glass of 2 mm thickness making the two gaps of 1 mm each. Two layers (±HV) subjected to a high voltage of ±5600 V. The image also presents the ground connection, the readout pad and the guard strips, which are used to avoid crosstalk between read-out pads.

The Table 2.1 shows the different materials of TRAGALDABAS RPC, together with their corresponding width (in mm) and radiation length (in cm). The materials are: aluminum (Al), foam, copper (Cu), Printed Circuit Board (PCB) with a thin layer of Cu foil laminated (FR4), metacrilate, glass and freon R134a gas gap. The total width of a single RPC plane is 26 mm. The values of X_0 are taken from reference [16]. ΔX_0 (in cm) represents de radiation length weighted by the widht and density of the material. The total ΔX_0 through the RPC plane is 0.27 cm. The radiation length of lead is 0.5612 cm (6.37 g/cm^2) [16], so a layer of 1 and 1.5 cm of this material gives an ΔX_0 value of 0.5612 and 0.8418, respectively.

[3]FEE is defined in the section 2.4.2 “Front-End and Read-out electronics”

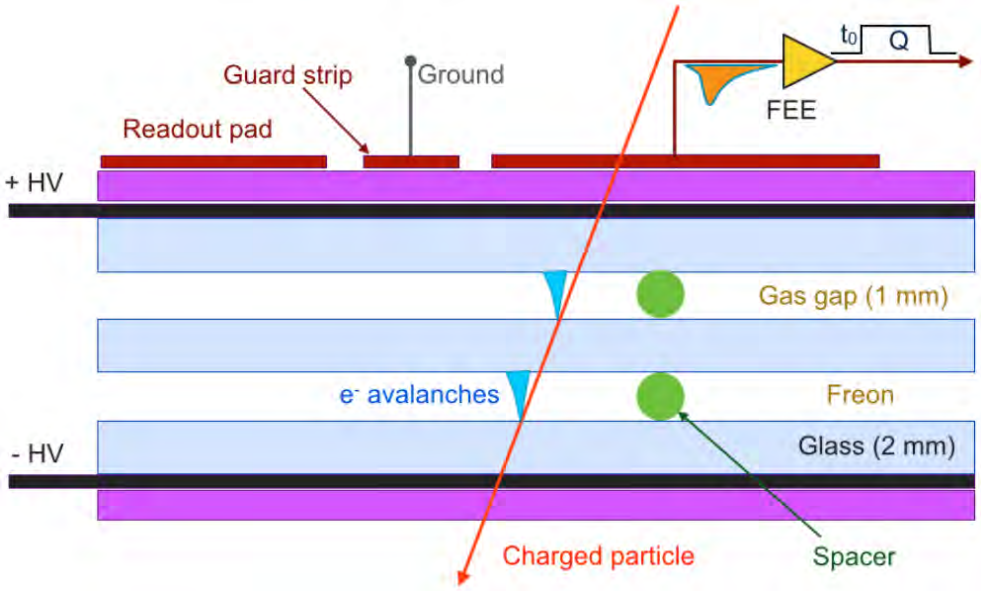

Figure 2.8: Symplified transversal cut of a Tragaldabas RPC cell. The picture show the particle crossing the device where an avalanche of electrons is generated in the gaps and producing a electrical signal going to the FEE.

Table 2.1: **Different materials of the TRAGALDABAS RPC cells, stacked in a sandwich-like configuration, together with their corresponding width and radiation lenght. The value of ΔX_0 represents the radiation lenght per material, wighted by its width and density. The total radiation lenght for a single RPC plane is about 0.27 cm.**

RPC layout	Width(mm)	X_0(cm)	ΔX_0
Al	3	8,9	0,034
Foam(dens=0.3)	8,7	142,0	0,006
Cu	0,03	1,4	0,002
PCB (FR4)	1,57	31,8	0,005
Metacrilate	1	40,8	0,002
Glass	1,9	3,2	0,059
Gas: R134a	1	26,5	0,004
Glass	1,9	3,2	0,059
Gas: R134a	1	26,5	0,004
Glass	1,9	3,2	0,059
Metacrilate	1,0	40,8	0,002
Al	3	8,9	0,034
Total	26		~0,27

2.4.2 Front-End and Read-out electronics

Clear and reliable electronics signals are essential in any Physics experiment. The RPC signal must be collected, read and amplified. An entire high performance electronic chain is setup for that: the so-called Front-End Electronics, FEE. The main component of the electronics is called Front-End Electronics (FEE). The FEE is the element of the detector that collects the first electrical pulse, elaborates it, and leads it to the data acquisition system. The Tragaldabas uses the FEE developed for HADES experiment [64]. The Tragaldabas FEE is divided in two different boards: the so-called Daughterboard (DBO) and Motherboard (MBO). Figure 2.9 show the different components of a DBO, this board has a size of this device is 5×4.5 cm^2. The objective of the device is to take the direct signal from the RPC and convert it into a signal whose data acquisition device can read. The analog signal is collected by the DBO with the DBO-RPC cable. The amplification, integration and discrimination of the signal is given in the same device. The analog signal is converted into a digital signal by the PECL-LVDS converter. The output of the signal is sent to the MBO. Each DBO holds 4 read-out channels.

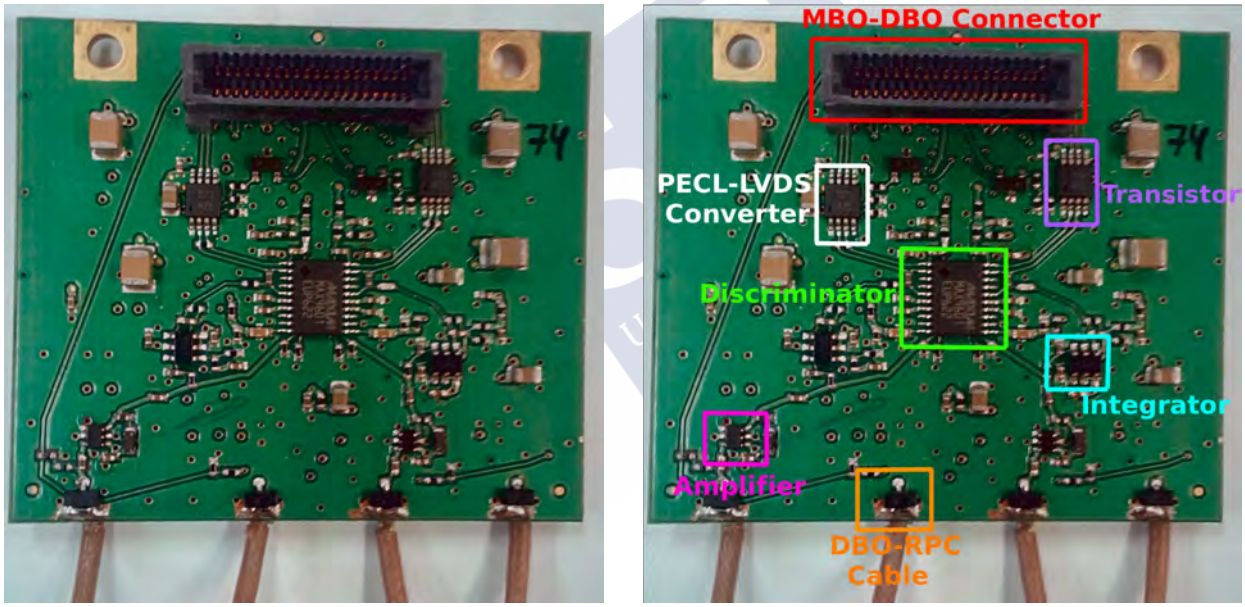

Figure 2.9: Photograph of the Daughterboard of Tragaldabas. The connection device collect the analog signal of a pad and converts it into a digital signal.

The Figure 2.10 presents the components of an MBO of the Tragaldabas experiment. This device has a size of 60×40 mm^2. Each MBO holds 8 DBO, having then 31 available data channels. Channel 32 is used for distributing a testing pulser signal. The voltage required by the DBO are ± 5 V and $+3.3$ V, and the current consuumptions are 80 mA. 40 mA and 35 mA respectively. The MBO sets and controls the acquisition thresholds throught DACs, and converts each data signal into LVDS signals that are sent to the final TRB acquisition boards. In addition, the MBO has a trigger logic stage where a logic trigger signal is produced after selection the desired data channels multiplicity.
The data acquisition (DAQ) of the Tragaldabas experiment is driven by the so-called

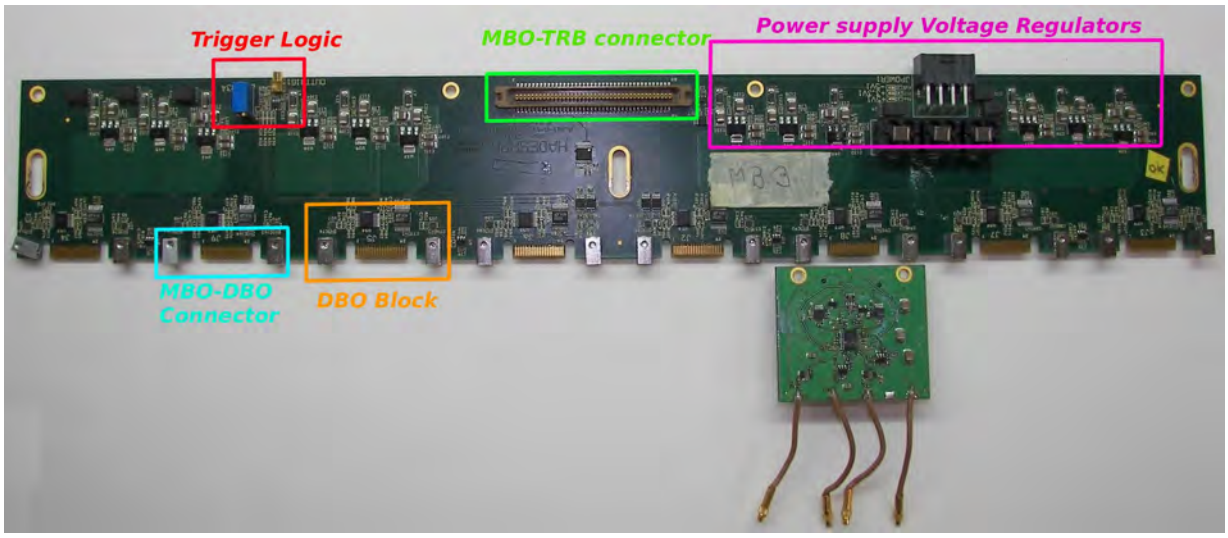

Figure 2.10: Motherboard and Daughterboard of Tragaldabas. The moterboard provides power supplies and collects the signal from these detecting devices and sends it to the TRB board with the connector. It also provides the multiplicity trigger signal.

TDC Readout Board, TRB. Actually, Tragaldabas is currently using the second version (TRBv2) of the device developed at GSI for the HADES experiment [65].

Figure 2.11 show the TRBv2 of a plane of the Tragaldabas detector, The size of this board is 200×230 mm^2.

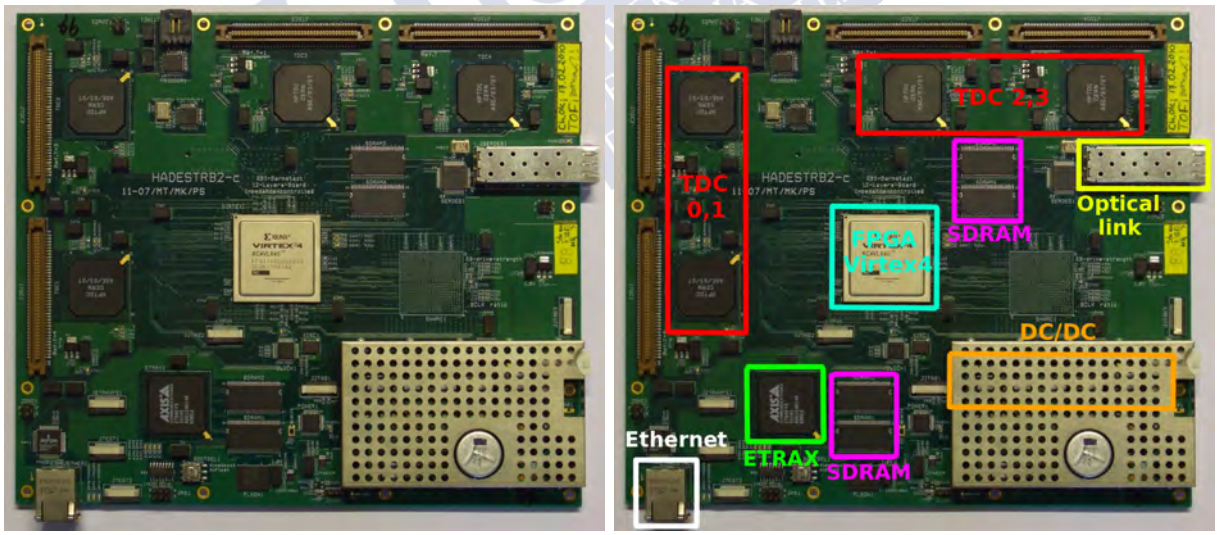

Figure 2.11: TRBv2 acquisition data. The photograph shows the electrical supply devices, TRB-moterboards connectors and signal assemblies, saving memory in SDRAM, analysis and filter data components, and signal sending with Ethernet to the central control unit.

The most important features of the TRB are: the time-to-digitals converters (TDCs), the synchronous dynamic random-access memory (SDRAMs), the field-programmable gate array (FPGA) Virtex4, the Ethernet Token Ring AXis (ETRAX), the ethernet, the Optical link and the DC-DC. A TRBv2 has four TOCs (0,1,2 and 3) and therefore enough

connectors to link a set of up to 4 MBO (32 DBO). The TDCs are used for the digital conversion of the signal pulses. The TDCs have multi-hit capabilities allowing the arrival time of several simultaneous signals. The High Performance TDC chip (HP TDC) was developed at CERN. The TRBv2 has 4×512 Mb SDRAM memory and a programmable FPGA device that contains logic blocks. Virtex is the flagship family of FPGA product developed by Xilinx. The FPGA Virtex-4 is a device was developed for the ALICE experiment en CERN to map and disentangle the trajectories of particles. The ETRAX is a processor for DAQ runs Linex kernel in 128 Mb and is directly connected to the Ethernet link of 100MBit/s. It is a high-performance network device used to move data to PC storage. The switching DC-DC converter modules provide a low voltage power (+5 V, -5 V and +3.3 V) to the RPCs of the plane. An optical link of 2 Gb/s connectivity can be used for a high speed data transport at synchronizing purposes between different boards or detectors.
Figure 2.12 show the low voltage power module (left figure) and the switching DC-DC converter modules (right figure). The low voltage power supply provides electrical current to the switching DC-DC converter modules. The device digitally offers the current and voltage values. The Figure shows a current of 8 amps and a voltage of 47.7 Volts applied to the system. The switching DC-DC converter modules provide a low voltage supply to the DC-DC of the TRBv2 and the MBO. 12 power cables are connected in the MBOs since only 3 planes of the Tragaldabas detector are currently working. The electronic card on the device provides the power supply to the TRBv2. 4 cables connected to the TRBv2+1 cable connected to the power supply+1 connected to the switcher.

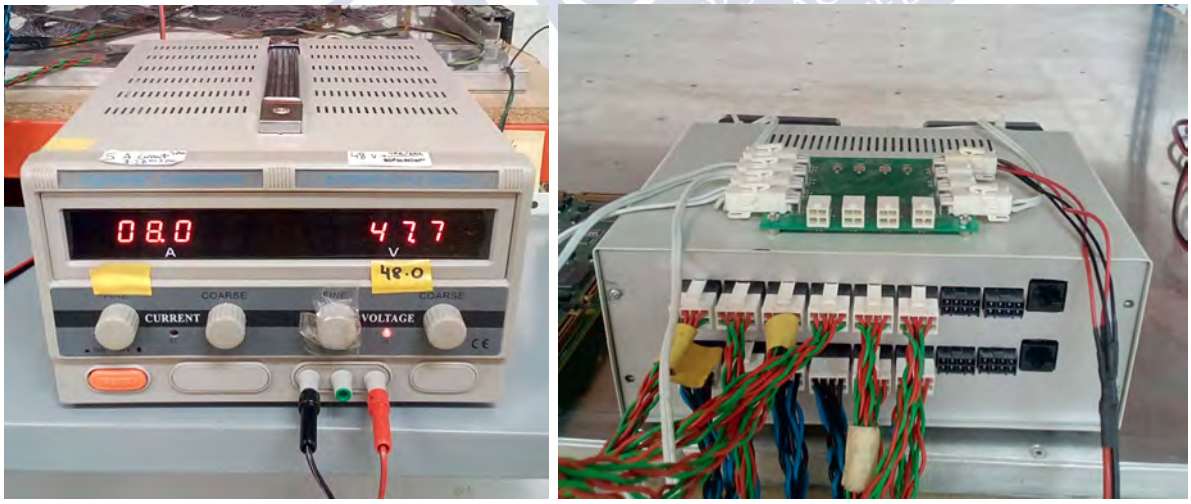

(a) (b)

Figure 2.12: Low voltage power supply (a). Low voltage and switching DC-DC converter modules connected to the TRBv2s (b).

The Figure 2.13 presents the high-voltage power supply of a detector plane. The device is connected by ethernet to the switchboard and provides a high voltage of 5600 V to the RPC cells of the plane. The system has a module for each plane.

Figure 2.13: Photograph of the custom made HV pwer supply of the Tragaldabas detector. A voltage of ±5600 V is fed to each RPC plane, and it can be controlled with a web interface.

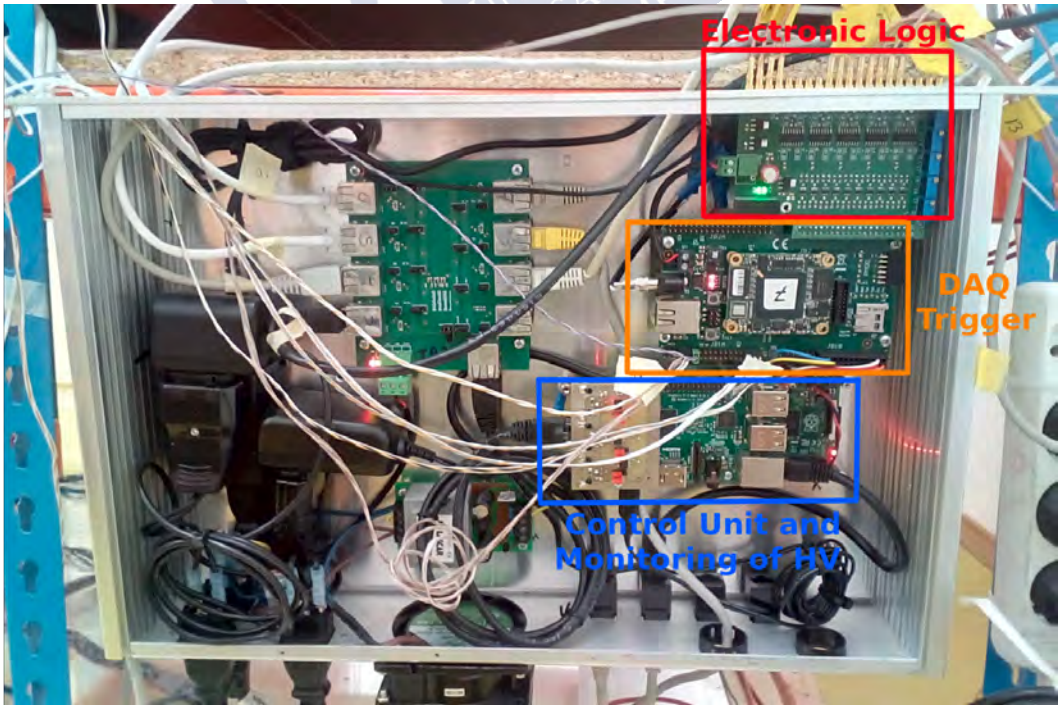

Figure 2.14: Data Adquisition Trigger, Control Unit and Monitoring of High Voltage.

The Figure 2.14 shows the switch box. This aluminum box collects the different devices. The devices are separated in defined modules such as: electronic logic, data acquisition trigger, Control Unit (CU), Monitoring of High voltage (HV), Ethernet connections and voltage power supply. The purpose of the electronic logic module is to collect the trigger signals of all the MBOs and execute the coincidence between trigger signals of the different detector planes. The device has 24 channels to collect the trigger signal which 12 channels are currently connected. The trigger DAQ collect the coincidence signal and after processing is returned to the TRBv2. The processing of the signal is done with an FPGA. The FPGA devices are responsible for configuring the trigger parameters, dead times and sending the synchronism signal to the detector planes. The CU module is connected to the FPGA. The CU is responsible for activating and deactivating the data capture of the FPGA. The monitoring of HV is responsible for receiving data from the sensors of the planes and is in communication with the high voltage sources.

The arrangement of the essential devices discussed above for a plane of the detector is described in Figure 2.15. The set is described for a single plane of the detector. The scheme includes the FEE+DAQ devices and the coincidence trigger (electronic logic module). The size of the plane is 1285×1650×25 mm^3, the active size of the plane is

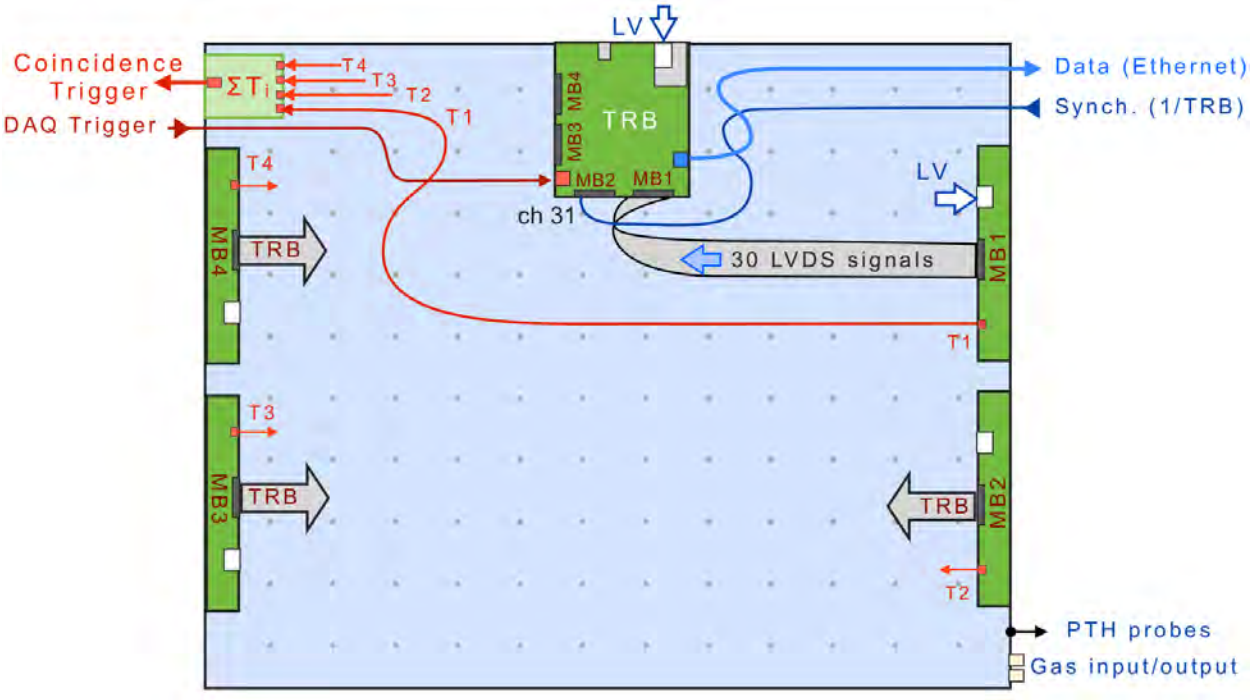

Figure 2.15: Layout of the FEE electronics of a single plane of the experimental system from Tragaldabas detector.

1200×1500 mm^2. Tragaldabas has 4 MBOs (MB1, MB2, MB3 and MB4) and a set of 30 pads for each of the MBOs. The MBOs connect to the TRB with 30 LVDS signals connections. The 4 trigger logic (T1, T2, T3 and T4) of the MBOs are connected to the electronic logic module located in the switch box. The gas input/output that provides

the performance of the RPC gaps is located under the right of the scheme. Near to the gas input/output is the high voltage connection. This provides the 5600 voltage to the RPCs. The freon gas is introduced with a slight overpressure to each detection plane in an independent way. An Ethernet data output can be seen in the upper right part of the image. The ethernet connection is connected to the personal computer (PC). The MB2 connector is used to synchronize all existing TRBv2s in the different planes of the detector. A dedicated gas circuit continuously feeds the Tragaldabas experiment. The freon gas is introduced with a slisht overpressure to each detection plane in an independent way.

An example of data structure HTPTDC collected from DAQ is presented in Figure 2.16 [66], where 2 events collected by TRB1&TRB2 with trigger between planes T1&T4 are shown. The data set in the red boxes are the signals produced in the gap from the RPCs and the orange high light are the cuts up-down of the signal that gives the charge. These give relevant information for time-charge corrections, events between triggers and others.

Figure 2.16: Example Data Structure from Tragaldabas.

USC
UNIVERSIDADE
DE SANTIAGO
DE COMPOSTELA

3 Simulation Tools

This chapter describes the software packages and simulation tools used and developed during the thesis work. First, I present an introduction to the commonly used Monte Carlo method for data generation. The definition and introduction to the C/C++ programming language and the tools used such as Geant or Root and the FairRoot and EnsarRoot frameworks are followed. The track reconstruction TimTrack method is theoretically exposed. The method is implemented in the EnsarRoot framework [67], and EnsarRoot was used to perform simulations and data analysis in this work. Basic notions about Corsika and CRY cosmic ray data generators are given. CRY generates general cosmic ray data at the ground level, and it is used for the general simulations of Tragaldabas detector and for the particle identification method development. On the other hand, Corsika generates EAS from different primary nuclei, and it is used for the study about EAS with Trasgos arrays.

3.1 Introduction to the Monte Carlo method

The Monte Carlo method (MC) [68, 69] is a mathematical procedure used to find a numerical solution to complex problems and difficult to evaluate accurately. Its name refers to the Monte Carlo casino in Monaco. The essence of the method was created from gambling to study phenomena of interest. The MC method was used by American scientists for the development of nuclear weapons during the Second World War in the National Laboratory of Los Alamos, 1940s USA. This involves the simulation of probabilistic hydrodynamic problems for the diffusion of neutrons in the fissible material. Finding a solution to a macroscopic system involves the simulation of its microscopic interaction. The repetitive calculation gives a solution to the problems. The solution to a problem can be determined by random sampling until the result converges. The computers are ideal for performing repetitive calculations.

MC is crucial in statistical physics, thermodynamics and Molecular Dynamics [70]. Nowadays, the application areas are diverse. The areas include: High Energy Physics, Nuclear Physics, development of particle accelerators, and studies in medical sciences, space and biological applications.

3.2 Simulation software frameworks

This section presents the frameworks and programming language used for simulation, event generation and data analysis. The definition of some programming language concepts is important before commenting on the set of software. A software framework is a piece of code, a set of classes, scripts and templates, providing a given functionality that can be selectively completed or modified by additional user-written code. The purpose as a so structured framework is to improve the efficiency of creating new software, increase the reliability of a new application and reduce the programming effort. Object-Oriented Programming (OOP) is a programming language model based on the concept of objects which may contain data, in the form of fields and code in the form procedures. An object can be a variable, a data structure, a function, or a method, and as such, is a value in memory referenced by an identifier.

C++ is an object oriented programming language, which evolved from standard C, and it is wide world currently used for many systems and developments. It is a portable programming language for a large number of platforms, versatile and low level that suits general purpose applications. It is very used in systems for building operating systems (OS), assembler, databases, and so on. The language presents an excellent interface for UNIX and Windows OS. C++ is a superset and is the successor of C. The C language was developed by Dennis M. Ritchie between 1969 and 1972 in the Bell laboratory [71]. The C++ language was developed by Bjarne Stroustrup in the mid-1980s [72]. C/C++ is an object-oriented language that uses so-called classes. Classes are data defined by the user that contains all the information needed to build an object and the set of operations that allow it to be handled. Today a multitude of frameworks are based on the C/C++ programming language to perform basic operations.

In this work, they have been used some important software toolkits and frameworks. Among others, here it comes a brief description of the most important ones:

Geant is a simulation tool of description of detectors and interaction of elementary particles with matter with the MC method. Geant3 is written in Fortran, while Geant4 is the C++ written Geant3 evolution. Geant was developed in the CERN laboratory under the need of simulation programs for the research and development of projects in particle and nuclear physics. Geant version 4 (Geant4) is one of Geant′s successors. The first version of Geant was developed in 1974 for the tracking of few particles per event inside a simple detector [73]. The beginnings in the development of Geant4 appear in independent studies carried out by the laboratories of CERN and KEK in 1993. The official creation activities of Geant4 begun in 1994 at CERN. It is written in C++ and is built based on oriented objects. This tollkit recreates physical processes that work in an energy range from about 250 eV to a few TeV. The Geant4 framework is composed of different packages allowing to define the important aspects of the simulation process: the geometry of the system, the materials involved the detector, the generation of event data

with MC, the simulated tracking by the passage of particles through matter, the detection of the passage of particles by the active materials, the run management, the interactive visualization, the user interface to facilitate the interaction of the experimenter with the computer and the analysis of the data with the ROOT program.

ROOT [74] or Root, is a framework for development of data analysis applications on a large scale developed at CERN. It is an object-oriented program written in the C++ language developed by René Brun and Fons Rademakers in 1994. It was developed in the context of the NA49 experiment at CERN. Currently it is being used in all major High Energy and Nuclear Physiscs laboratories around the world to monitor, to store and to analyse data. Root is based on GPL (General Public License) software and provides platform independent access to a computer′s graphics subsystem and operating system using abstract layers. Parts of the abstract platform are: a graphical user interface and a GUI (Graphical User Interface) builder, container classes, reflection[1], a C++ script and a command interpreter, object serialization[2] and persistence[3]. Root has a data container, in a tree-like structure, called TTree, with its substructures, branches and leaves. A tree can be seen as a cliding window to the raw data, as stored in a file. Root is designed for high computing efficiency, as it is required to process data from the Large Hadron Collider′s experiments estimated up to several petabytes per year. It is also used in other applications such as astronomy and data mining. The inclusion of a C++ interpreter makes this packages very versatile as it can be used in interactive, scripted and compiled modes.

FairRoot [75] is the object oriented simulation, reconstruction and data analysis is framework for the FAIR, Facility for Antiproton and Ion Research, experiments at GSI Darmstadt. It includes core service for detector simulation and offline analysis is of particle physics data. The FairRoot framework is fully based on the Root system. The user can create simulated data and/or perform the event reconstruction with the same framework. For simulation the Virtual Monte Carlo concept was chosen. It allows performing simulation using Geant3, Geant4 or Fluka without changing the user code or geometry description. The event reconstruction is organized in tasks that can be hierarchically arranged.

EnsarRoot [76] is the simulation and analysis framework for ENSAR [77]. It provides the software infrastructure and examples to develop an analysis and simulation code for Nuclear Physics experiments. It is written in C++, it is based on the FairRoot framework libraries and it loads the Root libraries providing a ROOT-like output structure. The EnsarRoot implements different examples of detectors and experimental setups, and uses the Virtual Monte Carlo concept for running simulations. ENSAR and ENSAR2 represent

[1]Reflection is a terminology used in computer science to manifest the ability of a computer program to examine, introspect and modify its own structure and behavior at runtime.

[2]Serialization is the process os translating data structures or object state into a format that can be stored or transmitted and reconstructed later.

[3]Persistence refers to the charateristic of state that oulives the process that created it.

integrating activity European scientist who are performing research in Nuclear Physics. It is funded by the European Commission within the HORIZON 2020 Programme. The EnsarRoot has been developed under the ENSAR Joint Research Activity SiNuRSE (Simulations for Nuclear Reactions and Structure in Europe), which continues as SATNuRSE (Simulations and Analysis Tools for Nuclear Reactions and Structure in Europe) in ENSAR2.

All simulations and data analysis of this work were performed with EnsarRoot.

3.2.1 TimTrack method

The Trasgo project and the new TRB board technologies developed at GSI motivated the collaboration scientists Tragaldabas to develop a trace tracking and reconstruction algorithm. The TimTrack name [78] is the abbreviation of Timing-Tracking. TimTrack has been tested to fit particle trajectories in spectrometers such as HADES in the past, with promising improvements in the obtained results. The method reconstructs the six parameters of the track at a reference planes: two coordinates, two slopes, the arrival time and the velocity of the particle. TimTrack may run directly in FPGAs making the track finding, the reconstruction and the analysis extremely easy and fast. TimTrack is based on the least squares method. It uses a matrix mathematical formalism. The notation used is as follows: bold letters are reserved to denote vectors capital font for matrices and regular fronts for constants. The parametric choice of particles motion is very important in an experiment and these must be analyzed before choosing the design of the detectors. Suppose a simple example of a particle motion in a detector. The position particle in an O reference system is determined by the position vector $\mathbf{r} = (x, y, z)$ and the initial time t. The particle will be in a new position $\mathbf{r}^{(1)} = (x^{(1)}, y^{(1)}, z^{(1)})$ after a time $t^{(1)}$. The position and time of the particle is given by the RPC detectors. The data processed by the TRB provide parameters related to the trajectory (position and time) of the particle. The set of parameters is called a SAETA (SmAllest sET of pArameters) vector. The saeta, whose name comes from the latin word *sagitta*, is composed of the minimum information to describe the movement of the particle:

$$\mathbf{s} = (X_0, X', Y_0, Y', T_0, S) \quad ,$$

where (X_0, Y_0) are the coordinates of trajectory in the reconstruction layer, the (X', Y') are the slopes respect the x and y propagation axes, the T_0 is the time at which the particle crossed the reference plane and S is the inverse of the velocity or slowness, of the particle. The TimTrack estimates the set of parameter $\mathbf{s}$ by taking some data $\mathbf{d}$ and a data describing model $\mathbf{d} = m(\mathbf{s})$. The fit is driven by a Least Square Methods (LSM) procedure. The LSM is defined as a numerical analysis procedure where the continuous function that best approximates the data or a data set is found. Moreover, it can be expressed in a clear and understandable way by using the matrix formalism. Let n_d be the dimension of $\mathbf{m}$ and $\mathbf{d}$, and n_s the dimension of $\mathbf{s}$, being that is possible to calculate

the set which minimise S ($n_d \geq n_s$). The functional S defined as follows:

$$S = \sum_{i}^{n_d} \left(\frac{d_i - m_i(\mathbf{s})}{\sigma_i} \right)^2 \ ,$$

where σ_i is the incertitude associated to the i-term of the sum. If the theory is in good agreement with the data, then d and $m(\mathbf{s})$ do not differ by much and hence the value S will be small. The latter equation can be expressed in matrix form as:

$$S = (\mathbf{d} - \mathbf{m}(\mathbf{s}))' \cdot W \cdot (\mathbf{d} - \mathbf{m}(\mathbf{s})) \ , \tag{3.1}$$

where W, or weight matrix, is the inverse of the variance matrix V and the prime coming denotes the transpose matrix transformation. The LSM method says that to minimize the functional S it must be satisfied that:

$$\frac{\partial S}{\partial \mathbf{s}} = 0 \ . \tag{3.2}$$

The Jacobian matrix of the $\mathbf{m}(\mathbf{s})$ with respect $\mathbf{s}$, $\partial \mathbf{m}(\mathbf{s})/\partial \mathbf{s} = G$, can be always expand $\mathbf{m}(\mathbf{s})$ linealy as:

$$\mathbf{m}(\mathbf{s}) = G \cdot \mathbf{s} + \mathbf{g}_0 \ ,$$

where $\mathbf{g}_0$ is defined as the difference $\mathbf{m}(\mathbf{s}) - G \cdot \mathbf{s}$. Then, if the mathematical model $\mathbf{m}(\mathbf{s})$ is linear the functional S takes the form:

$$S = (G\mathbf{s})' \cdot W \cdot (G\mathbf{s}) - 2(G\mathbf{s})' \cdot W \cdot (\mathbf{d} - \mathbf{g}_0) + (\mathbf{d} - \mathbf{g}_0)' \cdot W \cdot (\mathbf{d} - \mathbf{g}_0) \ . \tag{3.3}$$

The expression can be rewritten by imposing a few definitions:

$$\begin{aligned} K &= G' \cdot W \cdot G \ , \\ \mathbf{a} &= G' \cdot W \cdot (\mathbf{d} - \mathbf{g}_0) \ , \\ S_0 &= (\mathbf{d} - \mathbf{g}_0)' \cdot W \cdot (\mathbf{d} - \mathbf{g}_0) \ , \end{aligned}$$

where K is a square matrix with dimension $n_s \times n_s$ called configuration matrix and only depends on the fitting model and the variances of the measured data. The vector $\mathbf{a}$ is called reduced since the data dimension vector n_d is reduced to the n_s parameter dimension. The S_0 is a scalar. The expression (3.3) can be written in the compact form as:

$$S = \mathbf{s}' \cdot K \cdot \mathbf{s} - 2\mathbf{s}' \cdot \mathbf{a} + S_0 \ .$$

The equation (3.2) is rewritten in a very simple expression using the minimum condition of the LSM theory. The parameter vector that meets the minimum condition is written as:

$$\mathbf{s} = K^{-1} \cdot \mathbf{a} \ . \tag{3.4}$$

As K^{Text-1} is the error matrix $\mathcal{E}$, the equation can be rewritten as:

$$\vec{s} = \mathcal{E} \cdot \vec{a} \ ,$$

or "Sea" equation. The reduced data vector $\mathbf{a}$ and the scalar S_0 can be calculated known the Jacobain matrix G. Let remember that systems with n_d equations with n_s unknowns

always have a solution if $n_d \geq n_s$ is satisfied. If the model is linear with respect to the parameters $\mathbf{g_0} = \mathbf{0}$. The following is true if the uncertainties are small: the functional S has a parabolic behavior near to the minimum. The incertainties of the elements of $\mathbf{s}$ are given by the square roots of the diagonal elements of $\mathcal{E}$ and the non-diagonal elements represent the covariances.

When the $m(\mathbf{s})$ model is non linear then the $\mathbf{g_0}$ has a dependency on the parameters. The same happens with the K matrix and the $\mathbf{a}$ vector. The new saeta can be written recursively where the sub-index i refers to the number of iterations,

$$\mathbf{s_i} = K_{i-1}^{-1} \cdot \mathbf{a_{i-1}} \ .$$

Starting with an appropriate initial set of parameters, s_0, the convergence method of this model is very fast in Trasgo detectors.The variance-covariance matrix of the parameters is given by the inverse of the configuration matrix $\mathcal{E}$=K^{-1} like the linear data model.

The functional S and the χ^2 of the fitting are equal if the model is valid and the minimum condition is met. The statistic is near to zero if the deviation between the data and the model is very small. The greater the difference between data and model, the bigger the statistician. The track of the particle by the detector will tend to be more rectilinear if the statistic is smaller. More tortuous is the trace if the statistic is higher.

3.3 CORSIKA: Extensive air shower simulator

The successive nuclear interactions are essential physical processes in simulators for the propagation of particles of the cascade along the atmosphere and the response of the detectors to the particles incidence arriving at the ground level. The advantages and disadvantages of EAS simulation programs are of great importance. The incidence of primary CR in the atmosphere will have consequences on the evolution of the shower until reaching the ground level. The initial collisions are usually central, peripheral [79] or diffractive. Experiments with particle accelerators given relevant information about nuclear reactions and decays that may exist in the EAS, and thus, a phenomenological approach to nuclear reactions in the atmosphere. The evolution of showers depend on the density profiles and the days. On the other hand, the evolution of EAS is rather depending on the properties of the atmosphere right in the moment when a primary CR passes through.

CORSIKA (COsmic Ray SImulation KAscade) or Corsika, is a software package for detailed simulation of EASs induced by high energy CR. It simulates the evolution and properties of EASs in the atmosphere. It was developed to perform simulation for the KASCADE experiment by Dieter Heck, Tanguy Pierog and all. [80] at Karlshuhe in Germany. The Corsika program allows to simulate interactions, propagation and decays of nuclei, hadrons, muons, electrons and photons in the atmosphere produced by primary cosmic rays with energy up to some 10^{20} eV. It gives type, energy, location,

direction and arrival times of secondary particles that are created in air shower and pass selected observation level. Corsika uses FORTRAN and does not use libraries of additional programs for the air showers simulations. The program uses the hadronic interaction models VENUS (Very Energetic NUclear Scattering), QGSJET (Quark Gluon String with JETs) [81] and DPMJET (Dual Parton Model with JETs Version II.4) [82], which are based on the Gribov-Regge theory and SIBYLL [83] based on a minijet model for high energies. The hadronic interactions at lower energies are described either by the GHEISHA (Gamma Hadron Electron Interaction SHower code) module, by FLUKA (FLUktuierende KAskade) [84], or by the UrQMD (Ultra-relativistic Quantum Molecular Dynamics) [85] model. The electromagnetic interactions are treated by the EGS4 code or the analytical NKG formulas. Corsika can be used to simulate the generation of Cherenkov radiation and atmospheric neutrinos. The radio emission of showers may be treated by a link with CoREAS (COrsika-based Radio Emission from Air Showers) code.

The Corsika program works with 4 different modules. The first module is a general framework for the management of inputs and outputs, performing the decomposition of unstable particles and tracking of particles with the ionization loss and multiple scattering, and the geomagnetic field. The second module deals with hadronic interactions at higher energies. The third simulates the hadronic interactions at lower energies. The fourth module describes the transport and interaction of electrons (e^- and e^+) and photons. The Corsika program recognizes 50 elementary particles and many nucleous types using the code: $A \times 100 + Z$ ($2 \leq A \leq 56$).

The coordinates in Corsika are given by the Cartesian coordinate system. The axes point in specific directions: the z-axis points up, the y-axis points to the magnetic west and the x-axis points magnetic North. The zenital angle θ is positively defined by the momentum of the particle along the z-axis. The azimuthal angle ϕ is positive defined by the intersection point of the particle moment with the x-y plane along the x-axis. Default units used in Corsika are: length in cm, energy and mass in GeV, time in s, the magnetic field in μT, the density in g/cm^3, mass overburden in g/cm^2, angle in rad and wavelength in nm.
Figure 3.1 show the x-z projection of a EAS from a proton and iron primary nucleus compiled by Fabian Schmidt, Johhannes Knapp, University of Leeds (2005) [86] (UK), both showers are drawn in the same scale range.

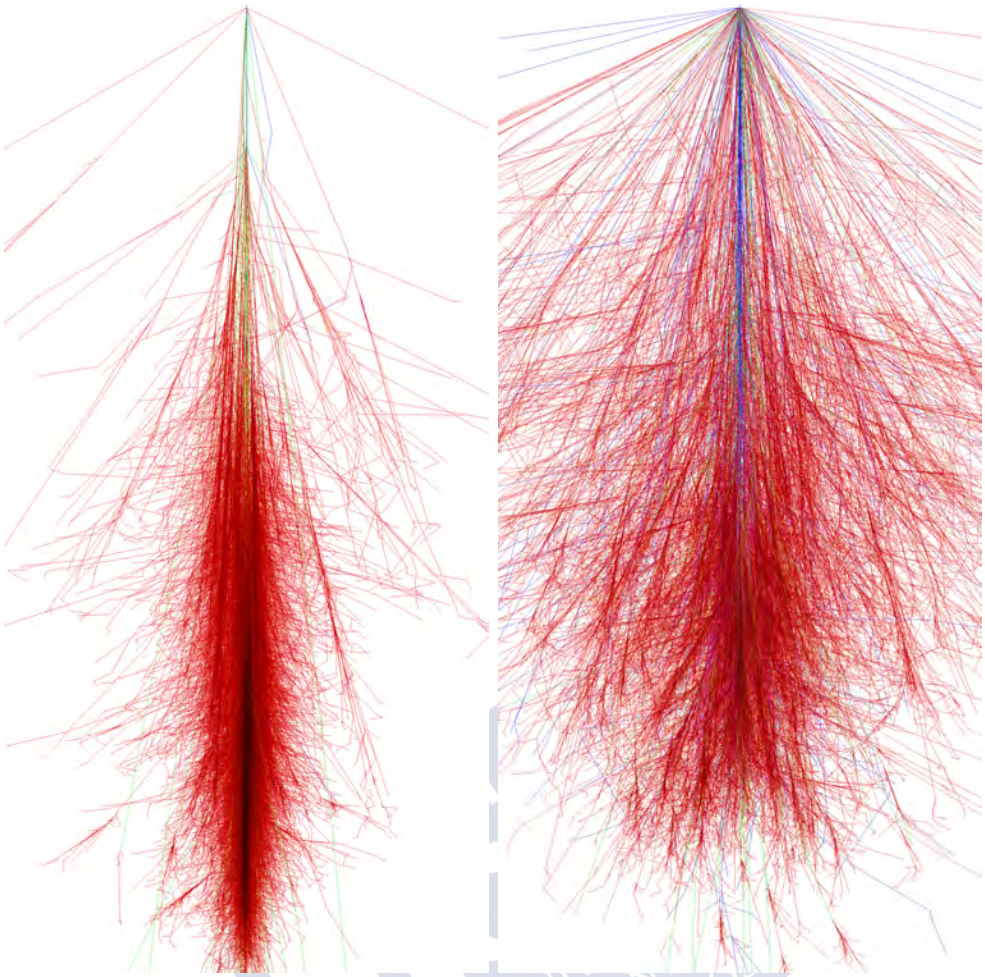

(a) (b)

Figure 3.1: EAS of a primary proton (a) and a primary iron (b) with vertical incident in atmosphere. As a larger mass of the primary cosmic ray, largest and widest is the shower.

The simulations were generated with a vertical incidence of the nucleus with an energy of 10^3 GeV in the top of the atmosphere. The image presents a larger EAS for the iron than for the proton. The tracks have the following color code: red for electrons, positrons and gammas; green for muons and; blue for hadrons. The different input parameters for the simulations are set with dedicated files. There are different input files for different types of studies. The Figure 3.2 shows the default input files of Corsika including the models QGSJET and GHEISHA (or FLUKA). The input parameters to the simulation comes with the acronym and a value. The following parameters were modified for the study in this work: the run number (RUNNR), number of first shower event (EVTNR), number of shower to generate (NSHOW), energy range of primary particle (ERANGE), range of zenith angle (THETAP), observation level (OBSLEV) and energy cuts of particles (ECUTS). All the definitions of the parameters and acronyms are in the tutorial reference.

```
RUNNR   2                          run number
EVTNR   1                          number of first shower event
NSHOW   1                          number of showers to generate
PRMPAR  14                         particle type of prim. particle
ESLOPE  -2.7                       slope of primary energy spectrum
ERANGE  1.E4  1.E4                 energy range of primary particle
THETAP  20.  20.                   range of zenith angle (degree)
PHIP    -180.  180.                range of azimuth angle (degree)
SEED    1   0   0                  seed for 1. random number sequence
SEED    2   0   0                  seed for 2. random number sequence
OBSLEV  110.E2                     observation level (in cm)
FIXCHI  0.                         starting altitude (g/cm**2)
MAGNET  20.0  42.8                 magnetic field centr. Europe
HADFLG  0  0  0  0  0  2           flags hadr.interact.&fragmentation
ECUTS   0.3  0.3  0.003  0.003     energy cuts for particles
MUADDI  T                          additional info for muons
MUMULT  T                          muon multiple scattering angle
ELMFLG  T   T                      em. interaction flags (NKG,EGS)
STEPFC  1.0                        mult. scattering step length fact.
RADNKG  200.E2                     outer radius for NKG lat.dens.distr.
LONGI   T  10.  T  T               longit.distr. & step size & fit & out
ECTMAP  1.E4                       cut on gamma factor for printout
MAXPRT  1                          max. number of printed events
DIRECT  ./                         output directory
USER    you                        user
DEBUG   F  6  F  1000000           debug flag and log.unit for out
EXIT                               terminates input
```

Figure 3.2: Corsika default input.

3.4 The CRY Cosmic-ray shower generator

CRY or Cry is a software package written in a basic C++ interface that generates correlated CR particle shower distribution [87]. Cry can generate distributions to be used as input to transport and detector simulation codes. This allows to generate CR particles in a wide range of energies with data tables. The data tables derive from the simulation with MCNPX 2.5.0 for muons, neutrons, protons, electrons, photons and pions for some altitudes. Cry generates shower multiplicities within an area (at most 300×300 m^2), arrival time and zenital angle of secondary particles. It allows to work with a geomagnetic limit dependent on the latitude of the spectrum of primary cosmic rays and the modulation of the spectrum over time based on the average solar cycle. It allows to select three possible elevations: the sea level, 2100 m and 11300 m. The energy ranges in which the program works are of [1, 10^5] GeV of primary particles and [1, 10^9] MeV in secondary particles. The simulation input parameters are done with the input file `parameters.file` located in the `test` folder of Cry. The data generation is executed using the following command:

```
g++ -L ../lib/ -I ../src/ testOut.cc -lCRY
```

The generated file is `a.out`, this is executed for 10 events as follows:

```
./a.out parameter.file 10
```

The Figure 3.3 shows the content of the input file by default with all the possible parameters of the data generation program.

```
returnNeutrons 1
returnProtons 1
returnGammas 1
returnElectrons 1
returnMuons 1
returnPions 1
altitude 0
latitude 90
date 7-1-2012
subboxLength 100
```

Figure 3.3: Cry default input.

USC
UNIVERSIDADE
DE SANTIAGO
DE COMPOSTELA

USC
UNIVERSIDADE
DE SANTIAGO
DE COMPOSTELA

4 TRAGALDABAS simulations and event generator tools

This chapter presents a complete study of the TRAGALDABAS detector system behaviour and response under simulated EAS data. All geometries were implemented in the EnsarRoot framework, and Corsika, CRY and a custom made particle generators were used. The geometric modifications in EnsarRoot were varied, rendering the second plane T2 to work with 3 RPC planes, implementing the relevant geometry of the Faculty of Physics building and implementing a 1 and 1.5 cm thickness of lead after the third plane of the detector for a Tragaldabas to 4 active RPC planes. Adding lead to the detector allows to know the calorimetric capabilities of the experiment. The simulations were carried out entirely with the EnsarRoot framework. Namely, simulations reproduce interactive behaviors between particles and the material medium of the detector.

4.1 Tragaldabas geometry

The complete Tragaldabas detector geometry is implemented in EnsarRoot. It has been built through the `TGeo` Geometry package of Root. The Reference System of the detector is chosen in the following way: the origin is located at ground level and the z-axis goes in the direction of the incident particles (Figure 4.1). The planes are located at -1873 mm (plane T1), -1348 mm (plane T2), -969 mm (plane T3) and -132 mm (plane T4). The simulations are launched with these two scripts (or macros): `tragall.C` and `tragsim.C`. The program `tragall.C` has all the environment options, functions and parameters of the simulation. The simulation environments are chosen by blocks according to the inputs of a class with box geometry (e.g. `tragbox` or `box`), with an ASCII data set or data from the cosmic generator Cry (`ascii` or `cry`). The program `tragsim.C` contains the options to define the configuration of the simulation in Tragaldabas: freedom of selection of particle propagation engine MC (`GEANT3`, `GEANT4`), the event generator (`box`, `tragbox`, `ascii` or `cry`), activating the TimTrack option, selecting the geometry, entering the number of events and so on. The transport parameters (statistics or environment) of the simulation can be selected in the program `tragsim.C`. The simulation is executed with Root using the following command:

```
root -l -q tragsim.C
```

The default output file generated is `tragall.root`. That Root file contains an event TTree structure whose branches correspond to each data level in the reconstruction process, and they are automatically filled in EnsarRoot. Those branches are `MCTrack`,

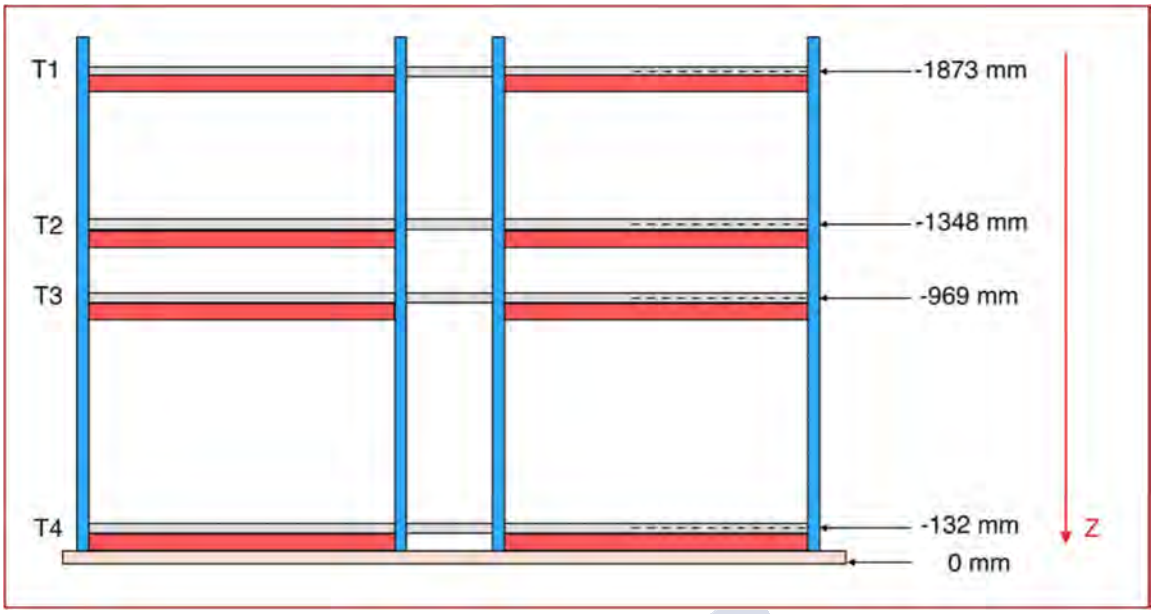

Figure 4.1: Planes position of Tragaldabas experiment.

`RPCPoint`, `RPCHit`, `RPCSaeta` and `MCEventHeader`. `MCTrack` contains relevant information of all the particles generated in the simulation, independently whether they interact with the detector or not. `RPCPoint` contains information about the points of interaction of the particles with the active material in each plane. `RPCHit` provides information about Hits on each plane. The information in the branch `RPCHit` is basically digitized information from `RPCPoint`. A digitalization is a method of processing simulated data where the planes have pads. The pads have two gaps of active medium. `RPCSaeta` contains information from the trajectory reconstruction from hits in the planes after running the TimTrack fitting method. Finally, `MCEventHeader` provides all technical information of the simulated event.

Figure 4.2 shows the simplest description of the detector with the four RPC planes, and a 100 MeV eletron passing throught the system. The electron was generated from a plane located just above the detector, with a motion direction following the standard arrival cosmic ray angular distribution. Secondary particles are generated after the interaction of the electron with the materials of the planes. Those secondaries are mainly low energy photons. The image was displayed with the event viewer tool of the EnsarRoot framework which is based on the TEve feature of Root. The yellow traces correspond to electrons e^-, the pink traces to photons γ, the green traces to positrons e^+, the violet traces correspond to muons μ^- and white traces to antimuons μ^+. The thickness of the traces shows the energy difference of the particles. The trace will be thicker as the energy of the particles increases.

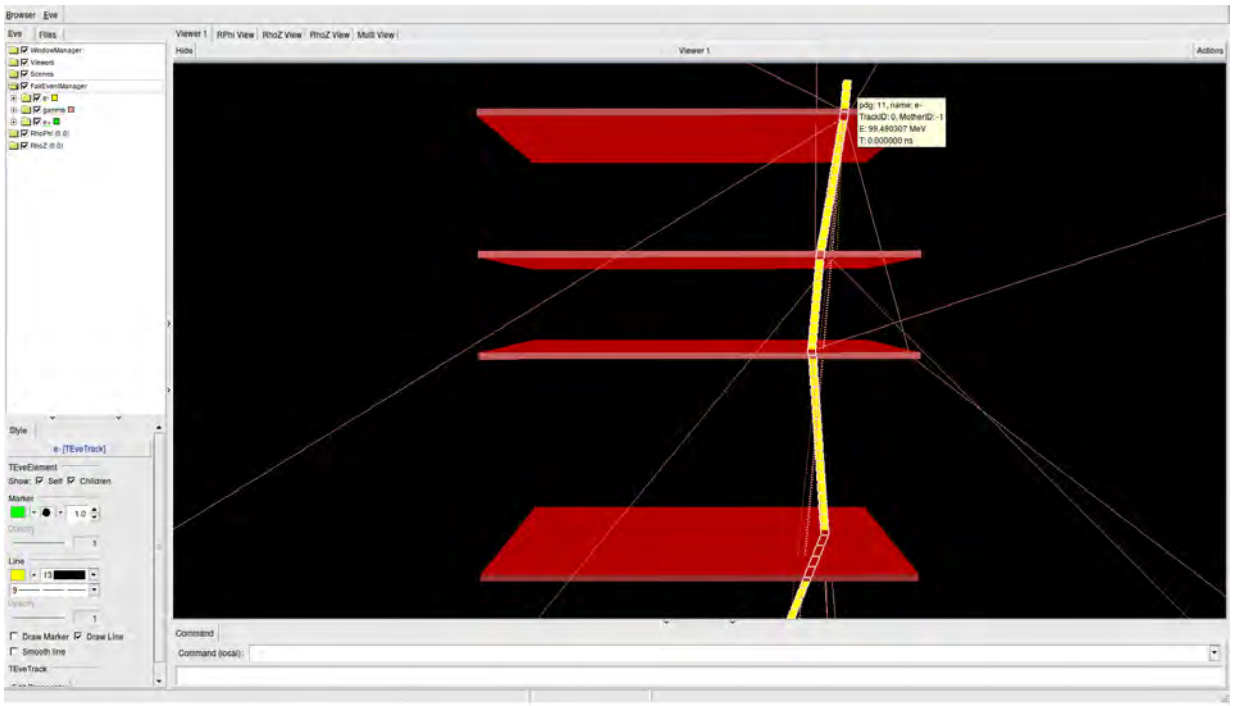

Figure 4.2: Representation of a simulated cosmic ray event over the detector system within the EnsarRoot framework. A primary electron with an energy near to 100 MeV interacts with the detector materials. The four active RPC planes of the detector are drawn.

A realistic description of materials, geometry and dimensions of the Faculty of Physics building, which houses the Tragaldabas detector, was implemented in EnsarRoot. An important task of the thesis is to add the essential elements to the construction of these geometric implementations. Therefore, the code was modified to add the geometry of the essential components of the north wing of the Faculty of Physics where the detector is located. All dimensional measurements have been taken from the building blueprints. The Figure 4.3 shows the successive interaction of an electron of 999.5 MeV with the building′s floors in its trajectory to the detector. The product of the interactions gives a jet of particles that collides on Tragaldabas. The jet is composed mostly of low-energy photons and other particles such as electrons or positrons. The incident particles on the detector is a clear example of multiple interaction from the same cosmic ray (secondary). To remember that, the simulations are performed with the incidence of a single particle on the detector. The trigger of the analytical method is simple and very powerful.

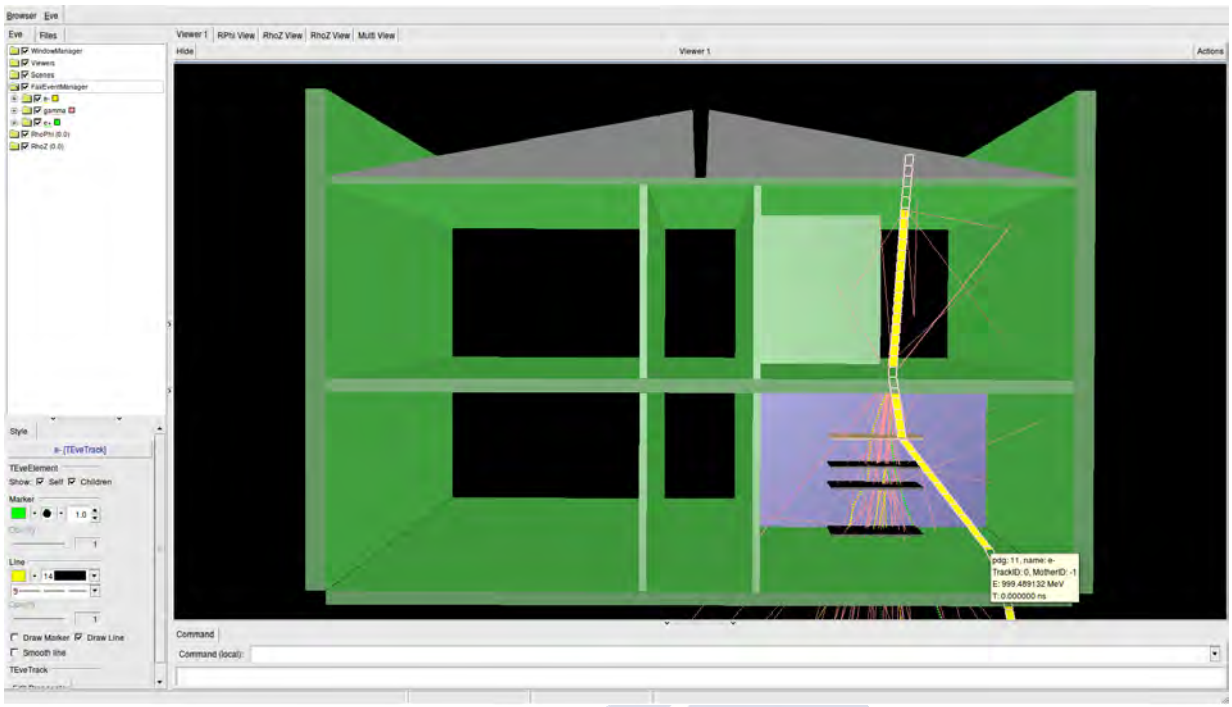

Figure 4.3: Representation of a simulated cosmic ray event over the full system of building plus detector wiin the EnsarRoot framework. In the drawn case, a primary electron with an energy close to 1 GeV interacts with the building materials and a secondary shower reaches the Tragaldabas detector. Only the four active RPC planes of the detector are drawn.

The materials used to recreate the building were mainly concrete, silicon and plaster. The complete description of those materials properties were implemented and included in the EnsarRoot general media file `media_ensar.geo`. The building geometry includes the roof composed of a silicon material with a thickness of 1 cm. First and second floors are 20 cm thick concrete plates, while third floor is only 10 cm thick. The side walls have a thickness of 29.17 cm and are made of concrete. The wall near to the detector has been added to the geometry and has a thickness of 2 cm of plaster. In addition, the electron stopping power is about 700 MeV for 30 cm of thickness in silicon according to the data bases of NIST (National Institute of Standards and Technology) providing a excellent cutoff energy to the simulations.

A calorimetric study of the detector has been carried out in this work with a layer of lead after the third plane. The lead layers added to the geometry of the detector were of 1 cm and 1.5 cm of thickness. Such lead layers were placed between the third and the fourth planes, at a distance is 16.4 cm from the third plane. The Figure 4.4 shows an event over Tragaldabas with a lead plate of 1.5 cm thickness. The incident particle is a photon of 777 MeV. The event presents a frontal jet when the photon interacts with the lead layer. The front of the jet deflected slightly according to the incident photon. Many of the jet particles are low-energy photons and some electron and positron.

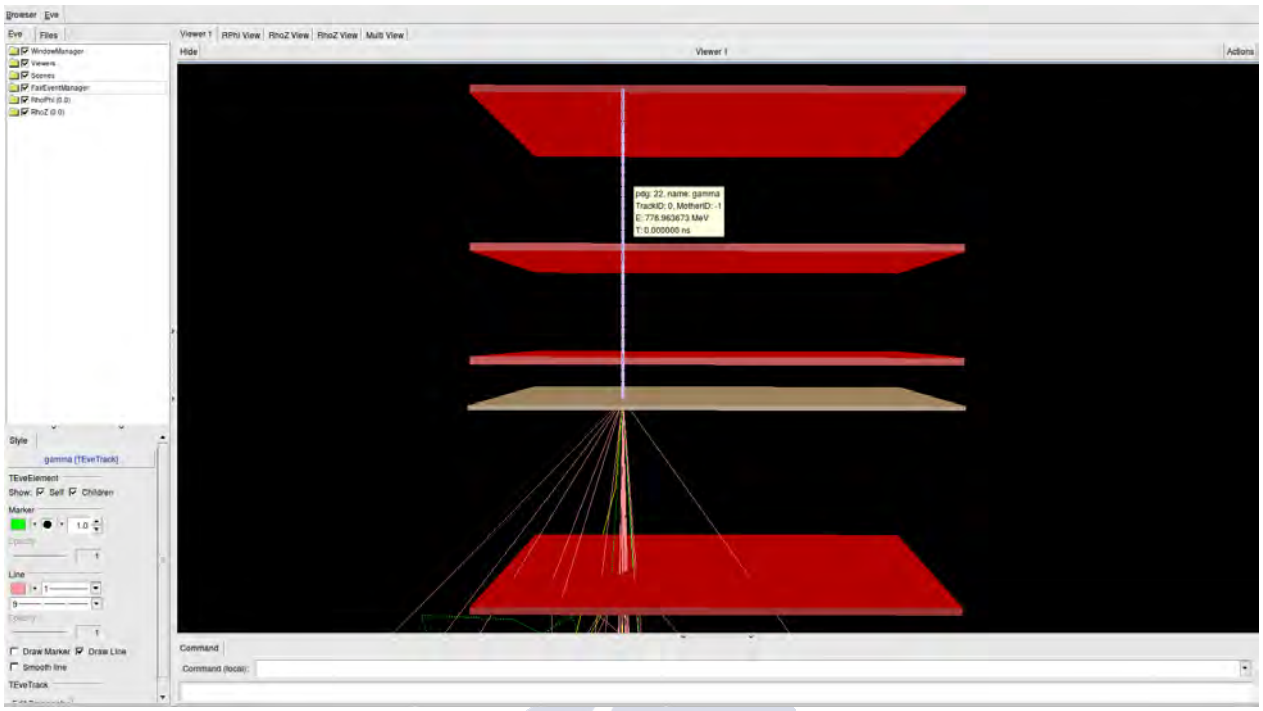

Figure 4.4: Representation of a simulated event on the 4 plane system with lead layer within the EnsarRoot framework. A 777 MeV photon crosses the detector interacting with the building materials and a shower arrive at the fourth plane of the Tragaldabas. The geometry incorporates 4 active RPC planes and a 1.5 cm thickness of lead layer after the third plane.

4.2 Simulation in TRAGALDABAS detector

4.2.1 Definition of physical observables

In order to a deeper understanding of the Tragaldabas events phenomenology, and a further development of a Particle Identification method, some physical observables have been defined and used in simulation. Among others, the most important are:

- the **absolute efficiency of particles detection** (ε_{eff}), value that is independent of whether the primary particle interacts with the first plane or not.
- the **average, maximum and minimum multiplicity** (**M**) of the electromagnetic shower. The multiplicity is the number of hits (valid signals) over the full detector system in a single event.
- the **mean hit plane per event**, is the mean number of planes with hits per event.
- the **scattering angle** (θ) is the angle between the trace joining the points of interaction of particles and the vertical. The first impact is taken always over the first plane, while the second impact can happen at any of the other planes of the

detector. The **maximum scattering angles** ($\boldsymbol{\theta_{max}}$), is the maximum angular aperture of particle after the interaction of the primary with the first plane.

- the **weighted range** ($\mathbf{a_n}$) is the distance reached by a track or a shower in number of planes, weighted by the hit multiplicity in each plane. It can be described as $a_n = \sum_i^p m_i n_i$, where p is the plane number, m_i is the multiplicity in each plane and n_i is a weight that goes from 0 (plane 1) to 3 (plane 4).
- the **chi-square** ($\boldsymbol{\chi^2}$) is the value of the track fitting provided by the TimTrack method. Crossing the maximum number of available RPC planes, the value of the χ^2 gives an estimation about the deviation of the track from a straight line.

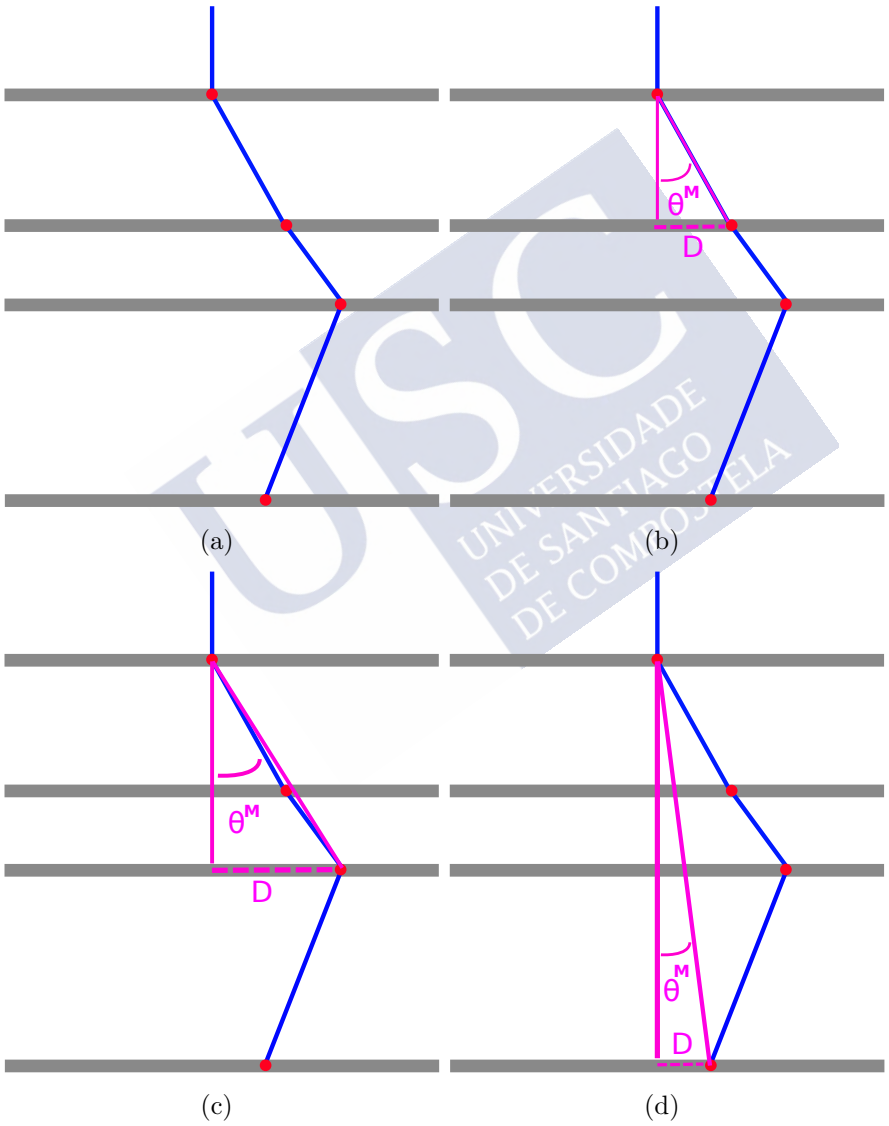

Figure 4.5: Maximum scattering angles selection. The scheme shows how to calculate the maximum angle of an example event. Trace and hits of the event (a), scattering angle between the first and the second plane (b), scattering angle between the first and the third plane (c), and, scattering angle between the first and the fourth plane (d). Scheme (c) shows the maximum angular aperture of the event.

These observables are estimators that represent a set of data and the error is statistical uncertainty. An estimator is defined to the real value obtained in a statistical way to represent a data set or a statistical model. It is necessary to remember the definition of Hit to continue with the section A Hit is the interaction of a particle with the active material of the RPC. The definition is totally true in simulation and the code is implemented in the folder `tragaldabas` of EnsarRoot.

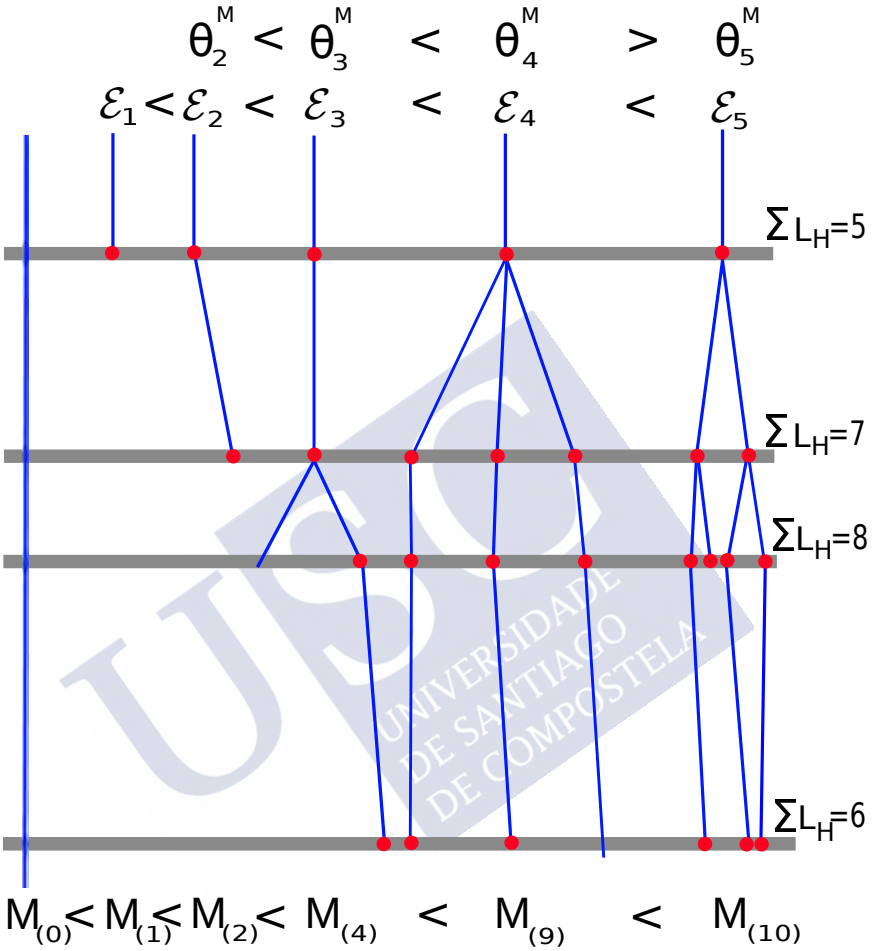

Figure 4.6: Simple scheme to classify events in a Trasgo detector with 4 planes. This shows how to identify and separate different events using physical observables. The 4 event has a maximum scattering angle greater than the others, it has a multiplicity of 9 and an L_H is equal to 1 for the first plane, 3 for the second and third planes and 2 for the fourth plane.

The application of the observables to the calculations are described below with simple schemas. The calculation of the maximum scattering angle θ_{max} is the first method explained. Given two hits in vertically separated planes a distance D and a horizontal separation ρ between them, the angle is calculated with the inverse tangent ($\tan\,\theta = D/\rho$). Figure 4.5 show the selection of the maximum scattering angles with an example of events. The event is given by hits or signal in the 4 planes of the detector (left up of the figure). The red dot represents the hit and the blue line represents the trace of a hypothetical particle. The images shows the scattering angles between two hits in different planes.

The pattern to follow is always the same. The angle between planes (2,3 and 4) is always calculated from the first plane. It is easy to realize in this example that the angle with maximum scattering is the event with hits in the first and third planes (right up figure).

The Figure 4.6 presents a simple diagram showing 5 events at different energies interacting with the detector. The ϵ represents the total energy of the event, M is the multiplicity of the same where the index is the value of the multiplicity of the event (e.g: a multiplicity of 4 is given by M_4) and $\sum L_H$ is the sum of hits per plane for all events. A supplementary event is M_0, where it represents zero interaction with the detector planes. The scheme helps intuitively calculate the parameters and understand the appearance of the shower inside the detector. Any comment of the scheme will be carried out on increasing order in energy E (from left to right) and in increasing order in number of planes (from top to bottom). Again, the traces are represented in blue lines and the hits with red dots. The traces are larger and the shower grows as the energy increases. The shower grows length and width until the energy is large enough for the shower to narrow and the distance between traces thin. The multiplicity per event grows as energy increases. The multiplicity values (event numbers) are from M_0 (first event), M_1, M_2, ..., to M_{10}. Conversely, the maximum angle θ^M decreases as E. $\sum L_H$ has no tendencies, it changes according to more or less particle-detector interactions.

4.2.2 Study of vertical and non-vertical incidence of particles

This section studies different behaviors of particle incidences in the detector. The vertical incident particle incides in the center of a pad near the center of the first plane and completely perpendicular to the plane. The Non-verticaly incident of particles are defined when the incident particle is randomly surface of the first plane of the detector and with any incident angle. The simulations were performed with 100k unitary electromagnetic particles (electrons, photons and muons) with an range in energies of [1, 100] MeV for photons and electrons, and [0.1, 10] GeV for muons. The energy of particles have a logarithmic scale with 4 steps of $10^{\frac{2}{8}}$ per decade: 0.1, 0.178, 0.316, 0.563, 1, ..., 10 GeV (muonic case). The vertical incident case, the geometric center is a particle generator located a few centimeters above the detector. The Non-vertical case, the simulation starting randomly from a virtual plane similar to Tragaldabas plane, located a few cm above the detector and with direction uniformly distributed in ϕ and $\cos\theta$, with θ between 0 and 90°. The trigger condition was to have a hit, and only one hit, in the RPC plane 1.

The evolution of the shower for electrons of different energies with vertical incidence on the Tragaldabas detector is illustrated below. Figure 4.7 show 3D plots of hits produced by 100k events. 3 plots are seen at different energies of electron incidence: 100, 316 and 1000 MeV. The axes are given in centimeters. In the first plane of the plots a single spot is observed due to the incidence of vertical electrons in the center of the plane. These plots give the reader a visual understanding of the trigger imposed in the data analysis programs. A cloud of hits of different sizes is visible in the other planes of plots. The hit population becomes denser as one approaches the geometric center of the planes. A

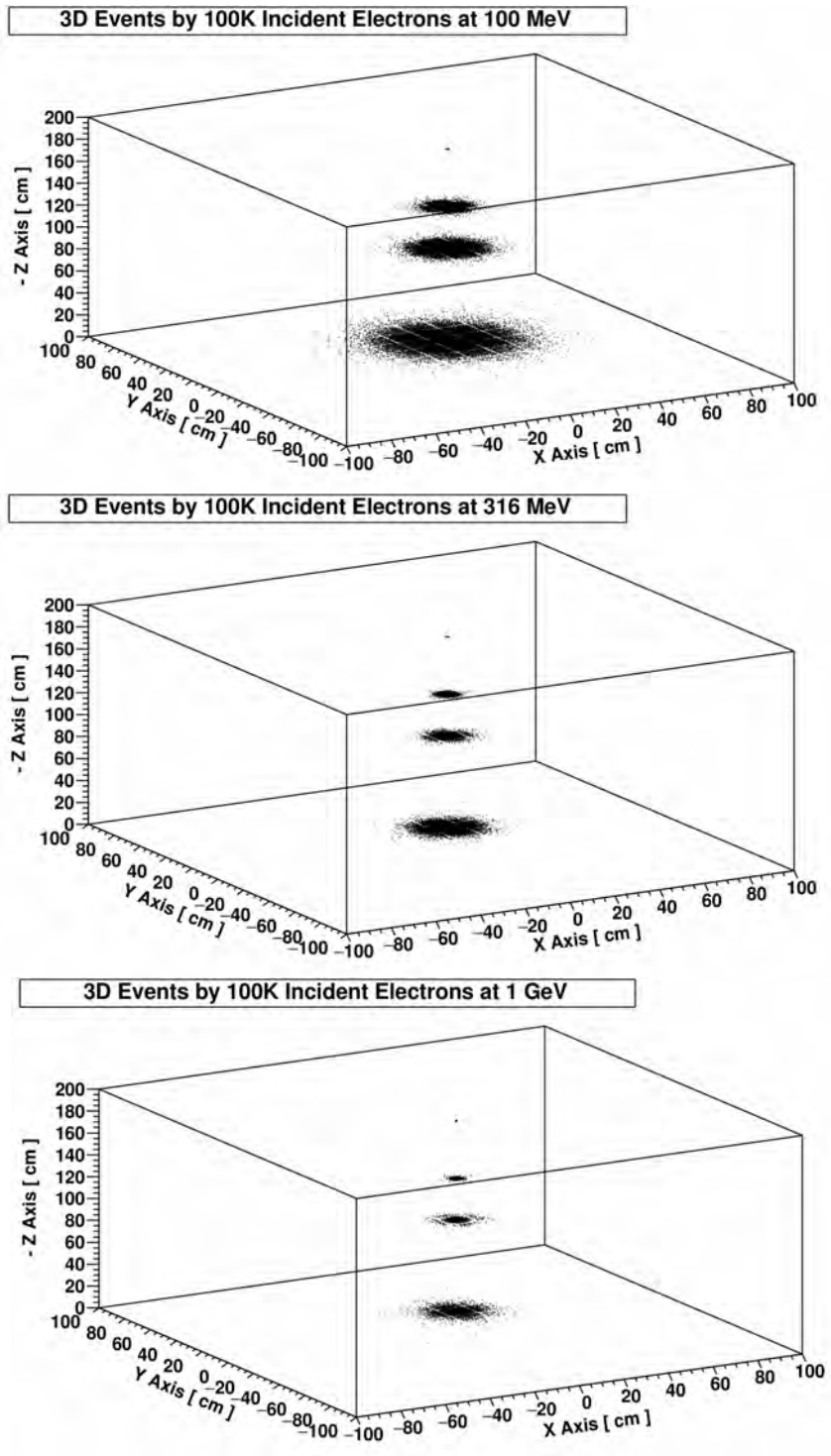

Figure 4.7: 3D plots evolution of 100k electrons events in Trasgo detector. Up: 3D plot for incident electron of 100 MeV. Center: 3D plot for incident electron of 316 MeV . Down: 3D plot for incident electron of 1 GeV. The jet come broadening is bigger as the energy decreases.

privileged direction of the traces may exist which would explain the central density effect. The traces reconstructed by the dots deviated very little from the initial vertical trajectory. The spots of the planes (T2, T3 and T4) become smaller as the energy increases. This

effect can be understood with the traces: the traces deviate less than the initial trajectory as the energy of the incident electrons grows. At first sight, one can realize that most of the hits can come together within a conical geometry with a certain angular aperture (θ). Then, one can say that the particles shower forms a cone.

Figure 4.8 show the 2D plot produced by 100k electrons of 100 MeV with vertical incidence in interaction with planes T2, T3 and T4. The x-axis and y-axis are in centimeter. The plots shows some spots in the geometrical center of the planes due to the high density of hits. Thus, the deviation of the trajectories increases compared to the incident electron as the planes grow. The density of hits near the geometric center varies by an order of magnitude by comparing the plane T2 and T4. The cloud of hits shows well the dimensional limits of the detector planes, pads and hollows of the stripes. A phenomenological analysis of showers inside the detector can be made with simple event-detector simulations shown in the previous results performed with Geant. Then, the vertical and non-vertical study of particles showers are studied below with physical observables.

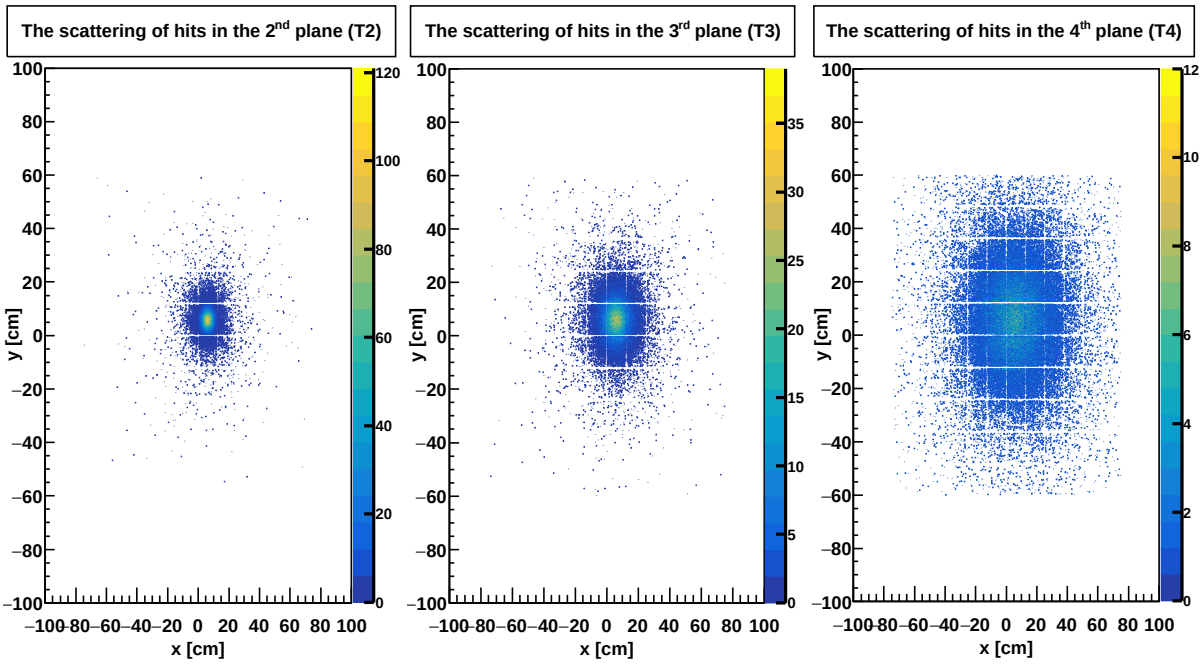

Figure 4.8: Scattering of hits in the planes of Tragaldabas. Left: x-y graph of the second plane (T2). Center: x-y graph of the third plane (T3). Right: x-y graph of the fourth plane (T4). The cloud of hits grows on the surface as the e.m jets cross the planes.

The Figure 4.9 represents the multiplicity histograms. The histograms present the multiplicity per plane for the incidence of 100k electrons and muons of 100, 316 MeV and 1 GeV. The red, green and blue lines represent respectively the multiplicity for planes 2, 3 and 4. The multiplicity of electrons increases as the energy grows, this is visible in the evolution of 100-316 MeV histogram. The multiplicity decreases for the histogram at 1 GeV. Then, a global maximum multiplicity exists in the energy evolution of the data. The multiplicity is maximum (M=6) for the 4 plane of the histogram at 316 MeV. The

multiplicity is minimal (M=3) for the other planes and energies. For muons, a different situation is observed. An increase in multiplicity as a function of energy is not visible in the histograms. The multiplicity at 100 MeV is higher than the rest of the cases. This indicates that, the increase of muon energy does not imply and increase in the number of hits. The mutilicity is M=4 (maximum) for the 2 plane of the histogram at 1 MeV and M=1 (minimum) for all planes and energies.

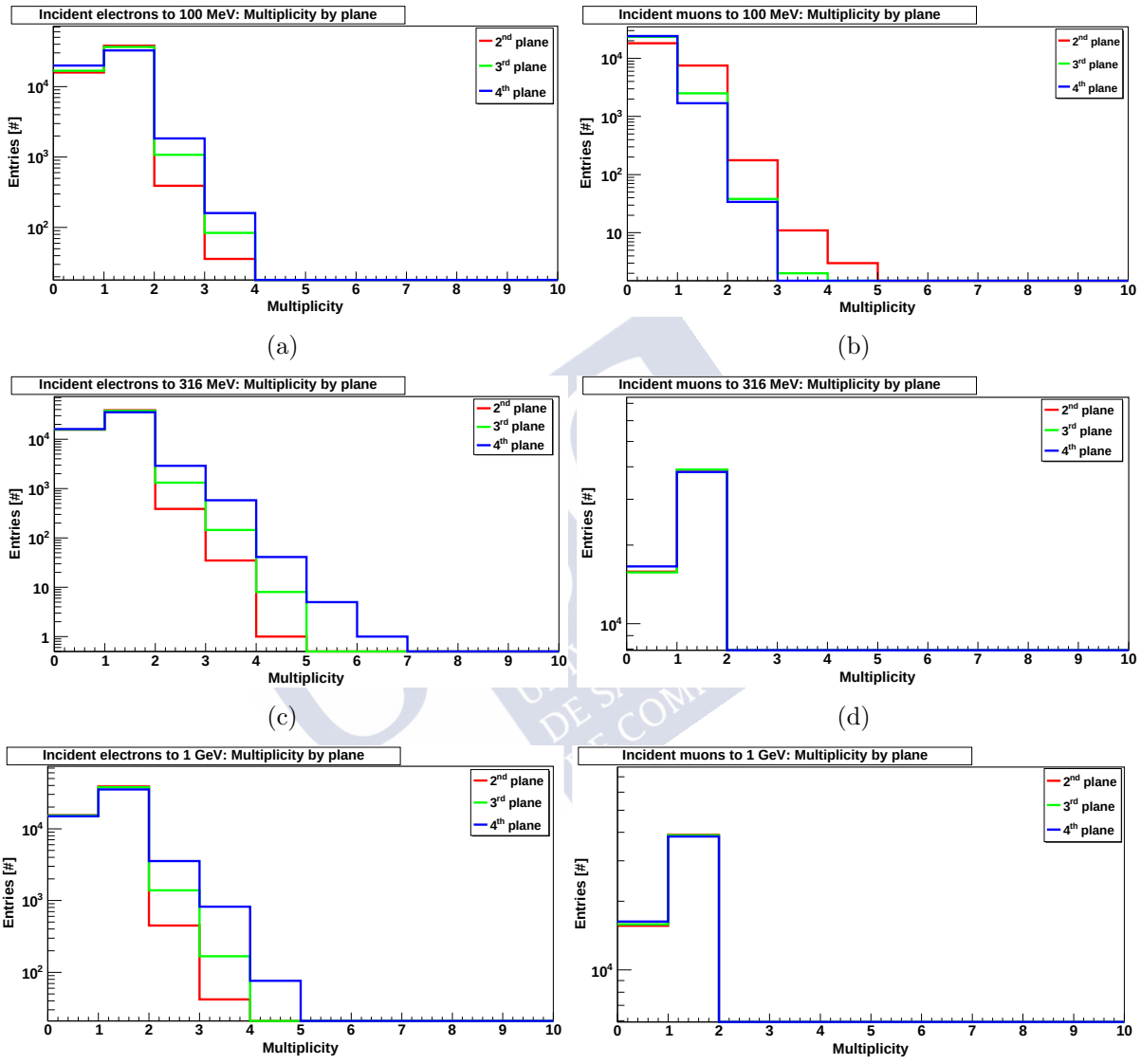

Figure 4.9: The evolution of Multipicity by plane of 100k electronic and muonic events. Incident electrons to 100 MeV (a), muons to 100 MeV (b), incident electrons to 316 MeV (c), muons to 316 MeV (d), incident electrons to 1 GeV (e) and incident muons to 1 GeV (f). The multiplicity increases as the energy increases for electrons while the multiplicity of muons decreases with the energy until stagnated from 316 MeV.

In order to a better characterization of the showers produced in Tragaldabas, the total multiplicity, scattering angles and a maximum reached layers are also studied. The maximum layer is the further plane in which a hit has been recorded by the detector.

The data is refleced on the histograms of the Figure 4.10. To obtain these histograms, the interaction of 100k electrons at 100 MeV was simulated on the first layer of the detector. Not to forget, that the electrons have a vertical incident on the center of the layer.

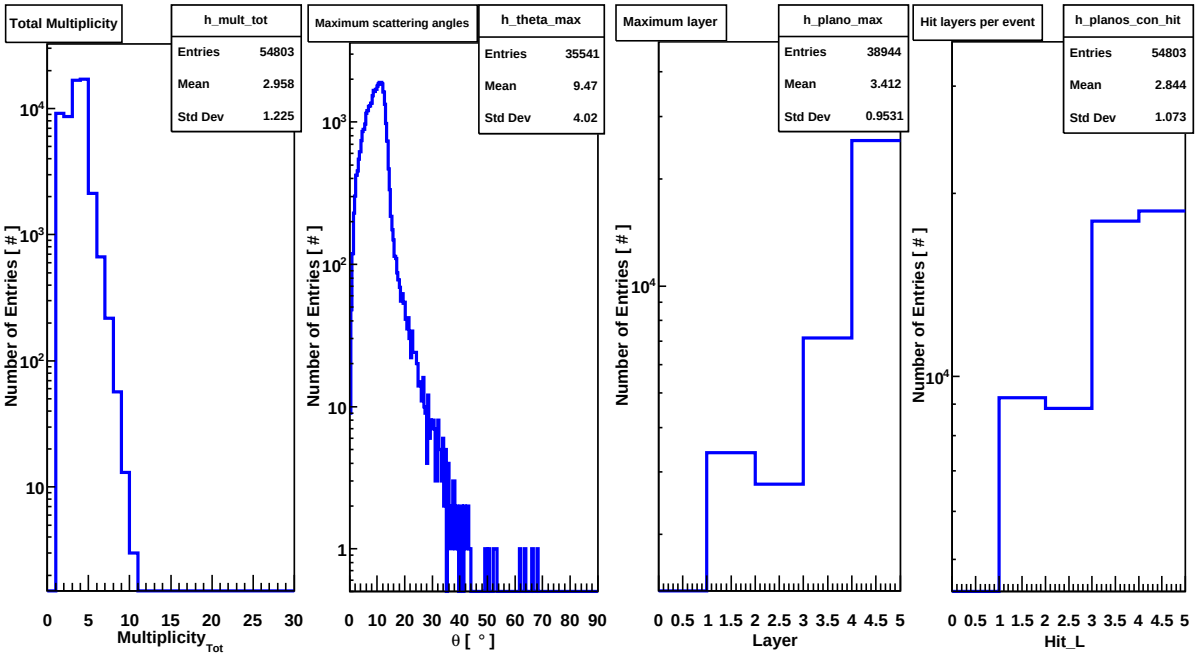

Figure 4.10: Histograms results of 100k electrons incidents to 316 MeV. Histograms of total multiplicity, maximum scattering angle, maximum layer and hit layer per event are presented.

The observables corresponding to the Figure 4.10 are presented below. The Multiplicity results are of 10 (maximum), 1 (minimum) and 2.95 ± 1.23 (average). To estimate the maximum angular aperture, the `GetMaximumBin()` and `GetBinCenter()` functions of Root analysis program were used. The values collected from the second histogram is of $\hat{\theta}_{max}$=11.475°. In the third histogram, it′s important to know the length of the shower, up to the 4^{th} plane. The detection efficiency value and the mean value of layer with hits per event are collected from the fourth histogram. The values are $\hat{\varepsilon}_{\text{eff}}$=0.054803 (or 0.55%) and mean value of hits layer per event is 2.844 ± 1.073.

After the analysis of the simulated data, the study is divided into two sets of results: vertical incidence and non-vertical incidence. To facilite the reading of results, the legend of graphs will be commented. All graphs use the following criteria described in the legend "except one″, the maxima and minima results. Red dots represents the incidence of photons in the detector, blue rectangles the incidence of electrons and violet stars represents the incidence with muons. The legend of multiples maxima and minima graph provides the following selection: 1.- red dots, blue diamonds and violet stars represent maximum multiplicities of respectevely photons, electrons and muons. 2.- red rectangles, blue inverted triangle and violet rectangles represent minimum multiplicities of photons, electrons and muons, respectively.

The particles collided in the center of the first plane is the trigger imposed in the vertical incidence task. Figure 4.11 shows the graph of efficiency, average, maximum and minimum multiplicity, and planes with hits for the 3 primary particles studied. The efficiency graph shows the absolute efficiency ε_{eff} as a function of the energy for primary particules. The electron curve grows step by step from about null ε_{eff} value at 1 and 1.78 MeV to 1 at approximatelly 31.6 MeV. The muon curve is rather flat and the values ε_{eff} remain close to 1 for all range of evaluated energies studied.

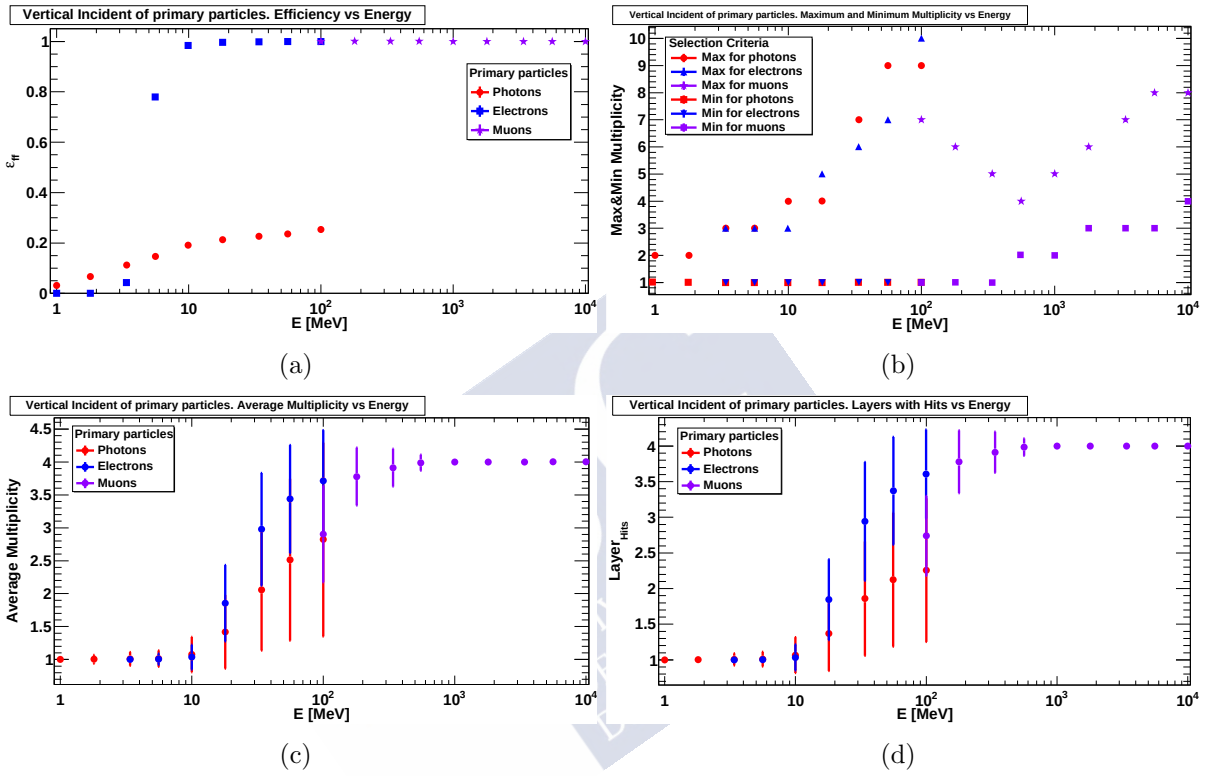

Figure 4.11: Analysis results by vertical incident of 100k primary particles. Efficiency graph (a), graph of average total multiplicity (b), maximum and minimum multiplicity graph (c), and, planes with hits graph (d). The efficiency graph shows a factor 10 between electron and photon data, and electrons are relevant from about 10 MeV. Results shows a majority of electrons and muons arrive respectively at the 4 plane at 100 MeV and 200 MeV, both cases with multiplicity near 4.

The average multiplicity graph represent de mean multiplicity values (M_{averg}) and statistical uncertainties as a function of energy in MeV units. It was obtained a value of 2.8 for photons and 3.7 for electrons at 100 MeV . The average multiplicity for primary muons is remains at a value of 4 above 178 MeV. The M_{averag} grows up to a value of about 3 for photons and about 4 for electrons at 100 MeV. The layer with hits graph trends are very similar to average multiplicity graph. The changes are in the widths of the uncertainties and values of layer with hits close to 100 MeV. The layer with hits value a 100 MeV are 3.6, 2.6 and 2.1 for elecrons, muons and photons, respectively. Finally, the next graph shows the maximum multiplicity (M_{max}) and minimum multiplicity (M_{min}) as a function

of energy. The M_{max} of photons starts from a value of 2 at 1 MeV and grows up to a value of 9 at 100 MeV. The M_{max} of electrons starts from a value of 2 at 3.16 MeV and grows up to a value of 3.16 at 100 MeV. The minimum multiplicity for this same particle grows stepwise from M_{min} equal to 1 to 100 MeV to 4 to 10000 MeV. The M_{max} is equal to 4 at 562 MeV, this is a global minimum, for muons. The muon M_{max}=8 is highest to 10000 MeV.

In summary, the efficiency is maximum for electrons at 10 MeV and for muons in all energy range studied. Electrons only reach the fourth plane for energies above 100 MeV, while muons do so for their whole energy range.

The Figure 4.12 shows the maximum scattering angles of the primary as a function of the energy. The curve of photons is maximum at 15.53° to 1.78 MeV and minimum at approximately 9° to 5.62 MeV. The trend for electrons decreases as the energy increases. It starts with a θ_{max} value of approximately 23° to 10 MeV and ends at a value of approximately 3° to 100 MeV. The muon curve descrease asymptotically from a θ_{max} value of 6° to 100 MeV up to a value very near to zero at 10000 MeV.

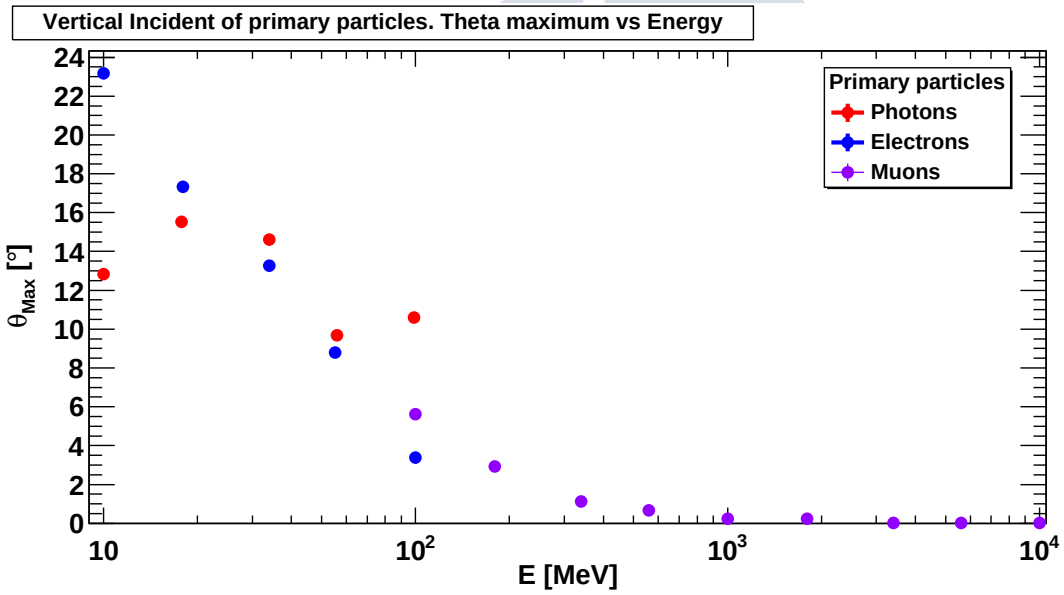

Figure 4.12: Results of maximum scattering angle for the three particles with vertical incidence. The graph shows a continuous decrease of the angle as a function of the energy for electrons and muons, differently it grows to a maximum in about 20 MeV for the photon and then decreases.

Now, the study of showers in the detector with **non-vertical incidence of particles** are explained. Particles hit in a random positron and with a random direction over the first plane of Tragaldabas. To do this, a starting virtual plane was generated with the appropriate dimensions and distance so that the particles have a completely random interaction on the detection plane.

Figure 4.13 shows the graph of efficiency, average, maximum and minimum multiplicity, and planes with hits of primary particles. The efficiency graph represent the absolute efficiency of particle detection as a function of energy. The electron data is very close to zero down to 3.18 MeV and grows strongly to 0.45 approximately at 100 MeV. The muon efficiency is 0.43 for its all energy range.

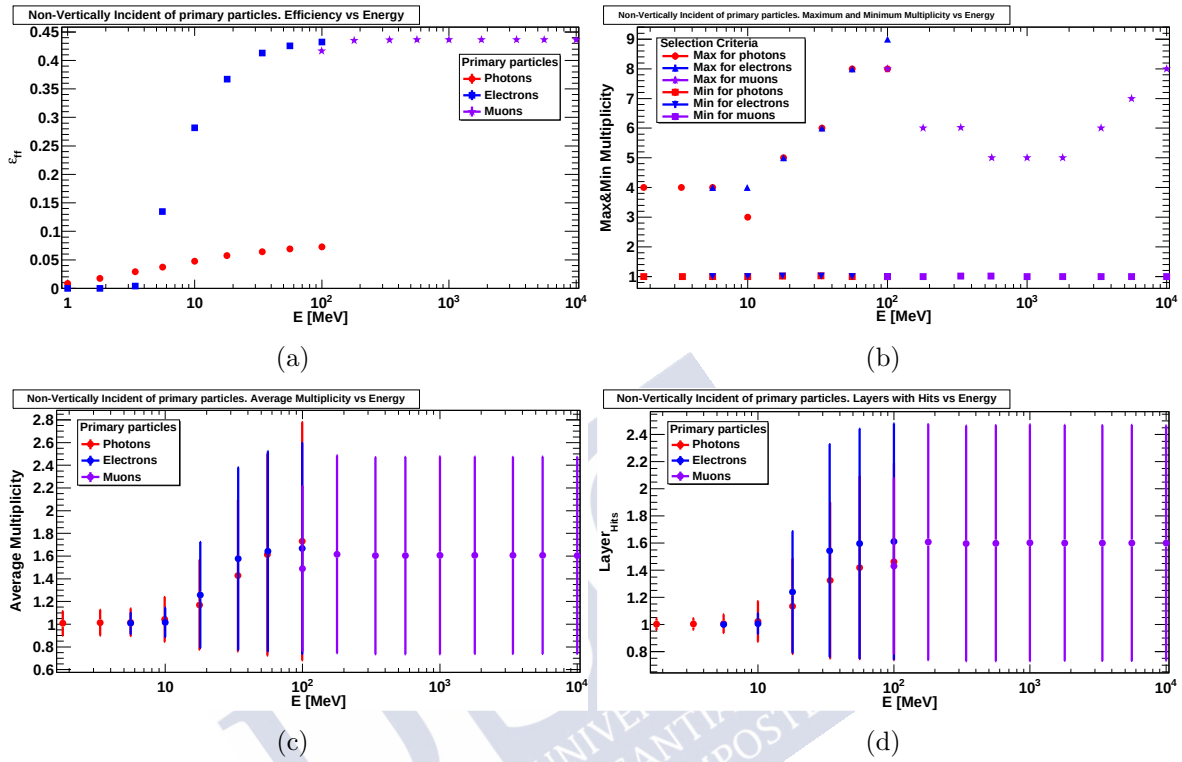

Figure 4.13: Analysis results by non-vertically incident of 100k primary particles. Efficiency graph (a), average total multiplicity (b), Maximum and minimum multiplicity graph (c) and layers with hits graph (d). The efficiency graph shows a factor 10 between electron and photon data, and electrons are relevant from about 100 MeV. Results shows a majority particles arrive at the 2 plane up to 100 MeV with M≈2, the uncertainties of values are large.

Another graph represents the average multiplicity M_{averag} as a function of the energy of incident particles on the detector. The photon data starts at 1.78 MeV (M_{averag}=1) up to 100 MeV (M_{averag} ≈1.8). The electron data starts at 5.62 MeV (M_{averag}=1) and extends up to 100 MeV (M_{averag}=1.75). The uncertainties also grows as the energy increases. Muon data is 1.6 to 10 GeV. The uncertainty of muons does not vary much as the energy grows. The graph of Min&Max Multiplicity represents the maxima and minima of multiplicity as a function of the energy for photons, electrons and muons. The maximum multiplicity is 4 in the energy range of [1.78, 5.6] MeV for photons. The maximum multiplicity of electrons starts from 4 to 5.62 MeV and grows up to 9 to 100 MeV. A minimum of multiplicity is visible between 562 and 1780 MeV for incident muons. Finally, the last graph represents the layer hit per event as a function of the energy for the 3 incident particles. The electronic data is from 1.6 to 100 MeV and muons 1.4 to 10 GeV. The uncertainties vary very little as the energy increases.

4.2.3 Conclusion of preliminary study

The study provides information about the behavior of the electromagnetic shower in the Tragaldabas detector using physical observables. The results show a maximum effective efficiency around 20 MeV for the electron with both vertical and non-vertical incidence. Many of the electrons arrive at the fourth plane with multiplicity around 4 to about 100 MeV for a vertical incidence and arrive to the second plane with M$\simeq$2 at the same energy for the random incidence. The angular aperture is very similar to 100 MeV for both electrons and muons.One can also start that, for muons, an efficiency compatible with 100% is observed, and they always give a hit in the four detection planes.

4.2.4 Geometric acceptance

Another important parameter used in detector physics is geometric acceptance. The **geometric acceptance** ($\mathbf{a_g}$) is a probability distribution of characterizing the trajectories of particles that cross the detector. This value depends only on the geometry of the detector, on the form of the pads and on the 4 planes of Tragaldabas. The values of acceptance are used to correct the real rate [Hz cm^{-2}] of particles measured by the detector.

The geometric acceptance will be studied by 3D density histograms. The histograms were calculated by simulating the non-vertical and random incidence of muons at 4 GeV over the all surfaces of the first plane. This configuration endures that the incoming particles will give a signal in any of the detector planes that it passes through. The first was used as a reference to calculate the a_g of the different planes of the detector. Geometric acceptance histograms represent the probability of being detected in the different planes when the incoming particle reaches a given section of the first plane with any angle. and the binning corresponds with the detector pads. The geometric acceptance is studied when the trigger is in a single plane, in two, in three or in all planes. Figure 4.14 represents the geometric acceptance histograms. Figure (a) is achieved with particles that cross the first plane of the detector (T1). Figure (b) shows particles crossing the first and second plane (T1&T2). Figure (c) shows a_g when particles cross the planes 1^{st}-2^{nd}-3^{rd}. Figure 4.14(d) gives the same physical observable values for the 4 planes of Tragaldabas.

The acceptance is higher for the cells near the ends than in the center of the plane. The values are even higher in the cells situated in the corners of the plane. This effect appears because non-vertical trajectories with maximum incidence angles are privileged trajectories. As the particle incidence angle in the plane decreases the a_g also decreases. This effect is not seen in the other cases. Figure 4.14 (b) shows that the data density is greater at the center than at the limits of the plane size. This happens because, the trajectories located in the limtis of the first plane size tend to approach the vertical and the events are concentrated in the center of the second plane.

Something similar happens for the histogram (c) of the Figure 4.14. The cells with high

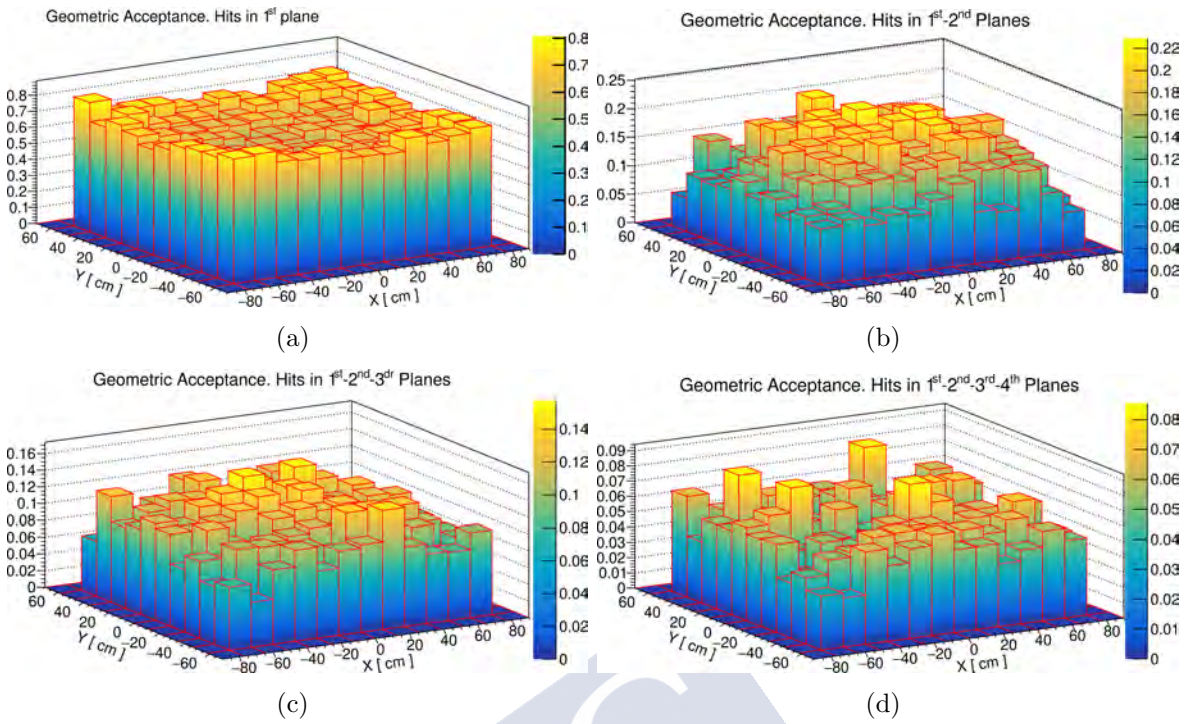

Figure 4.14: Geometric acceptance for different planes of the Tragaldabas detector. a_g of first plane (a), first and second plane (b); first, second and third plane (c). a_g of first, second, third and fourth plane (d). Results for corrections to be made in the real data collected from Tragaldabas.

density a_g are situated in the center of the plane, but it begins to see more scattered cells in the plane. Figure 4.14 (d) shows that there are few densities of a_g density. Also, the delocalisation of cells with maxima a_g is greater than in the previous histograms. This effect of delocalisation in the maximum of a_g can be understood with the cone of the e.m shower. As the shower propagates through the detector, the particle-detector interaction surface is greater. The maxima in density decrease strongly as the planes are taken in the calculations. The maximum density decreases by a factor 10 between the histogram (a) and (b).

To remember that, the greometric aceptance histograms are used to make further corrections to the real analysis of real data taken by Tragaldabas. And, in short, we can conclude that, when Tragaldabas is operating its four detection planes, and the four planes trigger is required (or at least a trigger signal given by the first and last planes), only an overall value of 5% of the incoming cosmic rays are geometrically accepted by reach detection cell.

4.3 Custom-made event generator

Based upon the Cry event generator output, a custom-made secondary cosmic ray event generator has been developed. It allowed for an easier and faster data production

an analysis in Tragaldabas. The inverse function method [16] is used for this purpose.

4.3.1 Inverse transform method

Given a density function $f(x)$, where $x \in (-\infty, +\infty)$. Rewriting the probability density (PDF) as $f(a)$, the integrated probability is $F(a)$ in the range [0,1] and where $a \geq x$. Given a u, such:

$$u = F(x) \ ,$$

the inverse function is the following:

$$x = F^{-1}(u) \ .$$

4.3.2 Analysis results

The task involves creating a simple cosmic ray generator with Cry. The Table 4.1 collects all input parameters to the Cry data generation program. The generation of data was done with specific input parameters. All charged particles were selected in the Cry input (protons, photons, electrons, muons and pions), neutrons included. The other inputs taken were 0 for the altitude (sea level), 42.88 for the latitude, 09-20-2018 for the date and 10 for the subboxLength.

Table 4.1: **Cry input values**.

parameters	customized
neutrons	1
protons	1
gammas	1
electrons	1
muons	1
pions	1
altitude	0
latitude	42.88
date	09-20-2018
subboxlength	10

To create an executable the following command must be written to terminal: `g++ -L ../lib/ -I ../src/ "FILE" -lCRY`, where FILE is the executable code file. "FILE" can be any program written in C/C++ language that is located in the `test` folder. This task involves generating output data in a file, so the program `testOut.cc` of Cry was used. The output executable generated by `testOut.cc` will have the following assignment `a.out`. To start generating data, the following command will be written by terminal: `./a.out parameter.file 10`, where 10 is the number of data generated. The output data file generated by Cry has 10 columns with data that represent the following parameters:

```
#  nEvent  nSecondary  KE  x  y  z  u  v  w
```

where # is each event generated, nEvent is the number of particles per events generated, nSecondary the identifier of the particle, KE the kinetic energy of the particle, (x, y, z) are the vertex components and (u, v, w) are the direction cosine of the same particule. Important, $20 \cdot 10^6$ data events was generated for this task.

Figure 4.15 shows the zenith angle distributions for different energy ranges and for both particles, photons and electrons. Histograms shows the number of events as a function of the cosine of the zenith angle, θ. The cosine range of the angle is between 0 and 1 ($\theta \in [0, 90]^\circ$). The electron and photon histogram are very similar, the cosine of the angle grows as the number of events increases. The following color code has been chosen: red for a range in energies from 700 to 1275 MeV, green for [1275, 1850] MeV, cyan for [1850, 2425] MeV and blue for [2425, 3000] MeV. The trend is increasing as cosine increases, the distributions are maximized for $cos\theta$=1.

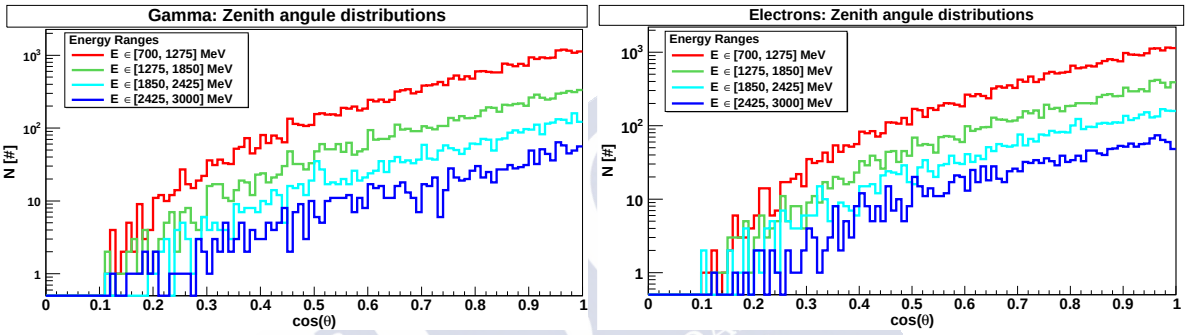

(a) (b)

Figure 4.15: Analytical results of zenith angle distributions at different energy ranges. Photon (a) and electron (b) distributions.

Figure 4.16 shows the angular distribution of muons, number of events as a function of the cosine of the zenital angle. The histogram is very similar to the previous ones although the curves grows in steps. The energy ranges are [250, 2200] MeV (red curve), [2200, 4200] MeV (green), [4200, 6100] MeV (cyan curve), [250, 2200] MeV (blue curve).
Figure 4.17 shows the energy distributions of gamma and electron for different ranges of zenital angle. The histograms represent the number of events per cosine of differential zenital angle as a function of energy in MeV for the 4 angle range already known. The events are maximum at low energies and decreases as the energy increases. The maximum energy studied of these histograms is 3000 MeV.

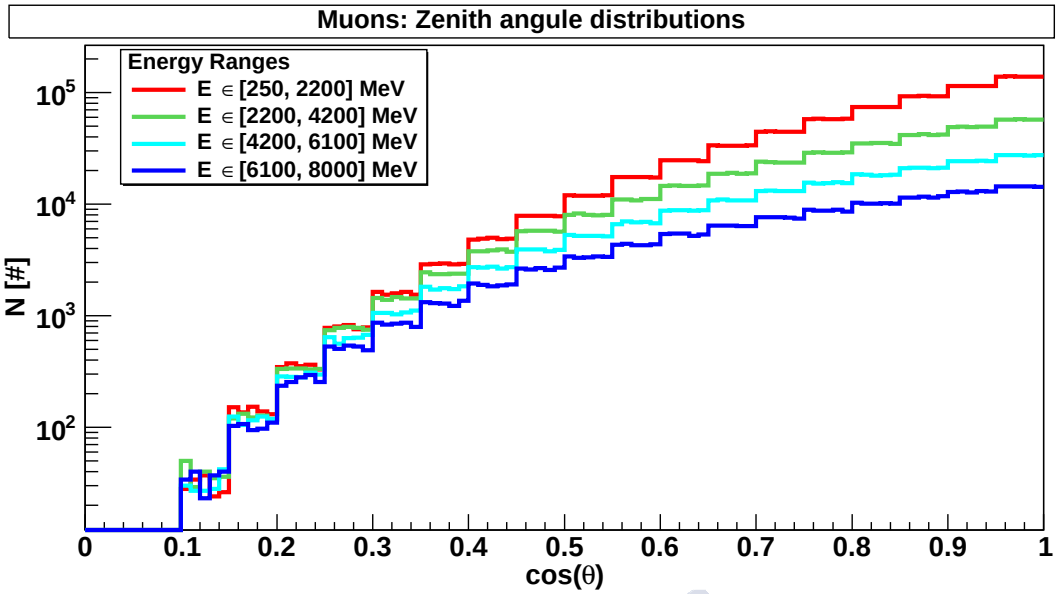

Figure 4.16: Analytical results of zenith angle distributions of muons at different energy ranges.

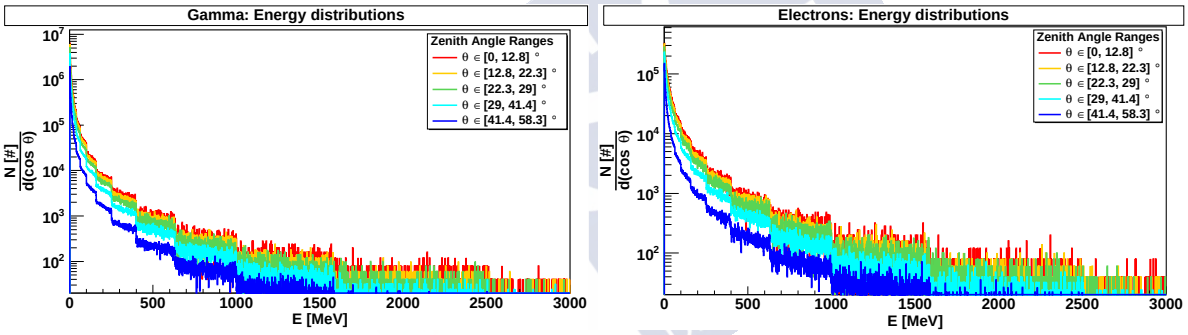

(a) (b)

Figure 4.17: Analytical results of energy distributions at different zenith angle ranges Photon (a) and electron (b) distributions.

Figure 4.18 shows the energy histograms for muons. The curves tend very different from the previous ones, they shows a maximum of 500 MeV. The curves decrease after the maximum. The maximum energy studied for this histogram is 8000 MeV. Some oscillations appear in the histograms possibly due to the generation of Cry program data.

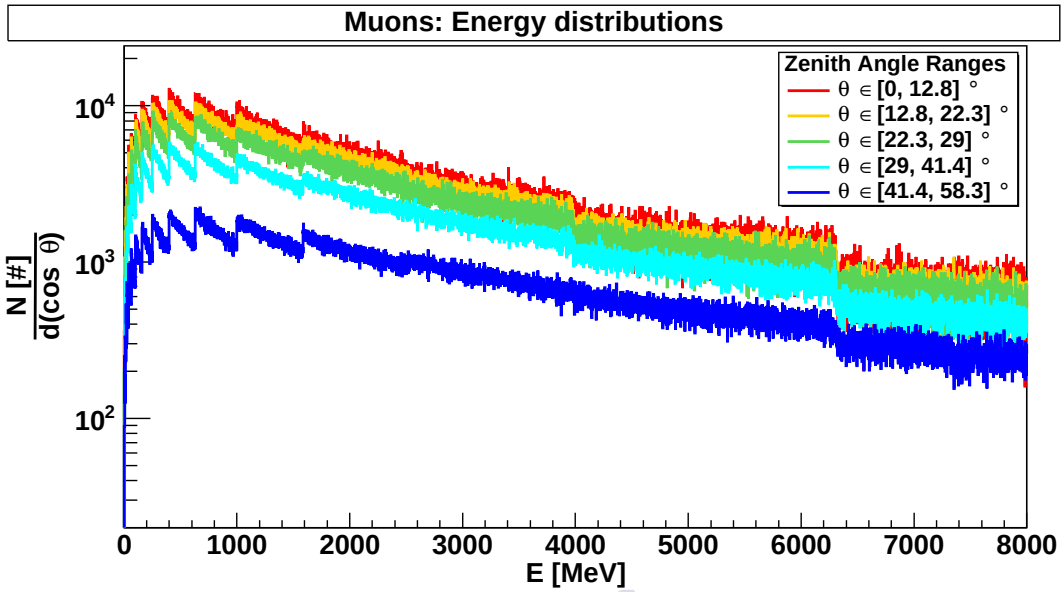

Figure 4.18: Analytical results of energy distributions of muons at different zenith angle ranges. The results show a great generation of muonic events at about 500 MeV.

The size of the Cry outputs is very large and difficult to work with to generate events in EnsarRoot. Then, a simple program for the generation of realistic Cry events in EnsarRoot was created using the inverse function method on the previous data. A distribution function $f(x)$ performed, this is normalized and the inverse function is done according to the distribution function. The functions of distributions have been fit the data of the angular distributions and energy distributions. The functions used in the fit were exponential. Function $f(x) = \mathrm{A}\,\mathrm{x}^{\alpha}$ fit the angular histogram data, where A and α are the adjustment parameters. The variable $\mathrm{x} = \cos(\theta)$ and zenital angle is bounded by [0, 1]. The inverse function of the angular distribution is the following:

$$\mathrm{I}_1(\mathrm{x}) = \mathrm{A}^{-1}\ \sqrt[\alpha+1]{\mathrm{x}}\ . \tag{4.1}$$

The result is simple since the function is bounded between 0 and 1.

The energy distribution data were fit to the function $f(\mathrm{y}) = \mathrm{B}\,\mathrm{y}^{\beta}$, where B and β are the adjustment parameters. The variable x for the distributions is the energy E. The selected energy renges are [100, 3000] MeV for photons-electrons and [100, 5000] MeV for muons. The inverse function of the energy distribution is written as:

$$\mathrm{I}_2(\mathrm{x}) = \mathrm{B}^{-1}\ \sqrt[\beta-1]{\kappa(x)[\lambda^{(1-\beta)} - 100^{(1-\beta)}] + 100^{(1-\beta)}}\ , \tag{4.2}$$

where $\kappa(\mathrm{x}) = \frac{100^{1-\beta}}{(1-\beta)} + \frac{\mathrm{x}^{(1-\beta)}}{(1-\beta)}$ and λ takes values of 3000 (electrons and photons) or 5000 (muons).

The fit values are shown in tables below for the 3 secondary particles ($e^{\pm}$, γ and $\mu^{\pm}$). The data of the histograms have two free parameters, so it is necessary to fix some of

these to fit. The energy distributions were fited for a fixed zenital angle of [0, 12.8]°. All zenital angle distributions for all energy ranges were fited. The values of uncertainties and goodness of fit were disregarded since a simple event generation program is desired.

Table 4.2 gives the fit parameters (A, α) of the zenital distributions for each energy ranges. The fit values are very similar between the different secondary particles.

Table 4.2: **Parameters fit of zenith angle distributions.**

Electrons			Photons			Muons		
E ranges [MeV]	A	α	E ranges [MeV]	A	α	E ranges [MeV]	A	α
[700, 1275]	$6.739 \cdot 10^5$	3.242	[700, 1275]	$1.385 \cdot 10^6$	3.254	[250, 2200]	$5.556 \cdot 10^7$	3.981
[1275, 1850]	$4.718 \cdot 10^5$	3.102	[1275, 1850]	$7.627 \cdot 10^5$	3.123	[2200, 4200]	$6.460 \cdot 10^6$	3.299
[1850, 2425]	$2.968 \cdot 10^5$	2.925	[1850, 2425]	$3.892 \cdot 10^5$	3.133	[4200, 6100]	$3.123 \cdot 10^6$	2.890
[2425, 3000]	$1.647 \cdot 10^5$	3.795	[2425, 3000]	$3.892 \cdot 10^5$	3.023	[6100, 8000]	$1.665 \cdot 10^6$	2.655

Table 4.3 shows the fit parameters of the energy distribution for all the analyzed particles. The parameters for electrons and photons are very similar but they change a lot for muons.

Table 4.3: **Parameters fit of energy distributions.**

Incident particles	B	β
Electrons	$1.7 \cdot 10^9$	2.596
Photons	$1.41 \cdot 10^{10}$	2.914
Muons	$3.17 \cdot 10^4$	0.0271

This event generation program was implemented and used succesfully in the EnsarRoot framework. The tabulated parameters are necessary for the generation of events with zenital and energy distribution in EnsarRoot. The weight values are essential for the generation of each of the particles.

USC
UNIVERSIDADE
DE SANTIAGO
DE COMPOSTELA

USC
UNIVERSIDADE
DE SANTIAGO
DE COMPOSTELA

5 Particle Identification with TRAGALDABAS detector

The design and implementation of a method for particle identification in the Tragaldabas detector was one of the aims of this work, and developed in this chapter. A robust algorithm was written and included in the EnsarRoot framework. It can identify muons and electrons with a certain accuracy starting from the events topology recorded by the detector. In start, the method analyzes three physical observables with simulated data, namely the total multiplicity, the weighted range and the chi-square, and creates a behaviour pattern that can be used with real data. Simulations and analysis are performed for 4 different Tragaldabas configurations: 4 active RPC planes (T1, T2, T3 and T4), 3 active RPC planes (T1, T3 and T4) and 4 active planes with a 1 cm and 1.5 cm thickness of lead. The whole method and its results are presented and discussed in the following sections, and the most important results have been also presented at the 36th International Cosmic Ray Conference, ICRC 2019, and a short version is published in [88].

5.1 The MIDAS particle identifiation method description

In this work, we develop and novel algorithm[1], called MIDAS (Multisampling IDentificAtion Software), intended to identify the different particle species detected by the Tragaldabas system.
MIDAS is based in the systematic analysis of the influence that different particles have over some dedicated observables. The behaviour of such observables was parameterized by means of simulation and applied later to real data. Thus, we obtain the electron/muon separation capabilities for Trasgo layouts and for Tragaldabas in particular. The selection of good observables is essential for the study of particle identification with Tragaldabas. Three observables already described in section 4.2.1, where the candidates for the study are: the total multiplicity M, the weighted range a_n and the chi-square χ^2 of the track fitting. These 3 observable physicists allow to carry out a complex study to achived algorithms for the identification of muons and electrons with the Tragaldabas detector. The study was done for four different detecta configurations: detector with trigger in the 3 planes, 4 planes and 4 planes with a lead layer of thickness 1 and 1.5 cm at a distance of 16.4 cm after the third plane. The second plane (T2) of Tragaldabas is not active for the 3-plane study. The studies with the lead layers allow to know the calorimetric capabilities of the experiment for the identification of electrons and muons. The addition

[1] An algorithm is a logical sequence of steps or guidelines for solving problems or performing calculations with any of the existing programming languages.

of lead would increase the stopping power in most electrons, forcing the interaction with lead and deflecting its trajectory, so that the observables would show greater differences between electron-muons and increase acurracy. The 4 active plane Tragaldabas with the 1 cm thickness lead layer, and the system inside the building, were already shown in Figures 4.4 and 4.3 respectively. As the track reconstruction can be done with different number of RPC active planes, the method also deals with that number and the algorithm design can change slightly.

5.1.1 Simulated data inputs

The generation of 10^5 events was done with unitary electromagnetic particles (electrons, muons and gammas rays) imping in the Tragaldabas starting randomly from a virtual plane of 200 $\times$ 200 cm^2, located 12.7 cm above de detector and achivied with direction uniformily distributed in ϕ and $\cos\theta$, where θ between 0 and 12.8°. The kinetic energy range in logarithmic scale is [10, 5620] MeV for electrons and [100, 5620] MeV for muons with 4 steps of $10^{\frac{2}{8}}$ per decade with a energy range of simulation per each kinetic energy value of 10%. The number of events is high enough to generate great statistics to have effective results, the virtual plane is large enough to collect a large number of events in all planes of the detector and that acceptance plays an essential roll, and finally, well-chosen angular parameters for optimal detection of all events in the detector were used with this input for simulated events over the detector, the three dedicated observables mentioned before were analyzed for each kind of simulated particle or track, and a phenomenological description was done. Then, an appropiate combination of the observables makes possible the particle identification for a real track.

The algorithm provides a particle identification, PID, and the probability of being a given particle, P(Id), mostly either a muon or an electron. In addition to the particle nature, the minimum energy E_{Min} is estimated. In the case when it is not possible to distinguish between different species, the probability of being a certain particle is given by the well known fluxes of cosmic rays at sea level, Table 1.1 from Kaye&Laby, National Physical Laboratory (NPL). The energy ranges of all this study were also collected from the same Table.

5.1.2 Four active planes configuration

Figure 5.1 shows the respective results for both electrons and muons for their respective energies of multiplicity (a) and (b), weigted range (c) and (d), and chi-squared (e) and (f). Histograms reveal the difference between the two particles interacting with the detector even though it is difficult to estimate a cutoff value of these. The behaviour of electrons with very high energy (above 200 MeV), even though with smaller flux of CR at ground level, is very similar to that for muons.

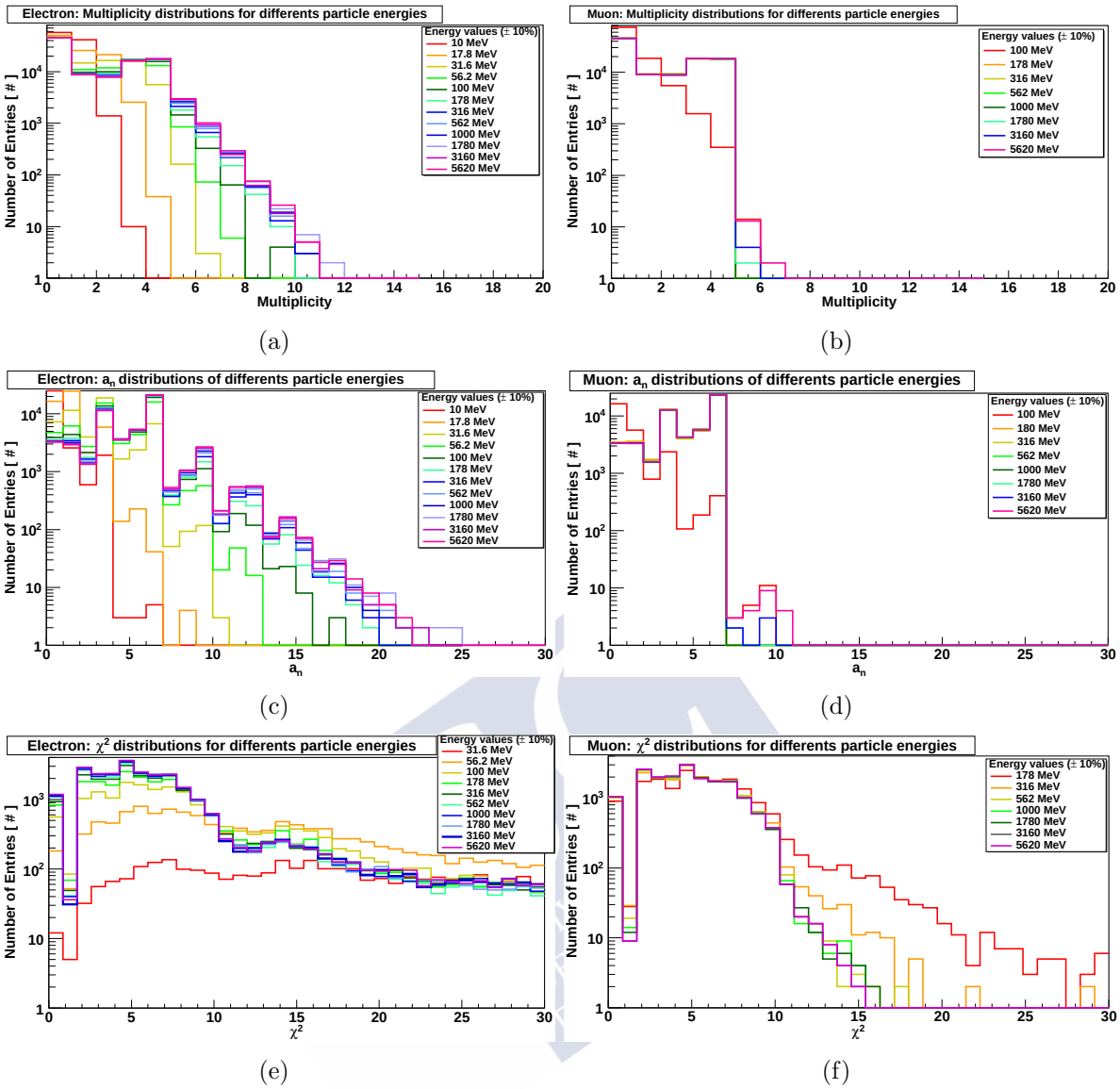

Figure 5.1: Results for 4 planes of Tragaldabas detector. Total Multiplicity distributions for different energy of electrons (a) and muons (b). Weighted range distributions for different energy of electrons (c) and muons (d). Chi-squared distributions for different energy of electrons (e) and muons (f).

Figure 5.2 shows the histograms of multiplicity (a), weigthed range (b) and chi-square (c) both muons and electrons for all energy working ranges. The results show great differences between muons and electrons. Electrons have a longer value of multiplicity, weigted range and chi-square than muons. The probability of electron detection is very high for χ^2 greater than 10, multiplicity greater than 5 and a_n greater than 7. It is clearly observed a bump around χ^2=15 in the electrons distribution. That bump was carefully studied and corresponds to the case where an electron is able to travel in straight line through 3 RPC consecutive planes. Figure 5.3 shows the 3D representation of hits for those precise events with an electron incidence energy of 56.2 MeV. The electron goes in straight line through T1 and T2, and then it is deflected in T3, reaching T4 with a different direction. In some

cases the generation of, at last, are secondary electron was recorded in T4. This scenario is exclusive for incident electrons. Thus, the use of the χ^2 parameter can be enough for a first electron/muon differentation, and indeed, it is the first input of the PID algorithm.

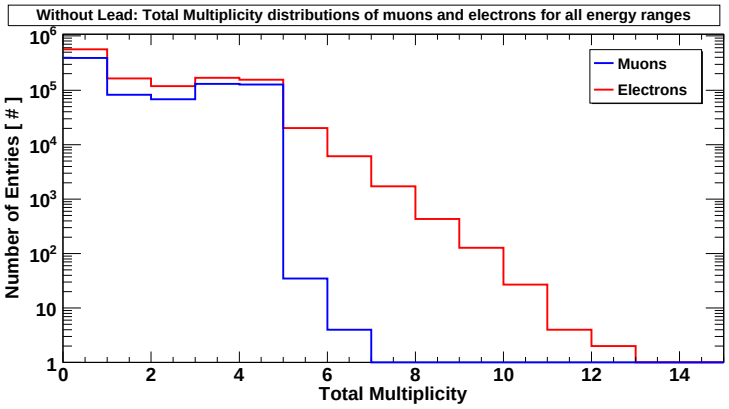

(a)

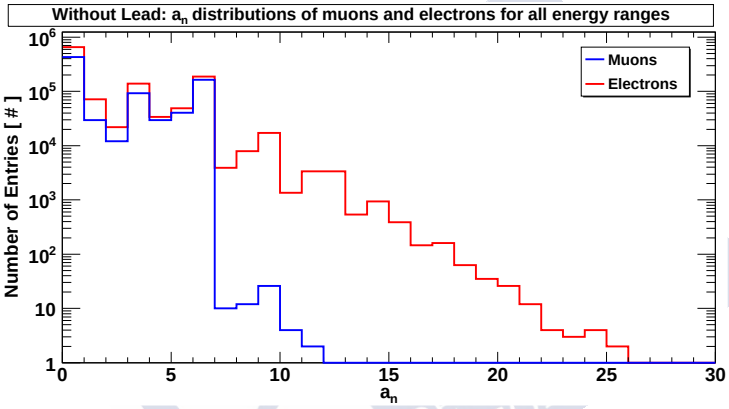

(b)

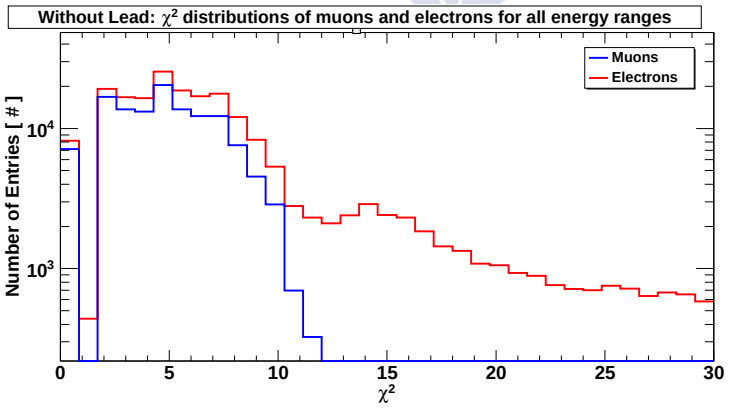

(c)

Figure 5.2: Results for 4 planes of Tragaldabas detector. Total Multiplicity histogram of electrons and muons (a). Weighted range histogram of electrons and muons (b). Chi-squared distributions of incident electrons and muons (c).

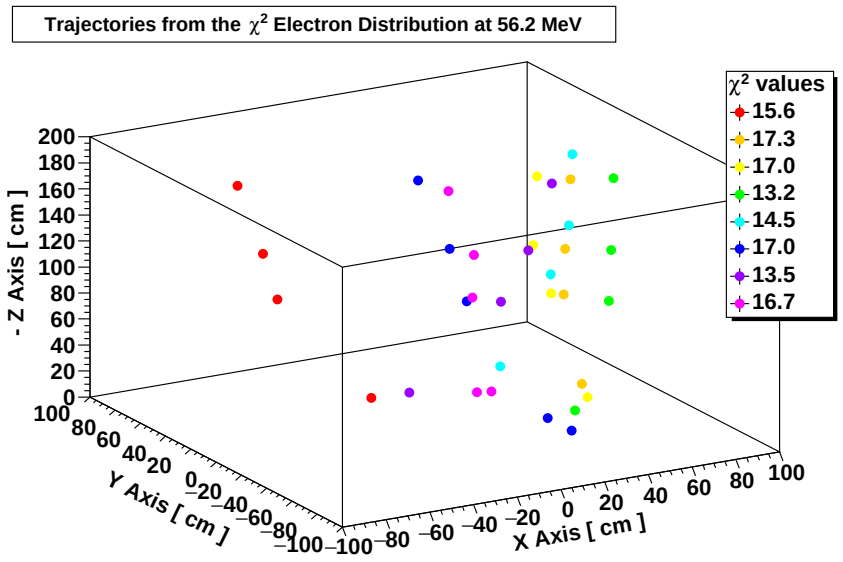

Figure 5.3: 3D hits plot from incident electrons at 56.2 MeV. The hits present the privileged trajectory of unit electrons where the deflection occurs between the third and fourth plane for all the events shown.

Figure 5.4 shows the 2D distributions in all energy ranges of respectively both electrons and muons for Multiplicity versus a_n (a) and (b), a_n versus χ^2 (c) and (d), and Multiplicity versus χ^2. One again, the distinction between distributions is large, electrons have greater multiplicity, a_n and χ^2 values than muons. The distributions also show the points density concentrated at low M, a_n and χ^2. Indeed, muons and electrons have M=4 or a_n=6 in most of cases, and for all energies, which corresponds to the clean case of the muon or electron (larger muon) crossing the four RPCs planes and giving only, and one only valid signal in each plane. Then, despite the correlation between M and a_n, the first can be also used for improve the electron/muon separation.

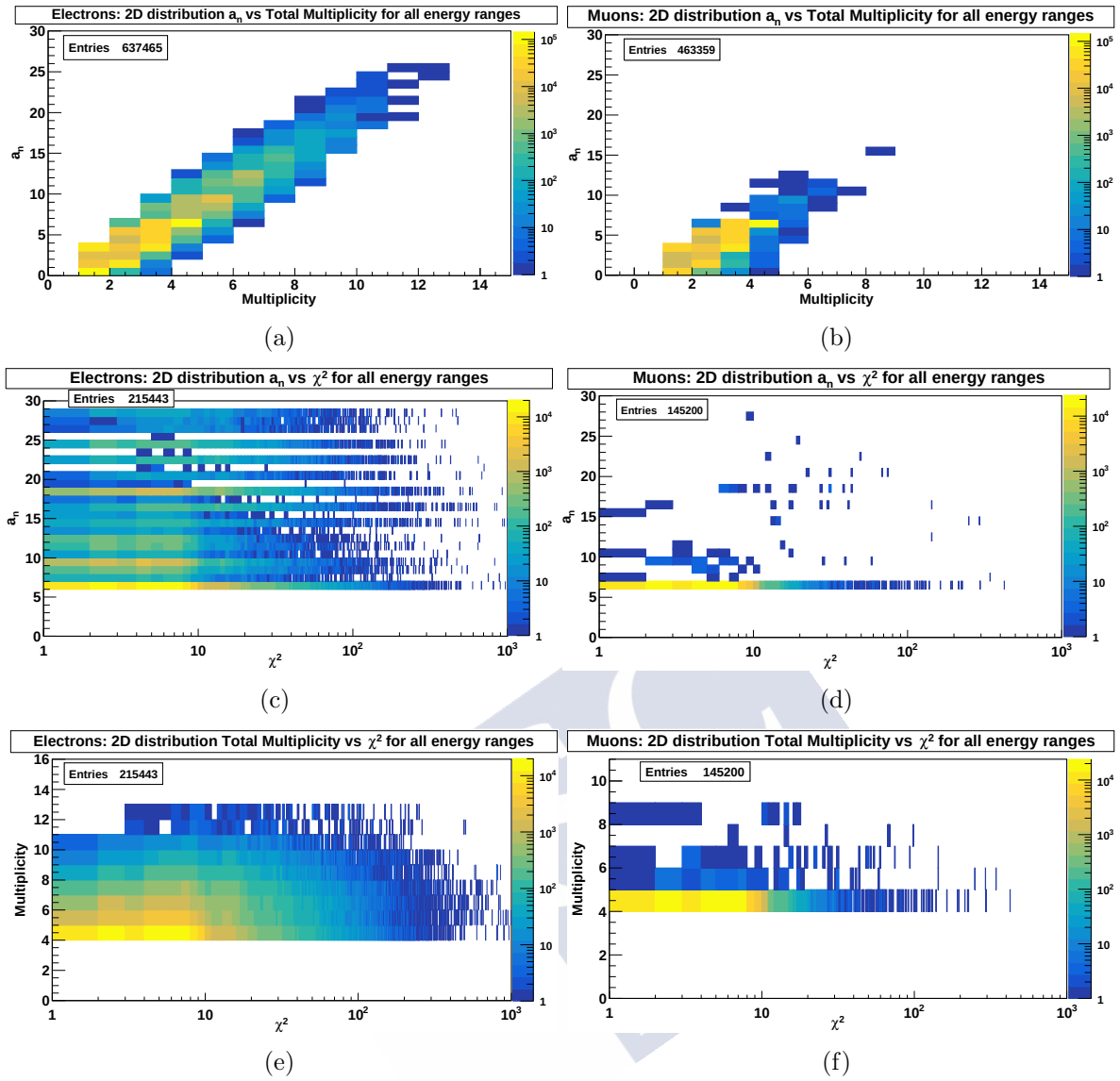

Figure 5.4: 2D electrons and muons histograms for all energy ranges. Weighted range vs total multiplicity distributions for electrons (a) and muons (b). Weighted range vs chi-squared distributions for electrons (c) and muons (d). Total multiplicity vs chi-squared distributions for electrons (e) and muons (f).

Figure 5.5 shows the flowchart of the algorithm for a maximum number of planes available in Tragaldabas. Starting from a first χ^2 evaluation, an appropriate combination of the three observables proposed makes possible an optimal algorithm and the final particle identification. Again, the probability and minimum energy of being muons is given by mean flux of secondary at ground level shown in the Table 1.1. Other possible cuts at low multiplicity and weighted range values were taken to optimize the identification, M=2 and a_n=2.

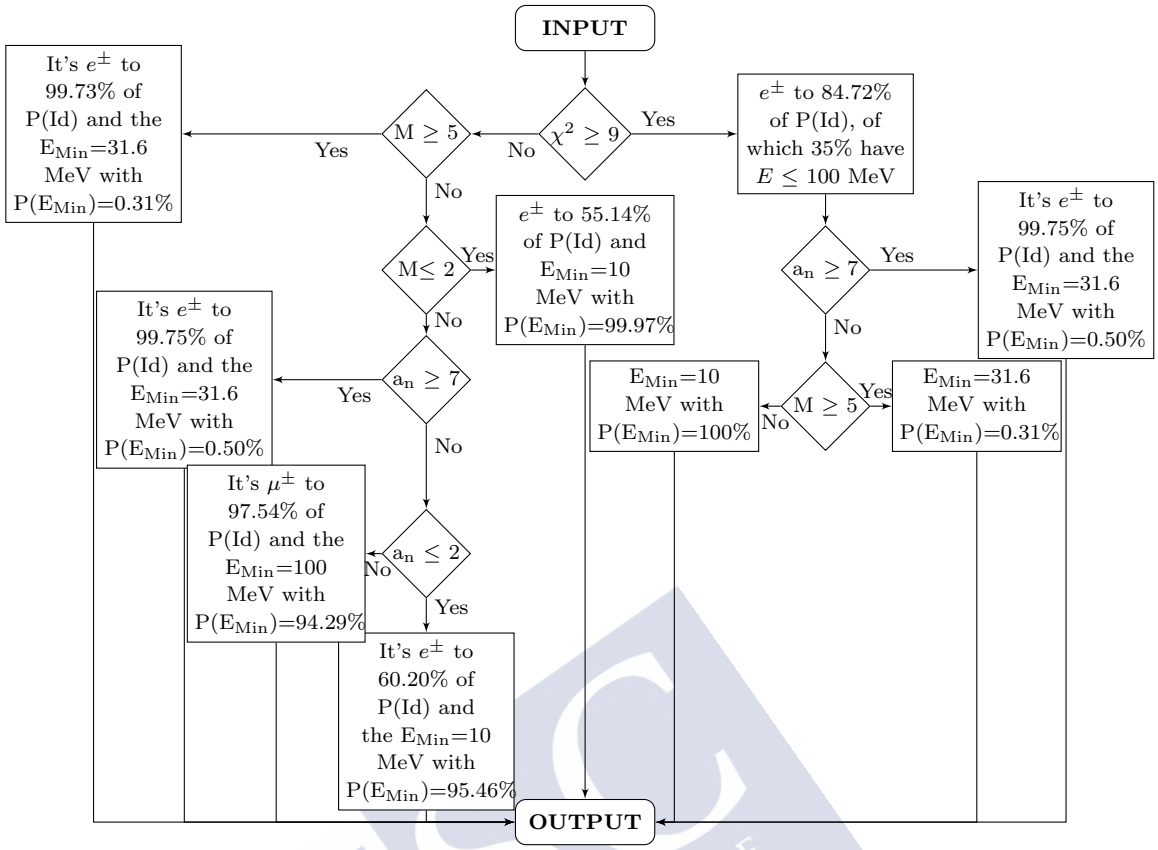

Figure 5.5: Flowchart for the MIDAS particles identification algorithm in the Tragaldabas detector. The solution procedure when 4 active RPC planes are available is shown.

5.1.3 Three active planes configuration

The same evaluation as that from previous section was done for the case when only three active planes of Tragaldabas (T1, T2 and T4) are available. Figure 5.6 shows the histograms both electrons and muons respectively of multiplicity (a and b), weighted range (c and d) and chi-squared (e and f) for a 3 RPC planes of Tragaldabas. The results show great differences between electrons and muons and even very long differences with the previous results with 4 and 3 active planes, especially in the case of electron incidence. The entries are very high for low multiplicities and weighted ranges. The highest electrons of 316 MeV have similar behaviors to muon.

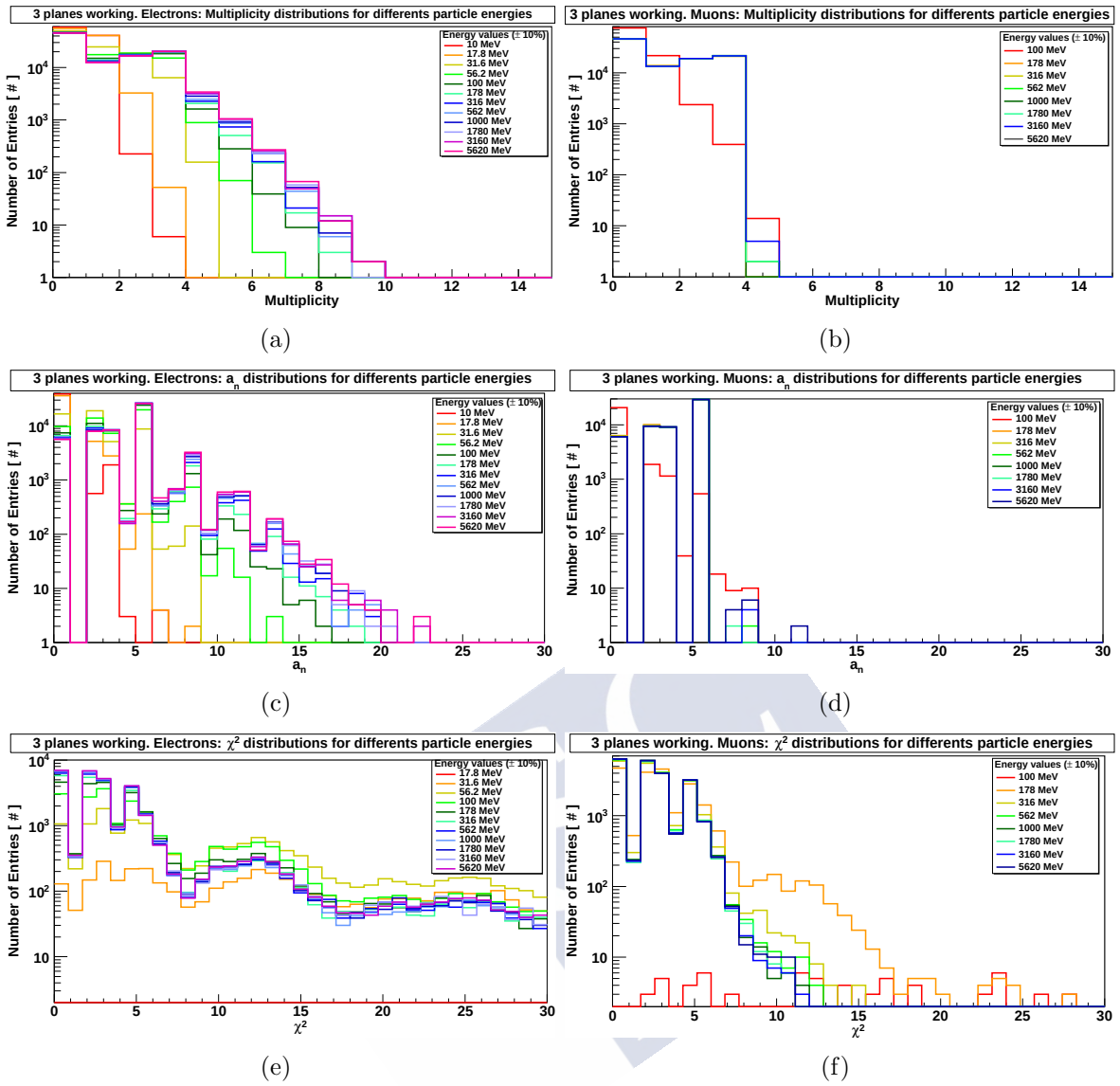

Figure 5.6: Results for 3 planes of Tragaldabas detector. Total Multiplicity distributions for different energy of electrons (a) and muons (b). Weighted range distributions for different energy of electrons (c) and muons (d). Chi-squared distributions for different energy of electrons (e) and muons (f).

Figure 5.7 shows the histograms both muons and electrons of multiplicity, a_n and χ^2 for all energy ranges and for 3 planes of Tragaldabas. The same equation described in the subsection 4.2.1 was used for the weithd range histogram even without the existence of the second plane of the detector, this was done due to the wide separation of data provided by the histogram for better analysis and identification. The high probability of electron identification is given for values greater than M=6, a_n=6 and χ^2=6. The bump is stronger in about χ^2=12 than in the previous case.

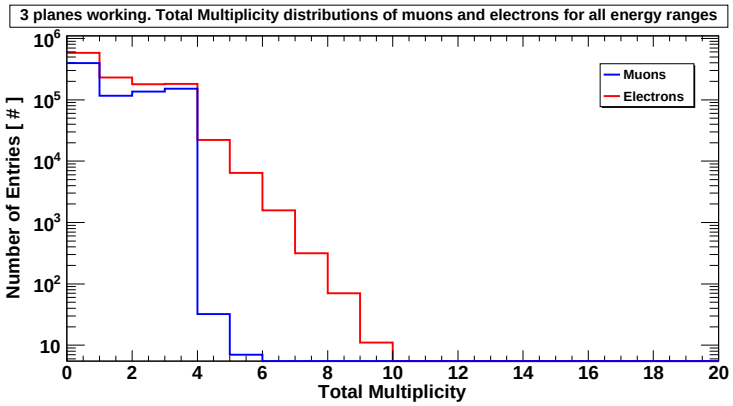

(a)

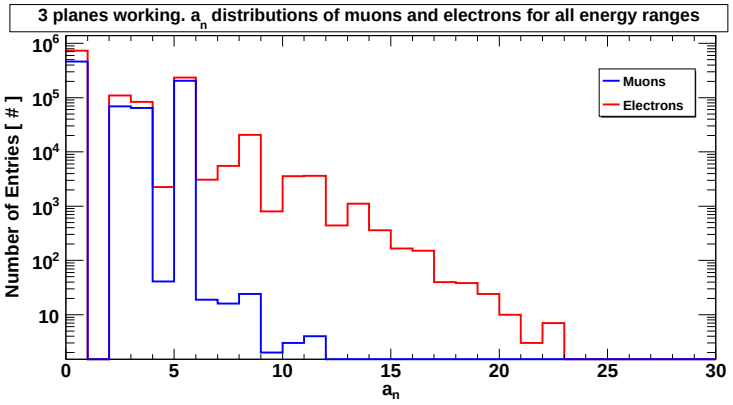

(b)

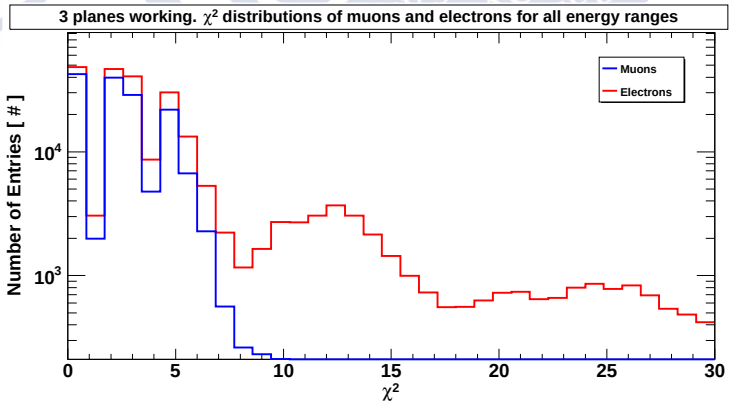

(c)

Figure 5.7: Results for 3 planes of Tragaldabas detector. Total Multiplicity histogram of electrons and muons (a). Weighted range histogram of electrons and muons (b). Chi-squared distributions of incident electrons and muons (c).

The Figure 5.8 shows the flowchart for 3 active planes configuration of Tragaldabas. The algorithm now is very different than the 4 active planes case due to the complexity of the histograms representing the 3 observables. Additional cuts of the 3 observables were imposed in the analyzes M=3 and a_n=4 The results of acurracy with simulated data are presented at the end of the section.

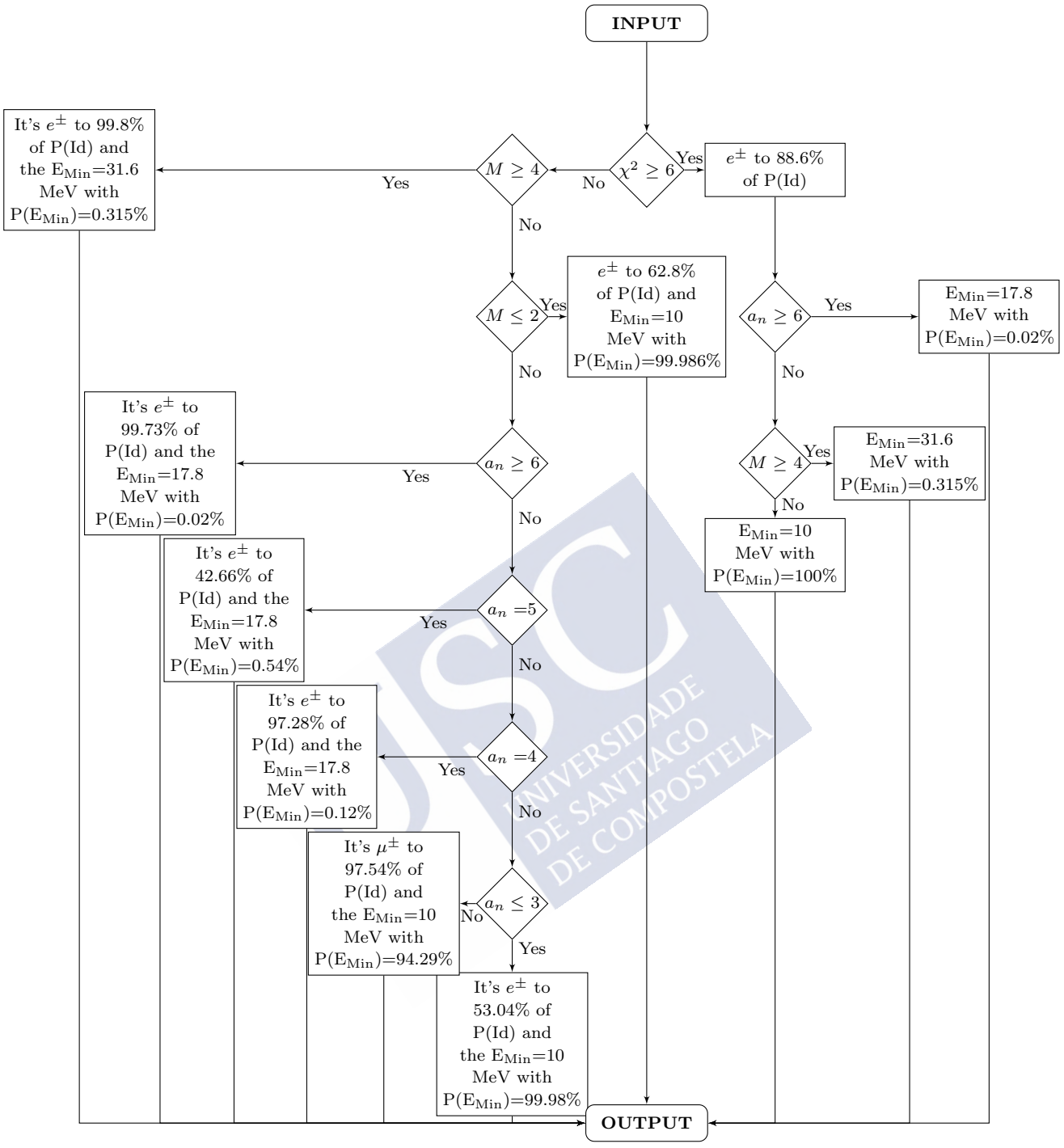

Figure 5.8: Flowchart for the MIDAS particles identification algorithm in the Tragaldabas detector. The solution procedure when 3 active RPC planes is shown.

5.1.4 Four active planes plus 1 cm lead layer configuration

The four active planes configuration was extended by placing a lead layer between T3 and T4. In this first case, the included lead layer has a thickness of 1 cm. The same analysis as that from previous section was done. Figure 5.9 shows the histograms both

electrons and muons respectively of multiplicity (a and b), weighted range (c and d) and chi-squared (e and f) for a 1 cm thickness of lead installed in Tragaldabas. The results show great differences between electrons and muons and even very long differences with the previous results with 4 and 3 active planes, especially in the case of electron incidence. The entries are very high for low multiplicities and weighted ranges. The highest electrons of 1780 MeV have similar behaviors to muon.

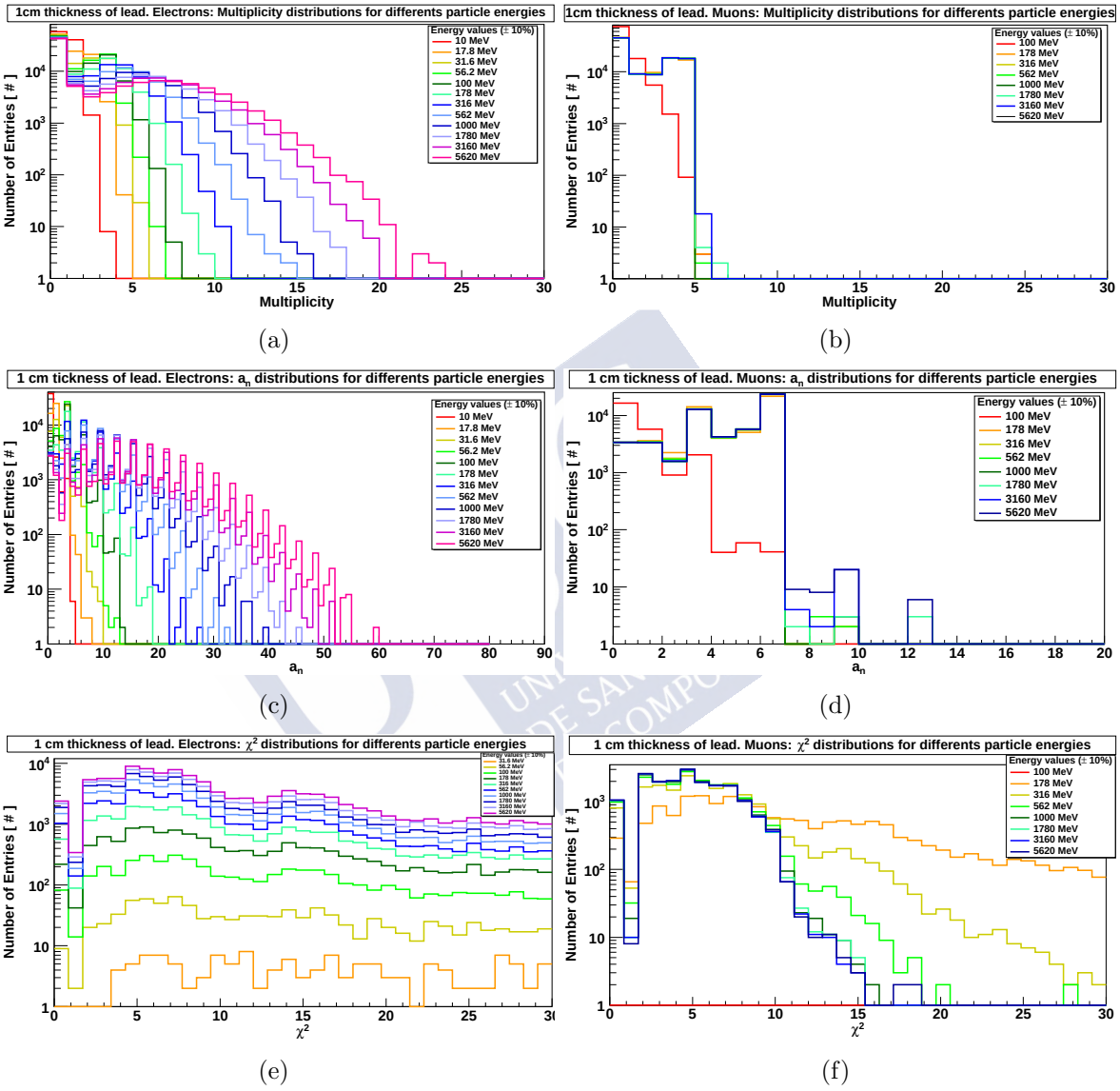

Figure 5.9: Results for 4 planes of Tragaldabas detector with 1 cm thickness of lead. Total Multiplicity distributions for different energy of electrons (a) and muons (b). Weighted range distributions for different energy of electrons (c) and muons (d). Chi-squared distributions for different energy of electrons (e) and muons (f).

Figure 5.10 shows the histograms of both muons and electrons of the 3 observable multiplicity (a), weighted range (b) and chi-square (c) for all energies range and for this case study with 1 cm thickness of lead. The parameters of high probability of identification of an electron are about M=5, a_n=7 and χ^2=10. The difference of the data is increasing to

those of the previous cases, the data of the electron tends to decrease to changes step by step as the multiplicity and weighted range increases. The bump of the chi-square histogram is stronger at $\chi^2 \simeq 15$ than in the previous cases.

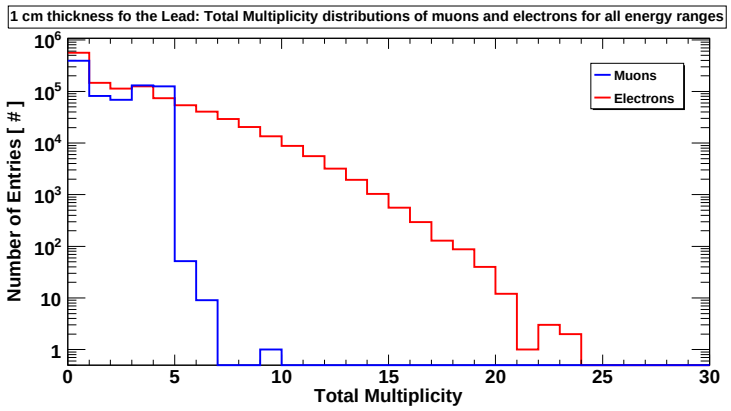

(a)

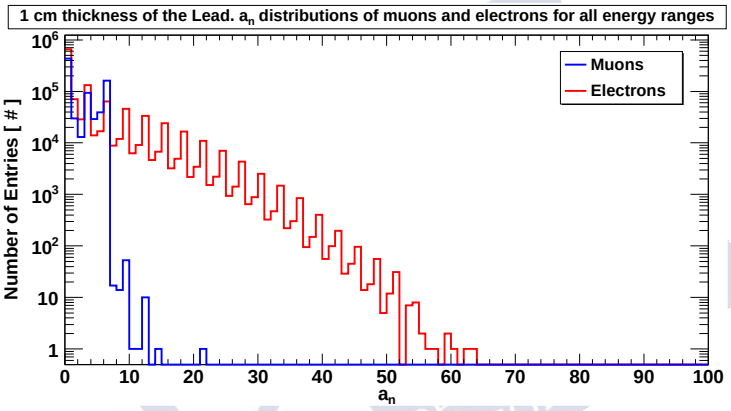

(b)

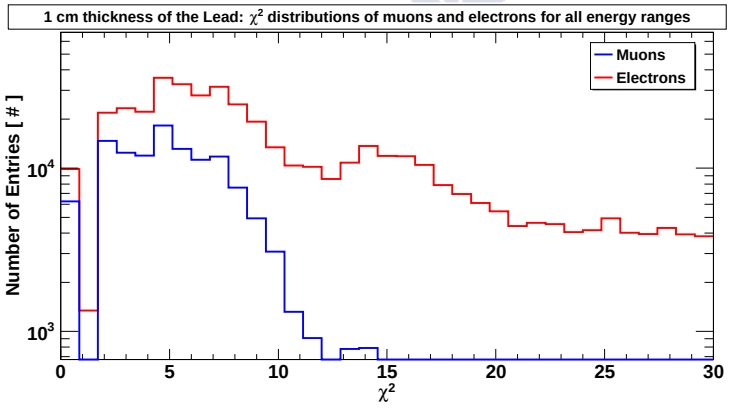

(c)

Figure 5.10: Results for 4 planes of Tragaldabas detector with 1 cm thickness of lead. Total Multiplicity histogram of electrons and muons (a). Weighted range histogram of electrons and muons (b). Chi-squared distributions of incident electrons and muons (c).

The Figure 5.11 shows the flowchart for the case of 1 cm thickness of lead after the third plane of Tragaldabas. The cutoff data of the 3 physical observables, minimum energies

and probabilities are very similar to those of the 4-plane cases. Again, the results of acurracy simulations are presented at the end of the section.

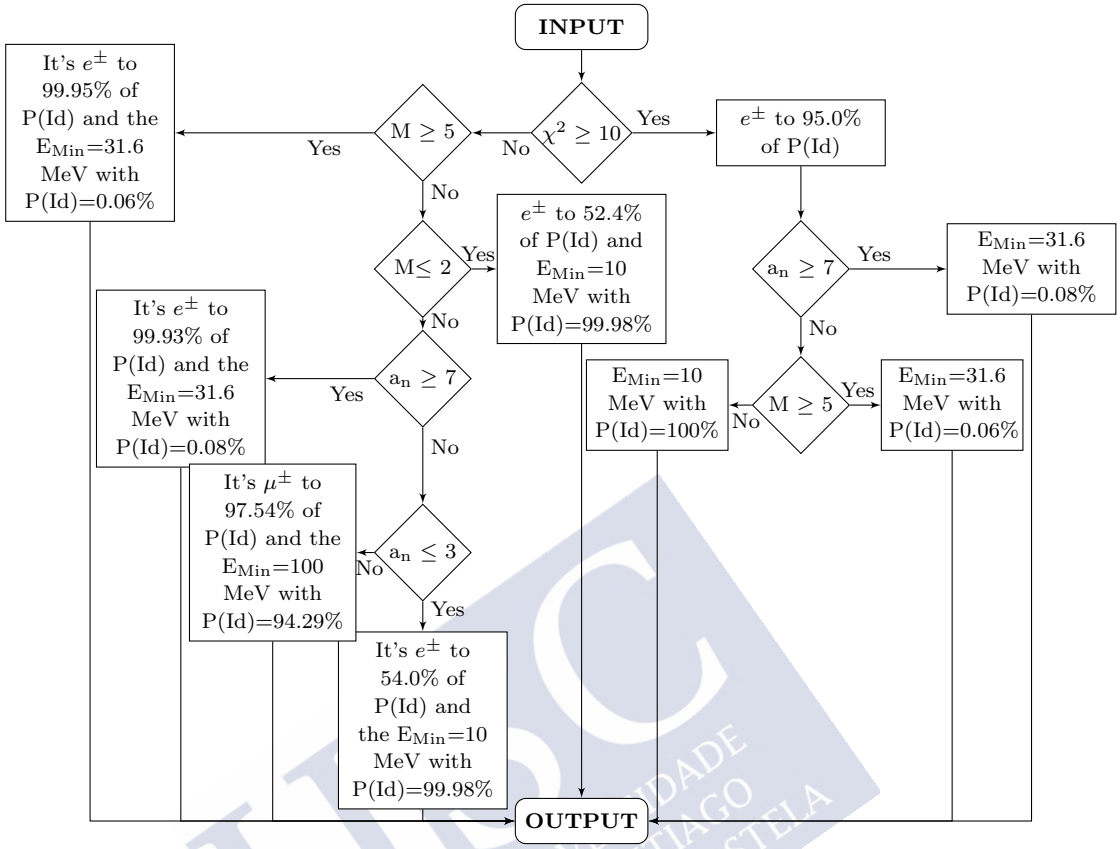

Figure 5.11: Flowchart for the MIDAS particles identification algorithm in the Tragaldabas detector. The solution procedure when 4 active RPC planes with 1 cm thickness of lead are available is shown.

5.1.5 Four active planes plus 1.5 cm lead layer configuration

Finally, the configuration of four active planes and a lead layer of 1.5 cm thick between T3 and T4 was studied. The histograms of both electrons and muons of multiplicity (a and b), weighted range (c and d) and chi-square (e and f) for a Tragaldabas to 4 planes with 1.5 cm thickness of lead are presented in the Figure 5.12. The data is a little longer than in the case at 1 cm thicknees of lead and therefore a greater difference between electrons and muons. The step by step changes are maintained due to the existence of lead in the detector system, easily visible in the electron histograms of multiplicity and weighted range. The highest energy electron has a similar behavior to the muon.

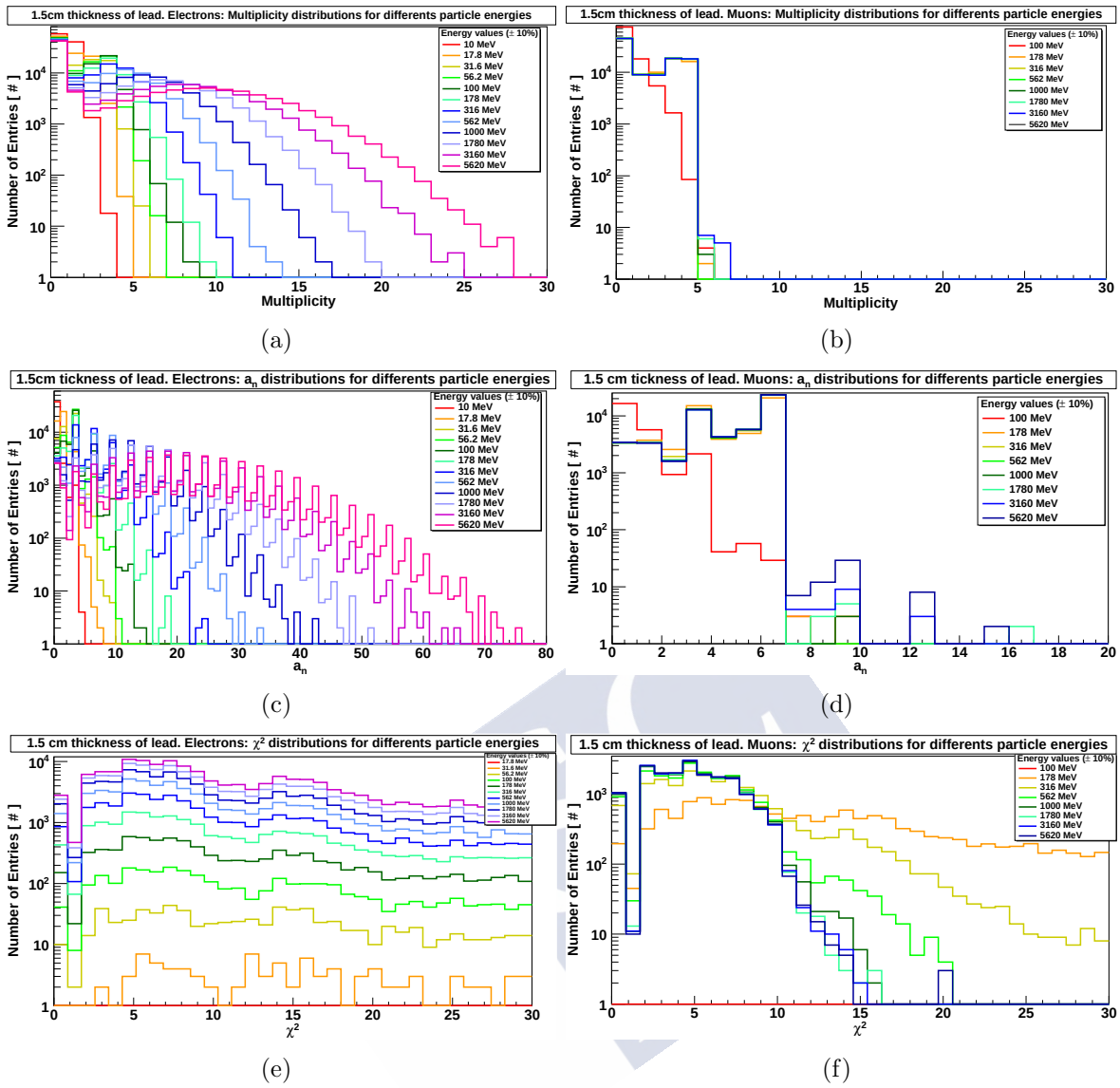

Figure 5.12: Results for 4 planes of Tragaldabas detector with 1.5 cm thickness of lead. Total Multiplicity distributions for different energy of electrons (a) and muons (b). Weighted range distributions for different energy of electrons (c) and muons (d). Chi-squared distributions for different energy of electrons (e) and muons (f).

Figure 5.13 shows the histograms both muons and electrons of multiplicity, a_n and χ^2 for the case of Tragaldabas with 1.5 cm thickness of lead after plane 3. Histogram data is a bit longer and the trends are very similar than in the 1 cm thickness of lead study, especially for electrons. The important cuts-off of the observables are very similar to the previous case, M=5, a_n=7 and χ^2=10. The bump tends to overlap with neighboring data and take a continuity with the curve, it is possible that the existence of lead is deviating more traces of electrons after the passage of the third plane.

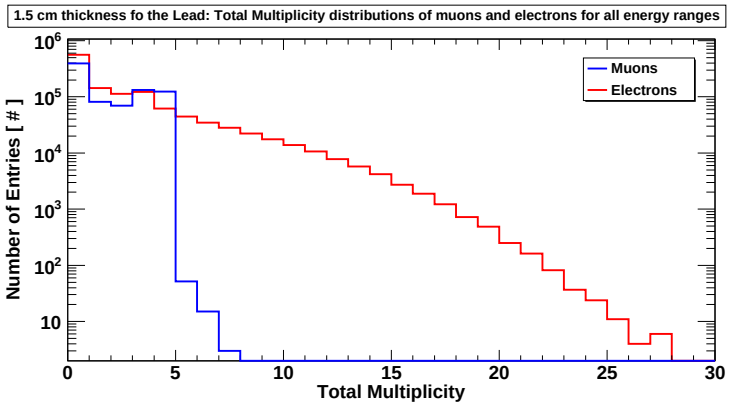

(a)

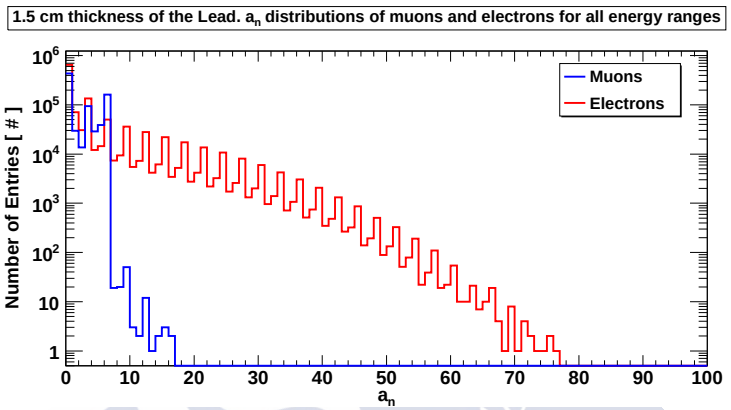

(b)

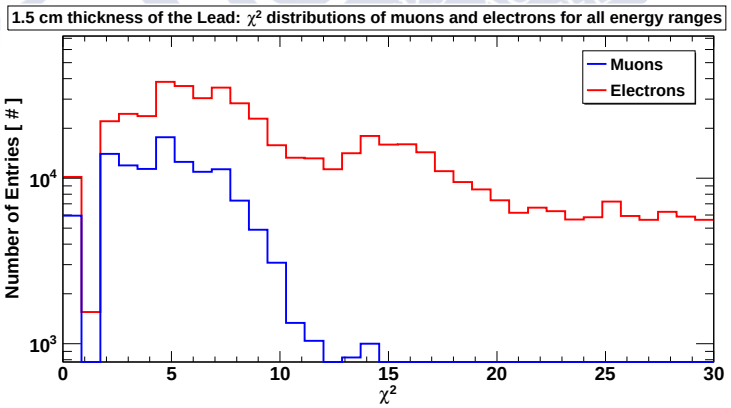

(c)

Figure 5.13: Results for 4 planes of Tragaldabas detector with 1.5 cm thickness of lead. Total Multiplicity histogram of electrons and muons (a). Weighted range histogram of electrons and muons (b). Chi-squared distributions of incident electrons and muons (c).

The Figure 5.14 shows the flowchart for 1.5 cm thickness of lead after the third plane of detector Tragaldabas. The values of the observables are very similar to the previous case, the values of probability and minimum energies are also similar. Again, accuracy values are presented in the following section.

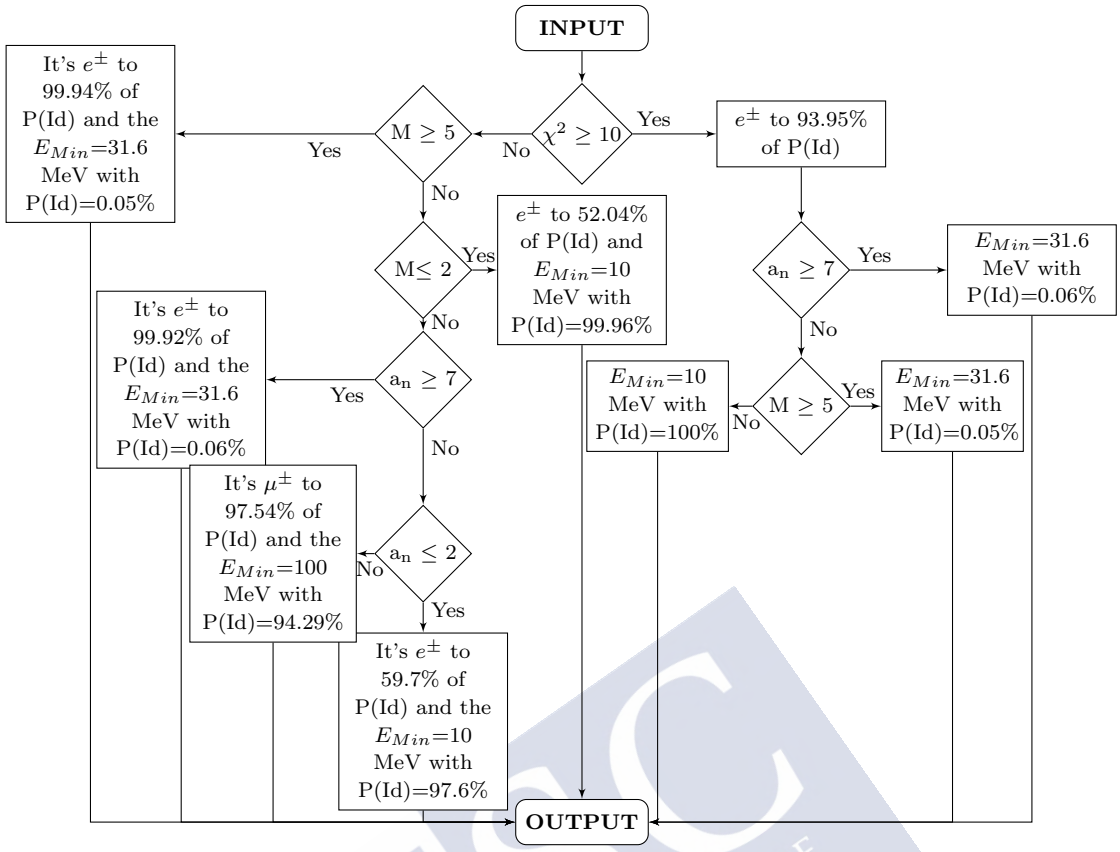

Figure 5.14: Flowchart for the particles identification algorithm in the Tragaldabas detector. The solution procedure when 4 active RPC planes with 1.5 cm thickness of lead are available is shown.

5.2 Acurracy results

The accuracy of the PID method for the different configurations was calculated with simulated data. The data generation and event propagation was done for two different scenarios: the so-called *realistic simulation* was done with the Cry input and the building was included; in so called simple *simulation*, input from the event generator described in section 4.3 was used, and the detector was placed at "open air". Data generation for realistic simulation is written below. 1 million data were generated with Cry with an input specified in Table 4.1, cutoff in kinetic energy of 500 MeV for both mions and electrons were applied. The particles were generated with EnsarRoot using this data from a virtual plane of 3×3 m^2 located just above the building. The particles cross the building and the detector (e.g: figure 4.2) for the different cases studied: 3 planes, 4 planes and 4 planes with a layer of 1 and 1.5 cm thickness of lead after the 3 plane of Tragaldabas.

Now, data generation for simple simulation is exposed. 1 million data was generated with the integrated simple program in EnsarRoot from a virtual plane of 1×1 m^2 located 12.7 cm above the detector and with direction uniformly distributed in ϕ and $\cos(\theta)$, with

θ between 0 and 90°, and the cutoff kinetic energy of 700 MeV for both photons and electrons, and 100 MeV for muons.

Namely, a trigger condition of having a single track crossing the detector was imposed in all cases for the data analysis program due to observable χ^2. Table 5.1 summarizes the accuracy probability of the method for the studied cases of realistic or simple simulations, having operative either four or three RPC planes, while The accuracy is supposed to increase as a lead sheet is implemented and its thickness increases, this is true for realistic simulation. The increase in acuraccy is very small, this may be due to the geometry of the detector and building. Table 5.2 shows the distribution of the misidentification events in % for the same analyzed situations. The arrows in the table boxes connecting two different particles mean that an actual incident particle a is misidentified as a particle of type b.

Table 5.1: **Accuracy results in [%] for the four analyzed cases. An accuracy close to 100% is achieved in the simple case, while a value about 90% is obtained in the realistic cases.**

Active Planes	Realistic Simulation	Simple Simulation
4	87.9 ± 1.5	99.3 ± 0.2
3	90.2 ± 1.4	99.3 ± 0.2
4 with 1 cm of Pb	91.9 ± 1.6	99.2 ± 0.2
4 with 1.5 cm of Pb	90.3 ± 1.6	98.8 ± 0.2

Table 5.2: **Percentage summary of misidentification events. The arrow means that a real incident particle a is misidentified as a particle of type b. It is observed how in most of the cases an incoming electron is wrongly assigned to be a muon. Those correspond to the higher energy electrons.**

	Misidentification				
Active Planes	e $\rightarrow \mu$	$\gamma \rightarrow \mu$	$\gamma \rightarrow$ e	p $\rightarrow$ e	p $\rightarrow \mu$
4	68.5	0.3	20.6	9.4	1.1
3	66.7	0.8	20.6	11	0.8
4 with 1 cm of Pb	47.3	0.9	36.5	14.9	0.4
4 with 1.5 cm of Pb	65.2	0.3	21.7	11.9	0.9

5.3 Conclusions

The MIDAS particle identification algorithm for cosmic rays has been developed for the Tragaldabas cosmic ray detector. After performing and studying different simulations of cosmic rays, the method uses a combination of different observables to obtain a probability of being a certain particle, and is also able to give a value for the possible energy. The different identification algorithms of the different Tragaldabas systems are presented in the

following flowchart: Figure 5.5 for a Tragaldabas system at 4 active RPC-plane, Figure 5.8 for 3 active RPC-plane of the system, the respective ones Figure 5.11 and Figure 5.14 for a 4 active RPC-plane system with a lead layer of 1 cm and 1.5 cm behind the third plane.

The method was tested in simulated data under different conditions and an accuracy close to 100% was obtained for the simplest cases, while a value of 90% was reached in the most realistic simulations. Also, the characteristics of the misidentified events were exposed, being the most frequent case that when an incoming high energy electron is wrongly identified as a muon. The results of acurracy are shown in Table 5.1 and the misidentification events in Table 5.1.

USC
UNIVERSIDADE
DE SANTIAGO
DE COMPOSTELA

USC
UNIVERSIDADE
DE SANTIAGO
DE COMPOSTELA

6 Structure and distributions of EAS at ground level

A phenomenological study of air showers at the ground level is presented in this chapter. The aim of the study in the analysis of several physical observables of the EAS secondary particles at the ground in order to be able to determine characteristics of the primary cosmic ray, such as mass, energy or arrival direction, with an array of Trasgo-like detectors at the ground level. The study starts from the simulation of four different primary nuclei (H, He, C and Fe) which a wide range of energy and incident angle in the atmosphere, and then, the proprieties topological and phenomenological of the generated muons and electrons over the surface are analyzed. Such analysis would allow to characterize the primary particle in a correct, precise and continuous way.

By means of the Corsika generator, EAS from the above mentioned primary nuclei were simulated at the geographic locations of both University of Santiago de Compostela and the Antarctica Spanich Base. The analysis of those data is long discussed. Most important methods and results were published at the 36th International Cosmic Ray Conference, ICRC 2019, reference [89].

6.1 Event generation method

Many large array observatories do studies at very high energies. In this work a whole study of the response of the Trasgo detectors and characteristics of the shower at ground level is carried out with energies under the knee (10^9-10^{15} eV) to know the characteristics of the primary CRs: mass, direction and energy. Data generation was performed with the Corsika simulation program. Simulating with Corsika leads the knowledge and management of the different simulation and analysis tools. The Corsika interface with the `coconut` executable provides the user with facilities in the selection of the different simulation environments. The selected environments in the Corsika interface and study method adapted to the conditions of the Trasgo detectors are discussed below. A work at low energies and short simulation times leads to the selection of interaction models GHEISHA version 2002d and QGSJET version 01C. The horizontal flat detector array option was selected in the detector geometry section providing greater geometric similarity with the Tragaldabas for an optimal particle detection. Finally, the program provides Root file outputs after loading the Root environment by selecting the `d2` option in the Corsika interface. After selecting these simulation work environments, Corsika generates the executable `corsika75600Linux_QGSJET_gheisha`. Input Files `all-inputs` are the

parameters that define the conditions or environment of the data simulation. The Figure 3.2 of the section 3.3 is an example of input file generated by Corsika.
The generation of simulated data is run with `corsika75600Linux_QGSJET_gheisha`, the simulations are executed with the following writing:

```
./corsika75600Linux_QGSJET_gheisha_root < all-inputs-10 > output
```

where `all-inputs-10` is an input file for protons with 10 GeV of energy. The output Root files generated by Corsika are `DATnnnnnn.root` and `DATnnnnnn.long`, where n is a number selected by users between 0 and 9. Primary nuclei of Hydrogen (proton), Helium, Carbon and Iron were chosen for the simulation. These atomic nuclei are the most abundant in the cosmos as evidenced by Figure 1.14 of the section "Development of a EAS in the Atmosphere". The identification codes of these nuclei by Corsika are 14 for the proton, 402 (4×100+2) for the Helium, 1206 (12×100+6) for the Carbon and 5626 (56×100+26) for the Iron. The energy range in logarithmic scale is [1.78, 10^5] GeV with 4 steps of $10^{2/8}$ per decade. 10k (10,000) events were simulated for a primary energy range of [1.78, 5620] GeV and 1k (1000) events for an range of [10^4, 10^5] GeV. An energy range of primary particle was chosen with steps of $10^{1/8}$. So for example, if the energy to simulate is 1.78 GeV,the energy range of primary particle is 1.316 and 2.37 GeV. This simulation method is maintained throughout this study unless changes are specified due to inconclusive results. The zenital angles are chosen to cover a wide section of the space in which the incidence of the primary CR in the atmosphere can occur. The zenital angle has a uniform separation in 6 ranges between 0 and 58.3°, with step in $\cos\theta$ of 0.025 according to $\cos 0 = 1$. Then, the zenital angle ranges used are: [0, 12.8]° (vertical incidence), [12.8, 22.3]°, [22.3, 29.0]° , [29.0, 34.4]°, [34.4, 41.4]° and [49.4, 58.3]°. The geographical and height positions at sea level chosen for the study are the following: (42° N, 8° W, 235 m) for the Faculty of Physics of the University of Santiago de Compostela (USC) of A Coruña (Spain) and (62.7° S, 60.4° W, 10 m) for the Spanish Antarctic Base (BAE) Juan Carlos I located in Livingston (Antarctica). These are translated into a magnetic field parameters for the Corsika input files of respectively (19.7, -4.2) and (24.2, 38.5) μT for the USC and the BAE. Finally, a selection of energy cutoff was performed to eliminate possible contamination or background and collect as many secondary as possible. The Table 6.1 collects the energy cutoff values for the secondary particles, 0.05 GeV for hadrons-muons and 0.09 GeV for electrons-photons. All other parameters of the input file were selected by default.

Table 6.1: **Energy cuts values**.

customized	hadrons	$\mu^{\pm}$	$e^{\pm}$	γ
E-cuts [GeV]	0.05	0.05	0.09	0.09

6.2 Estimating primary energy of CR with TRASGO detectors

6.2.1 Theorical introduction and motivation

Nowadays, it is assumed by the community that the primary Cosmic Rays that arrive to the Earth come from astrophysical sources called cosmic ray accelerators. The generation, acceleration of cosmic rays by the sources and arrival on Earth were argued structurally in the first chapter of this work. The primaries CR collide with the atmosphere, generating successive interactions produced by fragments of the collision and make an atmospheric shower. The electromagnetic component of the shower formed by electronic and muonic secondaries is studied in this work. Secondary counting at ground level is carried out with the Trasgo Family detectors [2], and, in particular, with TRAGALDABAS [3] and TRISTAN [90] detector systems which are located respectively at USC and BAE.

Detection devices installed on satellites, balloons or airplanes provide the detection of primaries CRs. Figure 6.1 [16] shows the energy spectrum of primary CRs measured by different experiments. The histogram shows the intensity of particles $\mathrm{d}N/\mathrm{d}E$ [$\mathrm{m^{-2}\,sr^{-1}\,s^{-1}\,GeV^{-1}}$] as a function of kinetic energy per nucleon [GeV] for 11 nuclei: hydrogen (proton), helium, carbon, oxygen, neon, magnesium, silicon, sulfur, argon, calcium and iron. Different scale factors are used for each nuclei to provide data to the reader. At first approximation the data can be adjusted with a linear regression model. Linearity increases as less heavy nuclei and nonlinearity increases as energy decreases, the nonlinearity appears below 10^{10} GeV for the H and He. The histogram in the upper right of the Figure shows the H-He ratio as a function of the stiffness of the particle in units of GV, data measured by the PAMELA and AMS02 experiments. The data differ between different experiments for a stiffness greater than 200 GV. It is known that at energies around GeV the intensity is modulated by solar radiation. The linearity of the energy spectrum has been well studied. The intensity of the primary nuclei from a few GeV up to a few hundred TeV is described with the following equation:

$$I(E) \simeq 1.8 \cdot 10^4 \cdot \left(\frac{E}{\mathrm{GeV}}\right)^{-2.7} \left[\frac{1}{(\mathrm{m^2 \cdot sr \cdot s \cdot GeV})}\right] \ , \tag{6.1}$$

where E is the energy of each nucleus. This equation arises naturally from the integral energy of the equation (1.2). The intensity is proportional to the abundance of nuclei arrive in the atmosphere. A 74% of the primary cosmic rays are protons and approximately 18% are heliums.

This work undertakes the called coupling functions [91] for the study of the response of a Trasgo detector. There is a relationship between the coupling function and the particule rate detected by experiments at ground level. The muons flux at ground level can be can be written as:

$$J_\mu^{GL}(E_\mu, \theta) = \int_{E_\mu}^{\infty} m^{GL}(E_{mu}, E, \theta)\, J_p(E)\, dE_\mu \ ,$$

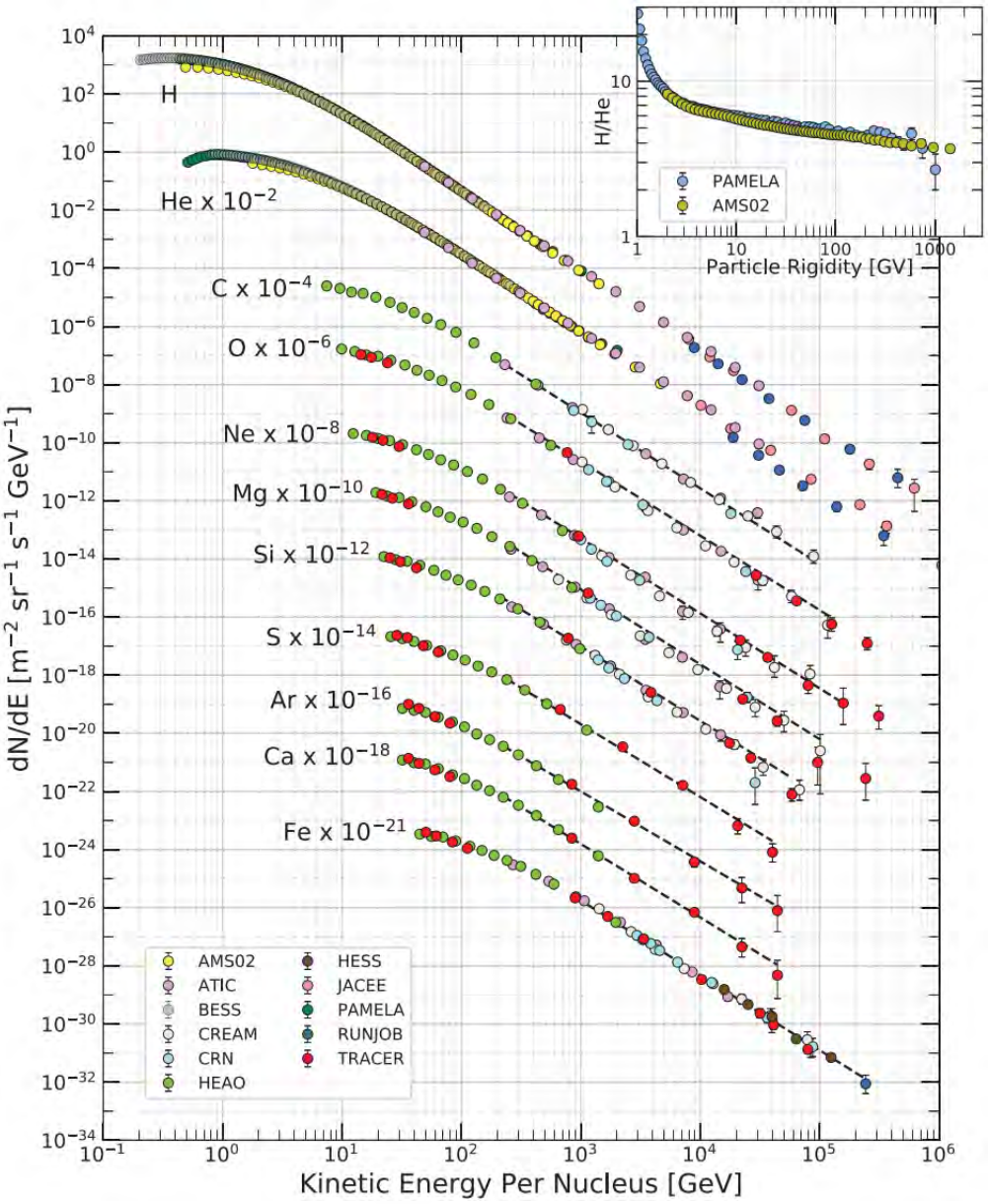

Figure 6.1: Energy spectra of primary cosmic rays.

where $m^{GL}(E_\mu, E, \theta)$ is the muon distribution function in energy E_μ with a zenith angle θ for a proton with energy E and $J_p(E)$ is the differential energy spectrum of primary protons. The Multiplicity function is the number of muons at the surface with energy greater than the threshold E_{th} of a proton with energy E. The Multiplicity function is written as follows:

$$M(E, \theta) = \int_{E_{th}}^{E} m^{GL}(E_{mu}, E, \theta)\, dE_\mu \ .$$

The Response function or commonly called response, G(E,θ_i, φ_i) [GeV$^{-1}\cdot$ s^{-1}], is the distribution of detector counting rate at a given in primary proton energy. It can be

written as:

$$G(E, \theta_i, \varphi_i) = M(E, \theta_i) \cdot J_p(E) \cdot \Delta S\Omega(\theta_i, \varphi_i) \tag{6.2}$$

where $M(E, \theta_i)$ is the multiplicity function, $\Delta S\Omega(\theta_i, \varphi_i)$ is the partial acceptance of the detector according to (θ_i, φ_i) and $J_p(E)$ is the differential energy ($J_p(E)$ could depend on the angles θ and φ).

6.2.2 Response of the detector, calculation method and results

The method used in the study of the response of a Trasgo detector and the results are presented below. The data analysis programs used are Python and ROOT. In this section, the study of the multiplicity function (MF) and response function (RF) for both muons and electrons and for 4 nuclei (H, He, C and Fe) is mainly carried out. The data are generated by the Corsika simulation program in two locations, the University of Santiago de Compostela (USC) and the Spanish Antarctica base (BAE) in livingstone. The data were generated for a specific value of energy and zenital angle. The multiplicity function $M(E, \theta)$ represents the number of particle counts (muons or electrons) normalized to the shower number, these provided by the Corsika simulations. The response function is calculated with the equation (6.2). To simplify the calculations, the differential energy spectrum is the intensity of primary nucleons collected in the equation (6.1). True for the proton since the correction coefficients are known, 0.74. The data of differential energy spectrum were taken directly from the Figure 6.1 for the rest of nuclei. The data representing the multiplicity function were fitted with a fifth degree polynomial function. The product of the function resulting from the fit and the differential energy spectrum function is the response of the detector, without the partial acceptance factor.

The calculation method of response with dimuons is the same as the previous one, but the acquisition of data with the analysis program is very different. Dimuons ($\mu\mu$) is the count of 2 muons in a action area, in other words, the signal detected by 2 single-muon trigger by a certain system or experiment. The dimuons analysis program does the count of 2 muons in a non-iterative[1] way in a action radius is 1 meter, where the action radius is carried out from the first interaction of a muon at ground level. Dimuonic candidates are counted and this used to calculate the response function. The study was done with muon energy cutoff of 150 MeV and 300 MeV.

6.2.2.1 The Response at the University of Santiago de Compostela (42° N, 8° W, 235 m)

Figure 6.2 show the 3D distributions of primary proton energy versus kinetic energy versus number of particle counts (electrons and muons). The range in kinetic energy is approximately [0, 3] GeV for the electron and approximately [0, 100] GeV for the muon. The energy range of the primary proton for both secondary is [1.78, 100000] GeV.

[1]The iterative method is described in the subsection 6.3.1 Simulation and analysis methods in section "Density microstrucutre of CR air showers".

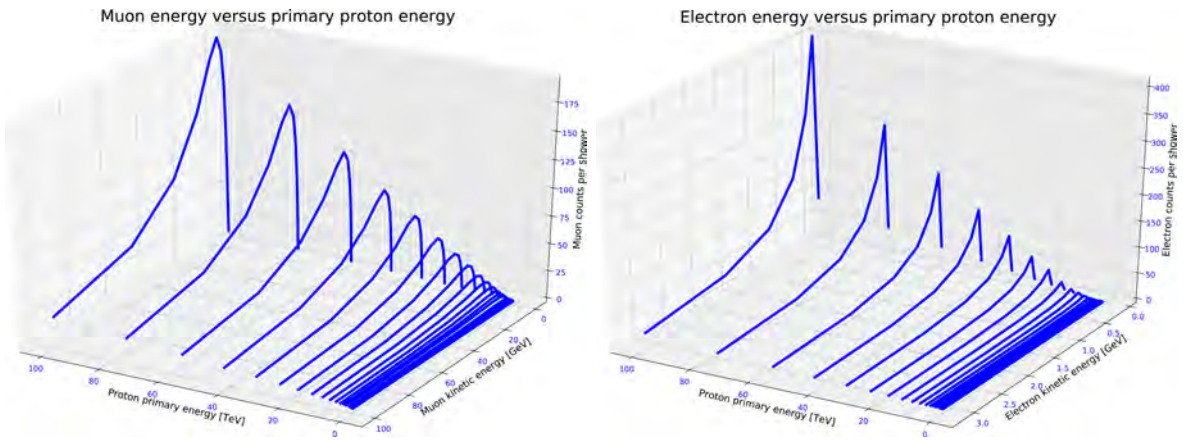

(a) (b)

Figure 6.2: Energy distributions for muons (a) and electrons (b) for a different energies of the primary H.

At first sight, the distribution peaks are located at low kinetic energies and the tails at high kinetic energy. The size distributions are narrow for the electron than muons graph. The importance of the comparison between mean values of both distributions fixed at an primary energy of approximately 100 TeV is important for an example of balance. The kinetic energies located at the mean of both distributions are about 10 MeV for electrons and 0.5 MeV for muons. The maximum of both distributions are about 180 muons and 370 electrons. Then, approximately twice as many electrons as muons arrive at ground level for a primary proton energy of 100 TeV.

Figure 6.3 show the energy spectrum graph and the multiplicity graph for the 4 primary nuclei. The intensity of primary nuclei [$m^{-2}\,sr^{-1}\,s^{-1}\,GeV^{-1}$] as a function of energy per nucleon [GeV/nucleus] is presented in the energy spectrum of Figure (a). The results behave as expected, the intensity decreases linearly as the energy grows except for carbon and iron at low energy. The multiplicity as a function of the energy per nucleon for the 4 nucleons with vertical incidence in the atmosphere is presented in the graph of Figure (b). The multiplicity graph shows a H curve smaller than the He curve, this curve is smaller than the carbon curve and so on until reaching the heaviest nucleus, iron. The curves grow strongly as the energy increases to a linear trend from a primary energy of 100 GeV. The response function is calculated as follows, the graph data is fit and multiplied with each other as imposed in the equation (6.1). The data adjustment function is fifth degree polynomial function. The energy spectrum adjustment function for the proton is given by the equation (6.2) multiplied by the abundance factor of 0.74.

The results of multiplicity and response detector for both muons and electrons, and different angles of incidence of the 4 primary in the atmosphere are presented and explained below. The data concerning the multiplicity and response functions study are presented in the Appendix “Data sheets of MF and RF study”. Namely, the partial acceptance factors of the detectors were not taken in the calculations, these data will be exposed in

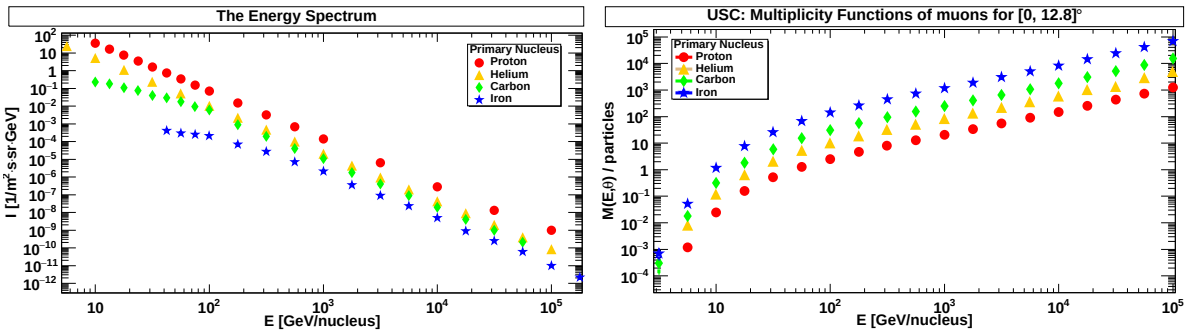

(a) (b)

Figure 6.3: Energy spectrum of primary CR particles (a). Multiplicity Functions of muons for a zenith angle of [0, 12.8]° calculated in USC (b).

the section 6.2.2.3. Therefore, the response function results calculated in the USC and in the BAS are exposed for an ideal detector. Important to know, the threshold energy of the Tragaldabas detector is a few hundred MeV.

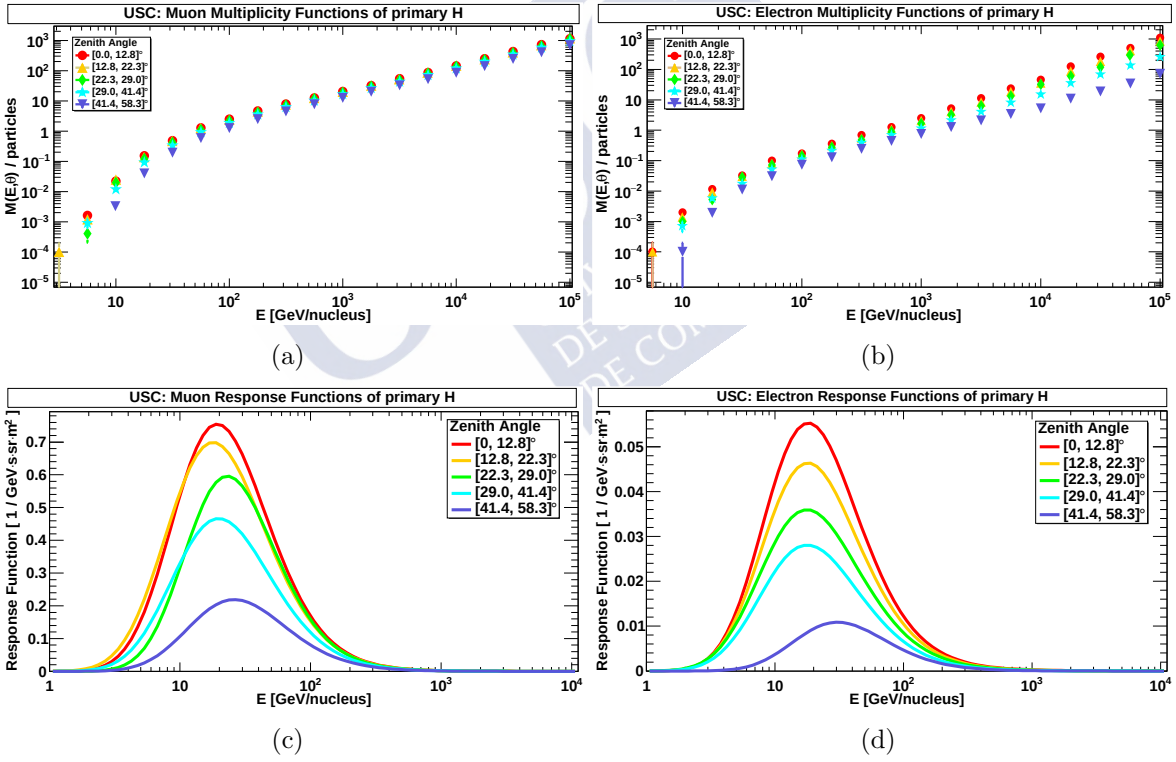

(a) (b)

(c) (d)

Figure 6.4: MF and RF analysis at USC for the incidence of primary H in the atmosphere. Muon MF (a), electron MF (b), muon RF (c) and electron RF (d).

Figure 6.4 show the electrons-muons graph of RF and MF for primary protons. The data of the electrons-muons MF graphs behave similarly to the results discussed in Figure 6.3 (b), they grow as the energy increases. The MF curves of muons are very near together while the MF curves of electrons tend to separate at high energies. The distributions are smaller as the zenital angle grows. The maximum distributions are around 0.73, 0.7, 0.6,

0.43 and 0.21 [$m^{-2}\,sr^{-1}\,s^{-1}\,GeV^{-1}$] for the respective increasing incidence angle ranges. The muon RF distributions have a swinging tendency and the mean distributions are around 20 and 30 GeV/nucleus. The mean of the RF distributions of the electron is around 20 and 30 GeV/nucleus and the values decrease as the zenital angle grows. The maximum of the distributions are around 0.056, 0.046, 0.036, 0.028 and 0.012 for the respective ranges in zenital angles.

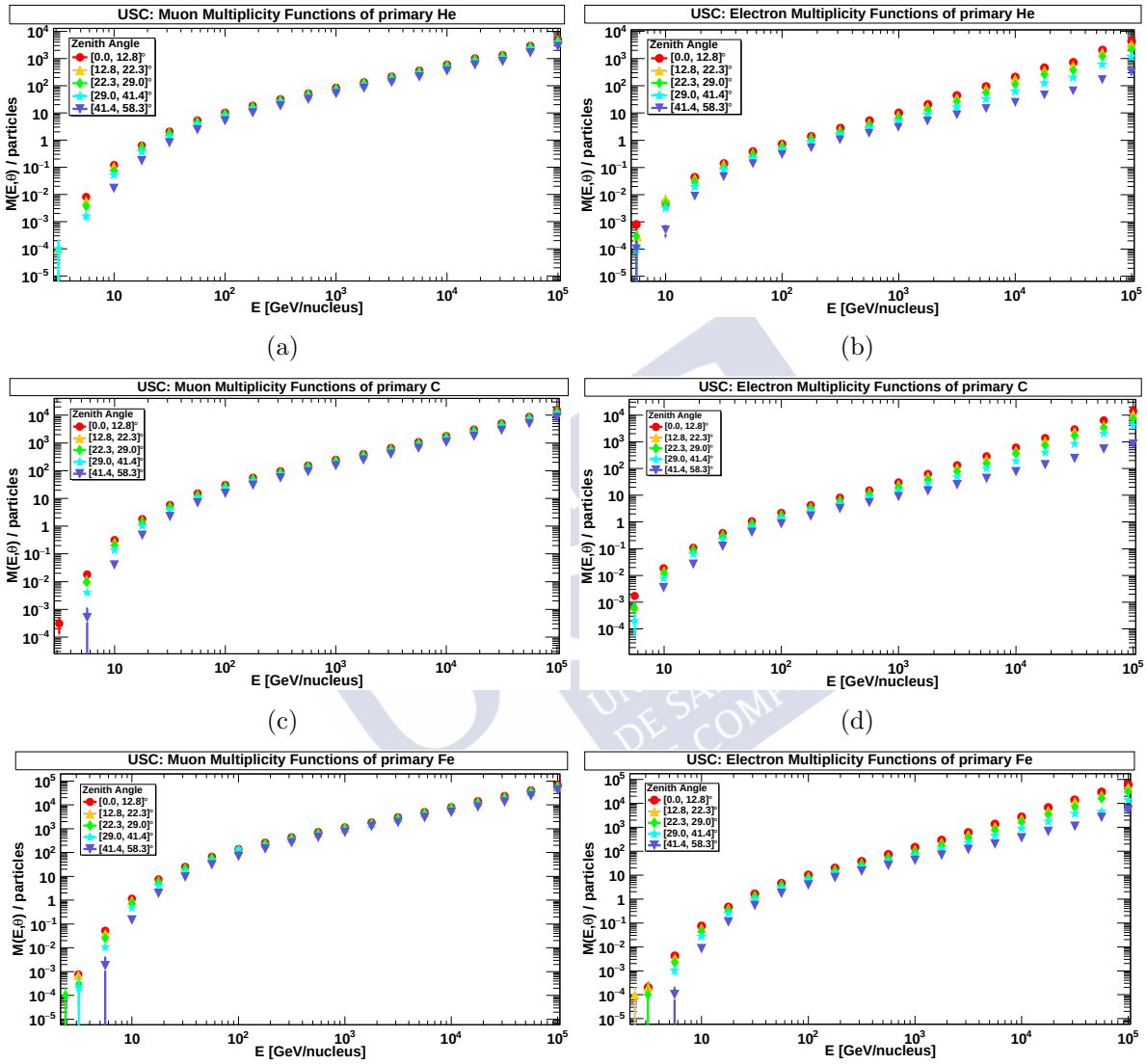

Figure 6.5: MF analysis at USC for the incidence of primary in the atmosphere. Muon (a) and electrons (b) for He, muon (c) and electrons (d) for C and, muon (e) and electrons (f) for Fe.

In summary, the distribution mean for both electrons and muons are between 20 and 30 GeV/nucleus. The maxima of the electron RF distributions are an order of magnitude below the muon RF distributions. The growth of the mean values of the distributions according to the zenital angle was expected due to a greater energy of the primary for a greater extension of the shower, although the results do not show it. Possibly, the cause

is the calculation method of the response function. The decrease of the maximum of the distributions versus the zenital angle behaves as expected since the greater the zenith angle, the fewer secondary will arrive at ground level. The difference between maxima of the electron-muon distributions is a factor of 10.

Figures 6.5 show the multiplicity for both muons and electrons for the respective He, C and Fe nuclei with different angles of incidence in the atmosphere, calculated in the USC. The graphs are very similar to the results of the primary H. Figures 6.6 show the response for both muons and electrons for the respective He, C and Fe nuclei with different angles of incidence in the atmosphere, in the USC. The mean values of the electron-muon distributions are about 30 GeV for He primary nuclei, 40 GeV for primary C and 100 GeV for primary Fe, for all angle angles. The maximum distributions values [$m^{-2}\,sr^{-1}\,s^{-1}\,GeV^{-1}$] for the respective zenital angles are approximately:

- 0.9, 0.9, 0.7, 0.5 and 0.25 for muon distribution with He nuclei,
- 0.058, 0.057, 0.042, 0.032 and 0.012 for electron distributions with He nuclei
- 0.35, 0.32, 0.26, 0.21 and 0.12 for muon distributions of C nuclei,
- 0.022, 0.02, 0.0161, 0.013 and 0.006 for electron ditributions of C nuclei,
- 0.3, 0.27, 0.25, 0.23 and 0.15 for muon distributions of Fe nuclei, and
- 0.021, 0.018, 0.016, 0.013 and 0.009 for electron distributions of Fe nuclei.

Figure 6.7 show the muon-electron ratio graphs calculated in the USC for each nucleus (H, He, C and Fe). The graphs show the ratio of muons-electrons with normalized entries as a function of the energy in GeV/nucleus of primaries for the 5 zenith angle ranges. The data show similarities between graphs, these tend to grow as energy increases to about 100 GeV/nucleus and decreases again. The ratio is higher at low energies for angles less than 41.4°, so the number of muons generated is 11 or 12 times higher than electrons at low energies. The ratio for zenith angle range of [41.4, 58.3]° remains practically constant, around 10. High energy primaries and with vertical incidence in the atmosphere have a ratio close to 1.

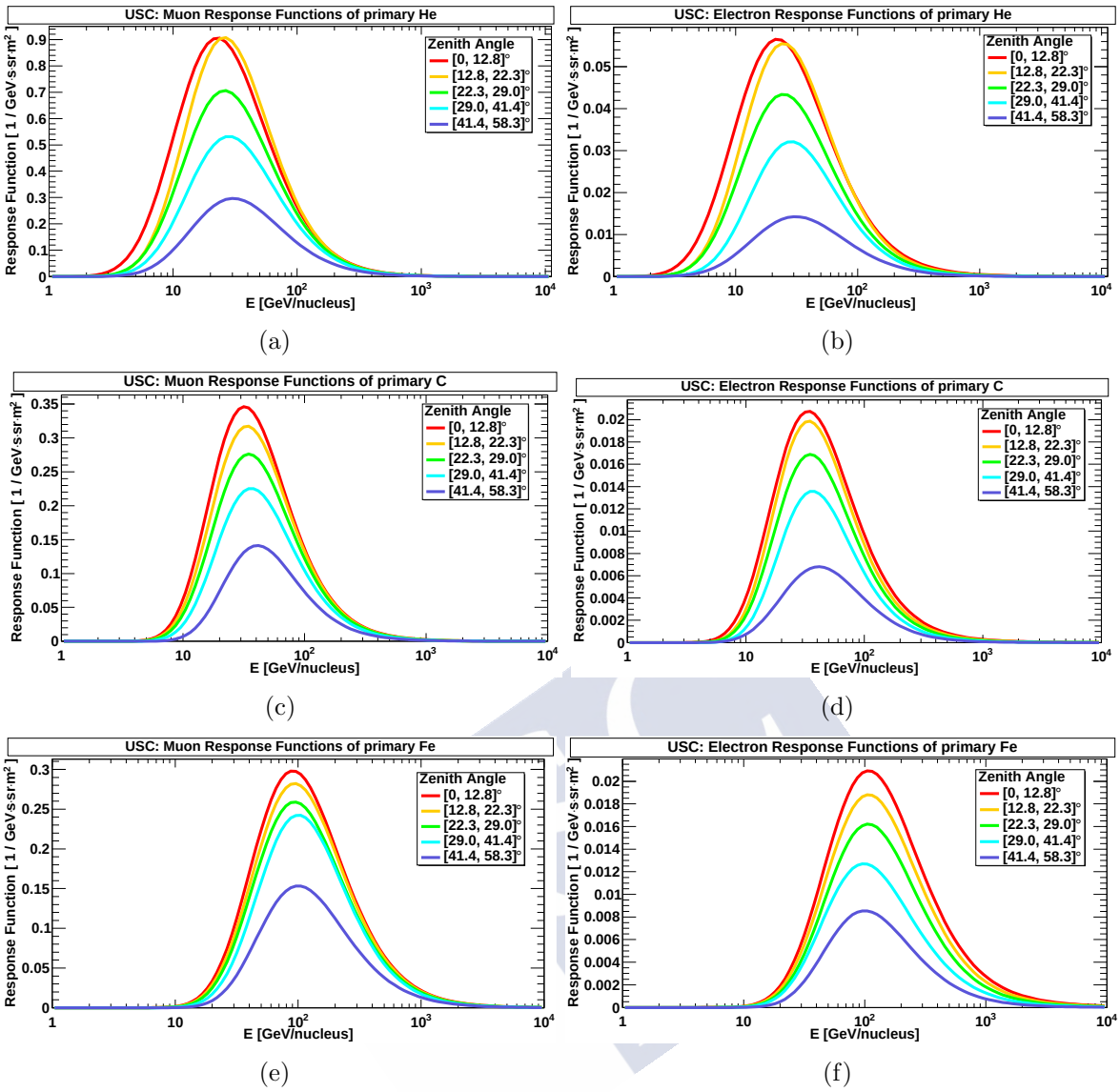

Figure 6.6: Response distributions of both muons and electrons calculates in the USC, distributions for He, (a) muons and (b) electrons, C, (c) muons and (d) electrons, and Fe, (e) muons and (f) electrons.

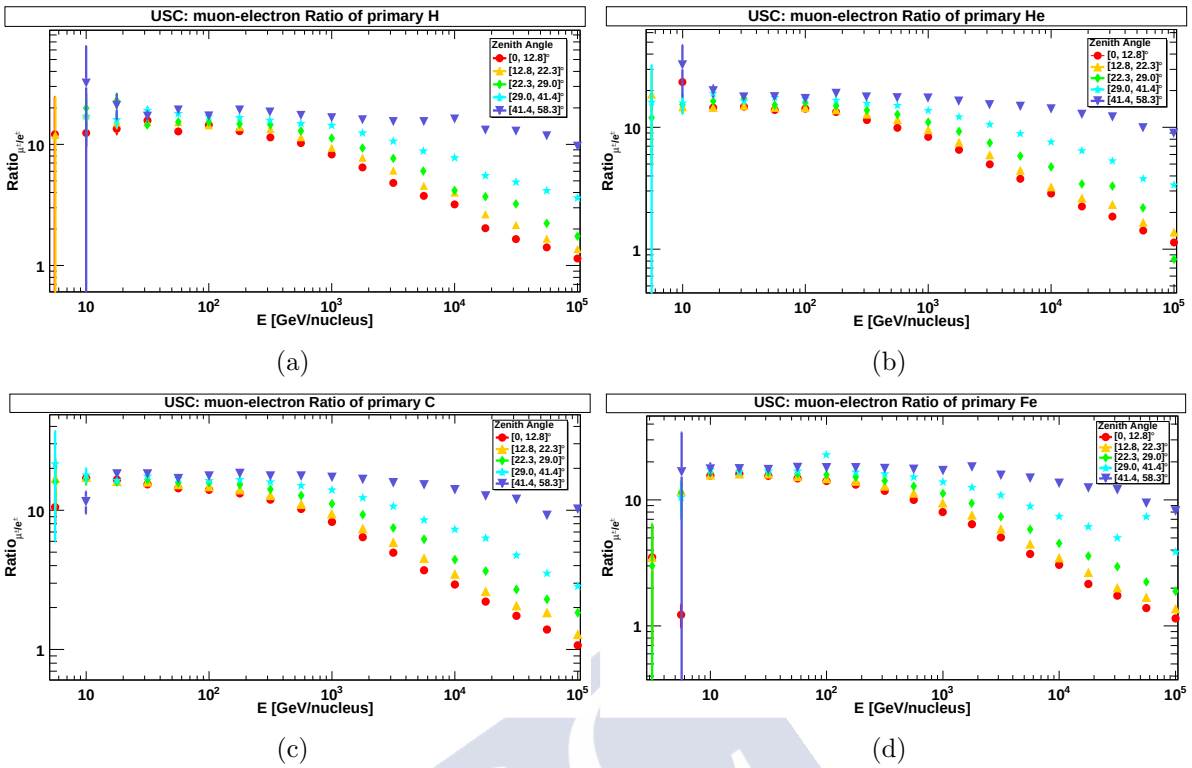

Figure 6.7: Muon-electron ratio analysis at USC for different zenith angles of incidence of nuclei in the atmosphere for H (a), He (b), C (c) and Fe (d).

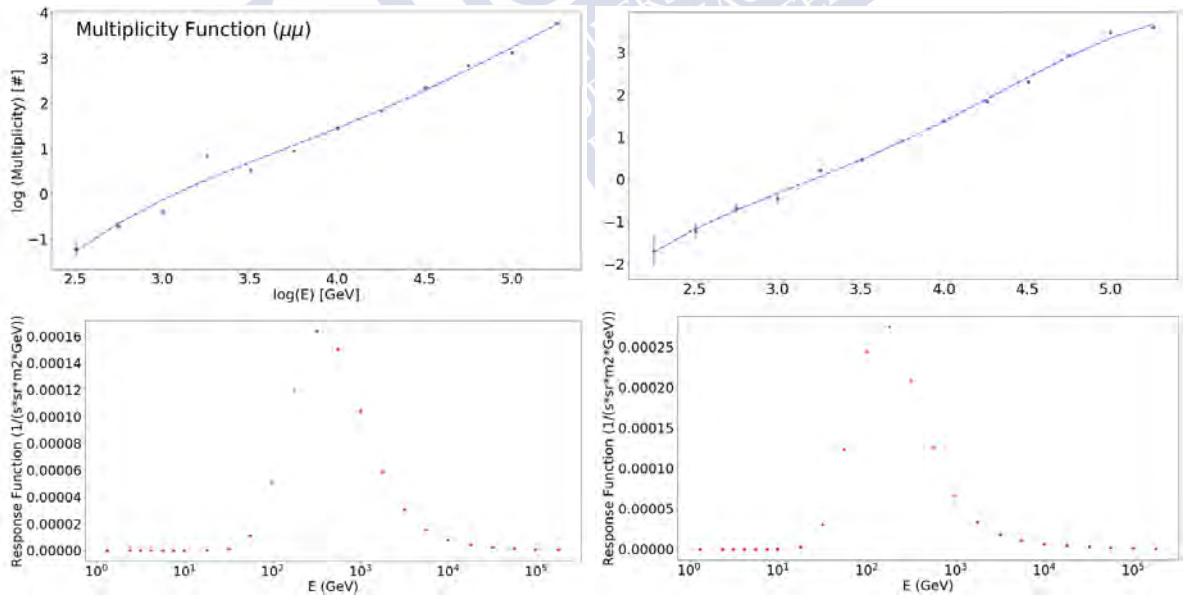

Figure 6.8: Multiplicity and response distributions of dimuons (see subsection "Response of the detector, calculation method and results") with both cutoff energy 150 MeV (a) and 300 MeV (b) for primary H with vertical incidence in the atmophere calculated in USC.

The capabilities of multiple cosmic interactions with detectors is important and therefore a dimuons response study was done. Figure 6.8 show the data of multiplicity and response

of dimuons achieved by protons of vertical incidence in the USC and for two muon energy cutt-off: 150 MeV and 300 MeV. The multiplicity function data is dispersed at low energies, the fit of the fifth degree polynomial to the data was done correctly. The mean of the distributions of the response graphs are about 300 MeV for both the 150 and 300 MeV cutoff energies. The maximum of the distributions are respectively about $1.7{\cdot}10^{-4}$ and $2.8{\cdot}10^{-4}$ [$m^{-2}\,sr^{-1}\,s^{-1}\,GeV^{-1}$] for the cutoff energies of 150 and 300 MeV, results well below the previous ones.

6.2.2.2 The Response at the Antarctica Spanich Base (62.7° S, 60.4° W, 10 m)

Figure 6.9 show the multiplicity and response for incident protons with different zenital angles in the atmosphere for both muons and electrons calculated in the livingstone BAS. The results and trends are similar to those calculated in the USC but the muonic distributions behave as expected, the mean of distributions grow as the angle grows. Something similar occurs with electronic distributions up to an zenith angle range of [41.4, 58.3]°, where the mean of the distribution decreases. The existence of these phenomena may be due to the method used to calculate the response function. The mean of both muons and electrons distributions are around 20 and 30 GeV/nucleus. The maxima of the muon distributions are around 0.72, 0.65, 0.55, 0.42 and 0.2 [$m^{-2}\,sr^{-1}\,s^{-1}\,GeV^{-1}$] and the electron distributions are 0.06, 0.045, 0.03, 0.023 and 0.02 [$m^{-2}\,sr^{-1}\,s^{-1}\,GeV^{-1}$], for the respective ranges in zenital angles. The difference between maxima of the electron-muon distributions is a factor of 10. The Figure 6.10 show the electron-muon ratio for primary

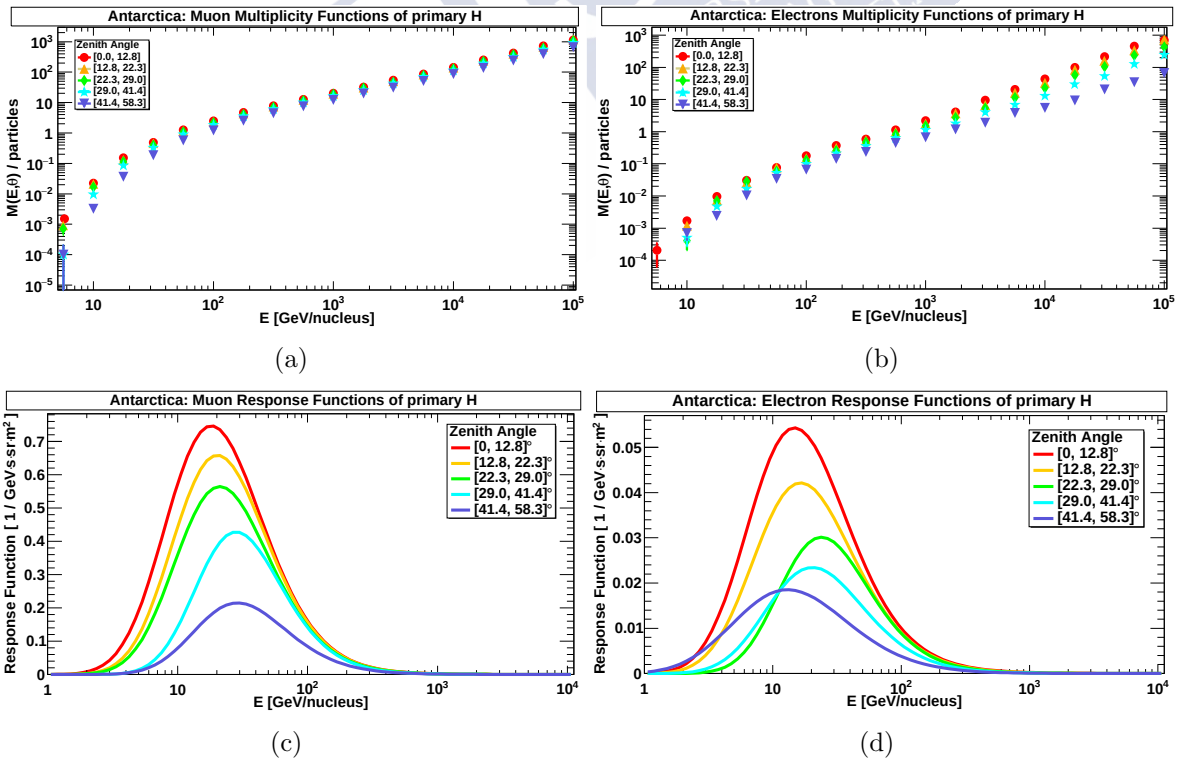

Figure 6.9: Multiplicity and response distributions for primary H calculated in BAE, multiplicity distributions of both muons (a) and electrons (b) and response distributions of both muons (c) and electrons (d).

protons incident in the atmosphere with different ranges of zenital angle calculated in the antarctic. The $e^{\pm}/\mu^{\pm}$ ratio is very similar to the results calculated in the USC. A maximum of the data is located about 70 GeV, which corresponds to a ratio equal to 11 and the ratio decreases at high energies, to 1 in the case of vertical incidence angle.

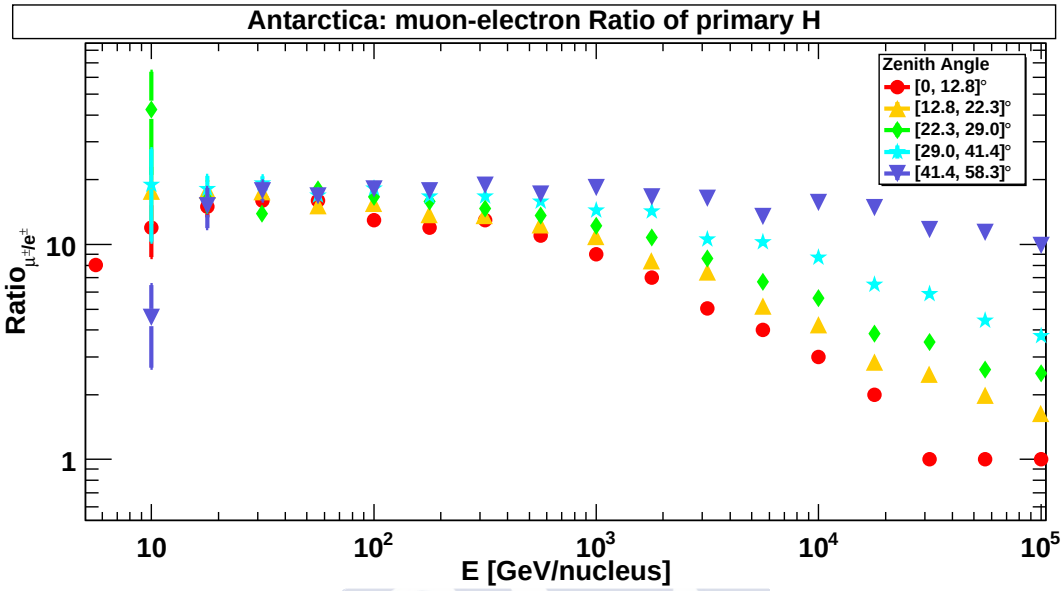

Figure 6.10: Results of muon-electron ratio analysis at Antarctica for different zenith angles of incidence of the primary H in the atmosphere.

Figure 6.11 show the response for both muons and electrons for He, C and Fe nuclei inciding in the atmosphere with different zenital angles, calculated in the BAS. The mean values of the electron-muon distributions are about 30 GeV for primary He and about 30-40 GeV for primary C and 100 GeV for Fe, for all zenith angles. The maximum distributions values [$m^{-2}\,sr^{-1}\,s^{-1}\,GeV^{-1}$] for the respective zenital angles are approximately:

- 0.9, 0.75, 0.65, 0.5 and 0.23 for muon distribution with He nuclei,
- 0.055, 0.05, 0.04, 0.03 and 0.012 for electron distributions with He nuclei,
- 0.33, 0.31, 0.25, 0.2 and 0.12 for muon distributions of C nuclei,
- 0.022, 0.016, 0.0155, 0.01 and 0.007 for electron ditributions of C nuclei,
- 0.3, 0.255, 0.245, 0.2 and 0.15 for muon distributions of Fe nuclei, and
- 0.022, 0.016, 0.015, 0.012 and 0.009 for electron distributions of Fe nuclei.

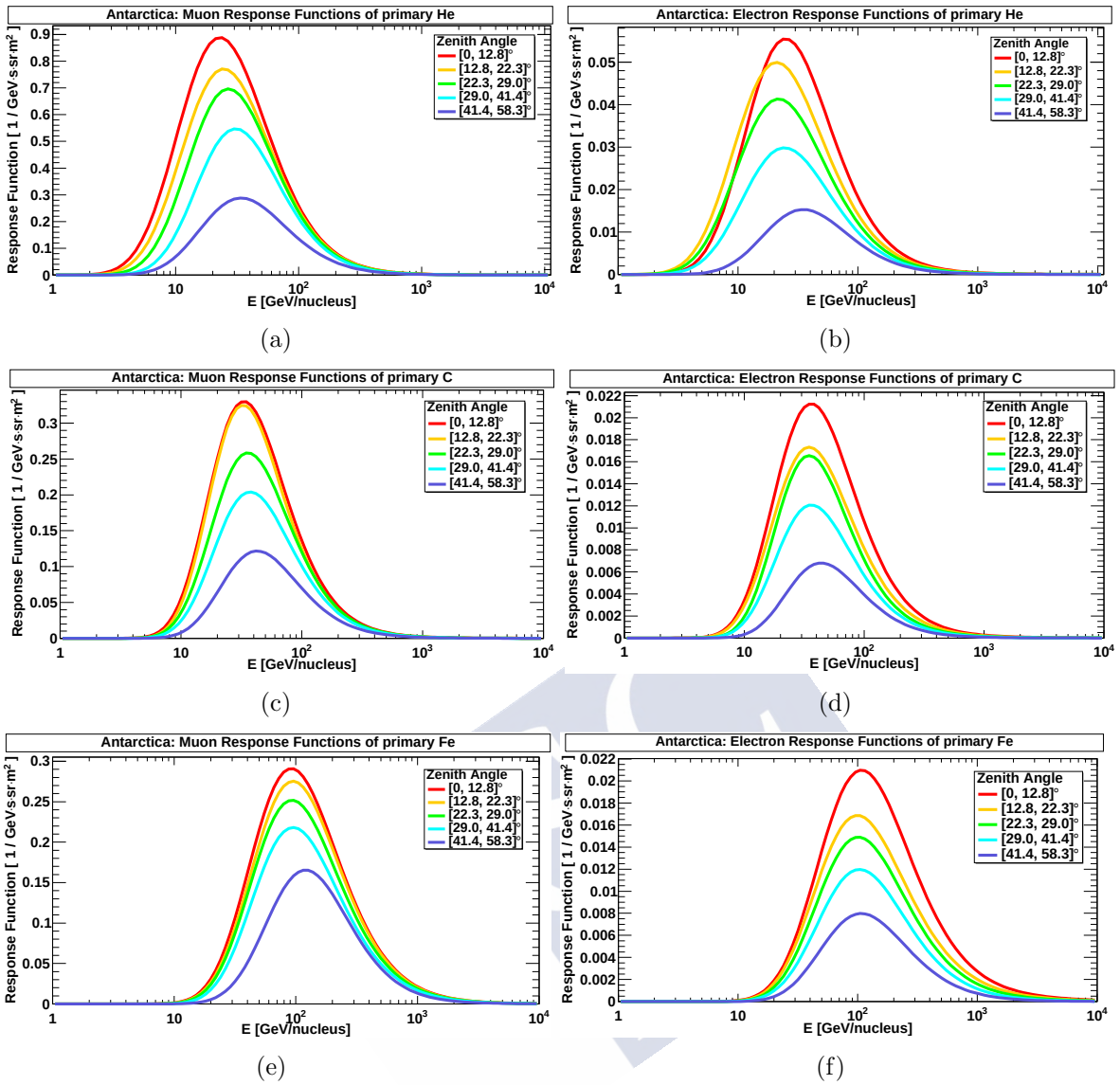

Figure 6.11: Response distributions of both muons and electrons realized in the BAE, distributions for He, (a) muons and (b) electrons, C, (c) muons and (d) electrons, and Fe, (e) muons and (f) electrons.

Figure 6.12 show the multiplicity and response of dimuons for H nuclei with vertical incidence for both a energy cutoff of 150 and 300 MeV. The mean values of the distributions are approximately 300 MeV for both graphs. The maximum distributions are about $1.4{\cdot}10^{-4}$ and $1.75{\cdot}10^{-4}$ [$m^{-2}\,sr^{-1}\,s^{-1}\,GeV^{-1}$] for energy cuts of 150 and 300 MeV, respectively.

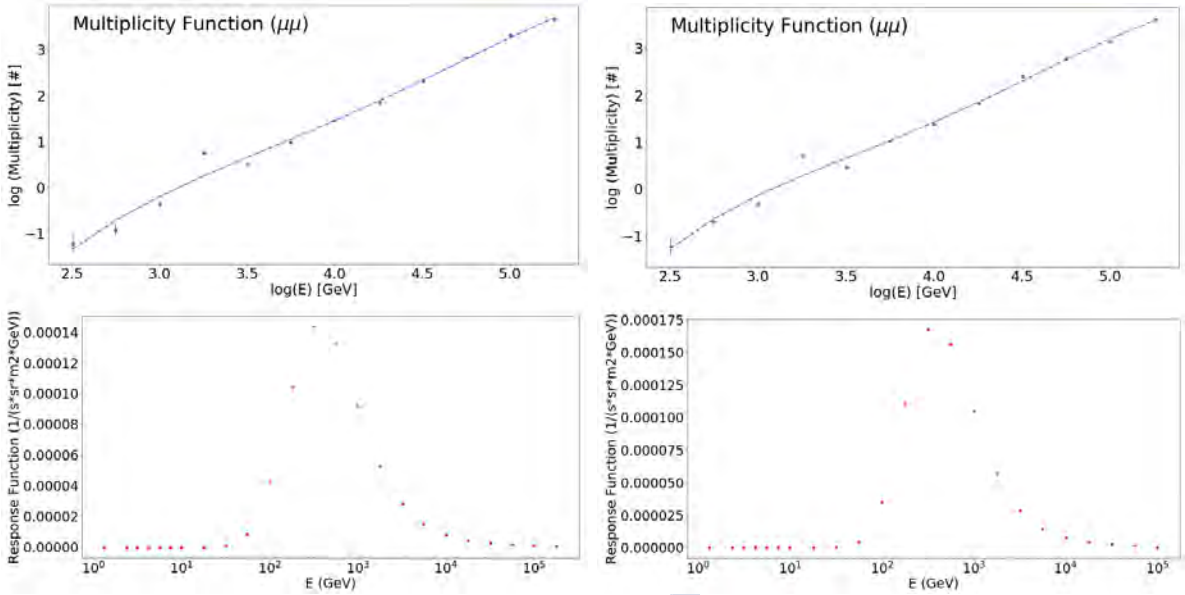

(a) (b)

Figure 6.12: Multiplicity and response distributions of dimuons with both cutoff energy 150 MeV (a) and 300 MeV (b) for primary H with vertical incidence in the atmophere calculated in BAE.

6.2.2.3 Trasgo detectors specificitions

The particle rate calculated with Trasgos is strongly correlated with geometry and configuration of the chosen set up.

The plane layout of the Tragaldabas and Tristan detectors involves an effective area S of particle detection, present in Figure 6.13. Figure shows the surface [m^2] as a function of the zenith angle [°]. The effective area of Tragaldabas can change according to the calculations in x-axis (1.5 m length) or y-axis (1.2 m length) view. The length on x-axis and y-axis are respectively 1.55 m and 1.225 m for Tristan. The data like a red dots is calculating the effective area fixing the x-axis and like a blue stars the area fixing the y-axis. The data are very similar to small zenith angles, the area is 1.8 m^2 (Tragaldabas) and 1.82 m^2 (Tristan) to null angle. The difference between data increases as the zenital angle increases. The curves of Tragaldabas and Tristan are very different. If the surface of Tragaldabas is equal to zero, the angles are about 33.5° for x-axis view and 40° for a y-axis view. The null surface angles of Tristan are about 36° (x-axis view) and 72° (y-axis view).

Table 6.2 show the partial acceptance $\Delta\Omega \cdot S$ [$sr \cdot m^2$] for each detector, Tragaldabas and Tristan, and for the different zenith angle range. The acceptances must be used for a rescaling of the response function distributionsfor both, the USC (partial acceptance of Tragaldabas) and the Antarctica (partial acceptance of Tristan). The partial acceptance is not very discrepancy between both detectors at low zenital angle but, it is large at high angle.

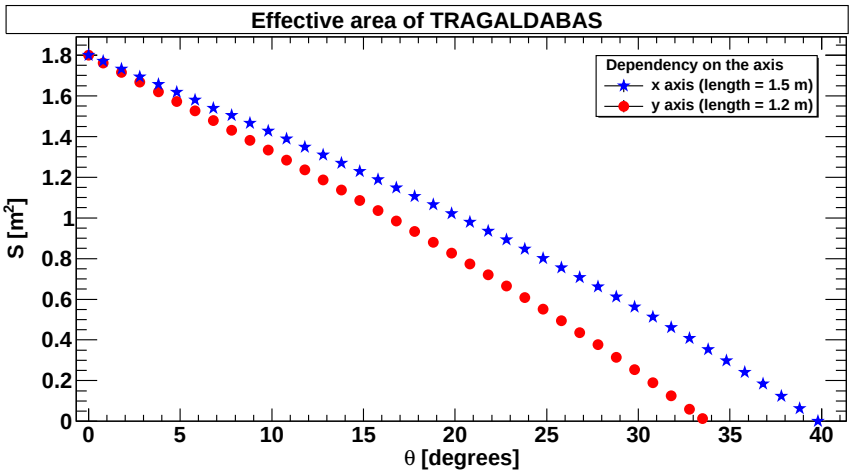

(a)

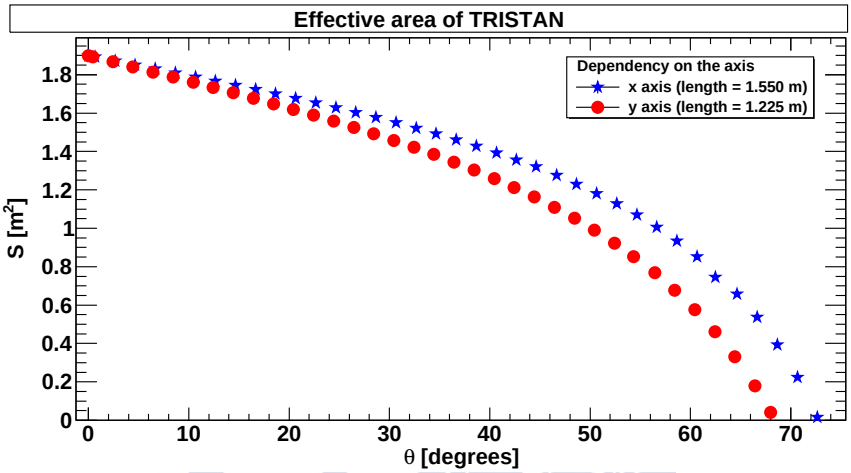

(b)

Figure 6.13: Effective area of Tragaldabas (a) and Tristan (b) for x-axis or y-axis view.

Table 6.2: **Partial acceptance of Tragaldabas and Tristan detectors for different ranges of zenith angles.**

	$\Delta\Omega$·S [sr·m^2]	
θ Range [degrees]	Tragaldabas	Tristan
[0, 12.8]	0.28	0.30
[12.8, 22.3]	0.54	0.60
[22.3, 29]	0.52	0.60
[29, 41.4]	1.15	1.49
[41.4, 58.3]	1.64	2.68

6.2.3 Future perspective

The response of Trasgo detectors allows to identify and estimate the primary CR energy. Collecting the maximum information from the atmospheric shower is necessary to know

the properties of the primary, in this a project by Labcaf with multiple Trasgo detectors in the USC called MEIGA (Mini Ensemble for Identifying GAlactic radiation) is developing. Several Trasgos deployed in a large area allows enough information to be collected to detect secondary from the same primary.

The Figure 6.14 is a simple diagram showing the response of 3 detectors, both the flow of primaries $dN/(dE \cdot dS \cdot dT \cdot d\Omega)$ and secondary multiplicity N_s/N as a function of the primary energy E_0. The result of 3 multiplicity functions (E_1, E_2, E_3) times the linear equation of the energy spectrum are three response functions (RF_1, RF_2, RF_3). The area generated by the superposition of the three distributions is the estimated primary energy. It is a simple and powerful method to accurately estimate the primary energy and eliminate any possible error from the sources with statistics.

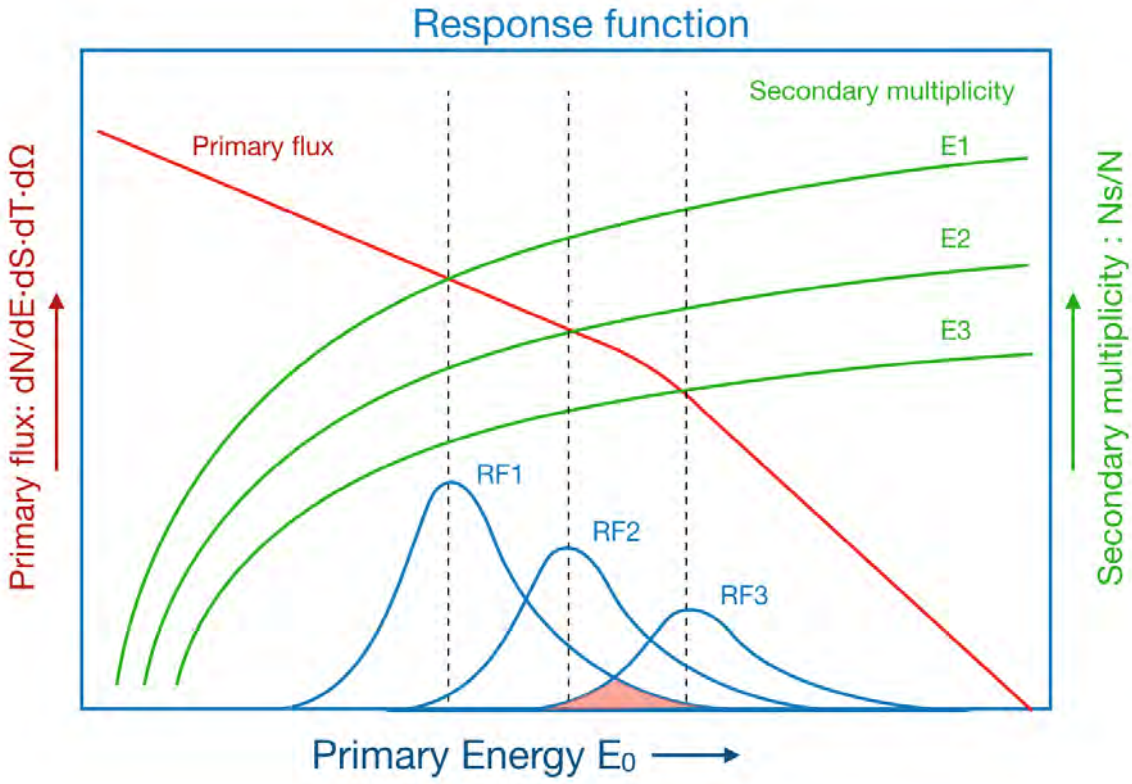

Figure 6.14: Response of the detector with a Trasgos array, the area given by the superposition of the 3 response functions provide the estimated energy of the primary cosmic ray.

6.2.4 Conclusion of the analysis for the energy estimation of the primary with a TRASGO detector

The detector response study is essential to calculate the event rate with particle detection experiments. The results will allow estimating the characteristics of the primary (mass, energy and arrival direction), reliable results will be achieved using a long surface experiment such as a Trasgos array. The mean values of RF distributions grow as the atomic weight of the nucleus increases, the results independent of the incidence angle are very similar for both USC and BAE locations and for both secondary muons and electrons. The average distribution of each nucleus is approximately: 20-30 GeV/nucleus for H, 30 GeV/nucleus for He, 50 GeV/nucleus for C and 100 GeV/nucleus for Fe. The mean distribution of dimuons for both a study in USC and BAE is 300 GeV/nucleus for protons with vertical incidence.

6.3 Density microstrucutre of CR air showers

6.3.1 Simulation and analysis methods

This section presents the method of generating events and analyzing the data used in the studies of lateral or radial distribution[2] and cluster distribution[3]. The event generation program is Corsika. Corsika generates secondary particles at ground level from primary nuclei with vertical incidence in the atmosphere. The position of the secondary is totally random. The energy range in logarithmic scale is [100, 10^6] GeV with 4 steps of $10^{2/8}$ per decade. The simulated primary number is 10k events for [100, 1780] GeV and 1k events for [3160, 10^5] GeV, for the radial study. The simulated primaries events is between 1k and 10 events in the energy range of [10^5,10^6] GeV according to the goodness of the data fit for this study. Namely, the generated protons were 30k events because the goodness of fit was not in good agreement with the chi-square test. The primary generated events was given according to 10k secondary for a minimum error of 1% in the calculations. The energy cutoff applied to the input Corsika simulations is shown in Table 6.1.

The study of radial distribution is essential to know the arrangement of air shower particles at ground level. Radial distributions provide relevant information about the density of particles as a function of the core distance of the EAS. The data analysis program has been written in order to collect the maximum information from the air shower. Two radial studies were developed, [31.6, 1000] meters with 13 dividing rings and [10, 562] meters with 15 dividing rings. The rings collect a number of secondary on a specific surface. The minimum core distances are 10 and 31.6 meters because smaller distances can produce perturbations in the count of secondary caused by the hadronic component

[2]The radial distribution is a density of secondary particles changes as a function of distance from the geometric center of the shower to the center of the rings, equation (6.3) defines this. See section 1.9 for more information.

[3]Cluster distribution is the grouping of particles that cover a space with many similarities. See section 1.9 for more information.

of the shower located in its core. The rings have a thickness w_r of 0.1 meters (10%). The core distance ranges are divided 8 steps of $10^{1/8}$ per decade: 10, 13.3, 17.8, 23.7, 31.6, 42.2, 56.2, 75, 100, ... The particle count has been done in a surface ring $2\pi\, r\, w_r$, where r is the distance from the geometric center of the shower to the center of the ring. The study was done with muons due to the complexity of the analysis of the distributions with electrons. Figure 6.15 shows the particles and rings at ground level. The concentric radii to the geometric center represent the rings. The rings are described by their radius $\vec{r}$ to the geometric center of the EAS and by the size of the ring w_r. The red stars represent the position of secondary particles. The position of the particles are completely random, generated by Corsika. Any particle inside the ring is counted. The particle density would

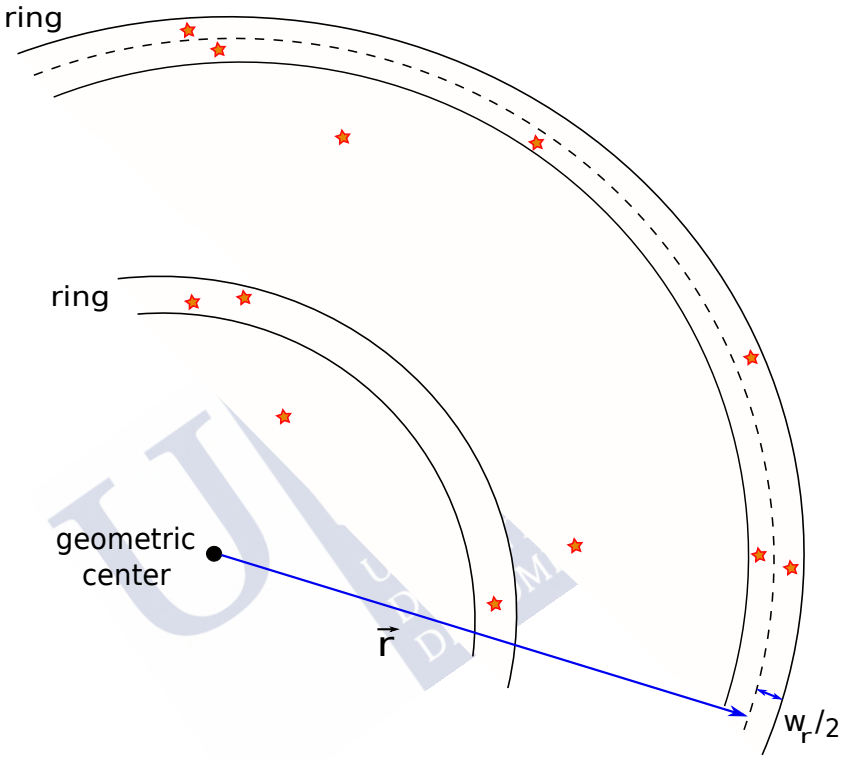

Figure 6.15: Easy study strategy graph: top view of particle distribution at ground level from a air shower and distribution rings density. The rings away $\vec{r}$ to the geometric center of the EAS and thickness w_r, group the particles (red stars) for a radial distribution analysis.

be expected to decrease as the radius of the ring grows.

Figure 6.16 shows the muon density distributions for primary protons with vertical incidence in the atmosphere. The graph shows the radial density (LDF) [m^{-2}] as a function of the distance to the core [m] for a distance range of [10, 1000] m and for divided energies $10^{4/8}$ per decade. The radial density decreases slowly as the core distance grows. Density curves increase as the primary energy grows. The data was adjusted using the following LDF formula:

$$\rho(r) = C \cdot \left(\frac{r}{r_0}\right)^{\alpha} \cdot \left(1 + \frac{r}{r_0}\right)^{\beta} , \tag{6.3}$$

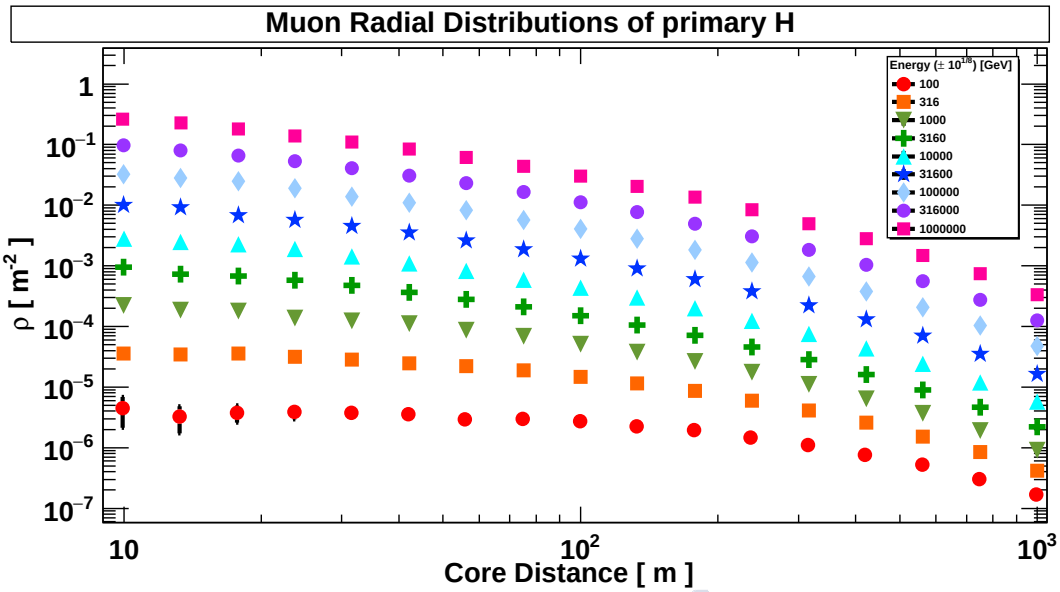

Figure 6.16: Results. Muon density distributions at ground level for a core distance range of [10, 1000] m from primary CRs proton with vertical incident in the atmosphere.

where r is the distance to the geometric center of the EAS and (C, r_0, α, β) are free parameters. T. Hara [40] used this equation to fit his experimental data and obtained the following values: r_0=280 m, α=-0.75 and β=-2.5. Given the references [37, 92], the C parameter may be correlated with N particles.

Another essential study, compatible and relevant to the previous one is the so-called **study of cluster distributions**. A set of particles from EAS grouped in a certain area at ground level is a study objective to know the radial characteristics of the shower and properties of the primary CR. Temporary properties of the cluster study are also important, but not a priority, so it has not been studied in this work. The cluster study was achieved with simulations of the Corsika program. The analysis program collects simulated characteristics of the first interaction, such as the radius to the geometric center $\vec{r}_c$ of the shower, and counts the particles in an action radius $\vec{r}^*$ of 2 meters from the first interaction. If a particle is counted in the action radius, the program has the possibility to re-count particles in a radius of 2 meters from this new particle, this count is called a new iteration. The iterations are repeated while new particles within the action radius exist. Double counts have been removed for performance analysis. A cutoff has been imposed on the analysis program so that the iterations are not excessively long, if the new iteration is less than 0.5 m from the previous one, this is carried out. Accurately locating very dense particle clusters is the objective with this analytical method of data. A long list of essential parameters is studied to characterize the shower cluster. The cluster analysis program is written in the Appendix "Source codes". All interactive particles with $\vec{r}_c$ below 10 meters of the core were neglected. Additional energy cuts to those in Table 6.1 were implemented in the analysis program to consider technical contributions a Trasgo-like detector, E_{cut}=0.1 GeV for electrons and E_{cut}=0.2 GeV for photons. The parameters provided by the analysis program were analyzed with the Python 2.7 [93]. A

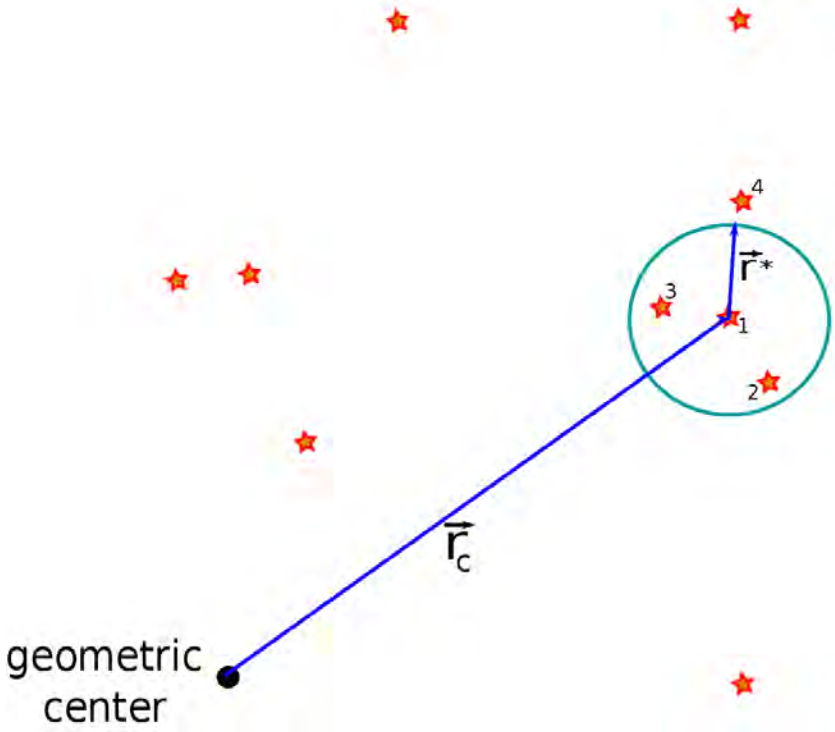

Figure 6.17: Easy study strategy graph: cluster distribution of secondary particles at ground level from a air shower.

simple graph of iteration counts process is shown in Figure 6.17.

6.3.2 Lateral distributions analysis

The relationship between primary CR energy and the number of secondary is extremely important when an EAS study is performed. The relationship is given by the equation (1.7), it can be rewritten as follows:

$$N_0 \simeq \frac{1}{\kappa^{1/b}} \cdot E_0^{1/b} \tag{6.4}$$

where the parameters κ and b take the value of κ=2.217 $\cdot$ 10^{11} and b=0.798 for protons (A.M. Hillas [21]).

Figure 6.18 show the average particles mix of shower as a function of the primary CR energy with vertical incidence in the atmosphere. The plots show dilogarithm graphs where the data was simulated in the USC for the 4 known cosmic rays (H, He, C and Fe). The energy has units of the electronvolt. The growth of standard deviation between neighboring data as the energy grows show the transition in number of simulated primary events performed. The data perfectly reflects a linear behaviour. The goodness (χ^2/ndf) [4] of the fittings is much less than 1 for all the graphs. This statistical quantity proves that the method of linear fit of the data is correct. The results of the fit have values of κ=4$\cdot$$10^{10}$

[4] ndf is the degrees of freedom of the system.

and b=0.94. Fit results take the following values for the different nuclei: κ=4·10^{10} and b=0.94 for H, κ=10^{10} and b=0.96 for He, κ=3.3·10^{9} and b=0.95 for C, and, κ=8.4·10^{8} and b=0.94 for Fe. The results from protons are in agreement with the previous results of A.M. Hillas.

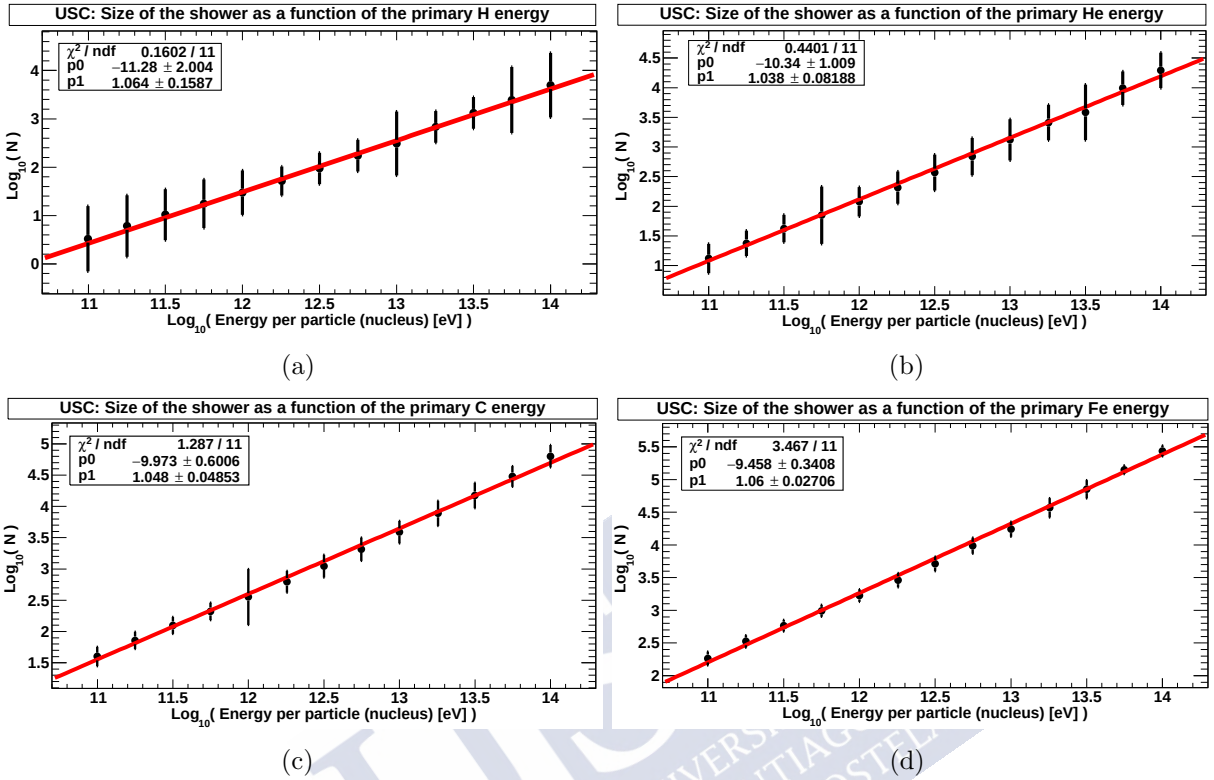

Figure 6.18: Size of the shower as a function of the different primary nucleus energy with vertical incident in the atmosphere for H (a), He (b), C (c) and Fe (d).

Next, the results of the parameterization performed on the data in Figure 6.16 (proton case) are commented using the equation (6.3). Important, double the standard deviation (uncertainty) 2·σ was applied to fit of the particle density data. The most relevant results are graphs for an range r of [31.6, 1000] m and [10, 562] m, the standard deviation of the data is neglected because trends are the most interesting. All data concerning the adjustment parameters are collected in Tables of the Appendix "Parametrization data sheets of LDF study".

Figure 6.19 show the differents parameters as a function of the energy for the primary nuclei. The graph (a) shows the evolution of C parameter with energy. The C data parameter has approximately a linear trend with the primary CR energy. This trend is very similar to the shower size graph, so it is assumed that the C parameter is correlated with N particles [37, 92]. Graph (b) shows the r_0 parameter, the result data decreases at a constant value as the energy grows. The data have an oscillating behavior. The oscillation can be caused by the simulations with Corsika and the fited LDF equation. The results tend to about 700 meters as the energy grows. Figure 6.19 (c) shows the α parameter, the data decreases asymptotically to a constant value as the energy grows.

The Figure 6.19 (d) shows the data growth up to a constant value for the β parameter. The oscillation is also with these data results. The α and β values trend to be -0.9 and -3.7 respectively.

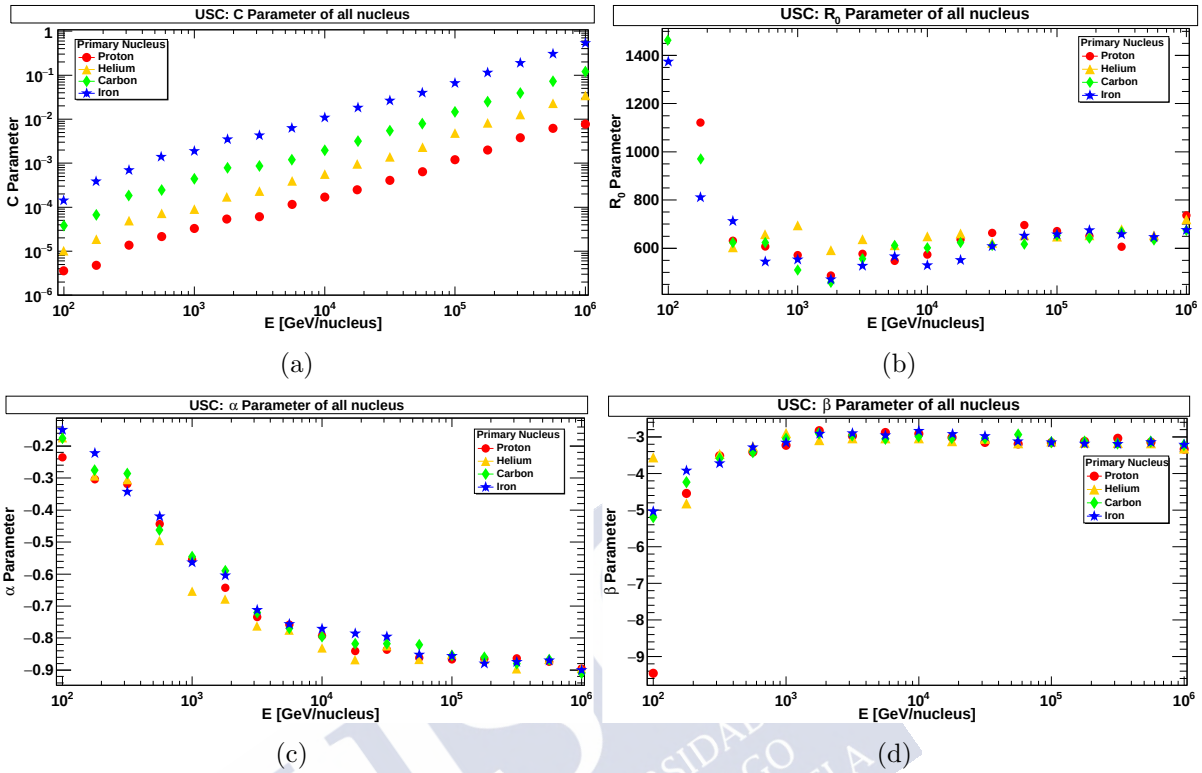

Figure 6.19: Study performed in a distance range to core of the shower of [31.6, 1000] m. Parametrization of C (a), r_0 (b), α (c) and β (d) LDF parameter value for nuclei with vertical incidence in the atmosphere.

The parameters of Figure 6.20, take a behavior and trends very similar to the previous results, but the tendency of the data at high energies is very different. The separation between data is greater as the nucleus changes. The oculations are persistent in these results, again, the simulated data with Corsika and the LDF fit equation are the possible causes. The parameters for high energies take values of r_0=220 m, α=-0.63 and β=-2.1. All trend results for high energies are in good agreement with the experimental results of T. Hara.

Figure 6.21 show the residuals plots for distance ranges of [31.6, 1000] m (a) and [10, 562] m (b) for the parameterization study with primary protons calculated in the USC. Plots show similar fluctuations at low r (core distances) and very different trends at high r. The fluctuations are high along the distance to the core r for the study at range of [31.6, 1000] m. The data is within an approximate range of $\pm$0.04. The fluctuations are high at low r and the data tends to be null at high r, for the study at range of [10, 562] m. The data is within an approximate range of [0.2, -0.15]. Namely, the residual scale between these two graphs differs by a factor of 10, therefore one can assume that the study at [10, 562] m has a higher precision and sensitivity values along the range distance than the study at [31.6, 1000] m.

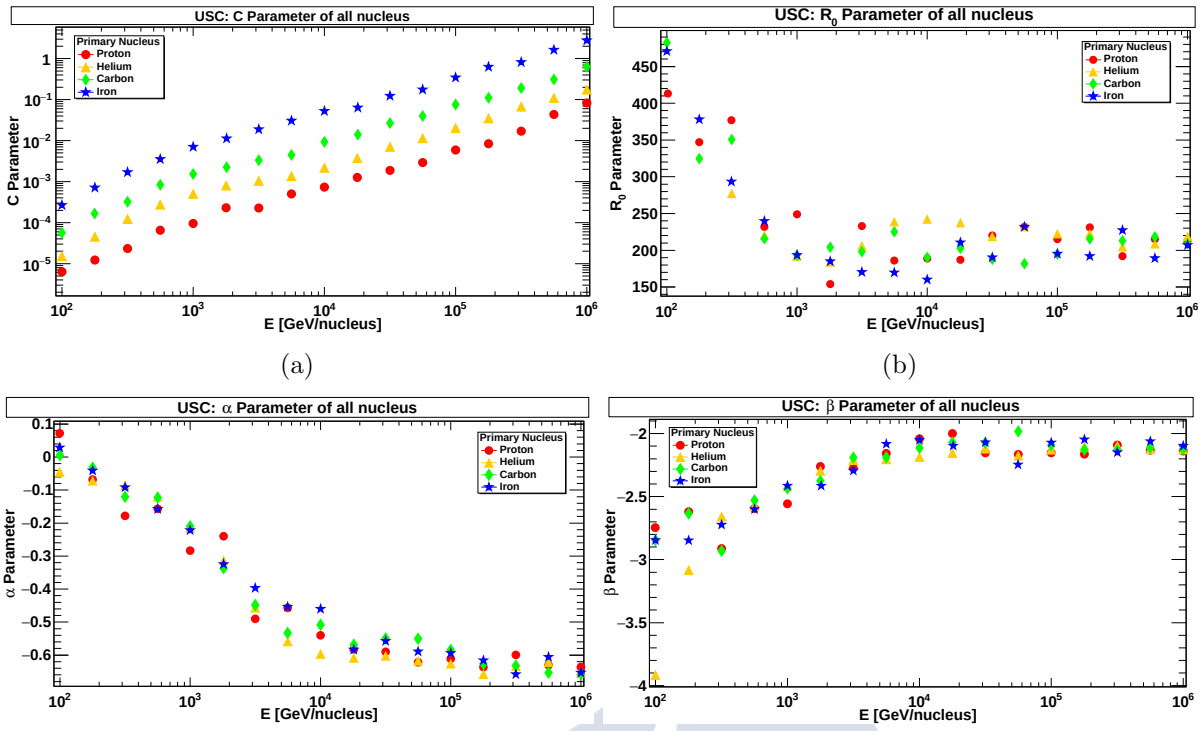

Figure 6.20: Study performed in a distance range to core of the shower of [10, 562] m. Parametrization of C (a), r_0 (b), α (c) and β (d) LDF parameter value for nuclei with vertical incidence in the atmosphere.

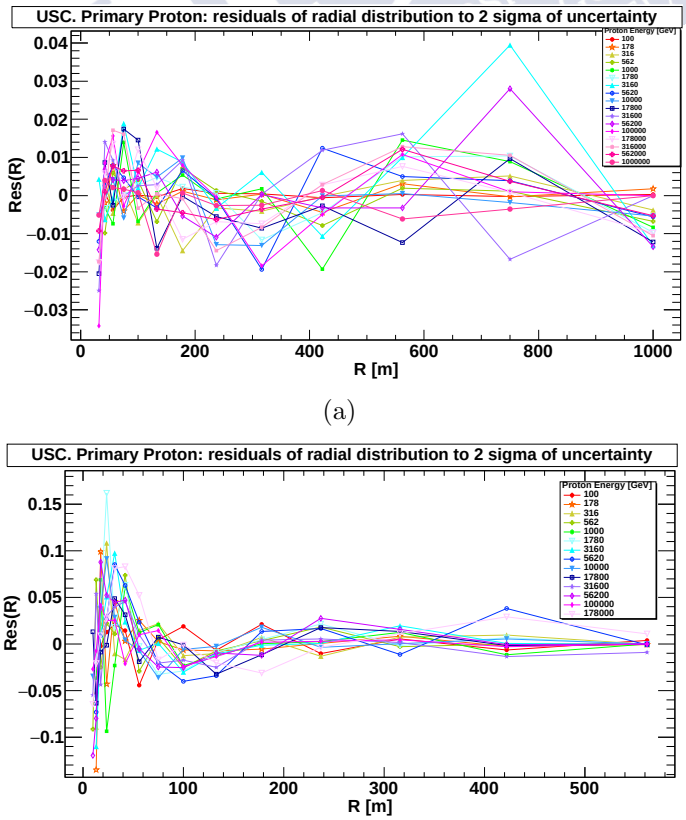

Figure 6.21: Residuals plot in r distance of [31.6, 1000] m (a) and [10, 562] m (b) for parametrization study of H nucleus.

6.3.3 Cluster analysis

The phenomenological study of clusters will provide useful information about the size of the air shower, the number of particles per cluster and their relationships with the energy of the primary, the nature of the particles in the cluster and the angle of incidence of the clusters at the level of the ground among others. Namely, the number of particles has always been normalized to the entries of simulated primaries. The study was carried out for H, He, C and Fe nuclei.

Figure 6.22 show the distribution of the secondary on the x-y plane at ground level for the main studied nuclei fixed at an energy of 10^4 GeV. The graphs clearly show the size of the air shower growing as the nucleon mass increases, the cloud dots of density is mainly located in the geometric center of the shower. Most of the secondary are located in a radius range of less than ± 500 m in x-y plane for each nucleus.

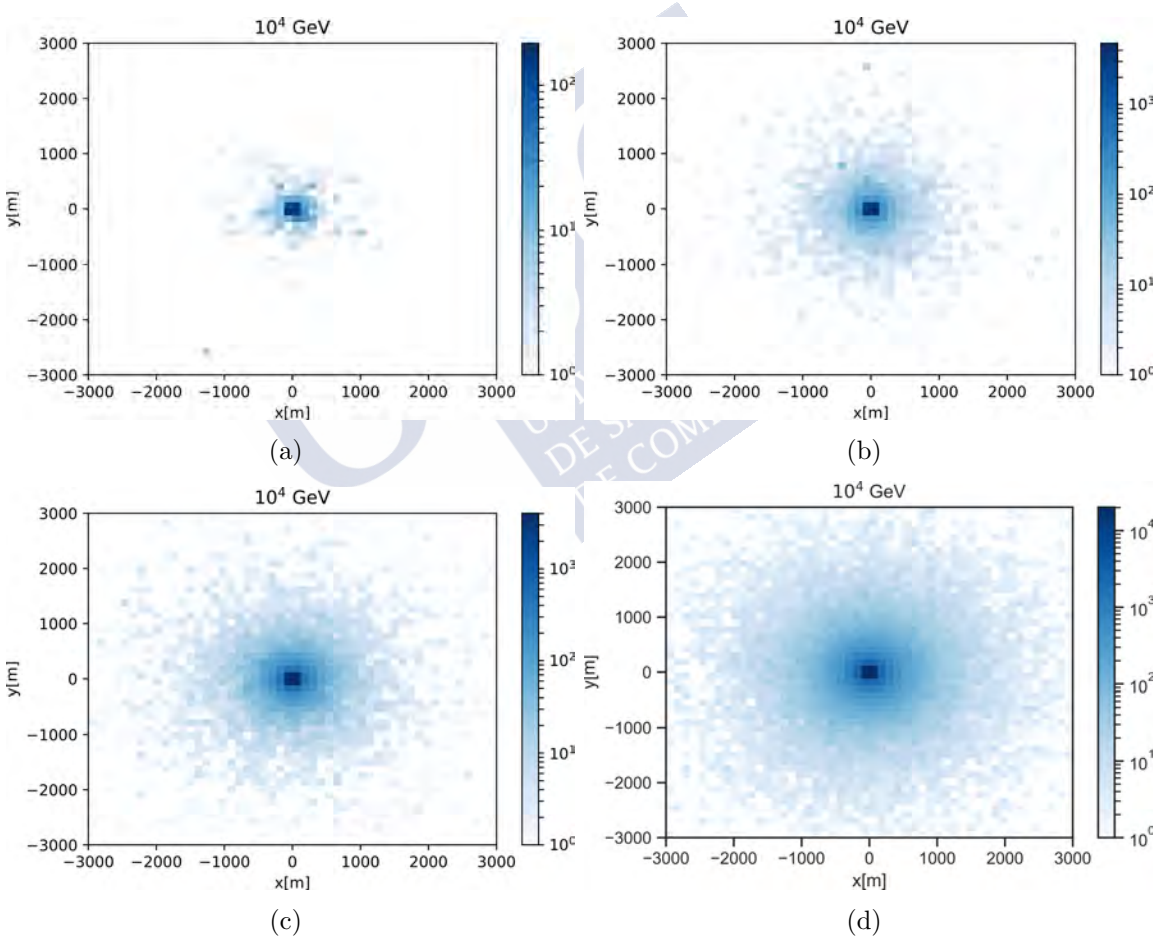

Figure 6.22: Position of clusters at ground level for different nuclei with a fixed energy of 10^4 GeV, for nuclei of H (a), He (b), C (c) and Fe (d).

The total particle rate (protons, neutrons, electrons, photons and muons) produced by

EAS is studied below. The total rate is calculated with the following equation:

$$X'_i = \frac{n_i}{n_T} \ , \tag{6.5}$$

where n_i is the number of particles of a particular nature (p, n, e, γ and μ) and n_T is the total number of secondary particles. Figure 6.23 show the particle rate per cluster as a function of the energy of each nucleus. Given the high generation of e.m showers, electrons and photons increase greatly compared to muons at high energies and therefore the rate reflects a decrease in muons and an increase in electrons and photons. The results show that muons are the most abundant recorded at ground level, abundance of about 70-90% (according to the nucleus) of muons for energies less than about $6{\cdot}10^4$ GeV. The most abundant particles are photons and electrons for energies higher than the value mentioned above, 80-90% of electrons for an energy of 10^6 GeV.

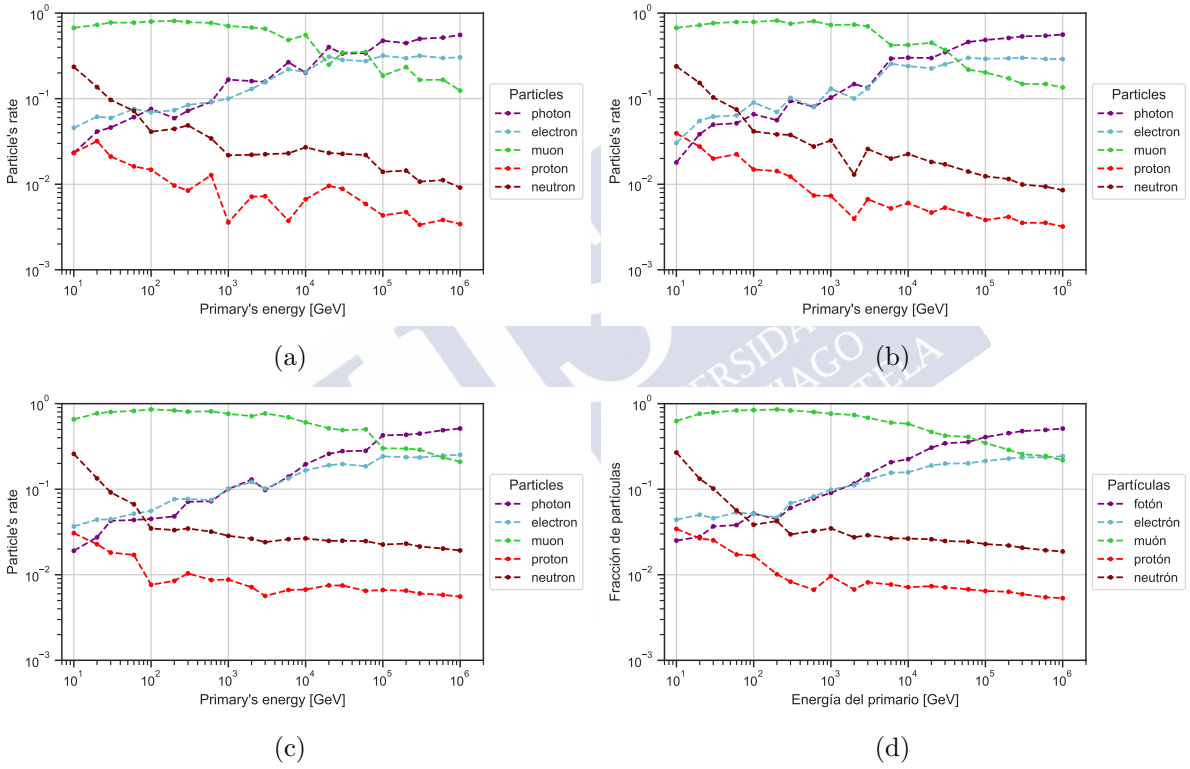

Figure 6.23: Total particle rate as a function of the energy of each nucleus, for nuclei of H (a), He (b), C (c) and Fe (d).

The following results study the density of normalized counts [m^{-1}]. It is understood as a normalized counts all cluster particles normalized to the number of primaries. The density parameter was calculated as follows:

$$G(r) = \frac{n(r)}{sd(r)} = \frac{n(r)}{[\pi \cdot (r_2^2 - r_1^2)]} \ [m^{-1}] \ , \tag{6.6}$$

where r is the radius to the cluster center, $sd(r)$ is the area between clusters and $n(r)$ the number of normalized counts. Figure 6.24 show the density of particles as a function

of the radius at the center of the clusters for the 4 nuclei and for 7 energies between 10 and 10^5 GeV. The densities are maximal near to the core of the air shower and decrease rapidly as the radius increases. The data varies according to the primary energy, higher densities for higher energies.

Important concepts, as the atomic number (Z) increases the nucleon is less penetrating into the atmosphere and the height of the first interaction is higher. The results show that the radii to the geometric center are equal as the mass number of the nucleon increases at the same energy, this phenomenon is possible because the height of the first interaction of each nucleon is different.

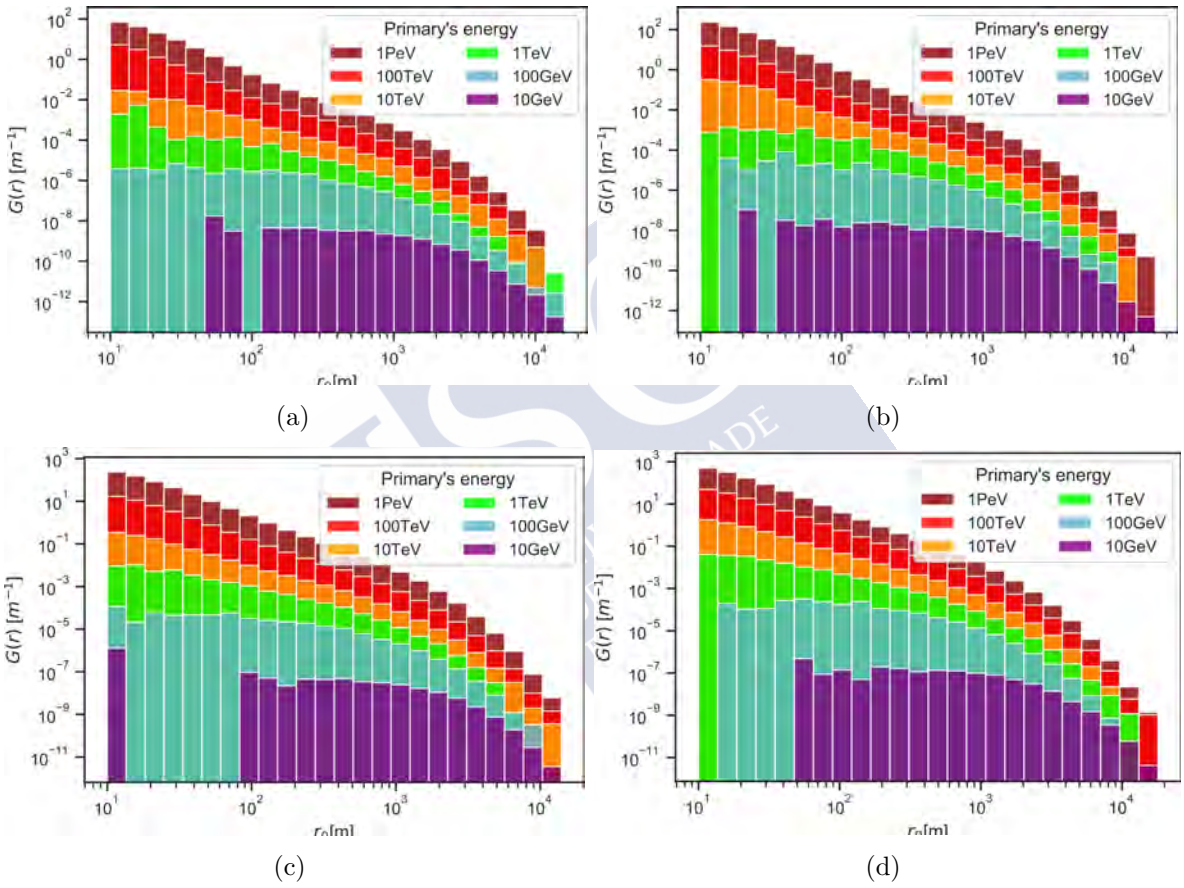

Figure 6.24: Relationship between the density of normalized counts and the radius of the clusters at different primary energies and nuclei. Histograms calculated for H (a), He (b), C (c) and Fe (d).

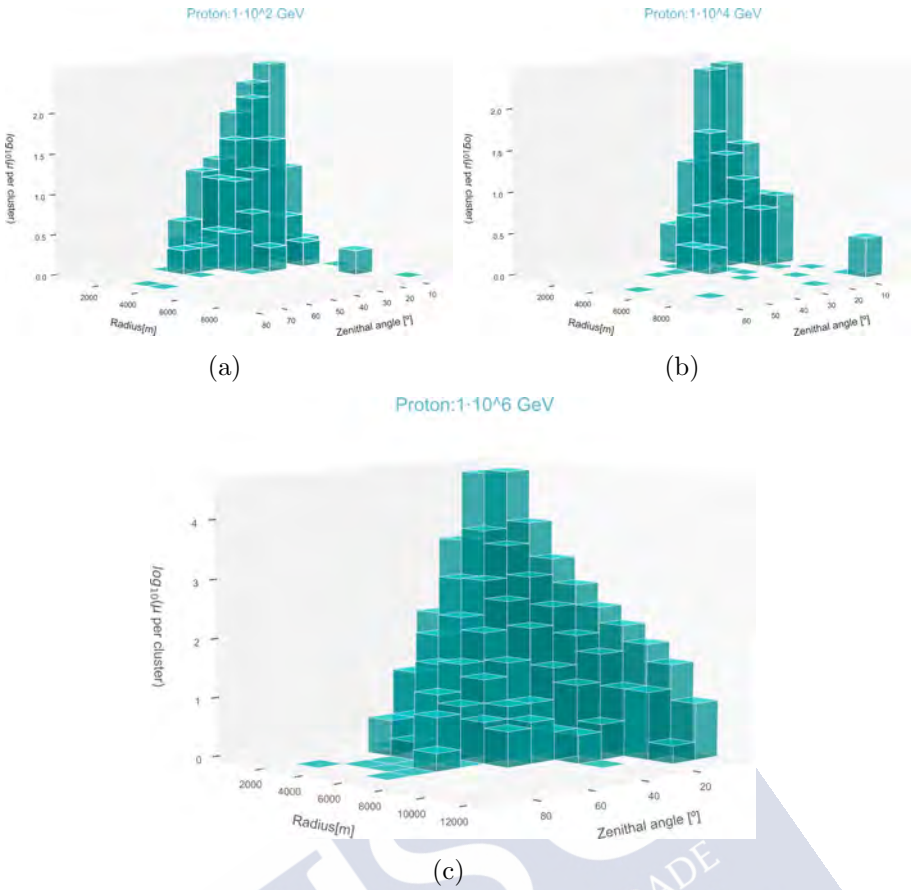

(a) (b)

(c)

Figure 6.25: Energetic evolution of 3D plots muon clusters from primary H nulceus without radial cutoff of 10 m. The histograms show the radius to the center of the cluster versus zenithal angle of secondary muons versus number of muons per cluster in logarithmic scale. Proton energies of 10^2 GeV (a), 10^4 GeV (b) and 10^6 GeV (c).

Figure 6.25 and 6.26 show the muons plots 3D for different energies (10^2 GeV (a), 10^4 GeV (b) and 10^6 GeV (c)) of the respective H and C, radius to the center of the cluster versus zenithal angle of secondary muons versus number of muons per cluster in logarithmic scale. The results include a minimum of 2 muons per cluster due to the contribution in logarithmic scale of the results. Most cluster muons are collected for radii smaller than 600 meters and zenital angles less than 30 degrees for low energies for both H and C. The size of the air shower and zenital angles increase rapidly with energy. The number of muons per clusters of the air shower can be estimated by knowing the radius of the air shower and/or zenital angle of the muons. The data changes little comparing between H and C at the same energy. Crucial information is the maximum in small zenital angle in the results, around 16°. Then, muons produced near the core of the shower have a privileged trajectory, leading to a zenital angle with greater muonic events.

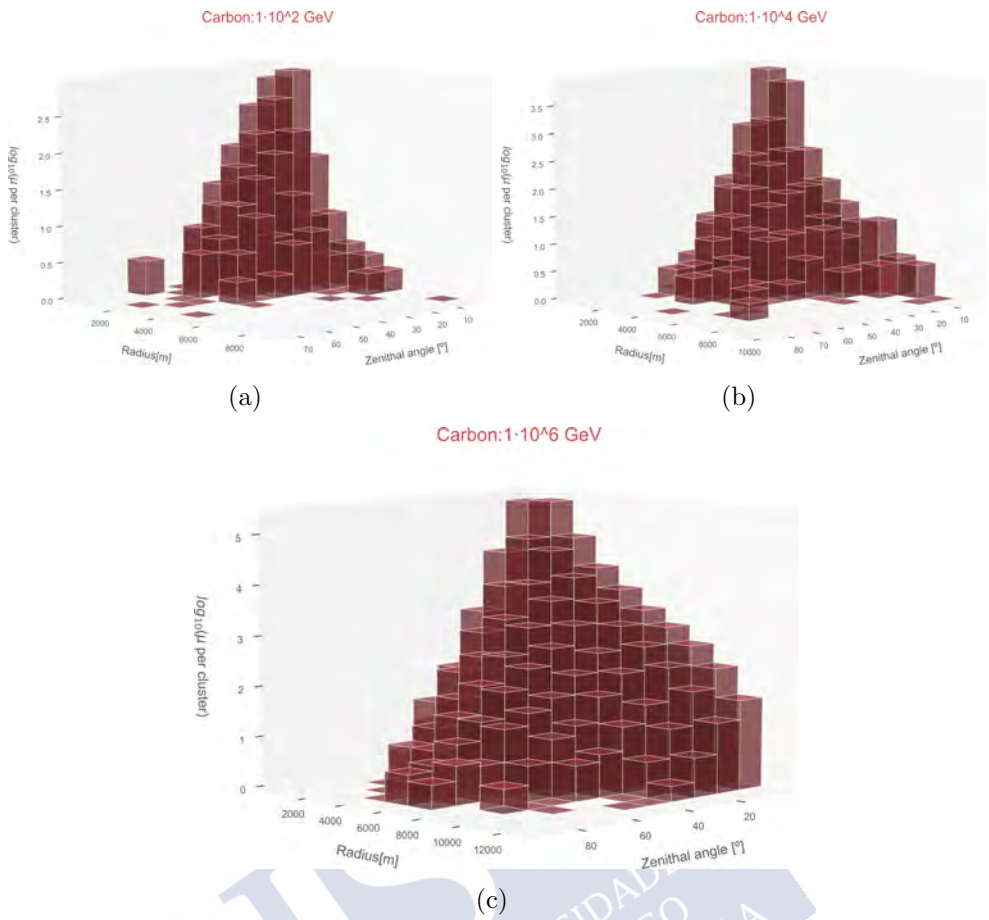

(a) (b)

(c)

Figure 6.26: Energetic evolution of 3D plots muon clusters from primary C nulceus without radial cutoff of 10 m. The histograms show the radius to the center of the cluster versus zenithal angle of secondary muons versus number of muons per cluster in logarithmic scale. Carbon energies of 10^2 GeV (a), 10^4 GeV (b) and 10^6 GeV (c).

Figure 6.27 and 6.28 show the distance between the center of the cluster to the geometric center of the EAS versus the primary energy versus the cluster size in logarithmic scale (only for electrons). The radius and the cluster size were calculated by sorting the data by the radius and separating it by sections of 10 m, for each section the mean cluster size and the mean radius are calculated. The data grows as the radius is smaller and the energy is higher for both electrons and muons. The absence of data at high electron energies is possibly due to a thinning of the shower size near of Earth′s surface accord with the mass of the primary nucleus. The primary source and its energy can be identified with the localized information about a variety of clusters, and a more detailed study is foreseen following this line. Muon plots show an increasing distribution as the mass of the primary increases. The maximum distributions are shown in Table 6.3. The maxima of the distributions increase as the primary mass and the radius of clusters to the center of the shower increases. This phenomenon is possibly due to the privileged angle of muons near the core and the height of interaction of the primary nucleus and/or mass of it.

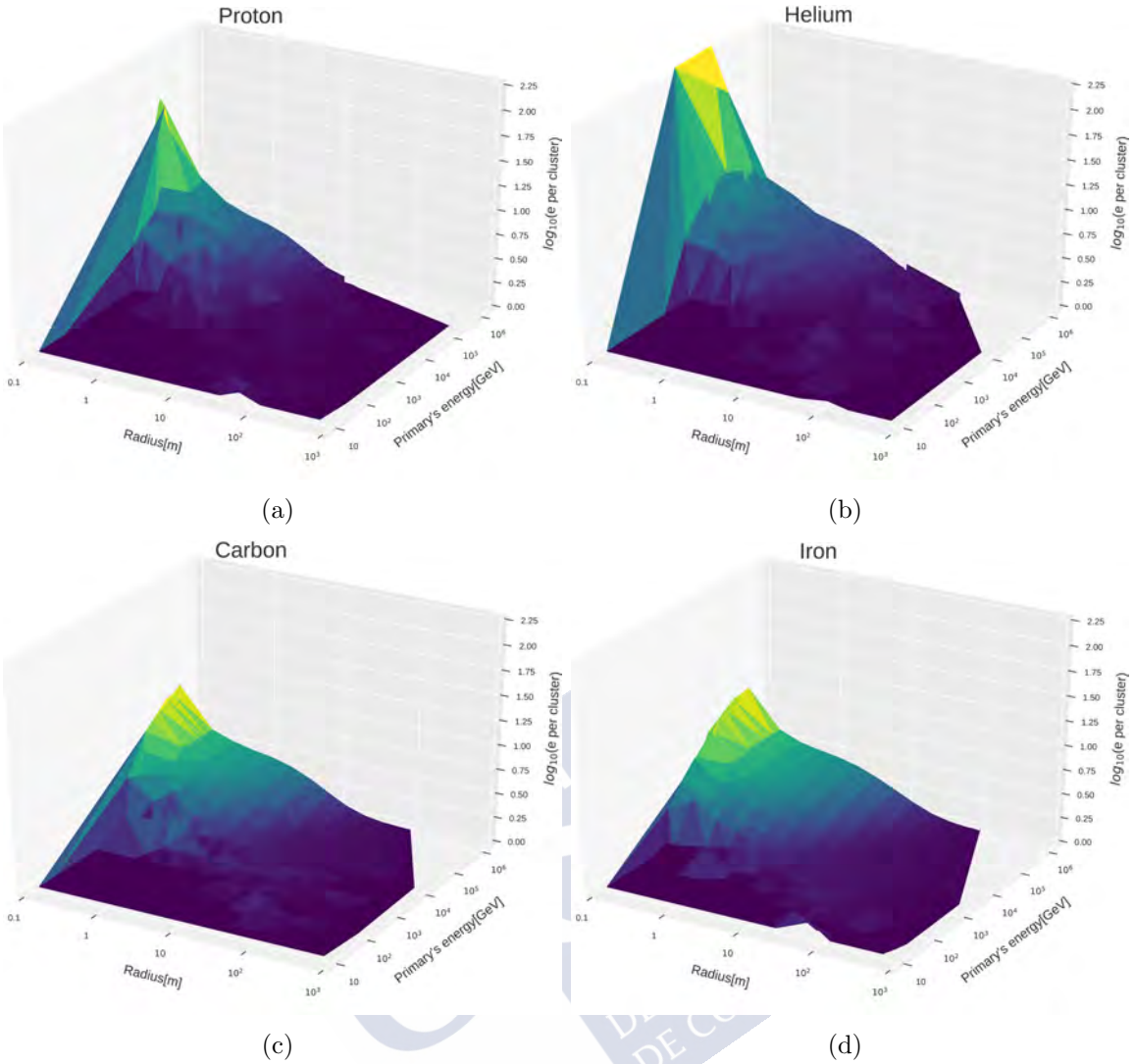

(a) (b)

(c) (d)

Figure 6.27: 3D plots electron clusters without radial cutoff of 10 m, relationship between the distance and size of the clusters at different primary energies and nuclei. Plots calculated for H (a), He (b), C (c) and Fe (d).

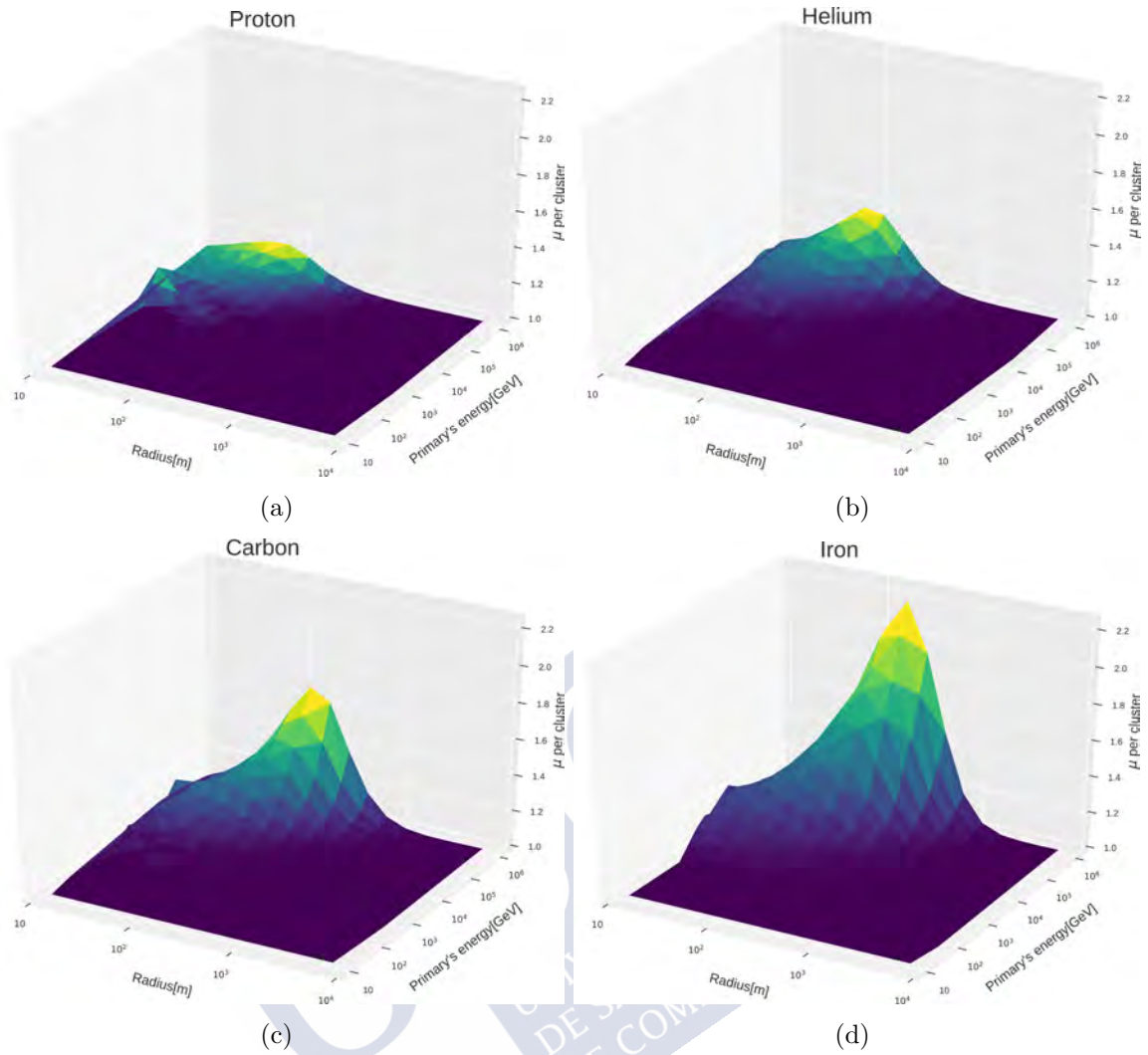

Figure 6.28: 3D plots muon clusters with radial cutoff of 10 m, relationship between the distance and size of the clusters in logarithmic scale at different primary energies and nuclei. Plots calculated for H (a), He (b), C (c) and Fe (d).

Table 6.3: **Maximum of muons surface distributions for 10^6 GeV. The maximum of the distributions increases greatly as the mass of the primary and the radius at the center of the shower increases.**

Primary nucleus	H	He	C	Fe
μ cluster size	1.2	1.4	1.7	2.2
Maximum radius [m]	80	81	128	203

6.3.4 Conclusion of the analysis for density microstructure

Studies shown the phenomenology of air showers at ground level from primary nuclei with vertical incidence, mainly: H, He and C. The lateral distribution results combined with the cluster study results can give an estimate of the array size of Trasgo-like detectors.

The **study of lateral or radial distribution** show results of primary energy (Figure 6.18) and density of particles (Figure 6.19 and 6.20) at high energies in good agreement with the results of A.M. Hillas and T. Hara, respectively. The results contribute to the evolution of the number of secondary as a function of the energy (or vice versa) and the density as a function of the radius to the geometric center of the shower for different primary energies. The **study of clusters distributions** gives the size of the air showers, total particle rate as a function of energy and density as a function of radius to the geometric center for these three primaries. The results of the Figure 6.23 show an abundance of about 90% for muons at primary energies below $6{\cdot}10^4$ GeV, above this value in energies the abundance of photons and electrons is the highest. The density is high near the core and decreases strongly with the radius to the geometric center, shown in Figure 6.24. The 3D plots muon clusters for both H and C provide information about the radius to the geometric center, zenital angle and muons per clusters for different energies. These give an estimate of the shower size and angle of arrival of muons at ground level. The 3D plots for both electrons (Figure 6.27) and muons (Figure 6.28) give relevant results on the correlation between the radius, primary energy and the cluster size. The radius to the geometric center with high cluster density are around a few tens of meters for electrons and a few hundred meters for muons. The optimal energies for the detection of many clusters are the highest of both electrons and muons.

USC
UNIVERSIDADE
DE SANTIAGO
DE COMPOSTELA

USC
UNIVERSIDADE
DE SANTIAGO
DE COMPOSTELA

Conclusions

The work presented in this document deals with particles detection in Trasgo-like detectors, and with the Tragaldabas system in particular. Trasgo is a family of particle detectors based on the Resistive Plate Chambers (RPCs) technology, and intended for cosmic rays measurements. Tragaldabas, the detection system located at the Faculty of Physics of the University of Santiago de Compostela, is now the first complete Trasgo-like detector. The system has been simulated completely from scratch, and its response to secondary cosmic rays was studied.

After a general introduction about Cosmic Rays Physics, particles interacting with matter and the principles of RPC detectors, a detailed description of the Tragaldabas experiment is given. Tragaldabas is a Trasgo-like detector consisting of four planes of RPCs, 1.3×1.8 m^2 each, arranged in a parallel configuration, which has started to take data in April 2015. However, it was only recently, during my PhD work, that the system was deeply analyzed with simulations data.

The first task was to implement the Tragaldabas detector into the EnsarRoot simulation framework. And not only the detector itself, but also the building where it is located was included. Then, two main studies were carried out with different simulated data each.

In the first study, the simulated data sent to the detector was extracted from the CRY cosmic ray particle generator at ground level, and also from a dedicated cosmic ray generator developed and implemented in EnsarRoot as well. That data allowed for the following:

- It was developed a complete study of the behavior of secondary cosmic electrons, photons and muons, with vertical and non-vertical incidence, and the full range of allowed energies, over the Tragaldabas detector. The detection efficiency for the three kinds of particles was calculated: it was obtained to be compatible with 100% for all energy muons, ranging from 10% for 2-3 MeV electrons to close to 100% for electron energies above 100 MeV, and never greater than 20% for gammas.

- The geometric acceptance (a_g) maps of the Tragaldabas detector were obtained for the first time. Those maps are necessary for further corrections in the real cosmic ray rate recorded by the system. As a conclusion, when Tragaldabas is operating its four detection planes, and the four planes trigger is required (or at least a trigger signal given by the first and last planes), only an overall value of 5% of the incoming cosmic rays are geometrically accepted by each detection cell.

- Based upon realistic CRY data, I have created dedicated cosmic muon, electron and photon generator to be used for Trasgo-like detectors studies. Those particles, with kinetic energies ranging from 100 MeV to 5000 MeV, are generated following real energy and angular distributions functions. The particle generator has been implemented in the EnsarRoot framework.

- A particle identification algorithm in cosmic rays, called MIDAS, was designed and implemented. Some physical observables were describe by means of simulation, like event multiplicity M, the so-called weighted range a_n and χ^2 of the tracking procedure, and then allow us to identify the nature of the particles measured by the Tragaldabas detector. The method was developed for different configurations of the Tragaldabas detector. The accuracy of the method resulted to be results of 90% for the most realistic cases. Also, the use of lead layers between detector planes enhanced the calorimetric capabilities of the system and improved the separation between muons and electrons.

In the second study, simulations data from CORSIKA was used. I studied the behavior of secondary cosmic rays at the ground level originated in extensive air showers by primary cosmic nuclei such as H, He, C and Fe, arriving at the atmosphere with a kinetic energy range of $[10^9, 10^{15}]$ eV. The characteristics of the primary cosmic rays: mass, energy and incident angle in the top of the atmosphere, can be addressed by studying the lateral and cluster distributions of secondary cosmic rays at the ground. In addition, the response function of Trasgo-like detectors. Complementing Tragaldabas, another Trasgo-like detector, called Tristan, will be located at the Antarctic Spanish Base. Then, the before mentioned response function was studied in both geographic locations, Santiago de Compostela, and Antartica Spanish Base.
Overall, this second study led me to extract the following main conclusions:

- We performed a phenomenological study of secondary cosmic rays at ground level in both USC and BAE with simulations of EAS using Corsika program, for different primary cosmic rays H, He, C and Fe at different incident angles of nuclei in the top of the atmosphere.

- A comprehensive study of the response of the Trasgo-like detectors for both electrons and muons can allows us to know the flux of secondary particles at different energies as a function of the energy of the primary nuclei. The maximum intensity of the distributions decreases as the nuclei mass increases and as the incident angle of the primary cosmic rays grows. The mean value of the distributions increases as the nuclei mass grows, and is about 20-30 GeV/nucleus for both primary H and He nuclei, 50 GeV/nucleus for primary C nuclei and 100 GeV/nucleus for primary Fe nuclei.

- The lateral distribution of muons at the ground level was studied for the before mentioned four significative nuclei. It was obtained a good agreement with the experiments of T. Hara. In addition, the results of the shower size as a function of the energy of primary cosmic rays gives the behavior and trend of the data, and fit results in good agreement with the experiments of A.M. Hillas.

- Also, the cluster distribution of both muons and electrons at ground level for the for nuclei was studied. It was observed the dependence of the cluster size, number of clusters and distance from the cluster to the center of the EAS with respect to the primary nucleus and its energy. Although the obtained results are not conclusive, they may open the door for the development of single detectors or small arrays of detectors at the ground level aiming to provide an estimate about the mass and the energy of primary cosmic rays. The method is very promising and other observables should be added in further studies, as the time profile of the clusters, the lateral spread (or termalization) of the particle of the clusters or the analysis of clusters with a mixed composition of muons and electrons.

The Tragaldabas detector system behaviour under cosmic rays was deeply analyzed by means of simulation and particle identification method for secondary cosmic rays was developed. The use of Trasgo-like detector arrays is suggested for analyzing the nature of primary cosmic rays.

USC
UNIVERSIDADE
DE SANTIAGO
DE COMPOSTELA

Resumen

En estas cuantas páginas, se resume el trabajo realizado sobre la detección de rayos cósmicos con un detector de tipo Trasgo como Tragaldabas. Tragaldabas es un detector de RPCs (Resistive Plate Chambers) de alta resolución espacial y temporal situado en el laboratorio LabCAF de la Facultad de Física de la Universidad de Santiago de Compostela (USC). El experimento está diseñado para medir la tasa de rayos cósmicos que llegan a nivel del suelo. Tragaldabas está compuesto por 4 planos paralelos RPCs separados aproximadamente 60, 30 y 90 cm, cada plano RPC tiene unas dimensiones de 1.2×1.8 m^2 y alberga en su interior 120 *pads* de dimensiones 11.2×11.8 cm^2. Los planos detectores RPC de Tragaldabas están formados principalmente por dos gaps de freón como medio activo gaseoso, donde se generan las avalanchas de electrones tras el paso de partículas cargadas.

El trabajo fue realizado en su ámplia mayoría con datos simulados. El entorno de *software* EnsarRoot fue usado para el estudio de observables físicos y de identificación de partículas realizado con el detector Tragaldabas. Este mismo programa fue usado para las modificaciones del sistema Tragaldabas e implementación del edificio de la Facultad de Física en la geometría. Un programa sencillo de generación de eventos procedente de Cry también fue implementado al programa. El sistema se modificó para 4 casos muy concretos: un sistema a 4 planos activos RPC, un sistema a 3 planos activos RPC y a 4 planos activos RPC con una lámina de plomo de 1 y 1.5 cm tras el tercer plano del detector. Este último, incrementa las capacidades calorimétricas de un detector de tipo Trasgo como Tragaldabas ya que el plomo aumenta las diferencias entre muones y electrones para una mejor identificación. Otra tarea, el estudio fenomenológico de cascadas atmosféricas que implica el uso del programa de generación de eventos simulados con Corsika. El estudio nos permite trabajar con partículas secundarias procedentes de cascadas atmosféricas generadas por rayos cósmicos primarios de diferentes masa dentro de un intervalo en energía cinética de $[10^9, 10^{15}]$ eV y con diferentes ángulos de incidencia de los núcleos en la atmósfera. El estudio permite estimar las propiedades del rayo cósmico primario (masa, energía y ángulo de incidencia sobre la capa alta de la atmósfera) por medio del análisis de secundarios a nivel del suelo usando observables físicos tales que la densidad lateral y parámetros relacionado con el estudio de agrupamiento de secundarios a nivel el suelo. Lo ideal para un estudio de este tipo, sería usar una instalación de varios detectores que cubre una amplia superficie de acción como por ejemplo, parte del campus sur de la USC. La estimación de una superficie de acción también se realizó en este trabajo por medio de los resultados 3D de agrupamiento de muones.

A continuación, se presentan y resumen las secciones más importantes del trabajo. La

primera sección se comenta los aspectos más relevantes de los rayos cósmicos, la segunda sección se plasma los cambios realizados en la geometría del detector implementados en el programa EnsarRoot y los resultados al estudio de los observables físicos realizado sobre un sistema a 4 planos RPC. En la tercera sección se resaltan los resultados más importantes hallados en el estudio de identificación de partículas con Tragaldabas. La última sección recoge y comenta los resultados más importantes del estudio de secundarios a nivel del suelo aplicado a un detector de tipo Trasgo, localizado tanto en la Universidad de Santiago de Compostela como en la Base Antártica Española.

Rayos Cósmicos

Victor Franz Hess encontró evidencias de una radiación cósmica de partículas que llegaban a nivel suelo terrestre, y años más tarde obtuvo el premio nobel de Física por el descubrimiento de los rayos cósmicos. Los rayos cósmicos son de origen solar, galácticos o extragalácticos, producidos en estrellas como el Sol, supernovas u otras fuentes extragalácticas como agujeros negros, enanas blancas y estrellas de neutrones. Los rayos cósmicos primarios (e.j núcleos) recorren largas distancias y se ven influenciadas por campos magnéticos y en menor medida por los campos gravitatorios (si estos no son agujeros negros) hasta llegar a nuestro sistema solar. Primarios cargados se ven desviados por los campos magnéticos generados por el sol y por el campo magnético terrestre. Algunas partículas cósmicas cargadas se ven atrapadas por trampas magnéticas si su velocidad no es lo suficientemente altas o simplemente desviadas sin interaccionar con la Tierra. Si tienen la suficiente energía cinética como para escapar al campo magnético terrestre, interaccionarán con la atmósfera de la Tierra generando una cascada atmosférica (*Extensive Air Shower*). Se pueden diferenciar varias partes de una cascada atmosférica: la primera interacción del cósmico con la parte alta de la atmósfera, el núcleo o *core* de la cascada y las diferentes componentes que la forman (hadrónica, electromagnética, muónica y nucleónica). Las partículas, productos de las sucesivas interacciones, llegan a nivel del suelo (muones, neutrones, electrones, fotones y en menor medida piones o kaones) o simplemente atraviesan la Tierra (neutrinos).

Los parámetros importantes que caracterizan una cascada atmosférica son la masa del primario, su energía y el ángulo de incidencia sobre la capa alta de la atmósfera. Dado que estos parámetros son de dificil acceso en los experimentos reales, se parte de observables físicos medibles experimentalmente como por ejemplo la longitud máxima de la cascada (*maximum depth of the shower*). Este es el trabajo realizado por los grandes experimentos de rayos cósmicos como Pierre Auguer situado en la Pampa (Argentina) o Telescope array situado en Utah (EEUU), entre otros. Estos experimentos usan la atmósfera como un gran calorímetro para medir las propiedades de los secundarios que llegan a la superficie terrestre y conocer las caracteristicas de la partícula primaria. Eso mismo se intenta hacer en este trabajo por medio de simulaciones, estimar las características del cósmico primario por medio de la respuesta del detector, el estudio de densidad lateral y un estudio fenomenológico de agrupamiento de secundarios o *clusters* a nivel del suelo, y, conocer la

naturaleza de los primarios con un detector o un conjunto de detectores de tipo Trasgo.

Geometría del detector Tragaldabas y resultados obtenidos con los observables físicos

Esta sección resume los resultados más importantes obtenidos sobre las propiedades físicas dadas por el detector Tragaldabas con eventos simulados y, geometrías y generadores de eventos realizados e implementados dentro del entorno de simulación EnsarRoot.

La Figura 1 muestra un evento en el que un electrón atraviesa el edificio de la Facultad de Física y el detector Tragaldabas en una configuración de 4 planos activos. El electrón con energía cinética de entorno 1 GeV interacciona con el suelo de la segunda planta del edificio generando un *jet* de partículas que interacciona con el detector. A saber que los programas usados para el análisis de datos del estudio de observables como el de chi-cuadrado, no se implemento para multiplicidades mayores de 1. De hecho, la condición de *trigger* impone un análisis de una sola traza.

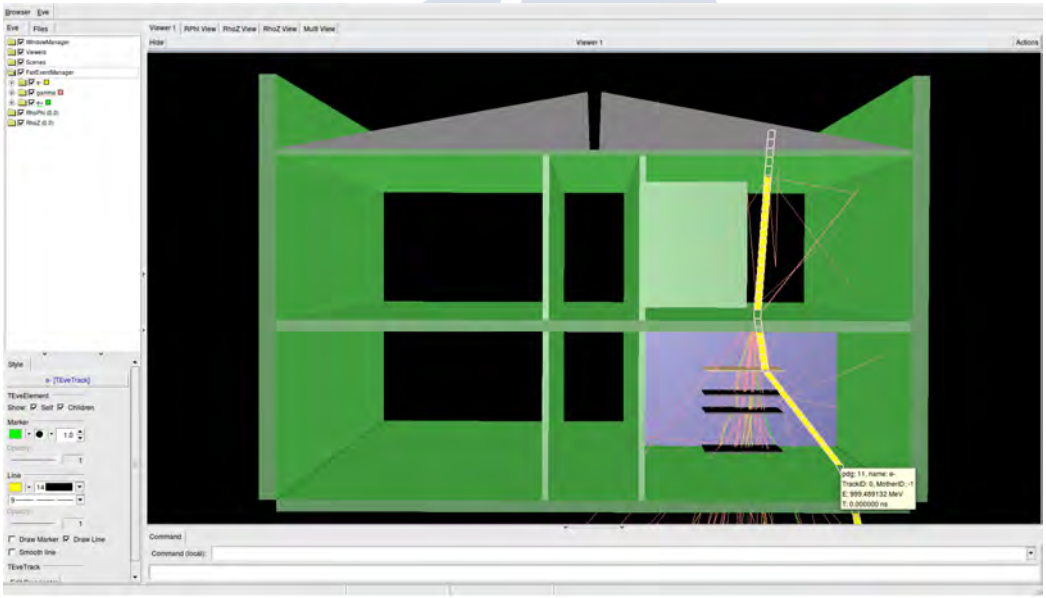

Figure 1: Simulación de un electrón cósmico con una energía aproximada de 1 GeV en interacción con los medios materiales del edificio de la Facultad de Física, donde un *jet* de partículas es emitido hacia el sistema Tragaldabas a 4 planos RPC.

Un fotón de alta energía (777 MeV) interacciona con el sistema Tragaldabas a 4 planos y con una lámina de plomo de 1.5 cm se muestra en la Figura 2. El fotón atraviesa los 3 primeros planos e interacciona con la lámina de plomo generandose un *jet* de partículas.

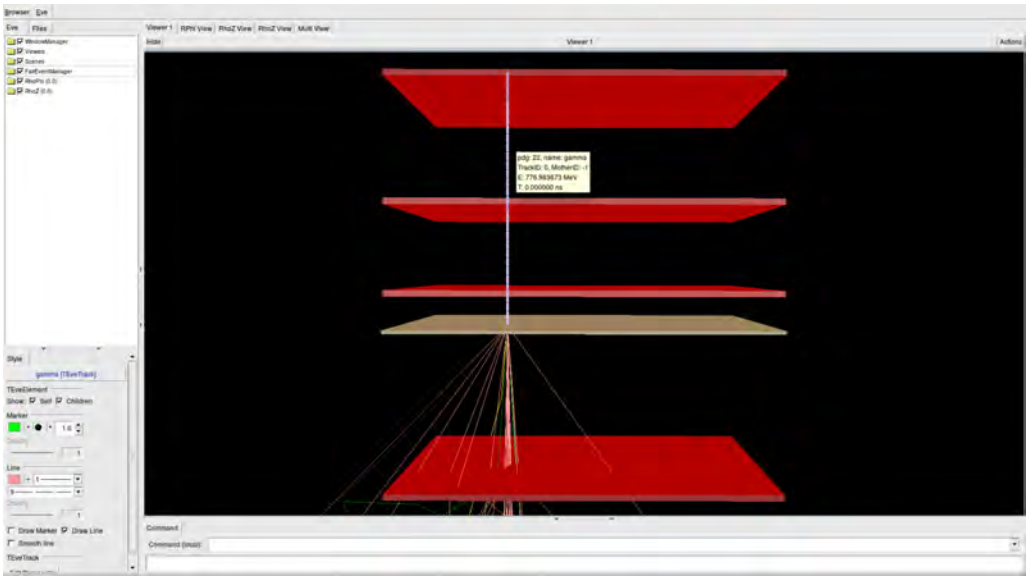

Figure 2: Simulación con EnsarRoot de un fotón cósmico de 777 MeV de energía sobre un sistema Tragaldabas a 4 planos con una lámina de plomo de 1.5 cm, donde el fotón cruza los 3 primeros planos hasta interaccionar con el tercer plano y formar un *jet* de partículas.

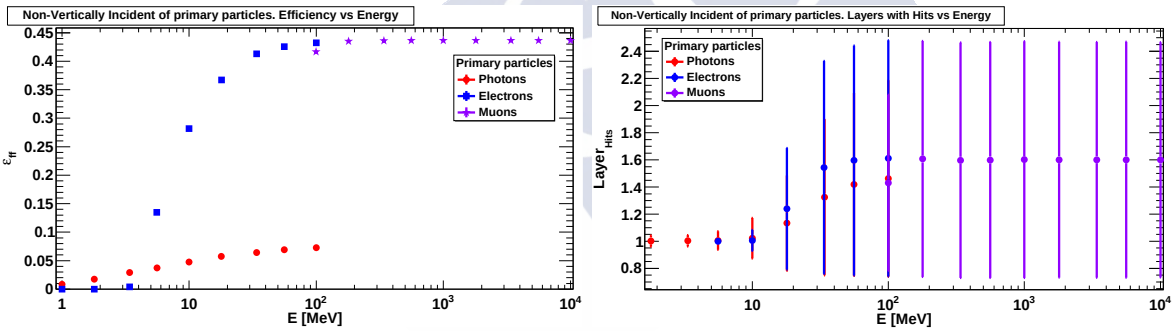

(a) (b)

Figure 3: Resultados del análisis de 100k cósmicos primarios con incidencia completamente aleatoria sobre un sistema Tragaldabas a 4 planos RPC, donde la gráfica (a) es de eficiencia efectiva y la gráfica (b) es de planos con *hits*. Los fotones a 100 MeV han dado 10 veces menos señal en el detector que electrones o muones a la misma energía, la probabilidad de detectar electrones es del 5% mientras que es de aproximadamente 45% para muones y electrones a esa energía de 100 MeV. La mayoría de partículas llegan al segundo plano a energías por encima de 100 MeV con M≈2, donde las incertidumbres son grandes y mayores que la unidad.

La Figura 3 muestra la eficiencia de detección para eventos con incidencia totalmente aleatoria sobre un sistema Tragaldabas a 4 planos activos, y el número medio de planos con señal. Los resultados dicen que la eficiencia de detección de electrones es máxima a partir de unos 100 MeV y para muones es de aproximadamente 45%, la eficiencia para fotones a 100 MeV es de aproximadamente 5%, una diferencia de un factor 10 con respecto a electrones y muones a la misma energía. La cascada electromagnética llega como máximo hasta el segundo plano para electrones y fotones a unos 100 MeV y para muones en todo

su intervalo en energías de trabajo. A tener en cuenta que, las incertidumbres de los valores estimados de plano con *hits* son grandes, mayor de 1 unidad.

La Figura 4 muestra los mapas de aceptancia geométrica obtenida para Tragaldabas. Estos representan la acumulación de trazas en linea recta por *pad* para los diferentes sitemas de detección Tragaldabas a plano/s 1, 1-2, 1-2-3 y 1-2-3-4 respectivamente. Estos resultados son muy importantes debido a que nos proporcionan la corrección a tasas reales colectada por el detector Tragaldabas.

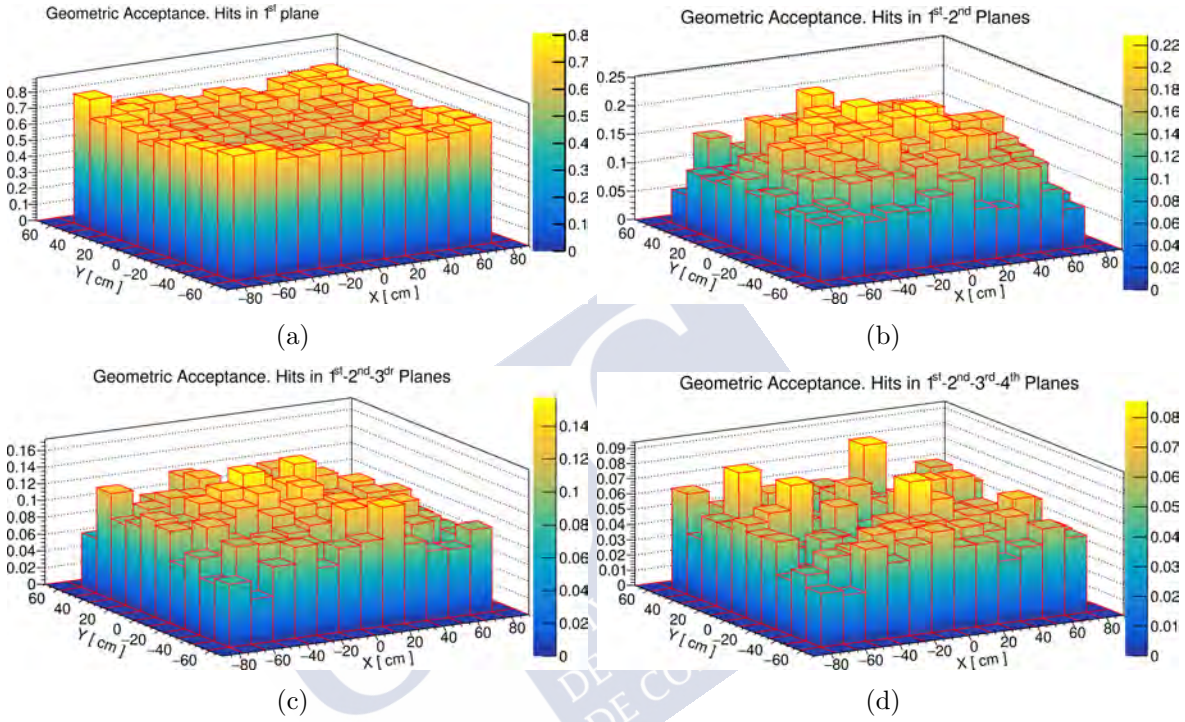

Figure 4: Mapas de aceptancia geométrica de un sistema Tragaldabas a 1 (a), 2 (b), 3 (c) y 4 (d) planos RPC. Las trazas en linea recta se acumulan en los bordes y vertices del plano en el histograma (a), las trazas se acumulan en el centro del sistema en el histograma (b), algo similar ocurre en el histograma (c) pero con menor intensidad que en el caso anterior y la acumulación de trazas es homogénea en el sistema a 4 planos del histograma (d). Los resultados sirven para realizar correcciones a la tasa de partículas colectadas por el detector Tragaldabas, estos muestran la corrección para cada celda RPC.

Identificación de partículas con Tragaldabas

En esta sección se detalla la concepción de un algoritmo de identifiación de partículas muónica o electrónica con diferentes configuraciones del detector Tragaldabas. Por medio de simulaciones, se han analizado tres observables físicos de multiplicidad total, alcance ponderado y χ^2 de la reconstrucción de trayectorias, para así, desarrollar un método que fenomenológicamente consiga diferenciar la naturaleza de distintas partículas, principalmente muones y electrones. A continuación se expone y comentan los resultados.

La Figura 5 muestra los histogramas de multiplicidad total y χ^2 tanto para electrones como muones. Se observa que la separación entre estos conjuntos de datos es grande, se puede distinguir un electrón de un muón en un valor de M=5 y de $\chi^2 \approx 9$. Por encima de M=5 (o $\chi^2 \approx 9$), seguro que se detecta un electrón, y por dbajo de este valor, se puede detectar un electrón o un muón. Algunos valores se pueden distinguir a una multiplicidad próxima de 2.

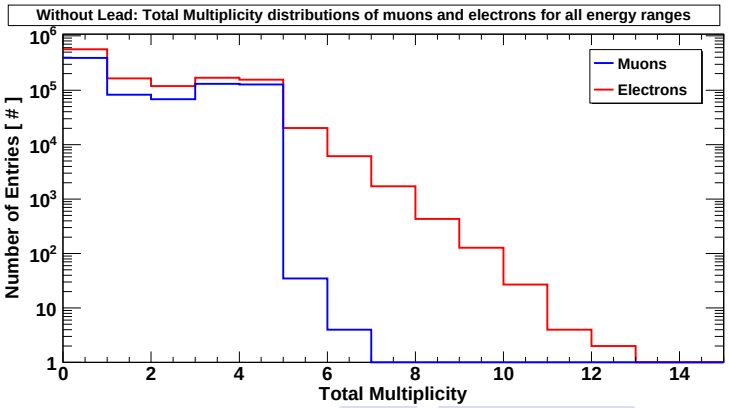

(a)

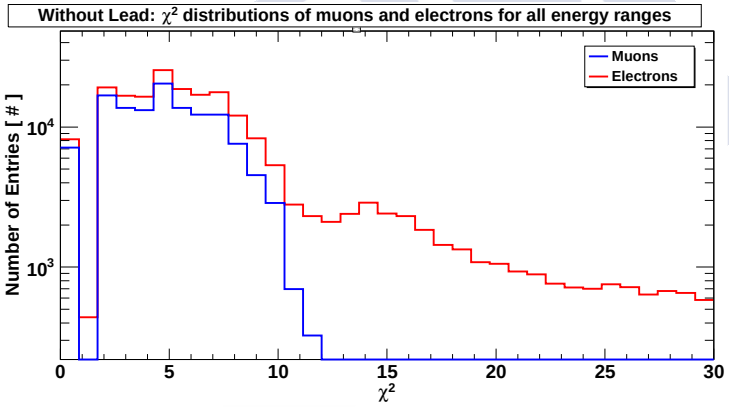

(b)

Figure 5: Resultados multiplicidad total (a) y χ^2 (b) al estudio de identificación de electrones y muones con un sistema a 4 planos. Los resultados muestran las grandes diferencias existentes entre un tipo de partículas y otras, un valor de distincción entre electrones y muones es de M=2 y M=5, y, $\chi^2 \approx 9$.

El algoritmo 6 muestra el diagrama de flujos para un sistema de 4 planos RPC activos del detector. En este diagrama se especifican los valores de los observables con mayor diferencia entre muones y electrones. El diagrama proporciona la naturaleza de la partícula, la probabilidad asociada, una energía mínima y su probabilidad asociada. A saber que el máximo de energía trabajado con estas partículas es de 5 GeV.

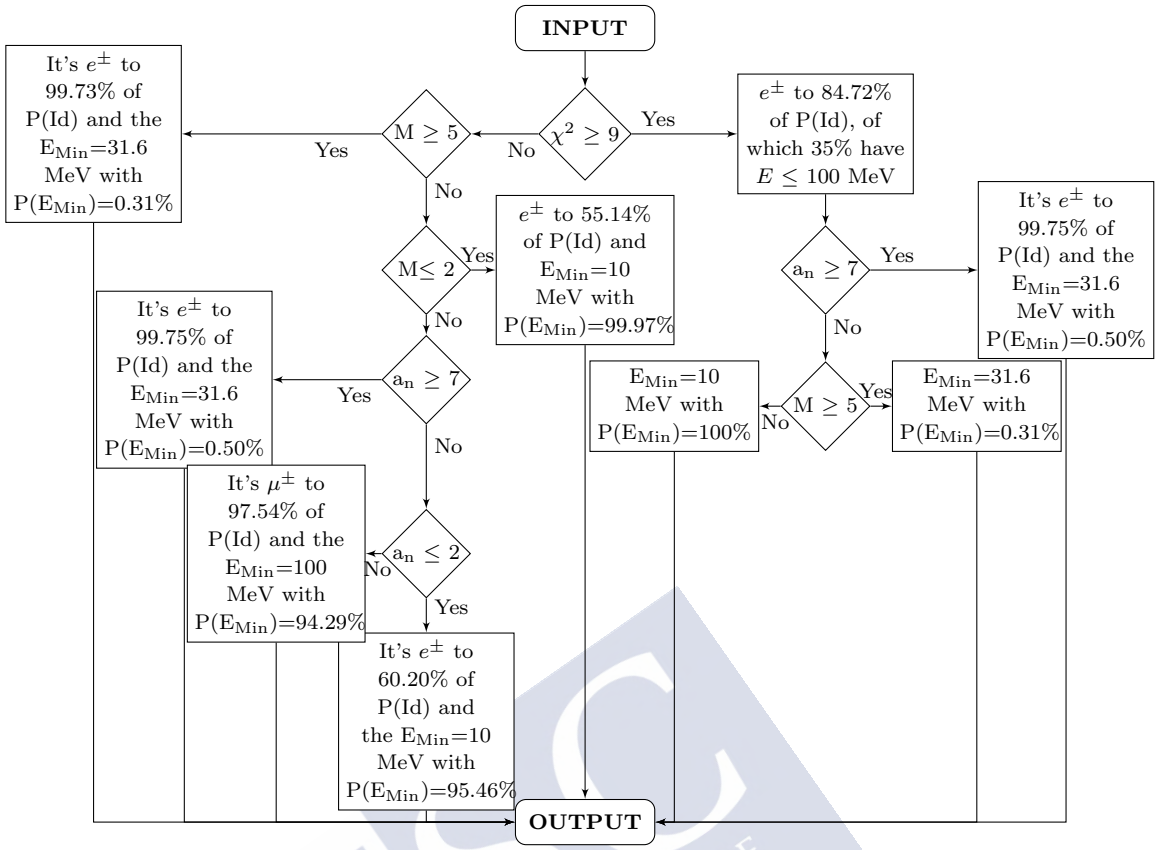

Figure 6: Diagrama de flujo para la identificación de partículas con un sistema Tragaldabas a 4 planos RPC activos. El diagrama muestra todos los pasos condicionales a cumplir, la naturaleza de la partícula (e/μ) y su probabilidad asociada, y, la energía mínima y su probabilidad asociada.

La Tabla 1 muestra los resultados de probabilidad de aciertos para los sistemas a 3 y 4 planos activos RPC. Los resultados se obtuvieron con 1 millón de datos simulados tanto con un programa simulación realista y sencillo implementado en EnsarRoot por medio de datos simulados Cry. En el caso de una simulación simple la probabilidad de aciertos es del 99% y en el caso de una simulación realista los acietos son aproximadamente 90%.

Table 1: **Resultados de aciertos en [%] para un sistema Tragaldabas a 3 y 4 planos RPC. Los aciertos son cercanos al 99% para una simulación simple y de aproximadamente el 90% para una simulación realista del detector en el interior del edificio de la Facultad de Física.**

Planos activos	Simulación realista	Simulación simple
4	87.9 ± 1.5	99.3 ± 0.2
3	90.2 ± 1.4	99.3 ± 0.2

La probabilidad de fallos en la identificación de partículas se muestra a la Tabla 2 para los dos sistemas mencionados con anterioridad. Los fallos más notables se dan en electrones generados e identificación de muones (∼70%) y de fotones generados e identificación de electrones (∼20%) por el diagrama código. Se supone que ello se darán en partículas

iniciales de muy alta energía ya que los casos presentan multiplicidad de 4 y alcance ponderado de a_n=6).

Table 2: **Eventos a identificaciones erróneas realizadas por el código en tanto por cien para un sistema Tragaldabas a 3 y 4 planos activos. La flecha señala la partícula erróneamente identificada por el código descrita como b generada por una partícula a ($a \rightarrow b$). Los casos de alta identificación errónea son electrones o gamma identificados respectivamente como muones o electrones, esto se debe a que las partículas iniciales eran de muy alta energía cinética haciendo que los observables tengan valores similares al de partículas identificadas erróneamente (M=4 o a_n=6).**

	Identificación errónea				
Planos activos	e $\rightarrow \mu$	$\gamma \rightarrow \mu$	$\gamma \rightarrow$ e	p $\rightarrow$ e	p $\rightarrow \mu$
4	68.5	0.3	20.6	9.4	1.1
3	66.7	0.8	20.6	11	0.8

Estructura de cascadas atmosféricas a nivel del suelo

En esta sección se presentan y exponen los resultados relevantes del estudio fenomenológico de cascadas atmosféricas hecha con el programa de simulación Corsika. Este trabajo de estudio necesita de la instalación de un gran conjunto de detectores de tipo Trasgo y de varias pruebas para poder realizar un trabajo de estudio de altas eficiencia de las propiedades de los rayos cósmicos primarios: masa, energía y ángulo cenital. También es necesario de una correcta selección de observables físicos para un estudio físico completo.

En este trabajo se especifica resultados fiables del estudio realizado en la USC de respuesta de un detector de tipo Trasgo para electrones/muones y para diferentes cósmicos primarios (H, He, C y Fe), y de resultados preliminares para la estimación de una superficie de acción de detección de datos, energía del primario y número de cuentas tanto de electrones y muones por *cluster* entre otros.

La Figura 7 muestra las distribuciones de función respuesta de diferentes primarios tanto para muones como electrones para nuestros 4 núcleos a diferentes intervalos de ángulo de incidencia cenital de primarios estudiados en la USC. Los resultados muestran una diferencia en intensidad de respuesta entre electrones y muones de un factor 10 aproximadamente y las medias de las distribuciones de ambos secundarios son muy parecidos entre ellos. Las diferencias entre protones y helios son muy pequeñas. Las medias de las ditribuciones son de aproximadamente 20 GeV/nucleón para protones, 30 GeV/nucleón para núcleos de He, 40 GeV/nucleón para C y 100 GeV/nucleón para nucleos de Fe. Se esperaría que la media de las distribuciones aumentaran a medida que crece el intervalo angular, ello es debido a que a mayor ángulo de incidencia la primera interacción se da a mas alta altitud y mayor debe ser la energía del primario para generar secundarios a nivel del suelo. Las distribuciones son algo oscilantes a medida que aumenta el intervalo angular, en el caso de respuesta de muones para H primarios.

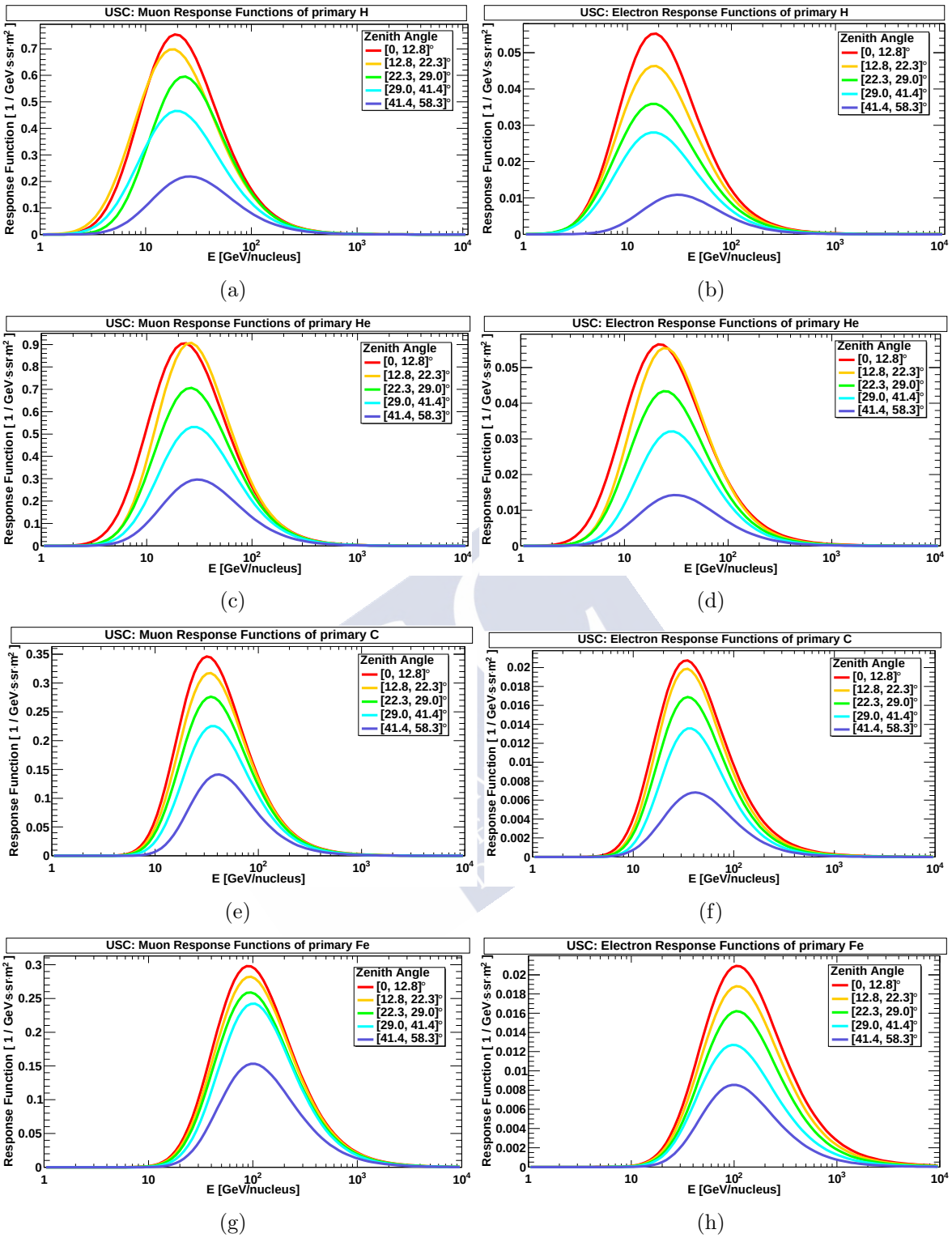

Figure 7: Resultados de función respuesta tanto de muones como electrones para diferentes ángulos de incidencia de primarios tales que H (a), He (b), C (c) y Fe (d).

La Figura 8 presenta los gráficos 3D de muones generados por los 4 núcleos estudiados con incidencia vertical ($[0, 12'8]°$). Los histogramas muestran el número de muones por *cluster* en función de la energía del primario [GeV] y el radio del centro de los *cluster* al centro

geométrico de la cascada [m] para un corte en 10 metros (datos cerca del core de la EAS). Los resultados muestran una distribución de muones/*cluster*, la distribución de muones aumenta a medida que la masa del núcleo crece. Los máximos de las distribuciones y el radio de estos puntos se muestran en la Tabla 3, estan asociados a la energía de 10^6 GeV. La tendencia es muy clara, el máximo de la distribución crece tanto en número de muones/*cluster* como en radio.

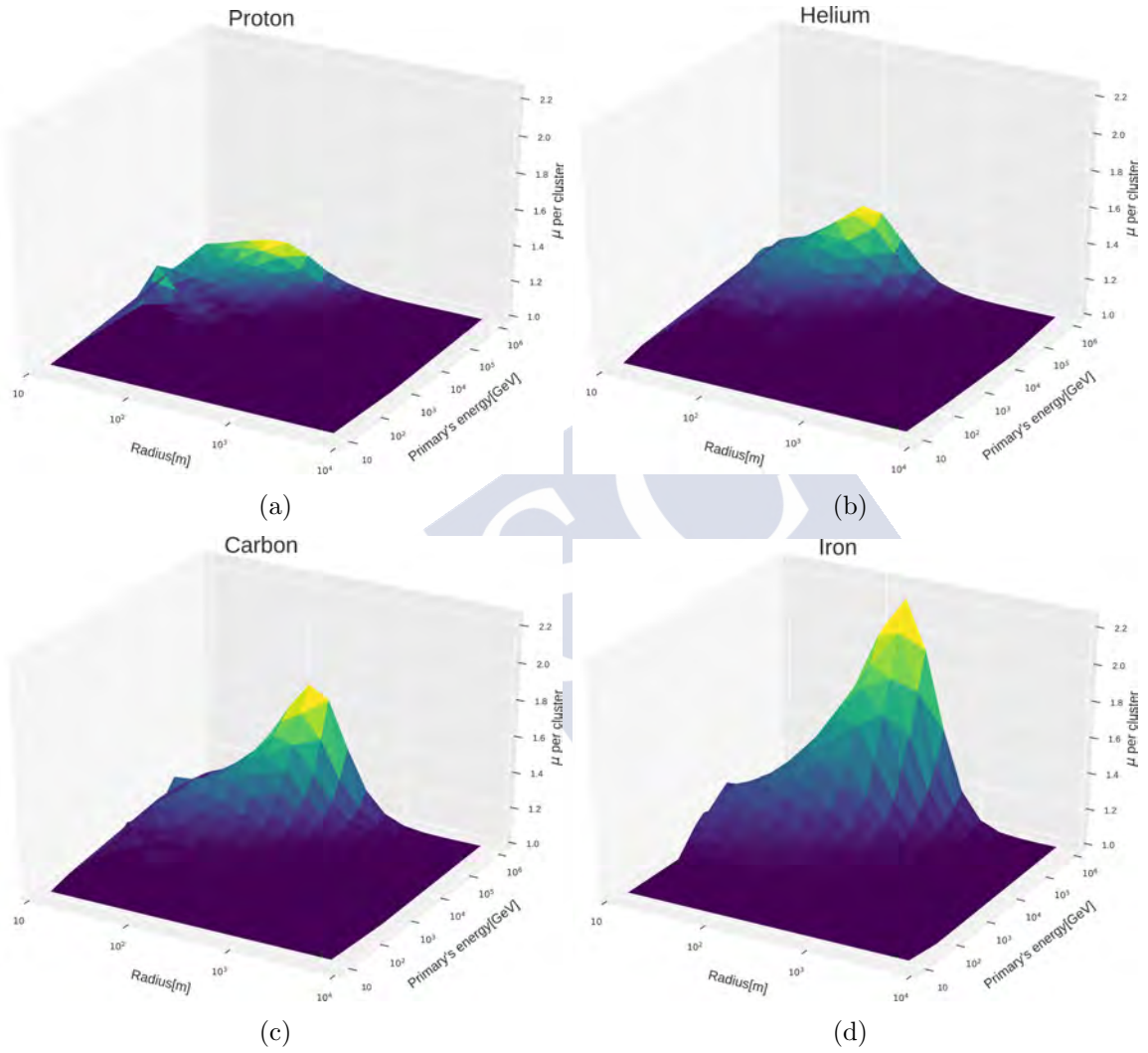

Figure 8: Gráficas 3D para *clusters* muónicos que presentan el número de muones por *cluster* en función de la energía del primario y radio de *clusters* al centro geométrico de la cascada procedente de diferentes primarios tales que H (a), He (b), C (c) y Fe (d).

Table 3: **Máximo de las distribuciones en superficie de muones. Los máximos de las distribuciones aumentan considerablemente a medida que la masa del primario y el radio al centro de la cascada aumenta.**

Cósmico primario	H	He	C	Fe
μ tamaño del *cluster*	1.2	1.4	1.7	2.2
Radio máximo [m]	80	81	128	203

USC
UNIVERSIDADE
DE SANTIAGO
DE COMPOSTELA

Bibliography

[1] Peter K.F. Grieder, *Cosmic Rays At Earth*, Elseiver (2001), p. 21-28.

[2] D. Belver *et al.*, *TRASGO: A proposal for a timing RPCs based detector for analyzing cosmic ray air showers*, Nucl.Inst.Meth. A, **661** (2012) S163-S167.

[3] H. Álvarez-Pol *et al.*, *Tragaldabas: A new high resolution detector for the regular study of cosmic rays*, J.Phys.:Conf.Ser. **632** (2015), no. 1, 012010

[4] V.J Martínez Pérez, *Astronomia fundamental*, Publicacions Universitat de Valéncia (2005), p. 194-204.

[5] Claus Grupen, *Astroparticle Physics*, springer (2005), p. 63-76.

[6] T. Wulf *Beobachtungen über die Strahlung hoher Durchdringungsfähigkeit auf dem Eiffelturm*, Physikalische Zeitschrift, 11 (1910), p.811-813.

[7] D. Pacini *La radiazione penetrante alla superficie ed in seno alle acque*, Il Nuovo Cimento, 3 **93** (1912).

[8] V.F. Hess *Über Beobachtungen der durchdringenden Strahlung bei sieben Freiballonfahrten*, Physikalische Zeitschrift **13** (1912), p.1084–1091.

[9] Peter Maria Schuster, *The scientific life of Victor Franz (Francis) Hess (June 24, 1883–December 17, 1964)*, Astroparticle Physics, **53** (January 2014), p.33-49.

[10] E.N. Parker, *Dynamics of the Interplanetary Gas and Magnetic Fields*, Astrophysical Journal, 2 **128** (1958), p.664.

[11] C. Pei *et al.*, *THREE-DIMENSIONAL WAVY HELIOSPHERIC CURRENT SHEET DRIFTS*, The Astrophysical Journal, 2 **744** (January 2012), p.170.

[12] E.N. Parker, *Cosmic-ray Modulation by Solar Wind*, Rev. 110 (1958), p. 1445-1449.

[13] M. Walt *Introduction to Geomagnetically Trapped Radiation*, Cambridge Atmospheric and Space Science Series (2005), p. 10-23.

[14] *Radiation Protection Considerations*, Journal of the International Commission on Radiation Units and Measurements, 2, 10 (2016), p.13-15.

[15] J.A. Garzón *TRAGALDABAS. First results on cosmic ray studies and their relation with the solar activity, the Earth's magnetic field and the atmospheric properties*, XXV European Cosmic Ray Symposium, Turin (2016).

[16] M. Tanabashi *et al.*, *(Particle Data Group)*, Phys. Rev. D 98, 030001 (2018), p. 424-432, 446-460.

[17] K. Greisen, *End to the Cosmic-Ray Spectrum?*, Physical Review Letters. 16 **17** (1966), p.748–750.

[18] G. T. Zatsepin and V. A Kuzḿin *Upper Limit of the Spectrum of Cosmic Rays*, Journal of Experimental and Theoretical Physics Letters 4 (1966), p.78–80.

[19] Aartsen *et al.* (IceCube Collaboration), *Neutrino emission from the direction of the blazar TXS 0506+056 prior to the IceCube-170922A alert*, Science, 361, 6398 (2018), p.147-151.

[20] S. Chandrasekhar, *The highly collapsed configurations of a stellar mass*, Monthly Notices of the Royal Astronomical Society, Vol. 95, p.207-225 (1935).

[21] A.M Hillas, *The origin of ultra-high-energy cosmic rays*, Ann. Rev. Atron: Astrophys, 22 (1984), 425-44.

[22] Federico Fraschetti, *On the acceleration of Ultra-High-Energy Cosmic Rays*, arXiv:0809.3057, Phil. Trans. R. Soc. A, 366 (2008).

[23] P.A.M Dirac, *Principles of Quantum Mechanics*, International Series of Monographs on Physics (4th ed.). Oxford University Press. p. 255. ISBN 978-0-19-852011-5 (1988).

[24] W. Pauli, *Liebe Radioaktive Damen and Herren*,Physikalisches Institut (1930).

[25] A. Pich, *Flavour Physics and CP Violation*, IFIC. University of València-CSIC.Spain , $arXiv$: 1112.4094v1 , p. 1-2 (2011).

[26] Paul Langacker, *The Standard Model and Beyond* , *CRC* Press Taylor & Francis Group , p. 453-468/475/508-526 (2010).

[27] T. Aoyama *et al.*, *Revised value of the eighth-order QED contribution to the anomalous magnetic moment of the electron*, Phys. Rev. D77:053012 (2008).

[28] D. B. Chitwood *et al.* (MuLan Collaboration), *Improved Measurement of the Positive-Muon Lifetime and Determination of the Fermi Constant*, Phys. Rev. Lett. 99.032001, 3, (2007).

[29] A. Pich, *Review of α_s determinations*, Proceedings of Science , p. 1-12 (2012).

[30] C. Rovelli, *Notes for a brief history of quantum gravity*, 9th Marcel Grossmann Meeting en Roma. p. p.5. $arXiv : gr - qc/0006061v3$.

[31] S. W Hawking and W. Israel, *Three Hundred Years of Gravitation*, Cambridge Unversity Press. ISBN 978-0-521-37976-2 (1989).

[32] *LIGO Scientific Collaboration and Virgo Collaboration*, *Observation of Gravitational Waves from a Binary Black Hole Merger*. Phys. Rev. Lett. 116 (6):061102 (2016), $arXiv$: 1602.03837.

[33] A. Pich, *The Standard Model of Electroweak Interactions*, IFIC. University of València-CSIC.Spain, $arXiv$: 1201.0537v1, p. 8-11, 20-24, 43-44 (2012).

[34] J. Matthews, *A Heitler model of extensive air showers*, Astroparticle Physics, 22 (2005), p. 387–397.

[35] Peter K.F. Grieder, *Extensive Air Showers*, Springer, vol. 1, (2010), p. 5, p.21, p.198-200, p. 648-650.

[36] A. Pacini, *Cosmic rays: Bringing messages from the sky to the Earth's surface*, Revista Brasileira de Ensino de Física. 39. 10.1590/1806-9126-RBEF-2016-0168 (2017).

[37] k. Greisen, *Cosmic ray showers*, Ann.Rev.Nucl.Part.Sci., 10 (1960) p. 63-108.

[38] J. Linsley, *Mini and super mini arrays for the study of highest enregy cosmic rays*, Proceedings 19th ICRC, 434 (1985).

[39] P. Bassi *et al.*, *Distribution of Arrival Times of Air Shower Particles*, Phys. Rev. **92**, 441, (1953).

[40] T. Hara *et al.*, *Characteristics of large Air Showers at ore distances between 1km and 2km*, 11 (1983) 276.

[41] J. Linsley *et al.*, *Extremely Energetic Cosmic-Ray Event*, Phys. Rev. Lett. 6, 9, p. 485-487 (1961).

[42] J. Linsley *et al.*, *Cosmic-Ray Composition at* 10^{17}-10^{18} *eV*, Phys. Rev. Lett. 9, 3, p. 123-125 (1962).

[43] J. Linsley *et al.*, *Arrival Times of Air Shower Particles at Large Distances from the Axis*, Phys. Rev. 128, 5, p. 2384-2392 (1962).

[44] A.J. Baxter, PR A2, (1969), 5.

[45] A.A. Watson *et al.*, *Fluctuation studies of large air showers: the composition of primary cosmic ray particles of energy Ep∼1018eV*, Journal of Physics A: Mathematical, Nuclear and General, 7, 10, p. 1199-1212 (1974).

[46] J. Linsley *et al.*, *The longitudinal particle distribution in the extensive air shower disc*, J. Phys. A: Math. Gen., 8, 6 (1975).

[47] K. Kamata and J. Nishimura, *The Lateral and the Angular Structure Functions of Electron Showers*, Progress of Theoretical Physics Supplement 6 (1958), p. 93–155.

[48] J. Linsley, *Angular resolution of air shower array-telescope*, ICRC (1985), 3, p. 461-464.

[49] T. Bezboruah, *A non conventional method of UHE cosmic ray detection*, Astroparticle Physics, 11 (1999), p. 395-402.

[50] M.V.S Rao *et al.*, *Extensive Air Showers*, World Scientific, (1998), p. 26-29, 117-118.

[51] http://www-hades.gsi.de

[52] D. Belver *et al.*, *The HADES RPC inner TOF wall*, Nucl. Instr. and Meth. A, 602 (2009) 687.

[53] D. Belver *et al.*, *Analysis of the space-time microstructure of cosmic ray air showers using the HADES RPC TOF wall*, JINST 7-10 (2012).

[54] Marcello Abbrescia *et al.*, *Resistive Gaseous Detectors. Designs, Performance, and Perspectives*, Wiley-VCH (2018), p. 193-201.

[55] R. Santonico et *et al.*, *Development of resistive plate counters*, Nucl.Instr. and Meth: A 187 (1981), p. 377-380.

[56] M.V. Babykin *et al.*, *Plane-parallel spark counters for the measurement of small times; resolving time of spark counters*, Sov. J. At. Energy, 4 (1956), 627.

[57] V.V Parkhomchuk *et al.*, *A spark counter with large area*, Nucl. Instrum. Methods, **93** (1971), 2, p. 269–270.

[58] P. Fonte *et al.*, *High resolution RPCs for large TOF systems*, Nucl. Instrum. Methods Phys. Res., Sect. A, 449 (2000), 295.

[59] G. Aad *et al.* (ATLAS Collaboration), *The ATLAS Experiment at the CERN Large Hadron Collider*, Institute of Physics publishing and sissa, $Jinst8 - 08 - s08003$, p. 1-18 (2008).

[60] K.Aamodt *et al.* (ALICE Collaboration), *The ALICE experiment at the CERN LHC*, Institute of Physics publishing and sissa, $JINST$-3-$S08002$, p. 1-8 (2008).

[61] *The HADES Collaboration*, Journal of Physics G: Nuclear and Particle Physics, 37, 9:099802 (2009).

[62] Glenn E. Knoll, *Radiation Detection and Measurement*, Wiley, New York (1979), p. p. 159-160, 169-184.

[63] J.S. Townsend, *The conductivity produced in gases by the motion of negatively charged ions*, Phil. Mag. 6-1 (1901) 198-227.

[64] D. Belver, *The front-end electronics of the HADES timing RPCs wall, design, development and performances analysis*, (2010) PhD thesis, Universidad de Santiago de Compostela, Departamento de Física de Partículas.

[65] I. Fröhlich *et al.*, *A General Purpose Trigger and Readout Board for HADES and FAIR-experiments*, IEEE Trans. Nucl. Sci. **55** 59 (2008).

[66] https://hades-wiki.gsi.de/foswiki/bin/view/DaqSlowControl/RpcDataStructure.

[67] J.J. Cuenca García, *Simulation and recontruction algorithms for a commercial muon temography system*, PhD thesis, Universidad de Santiago de Compostela, Departamento de Física de partículas (2018).

[68] N. Metropolis, *The Beginning of the Monte Carlo Method*, Phil. Mag. 6-1 (1901), p. 198-227.

[69] N. Metropolis et S. Ulam, *The Monte Carlo Method*, Journal of the American Statistical Association, 44, 247 (1949), p. 335-341.

[70] D. Frenkel et B. Smit, *Understanding Molecular Simulation*, Academic Press 2002 (2001).

[71] B.W. Kernighan, *A programming language called C: The C programming language is claimed to be compact, efficient, and expressive, to the point of supplanting assembly language on Unix. Potentials* (1983), IEEE. 2. 26-30. 10.1109/MP.1983.6499601.

[72] B. Stroustrup, *The C++ Programming Language*, fourth edition, Addison-Wesley (2013).

[73] S. Agostinelli *et al.*, *GEANT4- A Simulation Toolkit*, Nucl. Instrum. Meth. A 506 (2003) 250-303.

[74] R. Brun et F. Rademakers, *ROOT-An object oriented data analysis framework*, Nuclear Instruments and Methods in Physics Research Section A: Accelerators, Spectrometers, Detectors and Associated Equipment, 389(1):81–86 (1997).

[75] D. Bertini *et al.*, *The fair simulation and analysis framework*, Journal of Physics: Conference Series, 119(3):032011, 2008.

[76] P. Cabanelas *et al.* (SATNuRSE workpackage of ENSAR2), *TEnsarRoot: The framework for simulation and data analysis for ENSAR.*,Journal of Physics: Conference Series, 1024(1):012038, 2018.

[77] http://www.ensarfp7.eu/

[78] J.A. Garzón and P. Cabanelas, *TimTrack: A matrix formalism for a fast time and track reconstruction with timing detectors*, Nucl.Inst.Meth.Phys.Res. A, **661** (2012) S210-S213.

[79] I.M. Dremin *et al.*, *Central and peripheral interactions of hadrons*, V.A. & White, S.N. Eur. Phys. J. C (2017) 77: 910.

[80] D. Heck *et al.*, Report FZKA 6019 (1998). Forschungszentrum Karlsruhe GmbH. http://www-ik.fzk.de/corsika/physics description/corsika phy.html.

[81] N.N. Kalmykov *et al.*, *he Nucleus-nucleus interaction, nuclear fragmentation, and fluctuations of extensive air showers*, Phys. Atom. Nucl. 56 (1993), p.346-353.

[82] J. Ranft, *New features in DPMJET version II.5*, Phys. Rev. D51 (1999) 64, arXiv:hep-ph/9911213.

[83] R. S. Fletcher *et al.*, *sibyll: An event generator for simulation of high energy cosmic ray cascades*, Phys. Rev. D 50, 5710.

[84] A. Ferrari *et al.*, *FLUKA: a multi-particle transport code*, CERN 2005-10 (2005), INFN/TC 05/11, SLAC-R-773.

[85] S. A. Bass *et al.*, *Charge Fluctuations in pp and AA Collisions at RHIC and LHC Energies*, Prog.part.Nucl.Phys. 41, 225 (1998).

[86] F. Schmidt, J. Knapp, *CORSIKA Shower Images* (2005) https://www-zeuthen.desy.de/ jknapp/fs/showerimages.html .

[87] C. Hagmaann *et al.*, *Cosmic-Ray Shower Generator (CRY) for Monte Carlo Transport Codes*, IEEE Nuclear Science Symposium Conference Record, 2007.

[88] Y. Fontenla *et al.*, *MIDAS: A particle identification tool for the Tragaldabas Cosmic Ray telescope*, PoS and sissa 358, 72 (2019).

[89] A. Alvaréz Díez *et al.*, *Study of the lateral distribution functions of electron and muon bundles using Trasgo detectors*, PoS and sissa 358, 67 (2019).

[90] D. García-Castro *et al.*, *The TRISTAN Antarctic Cosmic Ray detector*, Proceedings of this conference.

[91] Elena I Yakovleva *et al.*,*Coupling functions for muon hodoscopes* (2009), Bulletin of the Russian Academy of Sciences: Physics. 73. 10.3103/S106287380903023X.

[92] J.Espadanal, *3D simulation for Cherenkov emission in Extensive Air Showers*, LIP. $arXiv$: 1702.03276v1, p. 10 (2017).

[93] V. Rossum *et al.*,*Python tutorial* (1995), Centrum voor Wiskunde en Informatica Amsterdam, The Netherlands.

USC
UNIVERSIDADE
DE SANTIAGO
DE COMPOSTELA

USC
UNIVERSIDADE
DE SANTIAGO
DE COMPOSTELA

Appendix

Typography, footnote and legend color code

This section is intended to expose the information described or contained in the typeface, footnote and color code of histogram legends used in this work. The `typewrite` letter was used to write code command-lines and the **boldface** letter was used to separate methods, models and studies within the same section-subsection or paragraph. The boldface letter was also used to present vectors in the subsection 3.2.1 or the acronyms in the Appendix "Acronyms". Given the new rules for the development of thesis carried out by the University of Santiago, the boldface letter was also used in the Tables caption and section structure, the font size is smaller in the Figures and tables caption. Footnotes was used for definitions, reference of sub/sections and comments.

A color code was used to describe legends of a histogram according to the rainbow colors to present data of different energies or zenital angles in the same histogram. The range of colors used in the histogram legends was as follows: from range red colors for lower energy (or zenital angle) data to range blue colors for higher energy (or zenital angle) data.

Acronyms

AGN Active Galaxies Nucleus

BAE Base Antarctica Española

BR Branching Ratio

CKM Cabibbo-Kobayashi-Maskawa

CMB Cosmic Microwave Background

CME Coronal Mass Ejection

CORSIKA COsmic Ray SImulation KAscade

CR Cosmic Ray

CRY Cosmic-ray Shower Library

DBO Daughterboard

EAS Extensive Air Shower

e.m electromagnetic

FEE Front-End Electronic

FPGA Field-Programmable Gate Array

GCR Galactic Cosmic Rays

GRB Gamma Ray Burst

GSI Gesellschaft für Schwerionenforschung mbH

GZK Greisen-Zatsepin-Kuzmin cutoff

HADES High Acceptance Di-Electron Spectrometer

HCS Heliospheric Current Sheet

HV High Voltage

IMF interplanetary Magnetic Field

ISS International Space Station

KE Kinetic Energy

LDF Lateral Distribution Function

LSM Least Square Methods

MBO Motherboard

MC Monte Carlo Method

MEIGA Mini Ensemble for Identifying GAlactic radiation

MF Multiplicity Function

MIDAS Multisampling IDentificAtion Software

MPRC multiple-space RPC

NPL National Physical Laboratory

OOP Object-Oriented Programming

OS Operating Systems

PC Personal Computer

PCB Printed Circuit Board

PDF Probability Density Function

PID Particle IDentification

QCD Quantum Chromodynamics

QED Quantum Electroweak

RF Response Function

SNR Supernova Remnant

SPE Sun Proton Events

TOF Time of Flight

TRAGALDABAS TRAsGo for the AnaLysis of the nuvlear matter Decay; the Atmosphere; the earth B-FIeld And the Solar activity

TRB Trigger and Readout Board

TRISTAN TRAsgo para InveSTigaciones ANtárticas

USC Universidad de Santiago de Compostela

In order to facilitate reading the acronyms of names used in sentences are implemented.

Parametrization data sheets of LDF study

Table I: Parametrization data of LDF study for H nuclei for a distance range of [31.6, 1000] m

Proton: parameterization for the radial distribution study with a range distance core of [31.6, 1000] m						
Nevents	Primary energy	Parameter: values and errors				Chi2/ndf
		C	R0	alpha	beta	
50k	100 GeV	1.43E-06	3.39E+03	-0.2362	-9.451	4.12/8
		2.44E-07	1782	0.0228	4.34	
30k	178 GeV	4.75E-06	1.12E+03	-0.304	-4.546	0.9439/8
		2.90E-06	5.95E+02	0.1143	1.289	
30k	316 GeV	1.37E-05	631.1	-0.3183	-3.516	2.294/8
		5.96E-06	222.2	0.1155	0.4425	
30k	562 GeV	2.15E-05	6.07E+02	-0.4438	-3.414	3.881/8
		7.96E-06	1.68E+02	0.08902	0.3343	
10k	1000 GeV	3.29E-05	5.71E+02	-0.5545	-3.228	1.265/8
		1.75E-05	2.13E+02	0.118	0.4108	
10k	1780 GeV	5.48E-05	4.87E+02	-0.6432	-2.828	2.582/8
		2.65E-05	1.56E+02	0.1038	0.2618	
5k	316 GeV	6.63E-05	5.77E+02	-0.7341	-2.976	1.432/9
		2.83E-05	1.67E+02	0.07486	0.3221	
5k	5620 GeV	1.15E-04	5.48E+02	-0.7583	-2.884	2.812/9
		4.51E-05	1.45E+02	0.06776	0.276	
1k	10000 GeV	1.70E-04	5.74E+02	-0.7931	-2.917	1.27/9
		1.34E-04	3.04E+02	0.1274	0.585	
3k	17800 GeV	2.48E-04	6.36E+02	-0.8403	-3.019	2.011/9
		9.24E-05	1.59E+02	0.05508	0.3111	
3k	31600 GeV	4.07E-04	6.64E+02	-0.8364	-3.151	2.912/9
		1.30E-04	1.43E+02	0.0468	0.289	
1k	56200 GeV	6.35E-04	6.96E+02	-0.8622	-3.198	2.1/9
		3.19E-04	2.34E+02	0.0696	0.4731	
1k	100000 GeV	1.20E-03	6.71E+02	-0.8669	-3.158	0.7799/9
		4.98E-04	2.05E+02	0.07858	0.5529	
1k	178000 GeV	2.00E-03	6.51E+02	-0.8651	-3.12	1.551/9
		7.85E-04	1.69E+02	0.05615	0.3436	
500	316000 GeV	3.78E-03	6.06E+02	-0.8633	-3.04	1.728/9
		2.00E-03	2.08E+02	0.078	0.4186	
300	562000 GeV	6.15E-03	6.40E+02	-0.8742	-3.148	0.6801/9
		3.77E-03	2.56E+02	0.08702	0.5321	
100	1000000 GeV	7.74E-03	7.36E+02	-0.8955	-3.337	0.2764/9
		9.26E-03	5.87E+02	0.1528	1.237	

Table III: Parametrization data of LDF study for C nuclei for a distance range of [31.6, 1000] m

Carbon: parameterization for the radial distribution study with a range distance core of [31.6, 1000] m						
Nevents	Primary energy	Parameter: values and errors				
		C	R0	alpha	beta	Chi2/ndf
10k	100 GeV	2.84E-05	1462	-0.1755	-5.193	1.902/8
		1.20E-05	788.7	0.09773	1.669	
10k	178 GeV	6.70E-05	970	-0.2755	-4.242	2.776/8
		1.96E-02	276.3	0.06969	0.5877	
10k	316 GeV	1.80E-04	623.6	-0.286	-3.596	4.877/8
		3.83E-05	107.9	0.05886	0.2211	
10k	562 GeV	2.45E-04	623.9	-0.4631	-3.421	5.66/8
		4.67E-05	89.14	0.0445	0.1776	
10k	1000 GeV	4.44E-04	510.6	-0.5455	-3.056	7.593/8
		7.22E-05	57.27	0.03777	0.1045	
5k	1780 GeV	7.83E-04	459.1	-0.5894	-2.911	7.401/9
		1.29E-04	51.75	0.03605	0.09938	
5k	316 GeV	8.60E-04	556.7	-0.7208	-2.966	12.04/9
		1.23E-04	54.36	0.02553	0.1059	
1k	5620 GeV	1.20E-03	612	-0.7698	-3.049	2.999/9
		3.63E-04	127.2	0.04841	0.2547	
1k	10000 GeV	1.97E-03	601.4	-0.7955	-2.996	2.175/9
		5.33E-04	108.6	0.04162	0.2169	
1k	17800 GeV	3.16E-03	623.3	-0.8173	-3.04	4.149/9
		6.94E-04	87.63	0.03562	0.1644	
500	31600 GeV	5.50E-03	611.6	-0.8179	-3.045	3.624/9
		1.92E-03	143.7	0.05177	0.2929	
100	56200 GeV	7.92E-03	616.8	-0.8213	-2.943	0.7356/9
		5.69E-03	305.6	0.103	0.6055	
266	100000 GeV	1.35E-02	694.9	-0.8727	-3.226	0.3709/9
		9.49E-03	329.1	0.09303	0.693	
144	178000 GeV	2.36E-02	668	-0.867	-3.189	0.4918/9
		1.68E-02	317	0.09867	0.6599	
60	316000 GeV	3.90E-02	667.8	-0.8797	-3.186	0.352/9
		3.41E-02	382.2	0.1209	0.7859	
32	562000 GeV	7.26E-02	634.3	-0.8675	-3.133	0.304/9
		5.00E-02	299.1	0.1024	0.668	
16	1000000 GeV	0.1202	674.7	-0.9096	-3.225	0.1044/9
		0.2396	884.5	0.2563	1.897	

Table II: Parametrization data of LDF study for He nuclei for a distance range of [31.6, 1000] m

Helium: parameterization for the radial distribution study with a range distance core of [31.6, 1000] m						
Nevents	Primary energy	Parameter: values and errors				
		C	R0	alpha	beta	Chi2/ndf
30k	100 GeV	1.01E-05	1212	-0.1749	-4.525	3.029
		2.01E-06	365.8	0.05864	0.8797	
10k	178 GeV	1.88E-05	1198	-0.2936	-4.814	2.08/8
		9.94E-05	654.3	0.115	1.445	
10k	316 GeV	4.92E-05	689.9	-0.3467	-3.659	2.855/8
		1.08E-05	125.8	0.05472	0.2579	
10k	562 GeV	7.27E-05	657.5	-0.4955	-3.415	5.24/8
		9.93E-06	63.8	0.03631	0.1448	
10k	1000 GeV	9.08E-05	695.1	-0.6547	-3.317	9.649/8
		6.09E-06	38.38	0.01811	0.1222	
10k	1780 GeV	1.73E-04	592.4	-0.6784	-3.09	7.096/8
		4.28E-05	99.84	0.04776	0.1865	
10k	316 GeV	0.0002308	637.8	-0.7626	-3.09	9.437/8
		5.05E-05	93.55	0.03735	0.1749	
1k	5620 GeV	3.97E-04	612.3	-0.7756	-3.04	13.15/9
		5.97E-05	63.26	0.02411	0.1253	
1k	10000 GeV	5.64E-04	650	-0.8319	-3.037	1.645/9
		2.46E-04	192	0.06393	0.3765	
5k	17800 GeV	0.0009646	661.8	-0.8278	-3.118	9.752/9
		0.0001576	73.4	0.02381	0.148	
1k	31600 GeV	1.40E-03	622.8	-0.8246	-3.05	12.851/9
		6.12E-04	183	0.06456	0.369	
1k	56200 GeV	2.90E-03	6.45E+02	-0.8391	-3.126	10.01/9
		4.21E-04	62.78	0.02112	0.1292	
500	100000 GeV	4.82E-03	648.9	-0.8513	-3.126	1.821/9
		1.84E-03	165.6	0.05491	0.3382	
100	178000 GeV	8.30E-03	653.6	-0.8674	-3.16	0.7346/9
		7.14E-03	373.1	0.1183	0.7789	
100	316000 GeV	1.27E-02	678.4	-0.8969	-3.164	0.3134/9
		1.11E-02	389.5	0.1157	0.8062	
100	562000 GeV	2.31E-02	653.4	-0.8676	-3.17	0.4458/9
		1.60E-02	296.3	0.09826	0.6151	
50	1000000 GeV	3.47E-02	719.6	-0.8949	-3.315	0.2599/9
		3.95E-02	543	0.148	1.147	

Table V: Parametrization data of LDF study for H nuclei for a distance range of [10, 562] m

Proton: parametrization for the radial distribution study with a range distance core of [10, 562] m						
Nevents	Primary energy	Parameter: values and errors				
		C	R0	alpha	beta	Chi2/ndf
50k	100 GeV	5.27E-06	4.14E+02	0.07188	-2.747	3.132/10
		1.00E-06	167.2	0.07837	0.5722	
30k	178 GeV	1.22E-05	3.47E+02	-0.06817	-2.62	3.192/11
		6.28E-06	115.9	0.1669	0.6178	
30k	316 GeV	2.33E-05	376.8	-0.1784	-2.912	4.066/11
		8.89E-06	165.2	0.104	0.5001	
30k	562 GeV	6.56E-05	2.32E+02	-0.1313	-2.594	3.367/11
		1.77E-05	6.06E+01	0.08967	0.1711	
10k	1000 GeV	9.53E-05	2.49E+02	-0.2838	-2.557	2.637/11
		3.71E-05	8.83E+01	0.1072	0.2582	
10k	1780 GeV	2.55E-04	1.54E+02	-0.2397	-2.26	4.089/11
		7.85E-05	3.93E+01	0.1001	0.0974	
5k	316 GeV	2.27E-04	2.33E+02	-0.4906	-2.275	3.379/11
		9.24E-05	7.90E+01	0.08841	0.2194	
5k	5620 GeV	4.98E-04	1.86E+02	-0.4571	-2.158	5.904/11
		1.62E-04	4.90E+01	0.0742	0.1282	
1k	10000 GeV	7.32E-04	1.89E+02	-0.5402	-2.041	2.237/11
		4.53E-04	9.34E+01	0.1325	0.2424	
3k	17800 GeV	1.26E-03	1.87E+02	-0.5831	-1.999	2.114/11
		6.89E-04	7.99E+01	0.1115	0.2028	
3k	31600 GeV	1.88E-03	2.20E+02	-0.5899	-2.153	3.451/11
		8.68E-04	8.14E+01	0.08696	0.231	
1k	56200 GeV	2.90E-03	2.32E+02	-0.6221	-2.165	3.947/11
		1.15E-03	7.42E+01	0.00115	0.2186	
1k	100000 GeV	5.92E-03	2.15E+02	-0.6114	-2.153	0.9556/11
		6.18E-03	1.77E+02	0.1904	0.5158	
1k	178000 GeV	8.42E-03	2.31E+02	-0.637	-2.163	3.364/11
		2.44E-03	5.38E+01	0.04844	0.1623	
500	316000 GeV	1.69E-02	1.92E+02	-0.5995	-2.09	9.698/11
		7.06E-03	5.73E+01	0.07101	0.1703	
300	562000 GeV	8.27E-02	2.13E+02	-0.6358	-2.133	1.27/11
		1.24E-02	7.49E+01	0.07408	0.2345	
100	1000000 GeV	4.33E-02	2.15E+02	-0.6308	-2.139	1.209/11
		3.60E-02	1.44E+02	0.1403	0.4499	

Table IV: Parametrization data of LDF study for Fe nuclei for a distance range of [31.6, 1000] m

Iron: parameterization for the radial distribution study with a range distance core of [31.6, 1000] m						
Nevents	Primary energy	Parameter: values and errors				
		C	R0	alpha	beta	Chi2/ndf
10k	100 GeV	1.40E-04	1374	-0.1505	-5.037	5.092/8
		2.78E-05	347.7	0.04821	0.7386	
10k	178 GeV	3.80E-04	809.8	-0.2221	-3.925	4.387/8
		5.07E-05	102.6	0.03582	0.2144	
10k	316 GeV	6.90E-04	711.9	-0.3433	-3.724	9.892/8
		7.72E-05	66.02	0.02782	0.1375	
10k	562 GeV	1.38E-03	544.3	-0.4201	-3.286	20.88/8
		1.32E-04	38.08	0.02421	0.07328	
5k	1000 GeV	1.88E-03	553.3	-0.5637	-3.156	22.6/8
		2.39E-04	49.34	0.02805	0.09357	
1k	1780 GeV	3.46E-03	470.3	-0.6048	-2.914	8.864/9
		7.53E-04	70.94	0.04582	0.1377	
1k	316 GeV	4.30E-03	527.4	-0.7124	-2.904	9.068/9
		8.94E-04	75.7	0.03694	0.1491	
500	5620 GeV	6.31E-03	565.6	-0.7561	-2.962	3.834/9
		1.77E-03	109.4	0.046	0.2201	
100	10000 GeV	1.08E-02	529.5	-0.7714	-2.841	1.434/9
		6.44E-03	216	0.09765	0.4269	
100	17800 GeV	1.82E-02	551.1	-0.7862	-2.924	0.9957/9
		1.18E-02	243.4	0.102	0.4923	
150	31600 GeV	2.64E-02	608.6	-0.8141	-3.057	1.61/9
		1.25E-02	197.2	0.06935	0.4125	
50	56200 GeV	3.98E-02	651.9	-0.8519	-3.121	0.3916/9
		3.48E-02	387	0.1204	0.8081	
50	100000 GeV	6.62E-02	657.3	-0.8564	-3.152	0.266/9
		5.17E-02	348.5	0.1072	0.7364	
24	178000 GeV	1.14E-01	674	-0.8797	-3.19	0.2262/9
		1.47E-01	583.5	0.1686	1.241	
10k	316000 GeV	1.90E-01	658.1	-0.8749	-3.192	0.06091/9
		3.95E-01	900.1	0.2864	1.885	
6	562000 GeV	3.05E-01	646.7	-0.8699	-3.146	0.03005/9
		1.41E+00	2016	0.6089	4.255	
3	1000000 GeV	5.31E-01	675.8	-0.9001	-3.214	0.004769/9
		4.89E+00	4160	1.147	8.883	

Table VII: Parametrization data of LDF study for C nuclei for a distance range of [10, 562] m

Carbon: parametrization for the radial distribution study with a range distance core of [10, 562] m						
Nevents	Primary energy	Parameter: values and errors				
		C	R0	alpha	beta	Chi2/ndf
10k	100 GeV	5.61E-05	482.4	0.005827	-2.845	2.501/11
		2.04E-05	296.8	0.1221	0.7701	
10k	178 GeV	1.64E-04	324.5	-0.03219	-2.635	2.88/11
		3.97E-05	101.1	0.08395	0.273	
10k	316 GeV	3.22E-04	350.6	-0.1211	-2.931	5.998/11
		5.92E-05	74.21	0.05517	0.229	
10k	562 GeV	8.34E-04	215.9	-0.1225	-2.531	8.594/11
		1.16E-04	28.97	0.0471	0.07995	
10k	1000 GeV	1.53E-03	193.6	-0.2096	-2.436	9.913/11
		1.74E-04	19.55	0.03598	0.05379	
5k	1780 GeV	2.23E-03	204.3	-0.3364	-2.375	13.27/11
		3.10E-04	24.39	0.03732	0.06965	
5k	316 GeV	3.34E-03	198	-0.4479	-2.19	20.76/10
		4.82E-04	23.27	0.03526	0.05892	
1k	5620 GeV	4.50E-03	225.1	-0.5331	-2.188	6.463/11
		1.12E-03	46.6	0.04978	0.1329	
1k	10000 GeV	9.33E-03	190.3	-0.5087	-2.113	8.375/11
		2.02E-03	33.83	0.04641	0.09575	
1k	17800 GeV	1.41E-02	202.8	-0.5685	-2.071	10.63/11
		2.97E-03	35.49	0.03967	0.1022	
500	31600 GeV	2.68E-02	187.7	-0.5499	-2.072	6.329/11
		6.70E-03	38.7	0.04937	0.1156	
100	56200 GeV	2.68E-02	187.7	-0.5499	-2.072	6.329/11
		6.70E-03	38.7	0.04937	0.1156	
266	100000 GeV	7.62E-02	194.8	-0.5841	-2.093	4.914/11
		2.13E-02	44.84	0.05098	0.1407	
144	178000 GeV	1.12E-01	215.7	-0.6264	-2.129	1.973/11
		4.70E-02	73.98	0.07014	0.2338	
60	316000 GeV	1.92E-01	213	-0.6322	-2.13	1.108/11
		1.20E-01	106.9	0.1066	0.3293	
32	562000 GeV	3.09E-01	218.5	-0.6537	-2.111	0.4585/11
		2.53E-01	147.6	0.1276	0.4818	
16	1000000 GeV	6.32E-01	2.09E+02	-0.6578	-2.123	0.2427/11
		7.55E-01	201.2	0.1891	0.6637	

Table VI: Parametrization data of LDF study for He nuclei for a distance range of [10, 562] m

Helium: parameterization for the radial distribution study with a range distance core of [10, 562] m						
Nevents	Primary energy	Parameter: values and errors				
		C	R0	alpha	beta	Chi2/ndf
30k	100 GeV	1.54E-05	822.3	-0.04563	-3.913	1.893/11
		6.11E-06	644.1	0.1073	1.825	
30k	178 GeV	4.56E-05	449.9	-0.07112	-3.082	4.823/11
		1.16E-05	157.8	0.07682	0.4668	
30k	316 GeV	1.25E-04	277.3	-0.08572	-2.657	6.366/11
		2.21E-05	53.89	0.05928	0.1525	
30k	562 GeV	2.79E-04	220.6	-0.1195	-2.575	8.175/11
		3.77E-05	28.72	0.04613	0.08001	
10k	1000 GeV	5.07E-04	192.2	-0.2138	-2.417	9.093/11
		6.92E-05	23.17	0.04334	0.06207	
10k	1780 GeV	8.12E-04	184.2	-0.3127	-2.295	7.991/11
		1.33E-04	25.44	0.04686	0.06716	
1k	316 GeV	1.06E-03	206.2	-0.4562	-2.21	7.048/10
		1.71E-04	26.84	0.03918	0.06777	
1k	5620 GeV	1.38E-03	238.6	-0.558	-2.202	18.2/10
		2.01E-04	27.9	0.02936	0.07359	
1k	10000 GeV	2.22E-03	242.7	-0.5965	-2.185	13.42/10
		4.03E-04	35.26	0.03442	0.09433	
1k	17800 GeV	3.81E-03	237.4	-0.608	-2.153	16.67/10
		5.78E-04	28.69	0.0282	0.07723	
1k	31600 GeV	7.20E-03	219.2	-0.6018	-2.118	7.589/11
		1.26E-03	31.15	0.03198	0.09045	
1k	56200 GeV	1.16E-02	232.4	-0.6169	-2.173	5.261/11
		2.61E-03	42.73	0.03852	0.1298	
500	100000 GeV	2.06E-02	222.7	-0.6258	-2.127	3.636/11
		6.05E-03	53.15	0.05042	0.1599	
100	178000 GeV	3.54E-02	223.1	-0.657	-2.104	0.9518/11
		2.28E-02	116.1	0.1046	0.3571	
100	316000 GeV	6.86E-02	204.8	-0.6334	-2.094	1.72/11
		4.34E-02	103	0.1091	0.3106	
100	562000 GeV	1.12E-01	208.7	-0.6208	-2.122	1.3/11
		5.63E-02	86.57	0.08503	0.2792	
50	1000000 GeV	1.79E-01	219.2	-0.6531	-2.123	0.7189/11
		1.38E-01	135.9	0.1238	0.4261	

Table VIII: Parametrization data of LDF study for Fe nuclei for a distance range of [10, 562] m

Iron: parametrization for the radial distribution study with a range distance core of [10, 562] m						
Nevents	Primary energy	Parameter: values and errors				
		C	R0	alpha	beta	Chi2/ndf
10k	100 GeV	2.67E-04	470.8	0.02813	-2.845	3.548/10
		4.89E-05	146.2	0.06473	0.378	
10k	178 GeV	7.14E-04	378	-0.04083	-2.849	6.611/10
		9.15E-05	63.7	0.04244	0.1794	
10k	316 GeV	1.69E-03	293.1	-0.09179	-2.723	10.38/10
		1.64E-04	31.26	0.03191	0.08934	
10k	562 GeV	3.55E-03	239.8	-0.1579	-2.601	13.78/10
		2.72E-04	17.7	0.02455	0.04988	
5k	1000 GeV	7.01E-03	193.5	-0.2218	-2.414	19.56/10
		6.70E-04	16.23	0.03011	0.04233	
1k	1780 GeV	1.13E-02	185.1	-0.3248	-2.294	6.803/10
		1.67E-03	23.43	0.04308	0.06757	
1k	316 GeV	1.89E-02	170.3	-0.3971	-2.15	10.84/10
		3.41E-03	25.1	0.04758	0.06334	
500	5620 GeV	3.05E-02	169.5	-0.4536	-2.082	10.23/11
		6.34E-03	29.56	0.04788	0.08427	
100	10000 GeV	5.29E-02	160.1	-0.4604	-2.052	1.748/11
		2.15E-02	54.18	0.09369	0.1561	
100	17800 GeV	6.34E-02	210.7	-0.5839	-2.097	1.434/11
		2.97E-02	83.27	0.08299	0.2583	
150	31600 GeV	1.23E-01	190.3	-0.5578	-2.07	2.246/11
		3.74E-02	48.81	0.05678	0.1564	
50	56200 GeV	1.75E-01	231.9	-0.5896	-2.247	1.733/11
		1.44E-02	17.56	0.01751	0.1117	
50	100000 GeV	2.76E+00	206.9	-0.6536	-2.097	0.02917/11
		1.18E+01	727.3	0.6555	2.401	
24	178000 GeV	6.33E-01	191.9	-0.6162	-2.048	0.6228/11
		5.09E-01	126.6	0.1373	0.4031	
10k	316000 GeV	8.18E-01	227.3	-0.6579	-2.148	0.1924/11
		1.09E+00	248.8	0.2014	0.808	
6	562000 GeV	1.64E+00	189.2	-0.606	-2.061	0.06791/11
		3.84E+00	366.2	0.4044	1.183	
3	1000000 GeV	3.44E-01	195.1	-0.5938	-2.073	1.133/11
		1.79E-01	84.49	0.09167	0.2722	

Data sheets from MF and RF study

Table IX: Multiplicity and response function study in the USC for incidence angle ranges of primary H in the atmosphere of $[0.12.8]^\circ$, $[12.8, 22.3]^\circ$ and $[22.3, 29]^\circ$.

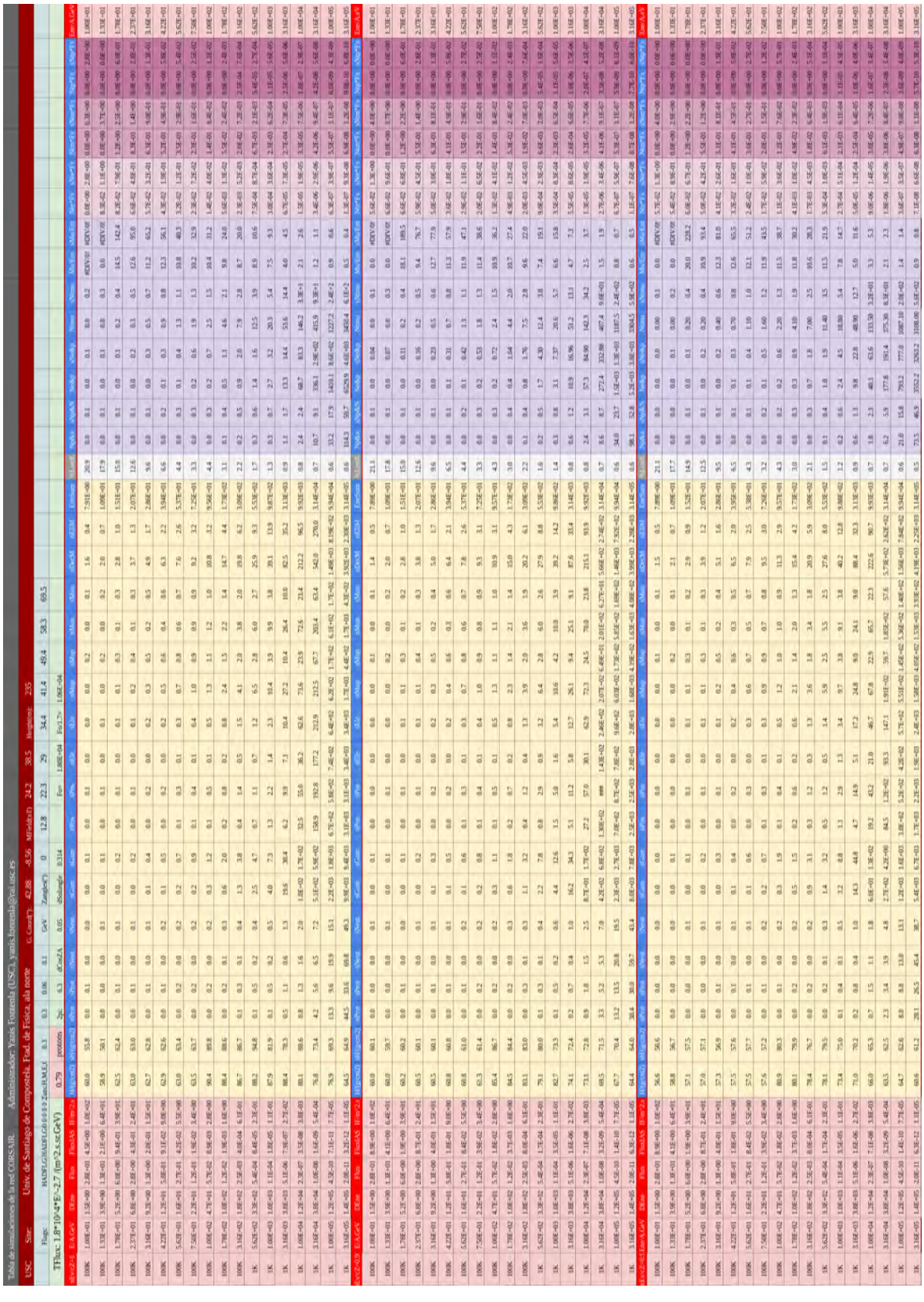

Table X: Multiplicity and response function study in the USC for incidence angle ranges of primary H in the atmosphere of [29,34.4]°, [34.4, 41.4]° and [41.4, 49.4]°.

E>cutZ=0.8	Ener.A.GeV	DEne	Flux	Flux1AS	Flux	H/cm^2.s	H(g/cm2)	cH(g/cm2)	nPion	nProt	nNeut	nAtmN	nGam	nGam	nPos	nPos	nEle	nEle	nMup	nMup	nMun	nMun	nDirM	nEHM	EneSum	%Lost	Npiles	cNpiMN	NnMgt	cNnMgt	Nmm	cNmm	Mu/Em	cMu/Em	Nm*Fx	cNm*Fx	Nnm*Fx	cNnm*Fx	Np*Fx	cNp*Fx	Em/A.eV
100K	1.00E+01	1.5E+00	2.6E+01	8.9E+00	1.0E+02		53.4	53.5	0.0	0.0	0.0	0.0	0.0	0.0	0.0	0.0	0.0	0.0	0.0	0.0	0.0	0.1	0.0	0.0	0.1	1.5	0.4	7.91E+00	20.9	0.0	0.0	0.0	0.0	0.0	0.1	0.0	#DIV/0!	2.6E-02	8.9E-01	0.0E+00	4.0E+00	0.0E+00	0.0E+00	1.00E+01
100K	1.33E+01	3.9E+00	1.3E+01	4.1E+00	6.4E+01		53.4	53.1	0.0	0.0	0.0	0.0	0.0	0.1	0.0	0.0	0.0	0.0	0.0	0.2	0.0	0.1	2.1	0.6	1.10E+01	17.6	0.0	0.0	0.0	0.1	0.0	0.2	0.0	#DIV/0!	4.5E-02	8.2E-01	0.0E+00	2.9E+00	0.0E+00	0.0E+00	1.33E+01
100K	1.78E+01	5.2E+00	6.8E+00	1.9E+00	3.9E+01		54.1	54.0	0.0	0.0	0.0	0.0	0.0	0.1	0.0	0.1	0.0	0.1	0.1	0.2	0.0	0.2	2.9	0.9	1.52E+01	14.8	0.0	0.0	0.0	0.1	0.1	0.3	12.5	152.1	4.8E-02	5.8E-01	6.0E-01	1.7E+00	0.0E+00	0.0E+00	1.78E+01
100K	2.37E+01	6.8E+00	2.6E+00	8.7E-01	2.4E+01		54.1	53.9	0.0	0.0	0.0	0.1	0.0	0.0	0.0	0.1	0.0	0.1	0.1	0.3	0.1	0.3	3.9	1.2	2.08E+01	12.4	0.0	0.1	0.0	0.1	0.2	0.4	13.1	121.3	4.2E-02	3.8E-01	5.5E-01	1.2E+00	0.0E+00	0.0E+00	2.37E+01
100K	3.16E+01	9.2E+00	1.3E+00	4.0E-01	1.5E+01		54.0	53.8	0.0	0.1	0.0	0.1	0.0	0.3	0.0	0.1	0.0	0.1	0.2	0.4	0.2	0.4	5.2	1.5	2.86E+01	9.4	0.0	0.1	0.0	0.2	0.4	0.6	14.2	100.9	3.6E-02	2.5E-01	5.1E-01	7.2E-01	0.0E+00	1.3E-01	3.16E+01
100K	4.22E+01	1.2E+01	5.8E-01	1.8E-01	9.0E+00		54.3	54.3	0.0	0.1	0.0	0.1	0.1	0.4	0.0	0.2	0.0	0.2	0.3	0.6	0.3	0.5	6.7	1.9	3.95E+01	6.4	0.0	0.1	0.0	0.3	0.6	0.8	12.6	72.2	2.8E-02	1.5E-01	3.5E-01	4.5E-01	0.0E+00	5.8E-02	4.22E+01
100K	5.62E+01	1.6E+01	2.7E-01	8.4E-02	5.5E+00		54.5	54.6	0.0	0.1	0.0	0.1	0.1	0.5	0.0	0.2	0.0	0.3	0.6	0.7	0.5	0.6	8.1	2.4	5.38E+01	4.3	0.0	0.1	0.1	0.4	1.1	0.9	13.7	60.5	2.2E-02	9.4E-02	3.0E-01	2.5E-01	0.0E+00	2.7E-02	5.62E+01
100K	7.50E+01	2.2E+01	1.2E-01	3.9E-02	3.4E+00		54.5	54.3	0.0	0.1	0.0	1.0	0.2	0.7	0.1	0.3	0.1	0.3	0.8	0.8	0.7	0.8	9.8	2.9	7.26E+01	3.2	0.0	1.0	0.1	0.4	1.5	1.1	12.7	48.9	1.4E-02	5.5E-02	1.8E-01	1.4E-01	0.0E+00	1.2E-02	7.50E+01
100K	1.00E+02	4.7E+01	5.7E-02	1.8E-02	2.8E+00		77.7	78.1	0.0	0.1	0.0	0.1	0.2	0.8	0.1	0.4	0.1	0.4	1.1	1.0	0.9	0.9	11.6	2.9	9.57E+01	4.3	0.0	0.1	0.2	0.5	2.0	1.3	12.7	42.4	8.9E-03	2.9E-02	1.1E-01	7.6E-02	0.0E+00	5.7E-03	1.00E+02
100K	1.78E+02	1.6E+02	1.2E-02	3.7E-03	1.6E+00		75.4	75.4	0.0	0.1	0.0	0.2	0.4	1.4	0.1	0.6	0.2	0.6	2.0	1.3	1.8	1.3	15.8	4.0	1.73E+02	3.0	0.0	0.2	0.3	0.8	3.8	1.8	12.5	34.8	3.6E-03	1.8E-02	4.5E-02	2.2E-02	0.0E+00	1.2E-02	1.78E+02
100K	3.16E+02	1.8E+02	2.5E-03	8.9E-04	6.1E-01		73.9	74.0	0.0	0.2	0.0	0.2	0.7	2.1	0.3	0.8	0.3	0.9	3.4	1.8	3.2	1.7	21.3	5.6	3.09E+02	2.1	0.0	0.3	0.5	1.2	6.6	2.5	12.1	27.0	1.4E-03	3.0E-03	1.7E-02	6.3E-03	0.0E+00	5.3E-04	3.16E+02
1K	5.62E+02	3.3E+02	5.4E-04	1.7E-04	2.3E-01		67.8	71.2	0.0	0.1	0.0	0.3	1.2	2.5	0.4	1.0	0.5	1.1	5.6	2.4	5.2	2.4	29.6	8.0	5.53E+02	1.5	0.0	0.3	0.9	1.5	10.8	3.4	12.1	20.1	4.8E-04	7.8E-04	5.8E-03	1.8E-03	0.0E+00	5.4E-05	5.62E+02
1K	1.00E+03	1.0E+03	1.1E-04	3.5E-05	1.1E-01		74.2	73.9	0.1	0.3	0.1	0.5	2.7	8.3	0.9	3.0	1.0	3.1	9.1	3.5	8.6	3.5	40.0	12.1	9.88E+02	1.2	0.2	0.6	1.5	4.4	17.7	4.9	9.3	21.3	2.2E-04	4.9E-04	2.0E-03	5.6E-04	1.1E-05	3.4E-05	1.00E+03
1K	3.16E+03	3.8E+03	5.1E-06	1.6E-06	2.7E-02		67.3	64.9	0.2	0.5	0.3	0.7	9.6	22.7	3.1	7.5	3.5	8.2	23.3	8.7	22.6	8.5	91.3	31.4	3.13E+03	0.9	0.5	0.9	6.7	11.1	45.9	12.2	6.9	11.5	3.4E-05	5.5E-05	2.3E-04	6.3E-05	1.0E-06	2.5E-06	3.16E+03
1K	1.00E+04	1.2E+04	2.3E-07	7.1E-08	3.8E-03		61.3	61.2	0.4	1.0	0.7	1.5	3.9E+01	9.6E+01	12.6	32.3	13.9	33.8	63.0	20.0	61.0	19.7	229.2	86.1	9.93E+03	0.7	1.1	1.8	26.4	46.7	124.0	26.1	4.7	8.4	6.0E-06	1.1E-05	2.0E-05	6.3E-06	9.0E-08	2.3E-07	1.00E+04
1K	3.16E+04	3.8E+04	1.0E-08	3.2E-09	5.4E-04		63.7	62.6	1.6	2.7	2.6	4.1	1.84E+02	3.60E+02	57.8	###	64.3	1.29E+02	1.38E+02	56.2	1.73E+02	54.6	5.94E+02	2.55E+02	3.14E+04	0.6	4.2	4.9	122.0	174.4	291.0	78.4	2.4	3.5	1.2E-06	3.8E-06	2.9E-06	7.9E-07	1.6E-08	2.7E-08	3.16E+04
1K	1.00E+05	1.2E+05	4.5E-10	1.4E-10	7.7E-05		58.0	58.0	5.7	7.1	9.4	10.5	8.1E+02	1.3E+03	2.5E+02	4.1E+02	2.8E+02	4.5E+02	5.0TE+02	1.42E+02	4.92E+02	1.38E+02	1.59E+03	7.47E+02	9.94E+04	0.6	15.1	12.7	533.1	610.1	998.4	198.0	1.9	2.2	2.4E-07	2.7E-07	4.5E-07	8.9E-08	2.6E-09	3.2E-09	1.00E+05
1K	3.16E+05	1.4E+05	2.0E-11	6.3E-12	1.1E-05		55.3	55.7	26.6	19.9	33.6	29.7	3.6E+03	4.5E+03	1.3E+03	1.5E+03	1.2E+03	1.6E+03	1.47E+03	3.86E+02	1.42E+03	3.75E+02	4.32E+03	2.20E+03	3.14E+05	0.5	54.2	35.8	2343.5	2191.4	2889.1	538.2	1.2	1.2	4.7E-08	4.4E-08	5.8E-08	1.3E-08	4.1E-10	4.0E-10	3.16E+05
E>cutZ=0.7	Ener.A.GeV	DEne	Flux	Flux1AS	H/cm^2.s		H(g/cm2)	cH(g/cm2)	nPion	nProt	nNeut	nAtmN	nGam	nGam	nPos	nPos	nEle	nEle	nMup	nMup	nMun	nMun	nDirM	nEHM	EneSum	%Lost	Npiles	cNpiMN	NnMgt	cNnMgt	Nmm	cNmm	Mu/Em	cMu/Em	Nm*Fx	cNm*Fx	Nnm*Fx	cNnm*Fx	Np*Fx	cNp*Fx	Em/A.eV
100K	1.00E+01	1.5E+00	2.8E+01	1.3E+01	1.0E+02		46.7	49.6	0.0	0.0	0.0	0.0	0.0	0.0	0.0	0.0	0.0	0.0	0.0	0.1	0.0	0.1	1.5	0.4	7.92E+00	20.8	0.0	0.0	0.0	0.0	0.0	0.1	0.0	#DIV/0!	2.2E-02	7.9E-01	0.0E+00	4.0E+00	0.0E+00	0.0E+00	1.00E+01
100K	1.33E+01	3.9E+00	1.3E+01	6.2E+00	6.4E+01		49.4	49.6	0.0	0.0	0.0	0.0	0.0	0.1	0.0	0.0	0.0	0.0	0.0	0.1	0.0	0.1	2.1	0.6	1.07E+01	19.5	0.0	0.0	0.0	0.0	0.0	0.1	0.0	#DIV/0!	2.7E-02	6.1E-01	0.0E+00	1.9E+00	0.0E+00	0.0E+00	1.33E+01
100K	1.78E+01	5.2E+00	6.0E+00	2.8E+00	3.9E+01		49.8	50.1	0.0	0.0	0.0	0.0	0.0	0.1	0.0	0.1	0.0	0.1	0.0	0.2	0.0	0.2	2.8	0.8	1.45E+01	18.8	0.0	0.0	0.0	0.1	0.0	0.3	0.0	#DIV/0!	3.1E-02	4.6E-01	0.0E+00	1.7E+00	0.0E+00	0.0E+00	1.78E+01
100K	2.37E+01	6.8E+00	2.8E+00	1.3E+00	2.4E+01		50.2	50.4	0.0	0.0	0.0	0.0	0.0	0.2	0.0	0.1	0.0	0.1	0.1	0.3	0.1	0.3	3.9	1.1	2.02E+01	14.9	0.0	0.0	0.0	0.1	0.2	0.4	18.4	199.4	3.0E-02	3.2E-01	5.5E-01	1.2E+00	0.0E+00	0.0E+00	2.37E+01
100K	3.16E+01	9.2E+00	1.3E+00	6.0E-01	1.5E+01		50.2	50.0	0.0	0.0	0.0	0.1	0.0	0.2	0.0	0.1	0.0	0.1	0.2	0.4	0.1	0.3	5.2	1.4	2.81E+01	11.0	0.0	0.1	0.0	0.2	0.3	0.5	13.5	108.0	2.8E-02	2.2E-01	3.8E-01	6.3E-01	0.0E+00	0.0E+00	3.16E+01
100K	4.22E+01	1.2E+01	5.8E-01	2.7E-01	9.0E+00		50.2	50.4	0.0	0.0	0.0	0.1	0.0	0.3	0.0	0.2	0.0	0.2	0.3	0.5	0.2	0.5	6.8	1.8	3.95E+01	6.5	0.0	0.1	0.0	0.2	0.5	0.7	12.3	75.9	2.4E-02	1.4E-01	2.9E-01	4.3E-01	0.0E+00	0.0E+00	4.22E+01
100K	5.62E+01	1.6E+01	2.7E-01	1.3E-01	5.5E+00		50.1	50.4	0.0	0.1	0.0	1.0	0.1	0.4	0.0	0.0	0.0	0.2	0.5	0.6	0.4	0.6	8.3	2.2	5.39E+01	4.1	0.0	1.0	0.1	0.2	0.9	0.8	14.3	52.5	1.7E-02	6.0E-02	2.4E-01	2.3E-01	0.0E+00	2.7E-02	5.62E+01
100K	7.50E+01	2.2E+01	1.2E-01	5.8E-02	3.4E+00		50.9	50.9	0.0	0.1	0.0	0.1	0.1	0.6	0.1	0.3	0.1	0.3	0.7	0.8	0.6	0.7	10.1	2.7	7.30E+01	2.6	0.0	0.1	0.3	0.4	1.3	1.1	12.7	53.2	1.3E-02	5.2E-02	1.6E-01	1.3E-01	0.0E+00	1.2E-02	7.50E+01
100K	1.00E+02	4.7E+01	5.7E-02	2.7E-02	2.8E+00		71.7	71.6	0.0	0.1	0.0	0.1	0.2	0.7	0.1	0.3	0.1	0.3	0.9	0.9	0.8	0.9	11.9	2.7	9.62E+01	3.8	0.0	0.1	0.1	0.5	1.7	1.3	12.7	45.7	7.6E-03	2.7E-02	9.6E-02	7.2E-02	0.0E+00	5.7E-03	1.00E+02
100K	1.78E+02	1.0E+02	1.2E-02	5.6E-03	1.6E+00		70.5	70.7	0.0	0.1	0.0	0.1	0.3	1.1	0.1	0.5	0.1	0.5	1.8	1.2	1.6	1.2	16.3	3.8	1.74E+02	2.4	0.0	0.1	0.3	0.7	3.4	1.7	12.9	36.1	3.1E-03	8.6E-03	4.1E-02	2.0E-02	0.0E+00	1.2E-03	1.78E+02
100K	3.16E+02	1.8E+02	2.5E-03	1.2E-03	6.1E-01		68.7	68.7	0.0	0.1	0.0	0.2	0.6	1.7	0.2	0.7	0.2	0.8	3.1	1.7	2.9	1.6	22.0	5.3	3.11E+02	1.5	0.0	0.2	0.5	1.0	6.0	2.3	13.1	30.3	1.2E-03	2.6E-03	1.5E-02	5.9E-03	0.0E+00	2.5E-04	3.16E+02
1K	5.62E+02	3.3E+02	5.4E-04	2.5E-04	2.3E-01		69.8	7.6	0.0	0.2	0.0	0.2	1.1	2.9	0.4	1.1	0.4	1.1	5.1	2.3	4.9	2.3	29.5	7.6	5.56E+02	1.0	0.0	0.3	0.8	1.6	10.0	3.3	12.9	26.6	4.1E-04	8.4E-04	5.4E-03	1.7E-03	0.0E+00	1.3E-04	5.62E+02
1K	1.00E+03	1.0E+03	1.1E-04	5.3E-05	1.1E-01		62.9	62.4	0.0	0.2	0.1	0.3	1.6	3.1	0.6	1.2	0.6	1.3	8.3	3.2	7.7	3.1	42.4	11.3	9.93E+02	0.7	0.1	0.4	1.2	1.8	16.0	4.5	13.6	21.3	1.3E-04	2.0E-04	1.8E-03	5.6E-04	0.0E+00	2.3E-05	1.00E+03
1K	3.16E+03	3.8E+03	5.1E-06	2.4E-06	2.7E-02		66.2	64.5	0.1	0.7	0.2	0.7	7.4	27.9	2.6	9.8	2.9	10.9	21.7	7.9	20.7	7.5	91.5	29.6	3.15E+03	0.5	0.3	1.0	5.4	14.7	42.4	10.9	7.8	21.3	2.7E-05	7.4E-05	2.1E-04	5.5E-05	5.1E-07	3.5E-06	3.16E+03
1K	1.00E+04	1.2E+04	2.3E-07	1.1E-07	3.8E-03		58.9	58.6	0.3	0.8	0.5	1.1	2.5E+01	6.4E+01	8.5	21.1	9.3	23.0	56.5	19.0	54.7	18.4	228.4	79.7	9.96E+03	0.4	1.8	1.4	17.8	31.2	111.2	26.4	6.2	11.0	4.0E-06	7.0E-06	2.5E-05	6.0E-06	1.0E-06	1.8E-07	1.00E+04
1K	3.16E+04	3.8E+04	1.0E-08	4.8E-09	5.4E-04		54.8	56.9	1.0	2.0	1.6	3.0	1.10E+02	2.49E+02	35.2	79.3	38.8	87.5	1.61E+02	51.3	1.58E+02	49.7	6.16E+02	2.41E+02	3.15E+04	0.3	2.6	3.6	74.0	108.1	319.0	71.4	4.3	6.9	7.5E-07	1.2E-06	3.2E-06	7.2E-07	1.0E-08	2.0E-08	3.16E+04
1K	1.00E+05	1.2E+05	4.5E-10	2.1E-10	7.7E-05		54.3	56.6	3.5	5.0	6.0	8.2	4.9E+02	9.0E+02	1.5E+02	2.9E+02	1.7E+02	3.2E+02	4.61E+02	1.31E+02	4.48E+02	1.28E+02	1.65E+03	7.86E+02	9.97E+04	0.3	9.5	9.6	321.0	427.1	909.0	183.1	2.8	3.8	1.4E-07	1.9E-07	4.1E-07	8.2E-08	1.6E-09	2.2E-09	1.00E+05
1K	3.16E+05	1.4E+05	2.0E-11	9.5E-12	1.1E-05		50.7	49.8	12.3	14.0	20.2	20.6	1.9E+03	2.7E+03	5.8E+02	8.6E+02	6.4E+02	9.5E+02	1.31E+03	3.45E+02	1.27E+03	3.35E+02	4.50E+03	2.87E+03	3.15E+05	0.3	32.5	24.9	1219.0	1282.0	2595.9	481.2	2.1	2.3	2.5E-08	2.6E-08	5.2E-08	9.7E-09	2.7E-10	2.8E-10	3.16E+05
E>cutZ=0.7	Ener.A.GeV	DEne	Flux	Flux1AS	H/cm^2.s		H(g/cm2)	cH(g/cm2)	nPion	nProt	nNeut	nAtmN	nGam	nGam	nPos	nPos	nEle	nEle	nMup	nMup	nMun	nMun	nDirM	nEHM	EneSum	%Lost	Npiles	cNpiMN	NnMgt	cNnMgt	Nmm	cNmm	Mu/Em	cMu/Em	Nm*Fx	cNm*Fx	Nnm*Fx	cNnm*Fx	Np*Fx	cNp*Fx	Em/A.eV
100K	1.00E+01	1.5E+00	2.8E+01	1.8E+01	1.0E+02		44.3	44.4	0.0	0.0	0.0	0.0	0.0	0.0	0.0	0.0	0.0	0.0	0.0	0.1	0.0	0.0	1.5	0.4	7.94E+00	20.6	0.0	0.0	0.0	0.0	0.0	0.1	0.0	#DIV/0!	1.3E-02	6.2E-01	0.0E+00	2.9E+00	0.0E+00	0.0E+00	1.00E+01
100K	1.33E+01	3.9E+00	1.3E+01	8.3E+00	6.4E+01		44.4	44.6	0.0	0.0	0.0	0.0	0.0	0.0	0.0	0.0	0.0	0.0	0.0	0.1	0.0	0.1	2.1	0.5	1.07E+01	19.4	0.0	0.0	0.0	0.0	0.0	0.1	0.0	#DIV/0!	1.9E-02	5.2E-01	0.0E+00	1.9E+00	0.0E+00	0.0E+00	1.33E+01
100K	1.78E+01	5.2E+00	6.0E+00	3.8E+00	3.9E+01		44.4	44.5	0.0	0.0	0.0	0.0	0.0	0.1	0.0	0.0	0.0	0.0	0.0	0.2	0.0	0.1	2.9	0.7	1.45E+01	18.6	0.0	0.0	0.0	0.1	0.1	0.2	0.0	#DIV/0!	2.3E-02	4.6E-01	0.0E+00	1.3E+00	0.0E+00	0.0E+00	1.78E+01
100K	2.37E+01	6.8E+00	2.8E+00	1.7E+00	2.4E+01		44.7	44.6	0.0	0.0	0.0	0.0	0.0	0.1	0.0	0.1	0.0	0.1	0.1	0.2	0.0	0.2	4.0	1.0	2.02E+01	14.8	0.0	0.0	0.0	0.1	0.1	0.3	12.2	153.4	2.3E-02	2.8E-01	2.9E-01	7.8E-01	0.0E+00	0.0E+00	2.37E+01
100K	3.16E+01	9.2E+00	1.3E+00	8.0E-01	1.5E+01		44.4	44.5	0.0	0.0	0.0	0.0	0.0	0.2	0.0	0.1	0.0	0.1	0.1	0.3	0.1	0.3	5.4	1.3	2.82E+01	10.8	0.0	0.0	0.0	0.1	0.2	0.4	12.2	104.5	2.1E-02	1.9E-01	2.5E-01	5.4E-01	0.0E+00	0.0E+00	3.16E+01
100K	4.22E+01	1.2E+01	5.8E-01	3.7E-01	9.0E+00		45.0	45.1	0.0	0.0	0.0	0.0	0.0	0.3	0.0	0.1	0.0	0.1	0.2	0.5	0.2	0.4	7.0	1.6	3.95E+01	6.3	0.0	0.0	0.0	0.2	0.4	0.6	13.8	98.1	1.7E-02	1.2E-01	2.5E-01	3.7E-01	0.0E+00	0.0E+00	4.22E+01
100K	5.62E+01	1.6E+01	2.7E-01	1.7E-01	5.5E+00		44.8	45.0	0.0	0.0	0.0	0.1	0.1	0.4	0.0	0.2	0.0	0.2	0.4	0.6	0.3	0.5	8.6	2.0	5.40E+01	4.0	0.0	0.1	0.1	0.3	0.7	0.8	13.4	74.7	1.4E-02	7.7E-02	1.9E-01	2.1E-01	0.0E+00	0.0E+00	5.62E+01
100K	7.50E+01	2.2E+01	1.2E-01	7.7E-02	3.4E+00		44.9	45.1	0.0	0.0	0.0	0.1	0.1	0.5	0.0	0.3	0.0	0.3	0.6	0.7	0.5	0.7	10.4	2.5	7.31E+01	2.5	0.0	0.1	0.1	0.4	1.1	1.0	14.0	67.6	9.6E-03	4.6E-02	1.4E-01	1.2E-01	0.0E+00	0.0E+00	7.50E+01
100K	1.00E+02	4.7E+01	5.7E-02	3.6E-02	2.8E+00		64.0	63.9	0.0	0.0	0.0	0.1	0.1	0.6	0.0	0.3	0.1	0.3	0.8	0.8	0.7	0.8	12.4	2.4	9.63E+01	3.7	0.0	0.1	0.1	0.4	1.5	1.1	14.8	60.1	5.7E-03	2.3E-02	8.5E-02	6.4E-02	0.0E+00	9.0E-04	1.00E+02
100K	1.78E+02	1.0E+02	1.2E-02	7.5E-03	1.6E+00		62.5	62.3	0.0	0.1	0.0	0.1	0.3	1.0	0.1	0.4	0.1	0.5	1.5	1.1	1.4	1.1	17.0	3.4	1.74E+02	2.3	0.0	0.1	0.2	0.6	2.9	1.6	13.8	43.4	2.5E-03	7.8E-03	3.5E-02	1.9E-02	0.0E+00	1.2E-03	1.78E+02
100K	3.16E+02	1.8E+02	2.5E-03	1.6E-03	6.1E-01		61.2	61.6	0.0	0.1	0.0	0.1	0.5	1.5	0.2	0.6	0.2	0.7	2.7	1.5	2.5	1.5	22.9	4.8	3.11E+02	1.5	0.0	0.1	0.4	0.9	5.2	2.1	14.0	35.4	9.4E-04	2.3E-03	1.3E-02	5.4E-03	0.0E+00	2.5E-04	3.16E+02
1K	5.62E+02	3.3E+02	5.4E-04	3.4E-04	2.3E-01		62.0	61.0	0.0	0.1	0.0	0.2	0.9	2.8	0.3	1.0	0.4	1.3	4.5	2.1	4.3	2.0	31.2	6.8	5.57E+02	1.0	0.0	0.2	0.7	1.6	8.8	2.9	13.4	33.8	3.5E-04	8.8E-04	4.7E-03	1.6E-03	0.0E+00	5.4E-05	5.62E+02
1K	1.00E+03	1.0E+03	1.1E-04	7.1E-05	1.1E-01		56.9	57.6	0.0	0.2	0.0	0.2	1.3	2.8	0.4	1.1	0.5	1.3	7.2	2.9	6.9	2.8	43.3	10.0	9.94E+02	0.7	0.0	0.3	1.0	1.7	14.1	4.0	14.7	26.3	1.1E-04	1.9E-04	1.6E-03	4.6E-04	0.0E+00	2.3E-05	1.00E+03
1K	3.16E+03	3.8E+03	5.1E-06	3.2E-06	2.7E-02		57.3	59.3	0.0	0.3	0.1	0.4	4.7	10.9	1.6	3.7	1.7	3.9	18.7	6.9	18.2	6.7	94.7	25.5	3.15E+03	0.4	0.1	0.5	3.3	5.3	36.9	9.6	11.1	18.0	1.7E-05	2.7E-05	1.9E-04	4.9E-05	0.0E+00	1.5E-06	3.16E+03
1K	1.00E+04	1.2E+04	2.3E-07	1.4E-07	3.8E-03		52.3	54.0	0.1	0.5	0.2	0.6	1.4E+01	3.2E+01	4.9	10.7	5.3	11.6	49.8	16.5	48.1	16.1	240.0	72.5	9.97E+03	0.3	0.3	0.8	10.1	15.8	97.9	23.1	9.6	15.1	2.3E-06	3.6E-06	2.2E-05	5.2E-06	2.3E-08	1.3E-07	1.00E+04
1K	3.16E+04	3.8E+04	1.0E-08	6.3E-09	5.4E-04		51.3	49.1	0.4	1.1	0.7	1.6	5.02E+00	1.06E+02	17.3	35.1	19.1	39.4	1.38E+02	40.9	1.34E+02	39.9	6.31E+02	2.13E+02	3.15E+04	0.3	1.1	1.9	36.4	52.

Table XI: Multiplicity and response function study in the USC for incidence angle ranges of primary H in the atmosphere of [49.4, 58.3]°, [58.3, 69.5]° and [0, 69.5]° (total particle counts for all zenith angle range).

Evt/Z=0.3	Ene/A GeV	DEne	Flux	Flux/IAS	H/m^2/s	H(g/cm2)	(H(g/cm2)	nProt	nProt	nNeut	nNeut	nGam	nGam	nPos	nPos	nEle	nEle	nMup	nMup	nMun	nMun	nDecM	nEDM	EneSum	%Lost	NpiKn	nQpiKN	NeKp	nNeKp	Nmes	nNmes	Mu/Ene	nMu/Ene	Ne*Fn	nNe*Fn	Nm*Fn	nNm*Fn	Np*Fn	nNp*Fn	Ene/A.e/n
100K	1.00E+01	1.5E+00	2.8E+01	2.2E+01	1.0E+02	37.2	37.2	0.0	0.0	0.0	0.0	0.0	0.0	0.0	0.0	0.0	0.0	0.0	0.0	0.0	0.0	1.5	0.3	7.97E+00	20.3	0.0	0.0	0.0	0.0	0.0	0.0	0.0	#DIV/0!	3.1E-03	3.0E-01	0.0E+00	0.0E+00	0.0E+00	0.0E+00	1.00E+01
100K	1.33E+01	3.9E+00	1.3E+01	1.0E+01	6.4E+01	37.2	37.4	0.0	0.0	0.0	0.0	0.0	0.0	0.0	0.0	0.0	0.0	0.0	0.0	0.0	0.0	2.2	0.4	1.08E+01	19.1	0.0	0.0	0.0	0.0	0.0	0.1	0.0	#DIV/0!	8.7E-03	3.5E-01	0.0E+00	1.9E+00	0.0E+00	0.0E+00	1.33E+01
100K	1.78E+01	5.2E+00	6.0E+00	4.7E+00	3.9E+01	37.4	37.4	0.0	0.0	0.0	0.0	0.0	0.1	0.0	0.0	0.0	0.0	0.0	0.1	0.0	0.1	2.9	0.6	1.45E+01	18.4	0.0	0.0	0.0	0.0	0.0	0.1	0.0	#DIV/0!	1.1E-02	2.0E-01	0.0E+00	8.5E-01	0.0E+00	0.0E+00	1.78E+01
100K	2.37E+01	6.8E+00	2.0E+00	2.2E+00	2.4E+01	37.4	37.5	0.0	0.0	0.0	0.0	0.0	0.1	0.0	0.0	0.0	0.1	0.0	0.2	0.0	0.2	4.1	0.8	2.03E+01	14.5	0.0	0.0	0.0	0.1	0.0	0.3	0.0	#DIV/0!	1.3E-02	1.6E-01	0.0E+00	7.8E-01	0.0E+00	0.0E+00	2.37E+01
100K	3.16E+01	9.2E+00	1.3E+00	1.0E+00	1.5E+01	37.7	37.9	0.0	0.0	0.0	0.0	0.0	0.2	0.0	0.1	0.0	0.1	0.1	0.3	0.1	0.2	5.5	1.1	2.82E+01	10.6	0.0	0.0	0.0	0.1	0.2	0.4	18.3	298.0	1.4E-02	1.6E-01	2.5E-01	4.6E-01	0.0E+00	0.0E+00	3.16E+01
100K	4.22E+01	1.2E+01	5.8E-01	4.6E-01	9.0E+00	37.6	37.7	0.0	0.0	0.0	0.0	0.0	0.3	0.0	0.1	0.0	0.1	0.2	0.4	0.1	0.3	7.3	1.4	3.96E+01	6.1	0.0	0.0	0.0	0.2	0.3	0.5	13.5	111.4	1.3E-02	1.0E-01	1.7E-01	2.9E-01	0.0E+00	0.0E+00	4.22E+01
100K	5.62E+01	1.6E+01	2.7E-01	2.1E-01	5.5E+00	37.7	37.7	0.0	0.0	0.0	0.0	0.0	0.4	0.0	0.2	0.0	0.2	0.3	0.5	0.2	0.5	9.0	1.7	5.40E+01	3.9	0.0	0.0	0.0	0.2	0.5	0.7	13.9	95.3	9.7E-03	6.5E-02	1.3E-01	1.9E-01	0.0E+00	0.0E+00	5.62E+01
100K	7.50E+01	2.2E+01	1.2E-01	9.7E-02	3.4E+00	37.8	38.0	0.0	0.0	0.0	0.0	0.1	0.5	0.0	0.2	0.0	0.2	0.5	0.6	0.4	0.6	10.9	2.1	7.32E+01	2.4	0.0	0.0	0.1	0.3	0.9	0.8	16.4	93.2	6.8E-03	3.8E-02	1.1E-01	1.0E-01	0.0E+00	0.0E+00	7.50E+01
100K	1.00E+02	4.7E+01	5.7E-02	4.4E-02	2.8E+00	54.2	54.3	0.0	0.0	0.0	0.0	0.1	0.5	0.0	0.2	0.0	0.3	0.6	0.7	0.5	0.7	13.0	2.1	9.64E+01	3.6	0.0	0.0	0.0	0.1	0.4	1.1	1.0	14.8	72.4	4.2E-03	2.0E-02	6.2E-02	5.6E-02	0.0E+00	0.0E+00	1.00E+02
100K	1.78E+02	1.0E+02	1.2E+02	9.4E+03	1.6E+00	52.7	52.7	0.0	0.0	0.0	0.0	0.2	0.9	0.1	0.4	0.1	0.4	1.2	1.0	1.1	0.9	17.9	2.9	1.74E+02	2.3	0.0	0.0	0.2	0.6	2.3	1.3	14.6	52.5	1.9E-03	6.7E-03	2.7E-02	1.6E-02	0.0E+00	0.0E+00	1.78E+02
100K	3.16E+02	1.8E+02	2.5E+03	2.0E+03	6.1E-01	51.5	51.5	0.0	0.0	0.0	0.0	0.1	0.4	1.3	0.1	0.6	0.1	0.6	2.2	1.3	2.0	1.3	24.3	4.0	3.12E+02	1.4	0.0	0.1	0.3	0.8	4.2	1.8	14.5	40.7	7.4E-04	2.0E-03	1.1E-02	4.7E-03	0.0E+00	0.0E+00	3.16E+02
1K	5.62E+02	3.3E+02	5.4E-04	4.2E-04	2.3E-01	50.5	51.9	0.0	0.0	0.0	0.0	0.7	1.9	0.3	0.8	0.3	0.9	3.7	1.8	3.4	1.8	32.9	5.9	5.57E+02	0.9	0.0	0.0	0.6	1.2	7.1	2.5	12.6	27.7	3.0E-04	6.6E-04	3.8E-03	1.4E-03	0.0E+00	0.0E+00	5.62E+02
1K	1.00E+03	1.0E+03	1.1E-04	8.9E-05	1.1E-01	47.2	45.6	0.0	0.0	0.0	0.1	1.1	2.8	0.4	1.3	0.4	1.2	6.1	2.5	5.6	2.5	46.2	8.6	9.54E+02	0.6	0.0	0.1	0.9	1.8	11.7	3.5	13.5	28.4	9.8E-05	2.9E-04	1.3E-03	4.9E-04	0.0E+00	0.0E+00	1.00E+03
1K	3.16E+03	3.8E+03	5.1E-06	4.0E-06	2.7E-02	45.3	43.9	0.0	0.1	0.0	0.2	3.2	9.0	1.2	3.4	1.3	4.2	15.2	5.1	14.3	4.9	99.6	20.6	3.15E+03	0.3	0.0	0.2	2.4	5.4	29.5	7.1	12.2	27.2	1.2E-05	2.7E-05	1.5E-04	3.6E-05	0.0E+00	5.3E-07	3.16E+03
1K	1.00E+04	1.2E+04	2.3E-07	1.8E-07	3.8E-03	44.9	46.3	0.0	0.2	0.1	0.3	8.0E+00	9.5E+00	3.1	3.7	3.3	4.0	41.1	13.4	39.7	13.0	247.8	59.7	9.57E+03	0.3	0.1	0.4	6.4	5.4	80.8	18.7	12.7	11.2	1.4E-06	1.2E-06	1.6E-05	4.2E-06	0.0E+00	4.5E-08	1.00E+04
1K	3.16E+04	3.8E+04	1.0E-08	7.9E-09	5.4E-04	43.2	41.6	0.1	0.4	0.2	0.6	2.55E+01	4.05E+01	9.2	12.7	10.1	14.4	1.11E+02	33.6	1.08E+02	32.4	6.49E+02	1.76E+02	3.15E+04	0.2	0.3	0.7	19.2	19.3	219.3	46.7	11.4	11.7	1.9E-07	1.9E-07	2.2E-06	4.7E-07	1.0E-09	4.0E-09	3.16E+04
1K	1.00E+05	1.2E+05	4.5E-10	3.5E-10	7.7E-05	39.9	41.7	0.3	0.9	0.7	1.4	7.9E+01	9.6E+01	2.8E+01	3.0E+01	3.0E+01	3.4E+01	3.39E+02	89.3	3.08E+02	86.7	1.78E+03	5.39E+02	9.98E+04	0.2	1.0	1.7	58.2	45.3	624.0	124.5	10.7	8.6	2.6E-08	2.0E-08	2.8E-07	5.6E-08	1.3E-10	4.9E-10	1.00E+05
1K	3.16E+05	1.4E+05	2.0E-11	1.6E-11	1.1E-05	39.1	36.6	1.5	2.9	2.9	4.8	2.7E+02	3.6E+02	9.5E+01	1.2E+02	1.0E+02	1.3E+02	9.03E+02	2.41E+02	8.82E+02	2.33E+02	4.96E+03	1.62E+03	3.15E+05	0.2	4.4	5.6	199.7	173.0	1784.2	334.9	8.9	7.9	4.0E-09	3.5E-09	3.6E-08	6.7E-09	3.0E-11	5.8E-11	3.16E+05
Evt/Z=0.4	Ene/A GeV	DEne	Flux	Flux/IAS	H/m^2/s	H(g/cm2)	(H(g/cm2)	nProt	nProt	nNeut	nNeut	nGam	nGam	nPos	nPos	nEle	nEle	nMup	nMup	nMun	nMun	nDecM	nEDM	EneSum	%Lost	NpiKn	nQpiKN	NeKp	nNeKp	Nmes	nNmes	Mu/Ene	nMu/Ene	Ne*Fn	nNe*Fn	Nm*Fn	nNm*Fn	Np*Fn	nNp*Fn	Ene/A.e/n
100K	1.00E+01	1.5E+00	2.8E+01	3.1E+01	1.0E+02	27.8	28.2	0.0	0.0	0.0	0.0	0.0	0.0	0.0	0.0	0.0	0.0	0.0	0.0	0.0	0.0	1.5	0.2	8.03E+00	19.7	0.0	0.0	0.0	0.0	0.0	0.0	0.0	#DIV/0!	5.7E-04	1.3E-01	0.0E+00	0.0E+00	0.0E+00	0.0E+00	1.00E+01
100K	1.33E+01	3.9E+00	1.3E+01	1.4E+01	6.4E+01	27.9	28.4	0.0	0.0	0.0	0.0	0.0	0.0	0.0	0.0	0.0	0.0	0.0	0.0	0.0	0.0	2.2	0.3	1.08E+01	18.6	0.0	0.0	0.0	0.0	0.0	0.0	0.0	#DIV/0!	1.4E-03	1.4E-01	0.0E+00	0.0E+00	0.0E+00	0.0E+00	1.33E+01
100K	1.78E+01	5.2E+00	6.0E+00	6.6E+00	3.9E+01	28.1	28.4	0.0	0.0	0.0	0.0	0.0	0.0	0.0	0.0	0.0	0.0	0.0	0.1	0.0	0.1	3.0	0.4	1.46E+01	17.9	0.0	0.0	0.0	0.0	0.0	0.1	0.0	#DIV/0!	3.6E-03	1.6E-01	0.0E+00	8.5E-01	0.0E+00	0.0E+00	1.78E+01
100K	2.37E+01	6.8E+00	2.0E+00	3.0E+00	2.4E+01	28.4	28.9	0.0	0.0	0.0	0.0	0.0	0.1	0.0	0.0	0.0	0.0	0.0	0.1	0.0	0.1	4.2	0.6	2.04E+01	14.1	0.0	0.0	0.0	0.0	0.0	0.1	0.0	#DIV/0!	5.4E-03	1.3E-01	0.0E+00	3.9E-01	0.0E+00	0.0E+00	2.37E+01
100K	3.16E+01	9.2E+00	1.3E+00	1.4E+00	1.5E+01	28.3	28.9	0.0	0.0	0.0	0.0	0.0	0.1	0.0	0.1	0.0	0.1	0.0	0.2	0.0	0.2	5.7	0.8	2.84E+01	10.2	0.0	0.0	0.0	0.1	0.0	0.3	0.0	#DIV/0!	6.8E-03	1.1E-01	0.0E+00	3.6E-01	0.0E+00	0.0E+00	3.16E+01
100K	4.22E+01	1.2E+01	5.8E-01	6.4E-01	9.0E+00	28.5	29.0	0.0	0.0	0.0	0.0	0.0	0.2	0.0	0.1	0.0	0.1	0.1	0.3	0.1	0.2	7.5	1.0	3.98E+01	5.8	0.0	0.0	0.0	0.1	0.2	0.4	19.1	224.7	6.1E-03	7.1E-02	1.2E-01	2.1E-01	0.0E+00	0.0E+00	4.22E+01
100K	5.62E+01	1.6E+01	2.7E-01	3.8E-01	5.5E+00	28.3	28.7	0.0	0.0	0.0	0.0	0.0	0.3	0.0	0.1	0.0	0.1	0.2	0.4	0.1	0.3	9.3	1.3	5.42E+01	3.6	0.0	0.0	0.0	0.2	0.3	0.5	15.9	148.8	5.1E-03	4.5E-02	9.0E-02	1.3E-01	0.0E+00	0.0E+00	5.62E+01
100K	7.50E+01	2.2E+01	1.2E-01	1.4E-01	3.4E+00	28.4	28.6	0.0	0.0	0.0	0.0	0.0	0.4	0.0	0.2	0.0	0.2	0.3	0.5	0.2	0.4	11.4	1.5	7.34E+01	2.1	0.0	0.0	0.0	0.3	0.5	0.6	14.2	106.3	4.3E-03	3.2E-02	6.2E-02	7.5E-02	0.0E+00	0.0E+00	7.50E+01
100K	1.00E+02	4.7E+01	5.7E-02	6.2E-02	2.8E+00	40.6	41.2	0.0	0.0	0.0	0.0	0.1	0.4	0.0	0.2	0.0	0.2	0.3	0.6	0.3	0.5	13.6	1.5	9.65E+01	3.5	0.0	0.0	0.0	0.3	0.6	0.8	13.4	87.3	2.5E-03	1.6E-02	3.4E-02	4.4E-02	0.0E+00	0.0E+00	1.00E+02
100K	1.78E+02	1.0E+02	1.2E+02	1.3E+02	1.6E+00	39.6	40.1	0.0	0.0	0.0	0.0	0.1	0.7	0.0	0.3	0.1	0.3	0.8	0.8	0.7	0.8	18.9	2.1	1.74E+02	2.1	0.0	0.0	0.0	0.5	1.5	1.1	16.0	79.0	1.1E-03	5.5E-03	1.8E-02	1.4E-02	0.0E+00	0.0E+00	1.78E+02
100K	3.16E+02	1.8E+02	2.5E+03	2.8E+03	6.1E-01	38.8	39.4	0.0	0.0	0.0	0.0	0.2	1.1	0.1	0.5	0.1	0.5	1.5	1.1	1.5	1.1	1.3	1.1	3.12E+02	1.3	0.0	0.0	0.2	0.7	3.0	1.6	15.4	54.2	4.9E-04	1.7E-03	7.6E-03	3.9E-03	0.0E+00	0.0E+00	3.16E+02
1K	5.62E+02	3.3E+02	5.4E-04	5.9E-04	2.3E-01	39.0	39.5	0.0	0.0	0.0	0.0	0.4	1.4	0.2	0.6	0.2	0.7	2.6	1.5	2.4	1.5	35.4	4.2	5.58E+02	0.8	0.0	0.0	0.3	0.9	5.0	2.1	14.5	40.3	1.8E-04	5.0E-04	2.7E-03	1.3E-03	0.0E+00	0.0E+00	5.62E+02
1K	1.00E+03	1.0E+03	1.1E-04	1.2E-04	1.1E-01	36.5	34.6	0.0	0.0	0.0	0.0	0.9	2.6	0.3	1.0	0.3	1.0	4.2	1.9	4.0	1.9	47.7	5.9	9.95E+02	0.5	0.0	0.0	0.6	1.4	8.2	2.7	12.7	28.0	7.3E-05	1.6E-04	9.3E-04	3.0E-04	0.0E+00	0.0E+00	1.00E+03
1K	3.16E+03	3.8E+03	5.1E-06	5.6E-06	2.7E-02	36.6	36.8	0.0	0.0	0.0	0.0	2.0	4.5	0.7	1.7	0.8	1.9	11.1	4.1	10.5	4.0	101.7	14.3	3.15E+03	0.2	0.0	0.0	1.5	2.6	21.6	5.7	14.0	23.6	7.8E-06	1.3E-05	1.1E-04	2.9E-05	0.0E+00	0.0E+00	3.16E+03
1K	1.00E+04	1.2E+04	2.3E-07	2.5E-07	3.8E-03	31.6	31.2	0.0	0.1	0.0	0.1	5.4E+00	7.5E+00	2.0	2.9	2.1	2.9	28.9	9.7	28.3	9.5	246.0	38.7	9.98E+03	0.2	0.0	0.1	4.3	4.1	57.2	13.6	14.0	14.5	9.2E-07	9.3E-07	1.3E-05	3.1E-06	0.0E+00	2.3E-08	1.00E+04
1K	3.16E+04	3.8E+04	1.0E-08	1.1E-08	5.4E-04	32.4	33.2	0.0	0.1	0.0	0.2	1.55E+01	1.40E+01	5.6	5.3	6.2	5.7	77.3	24.7	75.5	24.5	6.49E+02	1.18E+02	3.16E+04	0.1	0.0	0.2	11.9	7.7	152.8	34.8	12.9	8.9	1.2E-07	7.8E-08	1.5E-06	3.5E-07	0.0E+00	1.0E-09	3.16E+04
1K	1.00E+05	1.2E+05	4.5E-10	4.9E-10	7.7E-05	30.9	30.9	0.0	0.3	0.1	0.4	4.5E+01	3.1E+01	1.7E+01	1.2E+01	1.0E+01	1.2E+01	2.19E+02	67.6	2.15E+02	65.2	1.80E+03	3.68E+02	9.98E+04	0.2	0.1	0.5	34.4	17.2	433.7	93.9	12.6	6.9	1.5E-08	7.7E-09	2.0E-07	4.2E-08	0.0E+00	1.3E-10	1.00E+05
1K	3.16E+05	1.4E+05	2.0E-11	2.2E-11	1.1E-05	29.1	28.9	0.1	0.5	0.4	0.9	1.2E+02	6.8E+01	4.6E+01	2.5E+01	5.0E+01	2.7E+01	6.19E+02	1.82E+02	6.06E+02	1.77E+02	5.06E+03	1.12E+03	3.16E+05	0.2	0.5	1.0	95.4	36.7	1225.1	254.0	12.8	5.6	1.9E-09	7.4E-10	2.5E-08	5.1E-09	2.0E-12	1.8E-11	3.16E+05
Evt/Z=0.4	Ene/A GeV	DEne	Flux	Flux/IAS	H/m^2/s	H(g/cm2)	(H(g/cm2)	nProt	nProt	nNeut	nNeut	nGam	nGam	nPos	nPos	nEle	nEle	nMup	nMup	nMun	nMun	nDecM	nEDM	EneSum	%Lost	NpiKn	nQpiKN	NeKp	nNeKp	Nmes	nNmes	Mu/Ene	nMu/Ene	Ne*Fn	nNe*Fn	Nm*Fn	nNm*Fn	Np*Fn	nNp*Fn	Ene/A.e/n
100K	1.00E+01	1.5E+00	2.8E+01	8.9E+00	8.4E+02			0.0	0.1	0.0	0.1	0.0	0.3	0.0	0.2	0.0	0.7	0.0	0.5	12.0	3.1				100.0	0.0	0.1	0.0	0.3	0.000	0.9	0.0	#DIV/0!	1.8E-01	6.6E+01	0.0E+00	6.4E+02	0.0E+00	8.1E+00	1.00E+01
100K	1.33E+01	3.9E+00	1.3E+01	4.1E+00	1.0E+01			0.0	0.0	0.0	0.2	0.0	0.5	0.0	0.3	0.0	0.3	0.0	1.1	0.0	0.9	16.8	4.5		100.0	0.0	0.2	0.0	0.4	0.000	1.4	0.0	#DIV/0!	3.0E-01	2.9E+01	0.0E+00	3.6E+02	0.0E+00	0.0E+00	1.33E+01
100K	1.78E+01	5.2E+00	6.0E+00	1.9E+00	6.2E+00			0.0	0.2	0.0	0.2	0.1	0.8	0.0	0.5	0.0	0.5	0.4	1.7	0.3	1.4	23.0	6.3		100.0	0.0	0.3	0.1	0.7	0.700	2.2	12.9	164.2	3.3E-01	1.6E+01	4.2E+00	1.8E+02	0.0E+00	1.4E+00	1.78E+01
100K	2.37E+01	6.8E+00	2.0E+00	8.7E-01	3.0E+00			0.0	0.2	0.0	0.4	0.1	1.1	0.1	0.6	0.1	0.7	0.7	2.2	0.5	2.0	31.5	8.5		100.0	0.0	0.4	0.1	0.9	1.200	3.0	11.5	106.9	2.9E-01	6.9E+00	3.3E+00	6.8E+01	0.0E+00	5.0E-01	2.37E+01
100K	3.16E+01	9.2E+00	1.3E+00	4.0E-01	2.3E+00			0.0	0.4	0.0	0.5	0.2	1.9	0.1	1.0	0.1	1.0	1.4	3.1	1.1	2.7	42.0	11.1		100.0	0.0	0.6	0.2	1.4	2.500	4.1	12.6	91.8	2.5E-01	3.2E+00	3.2E+00	2.7E+01	0.0E+00	2.6E-01	3.16E+01
100K	4.22E+01	1.2E+01	5.8E-01	1.8E-01	1.4E+00			0.0	0.4	0.0	0.6	0.4	2.8	0.2	1.3	0.2	1.4	2.4	4.1	1.9	3.6	54.5	14.0		100.0	0.0	0.7	0.3	1.9	4.300	5.5	12.6	73.3	2.0E-01	1.3E+00	2.5E+00	1.0E+01	0.0E+00	5.4E-02	4.22E+01
100K	5.62E+01	1.6E+01	2.7E-01	8.4E-02	8.7E-01			0.0	0.6	0.0	1.7	0.7	3.8	0.3	1.6	0.3	1.9	4.0	5.1	3.2	4.6	66.6	17.3		100.0	0.0	1.0	0.6	2.5	7.200	6.9	12.6	55.6	1.5E-01	4.5E-01	1.9E+00	3.4E+00	0.0E+00	2.6E-02	5.62E+01
100K	7.50E+01	2.2E+01	1.2E-01	3.9E-02	5.3E-01			0.0	0.7	0.0	1.8	1.1	5.2	0.4	2.3	0.4	2.5	5.8	6.3	4.8	5.8	80.6	21.0		100.0	0.0	1.9	0.9	3.4	10.600	8.4	12.2	48.8	1.1E-01	1.8E-01	1.3E+00	1.1E+00	0.0E+00	7.4E-03	7.50E+01
100K	1.00E+02	4.7E+01	5.7E-02	1.8E-02	4.4E-01			0.0	0.7	0.0	0.9	1.5	7.2	0.6	2.8	0.6	3.0	7.5	7.2	6.5	6.7	95.5	20.8		100.0	0.0	1.1	1.2	4.1	14.000	9.8	12.0	43.1	6.6E-02	5.4E-02	7.9E-01	3.1E-01	0.0E+00	1.6E-03	1.00E+02
100K	1.78E+02	1.0E+02	1.2E+02	3.7E+03	2.5E-01			0.0	0.9	0.1	1.2	3.0	10.2	1.1	4.3	1.2	4.6	14.1	9.7	12.9	9.4	131.0	29.1		100.0	0.1	1.5	2.3	6.3	27.000	13.5	12.0	33.8	2.7E-02	5.6E-03	3.2E-01	2.6E-02	0.0E+00	1.2E-04	1.78E+02
100K	3.16E+02	1.8E+02	2.5E+03	8.8E-04	9.5E-02			0.1	1.2	0.2	1.5	5.6	17.9	2.0	6.9	2.2	7.5	24.5	13.2	22.9	12.9	152.7	39.0		100.0	0.3	1.9	4.2	10.2	47.400	18.5	11.3	27.7	1.1E-02	6.7E-04	1.2E-01	2.2E-03	2.5E-04	9.2E-06	3.16E+02
1K	5.62E+02	3.3E+02	5.4E-04	1.7E-04	3.6E-02			0.2	1.4	0.4	1.8	10.5	27.3	3.4	9.7	3.9	10.9	40.3	18.2	37.7	17.8	240.0	58.6		100.0	0.6	2.3	7.3	14.6	78.000	25.5	10.7	21.6	3.9E-03	6.3E-05	4.2E-02	1.9E-04	1.1E-04	5.6E-07	5.62E+02
1K	1.00E+03	1.0E+03	1.1E-04	3.5E-05	1.7E-02			0.4	2.1	0.7	2.7	19.2	48.3	6.6	17.9	7.1	19.1	65.6	25.9	61.8	25.3	338.1	88.8		100.0	1.1	3.4	13.8	26.2	127.400	36.2	9.2	17.8	1.6E-03	8.7E-06	1.4E-02	1.7E-05	4.5E-05	5.6E-08	1.00E+03
1K	3.16E+03	3.8E+03	5.1E-06	1.6E-06	4.3E-03			1.2	4.2	2.0	5.3	76.9	184.4	25.2	62.2	28.2	69.4	168.1	61.5	161.9	58.7	737.3	222.3		100.0	3.2	6.8	53.4	93.1	330.000	85.7	6.2	10.3	2.7E-04	2.2E-07	1.7E-03	1.9E-07	6.1E-06	4.5E-10	3.16E+03
1K	1.00E+04	1.2E+04	2.3E-07	7.1E-08	6.0E-04			3.2	7.2	5.7	9.9	3.4E+02	6.8E+02	1.1E+02	2.3E+02	1.2E+02	2.5E+02	4.5E+02	1.5E+02	4.4E+02	1.5E+02	1.8E+03	6.2E+02		100.0	8.9	12.2	231.0	3.4E+02	8.9E+02	2.1E+02	3.9	5.7	5.2E-05	5.7E-09	2.0E-04	2.2E-09	7.2E-07	2.5E-12	1.00E+04
1K	3.16E+04	3.8E+04	1.0E-08	3.2E-09	8.5E-05			12.9	29.5	20.8	28.5	1.6E+03	2.0E+03	5.0E+02	7.9E+02	5.5E+02	8.8E+02	1.2E+03	4.0E+02	1.2E+03	3.8E+02	4.8E+03	1.8E+03		100.0	33.7	55.1	1049.9	1.2E+03	2.5E+03	5.5E+02	2.3	2.7	1.1E-05	1.4E-10	2.5E-05	3.1E-11	1.3E-07	4.3E-14	3.16E+04
1K	1.00E+05	1.2E+05	4.5E-10	1.4E-10	1.2E-05			45.6	48.3	72.6	72.8	7.3E+03	8.8E+03	2.3E+03	2.9E+03	2.5E+03	3.1E+03	3.7E+03	1.0E+03	3.6E+03	1.0E+03	1.3E+04

Table XII: Multiplicity and response function study in the USC for incidence angle ranges of primary He in the atmosphere of [0.12.8]°, [12.8, 22.3]° and [22.3, 29]°.

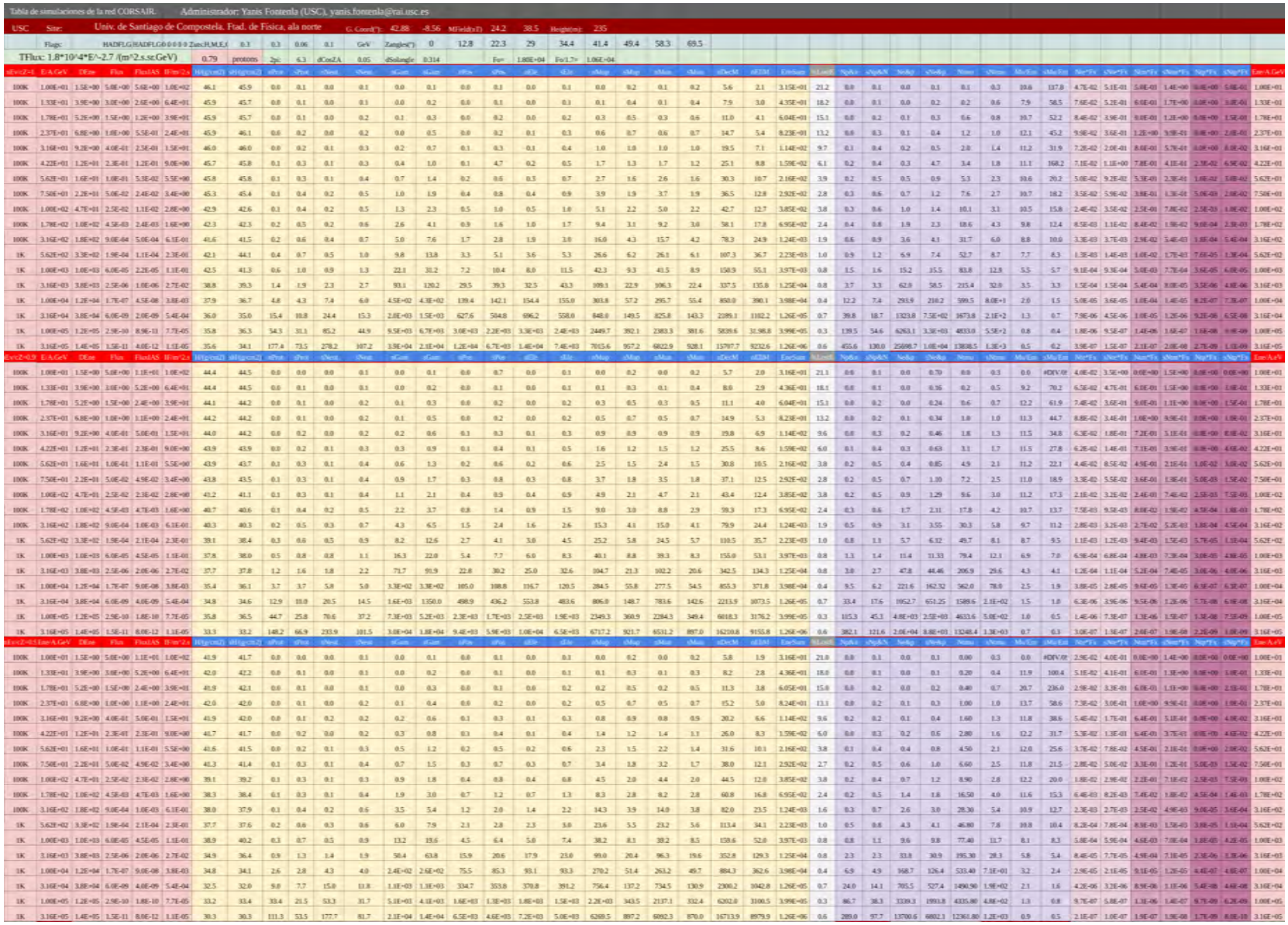

Table XIII: Multiplicity and response function study in the USC for incidence angle ranges of primary He in the atmosphere of [29,34.4]°, [34.4, 41.4]° and [41.4, 49.4]°.

E×vZ=0.8	Ener.A.GeV	DEne	Flux	FluxIAS	If·m^2.s	H(g/cm2)	sH(g/cm2)	xPos	yPos	xNeut	yNeu	xGam	yGam	xPos	yPos	xEle	yEle	xMup	yMup	xMun	yMun	xDecM	xESM	EneSum	%Leak	Nphot	sNphN	Nelep	sNelep	Nmuo	sNmu	MuTm	sMuTm	Ner*Fx	sNer*Fx	Nmr*Fx	sNmr*Fx	Nqr*Fx	sNqr*Fx	Ener/A.eV
100K	1.00E+01	1.5E+00	5.0E+00	1.1E+01	1.0E+02	39.7	39.9	0.0	0.0	0.0	1.0	0.0	0.1	0.0	0.0	0.0	0.1	0.0	0.2	0.0	0.2	5.8	1.9	3.16E+01	29.0	0.0	1.0	0.0	0.1	0.0	0.3	0.0	#DIV/0!	2.3E-02	3.5E-01	0.0E+00	1.4E+00	0.0E+00	0.0E+00	1.00E+01
100K	1.33E+01	3.9E+00	3.0E+00	5.2E+00	6.4E+01	39.5	39.5	0.0	0.0	0.0	0.1	0.0	0.1	0.0	0.1	0.0	0.1	0.1	0.3	0.1	0.3	8.3	2.6	4.36E+01	18.0	0.0	0.1	0.0	0.1	0.2	0.4	15.6	148.6	1.8E-02	3.6E-01	6.0E-01	1.3E+00	0.0E+00	0.0E+00	1.33E+01
100K	1.78E+01	5.2E+00	1.5E+00	2.4E+00	3.9E+01	39.6	39.6	0.0	0.1	0.0	0.1	0.0	0.2	0.0	0.1	0.0	0.1	0.2	0.4	0.2	0.5	13.5	3.6	6.05E+01	15.0	0.0	0.1	0.0	0.2	0.4	0.6	13.0	82.4	4.7E-02	2.9E-01	6.2E-01	9.6E-01	0.0E+00	1.5E-01	1.78E+01
100K	2.37E+01	6.8E+00	1.0E+00	1.1E+00	2.4E+01	39.7	39.7	0.0	0.1	0.0	0.1	0.1	0.4	0.0	0.2	0.0	0.2	0.4	0.6	0.4	0.6	15.4	4.8	8.24E+01	13.0	0.0	0.1	0.1	0.3	0.8	0.8	13.2	60.9	6.3E-02	2.7E-01	8.8E-01	8.5E-01	0.0E+00	1.0E-01	2.37E+01
100K	3.16E+01	9.2E+00	4.0E-01	5.0E-01	1.5E+01	39.4	39.4	0.0	0.1	0.0	0.2	0.1	0.5	0.1	0.3	0.1	0.3	0.7	0.8	0.7	0.8	20.6	6.3	1.14E+02	9.5	0.0	0.2	0.1	0.4	1.4	1.1	12.5	44.7	4.5E-02	1.6E-01	5.6E-01	4.5E-01	0.0E+00	4.0E-02	3.16E+01
100K	4.22E+01	1.2E+01	2.3E-01	2.3E-01	9.0E+00	39.2	39.0	0.0	0.1	0.0	0.2	0.2	0.7	0.1	0.4	0.1	0.4	1.3	1.1	1.2	1.1	26.6	7.9	1.59E+02	5.9	0.0	0.2	0.2	0.5	2.5	1.6	12.9	36.3	4.4E-02	1.2E-01	5.8E-01	3.6E-01	0.0E+00	2.3E-02	4.22E+01
100K	5.62E+01	1.6E+01	1.0E-01	1.1E-01	5.5E+00	39.1	39.0	0.0	0.2	0.0	0.2	0.4	1.0	0.2	0.5	0.2	0.5	2.1	1.4	2.0	1.4	32.3	9.7	2.16E+02	3.8	0.0	0.3	0.3	0.7	4.1	2.0	12.7	28.9	3.2E-02	7.1E-02	4.1E-01	2.0E-01	0.0E+00	2.0E-02	5.62E+01
100K	7.50E+01	2.2E+01	5.0E-02	4.9E-02	3.4E+00	38.8	38.9	0.0	0.2	0.1	0.3	0.6	1.4	0.2	0.6	0.2	0.7	3.1	1.7	2.9	1.7	38.9	11.6	2.93E+02	2.7	0.1	0.4	0.5	0.9	6.0	2.4	12.6	24.5	2.4E-02	4.6E-02	3.0E-01	1.2E-01	0.0E+00	1.0E-02	7.50E+01
100K	1.00E+02	4.7E+01	2.5E-02	2.3E-02	2.8E+00	36.8	36.8	0.0	0.2	0.1	0.3	0.8	1.6	0.3	0.7	0.3	0.8	4.1	1.9	4.0	1.9	45.7	11.5	3.85E+02	3.7	0.1	0.4	0.6	1.1	8.1	2.7	12.7	21.4	1.6E-02	2.7E-02	2.0E-01	6.7E-02	0.0E+00	5.0E-03	1.00E+02
100K	1.78E+02	1.0E+02	4.5E-03	4.7E-03	1.6E+00	36.5	36.5	0.1	0.3	0.1	0.4	1.6	2.7	0.6	1.1	0.6	1.2	7.7	2.7	7.5	2.7	62.4	16.1	6.95E+02	2.4	0.2	0.5	1.2	1.6	15.2	3.8	12.4	16.7	5.5E-03	7.3E-03	6.8E-02	1.7E-02	4.5E-04	1.4E-03	1.78E+02
100K	3.16E+02	1.8E+02	9.0E-04	1.0E-03	6.1E-01	36.0	36.1	0.1	0.3	0.1	0.5	2.9	4.5	1.1	1.7	1.2	1.9	13.4	3.7	13.1	3.6	84.1	22.6	1.24E+03	1.8	0.2	0.6	2.2	2.6	26.5	5.2	11.9	13.9	2.0E-03	2.3E-03	2.4E-02	4.6E-03	9.0E-05	2.7E-04	3.16E+02
1K	5.62E+02	3.3E+02	1.9E-04	2.1E-04	2.3E-01	34.3	34.9	0.2	0.5	0.2	0.6	6.0	11.1	2.2	3.6	2.3	4.2	22.0	5.3	21.7	5.0	115.3	32.8	2.23E+03	0.9	0.4	0.8	4.5	5.7	43.7	7.3	9.7	12.3	8.6E-04	1.1E-03	8.3E-03	1.4E-03	3.8E-05	8.3E-05	5.62E+02
1K	1.00E+03	1.0E+03	6.0E-05	4.5E-05	1.1E-01	34.5	33.9	0.2	0.6	0.3	0.8	10.0	14.3	3.5	4.9	3.8	5.3	35.6	7.3	34.7	7.3	162.9	49.0	3.97E+03	0.7	0.5	1.0	7.3	7.2	70.3	10.3	9.6	9.6	4.4E-04	4.3E-04	4.2E-03	6.2E-04	1.2E-05	3.6E-05	1.00E+03
1K	3.16E+03	3.8E+03	2.5E-06	2.0E-06	2.7E-02	33.5	33.6	0.6	1.1	1.0	1.6	37.8	47.4	12.5	16.1	1.4	17.6	92.7	19.2	89.8	18.2	360.2	123.3	1.25E+04	0.8	1.6	1.9	13.9	23.8	182.5	26.5	13.1	22.6	3.5E-05	6.0E-05	4.6E-04	6.6E-05	1.5E-06	2.8E-06	3.16E+03
1K	1.00E+04	1.2E+04	1.7E-07	9.0E-08	3.8E-03	32.8	32.4	1.9	2.6	3.1	3.5	1.7E+02	2.3E+02	55.5	74.6	61.1	82.2	252.0	58.3	244.9	48.5	902.0	345.6	3.98E+04	0.4	5.0	4.4	116.6	111.0	496.9	69.9	4.3	4.3	2.0E-05	1.9E-05	8.4E-05	1.2E-05	3.2E-07	4.4E-07	1.00E+04
1K	3.16E+04	3.8E+04	6.0E-09	4.0E-09	5.4E-04	32.0	31.0	6.6	5.8	10.8	8.6	7.1E+02	6.7E+02	221.3	214.2	245.0	298.5	708.4	125.9	688.1	121.5	2364.9	1013.3	1.26E+05	0.7	17.4	10.4	466.4	329.6	1396.5	175.0	1.0	2.1	2.8E-06	1.9E-06	8.4E-06	1.0E-06	4.0E-08	9.5E-08	3.16E+04
1K	1.00E+05	1.2E+05	2.9E-10	1.8E-10	7.7E-05	32.1	31.3	23.5	16.7	38.8	25.1	3.4E+03	3.1E+03	1.1E+03	1.0E+03	1.9E+03	1.3E+03	2049.9	331.9	1995.1	320.9	6394.2	3016.5	3.99E+05	0.3	62.3	30.1	2948.9	1489.6	4045.0	461.7	1.4	0.7	8.6E-07	4.3E-07	1.2E-06	1.3E-07	6.8E-09	4.8E-09	1.00E+05
1K	3.16E+05	1.4E+05	1.5E-11	8.0E-12	1.1E-05	28.3	27.9	79.6	45.2	130.9	69.0	1.3E+04	1.1E+04	4.3E+03	3.5E+03	4.8E+03	3.9E+03	5789.1	844.8	5628.0	822.0	17188.0	8663.4	1.26E+06	0.6	210.5	82.5	9140.2	5235.1	11417.1	1178.7	1.2	0.7	1.4E-07	7.9E-08	1.7E-07	1.8E-08	1.2E-09	6.8E-10	3.16E+05
E×vZ=0.7	Ener.A.GeV	DEne	Flux	FluxIAS	If·m^2.s	H(g/cm2)	sH(g/cm2)	xPos	yPos	xNeut	yNeu	xGam	yGam	xPos	yPos	xEle	yEle	xMup	yMup	xMun	yMun	xDecM	xESM	EneSum	%Leak	Nphot	sNphN	Nelep	sNelep	Nmuo	sNmu	MuTm	sMuTm	Ner*Fx	sNer*Fx	Nmr*Fx	sNmr*Fx	Nqr*Fx	sNqr*Fx	Ener/A.eV
100K	1.00E+01	1.5E+00	5.0E+00	1.7E+01	1.8E+02	36.7	36.7	0.0	0.0	0.0	0.0	2.8	0.1	0.0	0.0	0.0	0.0	0.0	0.1	0.0	0.1	5.9	1.7	3.17E+01	20.8	0.0	0.0	0.0	0.1	0.0	0.1	0.0	#DIV/0!	1.4E-02	2.7E-01	0.0E+00	7.1E-01	0.0E+00	0.0E+00	1.00E+01
100K	1.33E+01	3.9E+00	3.0E+00	7.8E+00	6.4E+01	36.6	36.6	0.0	0.0	0.0	0.1	0.0	0.1	0.0	0.1	0.0	0.1	0.1	0.2	0.1	0.3	8.4	2.5	4.37E+01	17.9	0.0	0.1	0.0	0.1	0.2	0.4	20.0	228.2	2.9E-02	3.1E-01	6.0E-01	1.1E+00	0.0E+00	0.0E+00	1.33E+01
100K	1.78E+01	5.2E+00	1.5E+00	3.6E+00	3.9E+01	36.7	36.7	0.0	0.0	0.0	0.1	0.0	0.2	0.0	0.1	0.0	0.1	0.2	0.4	0.2	0.4	11.7	3.4	6.06E+01	14.9	0.0	0.1	0.0	0.2	0.4	0.6	16.3	136.1	3.7E-02	2.6E-01	6.8E-01	8.5E-01	0.0E+00	0.0E+00	1.78E+01
100K	2.37E+01	6.8E+00	1.0E+00	1.6E+00	2.4E+01	36.7	36.6	0.0	0.1	0.0	0.1	0.1	0.3	0.0	0.2	0.0	0.2	0.3	0.6	0.3	0.6	15.8	4.5	8.25E+01	12.9	0.0	0.1	0.1	0.3	0.6	0.8	11.9	61.1	5.1E-02	2.5E-01	6.0E-01	8.5E-01	0.0E+00	1.0E-01	2.37E+01
100K	3.16E+01	9.2E+00	4.0E-01	7.6E-01	1.5E+01	36.6	36.7	0.0	0.1	0.0	0.1	0.1	0.5	0.0	0.2	0.0	0.3	0.6	0.8	0.6	0.8	21.1	5.9	1.15E+02	9.4	0.0	0.1	0.1	0.4	1.2	1.1	12.9	50.3	3.7E-02	1.4E-01	4.8E-01	4.5E-01	0.0E+00	4.0E-02	3.16E+01
100K	4.22E+01	1.2E+01	2.3E-01	3.5E-01	9.0E+00	36.6	36.7	0.0	0.1	0.0	0.1	0.2	0.7	0.1	0.3	0.1	0.4	1.1	1.0	1.1	1.0	27.2	7.5	1.59E+02	5.9	0.0	0.1	0.2	0.5	2.2	1.4	13.2	39.9	3.8E-02	1.1E-01	5.1E-01	3.3E-01	0.0E+00	2.3E-02	4.22E+01
100K	5.62E+01	1.6E+01	1.0E-01	1.6E-01	5.5E+00	36.4	36.5	0.0	0.1	0.0	0.2	0.3	0.9	0.1	0.4	0.1	0.5	1.9	1.3	1.7	1.3	33.1	9.1	2.16E+02	9.1	0.0	0.2	0.3	0.7	3.6	1.8	13.2	32.3	2.7E-02	6.5E-02	3.6E-01	1.8E-01	0.0E+00	1.0E-02	5.62E+01
100K	7.50E+01	2.2E+01	5.0E-02	7.3E-02	3.4E+00	36.3	36.5	0.0	0.2	0.0	0.2	0.5	1.2	0.2	0.6	0.2	0.6	2.7	1.6	2.6	1.5	48.0	11.0	2.92E+02	2.6	0.0	0.3	0.4	0.8	5.3	2.2	13.2	27.5	2.8E-02	4.1E-02	2.7E-01	1.1E-01	0.0E+00	1.0E-02	7.50E+01
100K	1.00E+02	4.7E+01	2.5E-02	3.4E-02	2.8E+00	34.5	34.5	0.0	0.2	0.0	0.2	0.7	1.4	0.3	0.7	0.3	0.7	3.6	1.8	3.5	1.8	47.0	10.9	3.85E+02	3.7	0.0	0.3	0.5	1.0	7.1	2.5	13.3	24.4	1.3E-02	2.4E-02	1.8E-01	6.4E-02	0.0E+00	5.0E-03	1.00E+02
100K	1.78E+02	1.0E+02	4.5E-03	7.1E-03	1.6E+00	33.6	33.7	0.0	0.2	0.1	0.3	1.3	2.3	0.5	1.0	0.5	1.1	7.0	2.6	6.8	2.5	64.5	15.2	6.95E+02	2.3	0.1	0.4	1.0	1.5	13.8	3.6	13.3	18.9	4.7E-03	6.5E-03	6.2E-02	1.6E-02	0.0E+00	9.0E-04	1.78E+02
100K	3.16E+02	1.8E+02	9.0E-04	1.5E-03	6.1E-01	33.1	33.2	0.1	0.3	0.1	0.4	2.4	3.7	0.9	1.5	1.0	1.6	12.1	3.5	11.9	3.4	86.9	21.2	1.24E+03	1.8	0.2	0.5	1.9	2.2	24.0	4.9	12.9	15.5	1.7E-03	2.9E-03	2.2E-02	4.4E-03	9.0E-05	2.7E-04	3.16E+02
1K	5.62E+02	3.3E+02	1.9E-04	3.2E-04	2.3E-01	32.3	34.0	0.1	0.3	0.2	0.5	4.3	5.6	1.5	2.1	1.7	2.4	20.3	4.7	19.9	4.7	119.2	31.1	2.23E+03	0.9	0.3	0.6	3.2	3.2	40.2	6.6	12.4	12.3	6.1E-04	6.0E-04	7.6E-03	1.3E-03	1.9E-05	5.7E-05	5.62E+02
1K	1.00E+03	1.0E+03	6.0E-05	6.7E-05	1.1E-01	31.9	32.1	0.1	0.4	0.2	0.6	7.4	11.7	2.6	4.0	2.8	4.3	32.7	7.2	31.9	7.0	168.6	44.9	3.97E+03	0.7	0.3	0.7	5.5	5.9	64.6	10.0	11.8	12.8	3.3E-04	3.5E-04	3.9E-03	6.0E-04	6.0E-06	2.4E-05	1.00E+03
1K	3.16E+03	3.8E+03	2.5E-06	3.0E-06	2.7E-02	32.5	31.3	0.3	0.8	0.6	1.1	25.8	33.4	8.8	11.5	9.5	12.2	84.6	16.8	82.8	16.5	370.8	117.7	1.25E+04	0.8	0.9	1.4	18.4	16.8	167.4	23.5	9.1	8.4	4.6E-05	4.2E-05	4.2E-04	5.9E-05	7.5E-07	2.0E-06	3.16E+03
1K	1.00E+04	1.2E+04	1.7E-07	1.3E-07	3.8E-03	29.4	30.4	1.2	1.9	1.9	2.5	9.8E+01	1.4E+02	32.5	43.6	35.8	48.1	227.6	43.3	221.6	42.1	918.9	322.2	3.99E+04	0.4	3.1	3.1	68.3	64.9	449.2	60.4	6.6	6.3	1.2E-05	1.1E-05	7.6E-05	1.0E-05	2.0E-07	3.2E-07	1.00E+04
1K	3.16E+04	3.8E+04	6.0E-09	6.0E-09	5.4E-04	28.9	28.9	3.9	4.4	6.4	6.0	4.2E+02	4.7E+02	135.5	154.6	149.6	170.8	638.7	114.3	622.5	110.4	2416.7	948.2	1.26E+05	0.6	10.3	7.4	285.1	230.4	1261.2	158.9	4.4	3.6	1.7E-06	1.4E-06	7.6E-06	9.5E-07	2.3E-08	2.6E-08	3.16E+04
1K	1.00E+05	1.2E+05	2.9E-10	2.7E-10	7.7E-05	30.0	29.1	14.7	12.2	24.4	18.5	1.9E+03	1.8E+03	6.0E+02	5.6E+02	1.6E+02	6.2E+02	1858.4	311.1	1808.4	301.4	6631.4	2861.6	3.99E+05	0.3	59.1	22.2	762.6	839.0	3667.8	433.2	4.8	5.3	2.2E-07	2.4E-07	1.1E-06	1.3E-07	4.3E-09	3.5E-09	1.00E+05
1K	3.16E+05	1.4E+05	1.5E-11	1.2E-11	1.1E-05	27.3	27.4	51.6	36.3	86.9	56.0	8.3E+03	8.2E+03	2.6E+03	2.7E+03	2.9E+03	2.9E+03	5302.2	784.4	5162.7	760.8	17577.9	8368.0	1.26E+06	0.6	138.5	66.7	5476.4	3945.3	10464.9	1052.7	1.9	1.4	8.2E-08	5.9E-08	1.8E-07	1.6E-08	7.7E-10	5.4E-10	3.16E+05
E×vZ=0.5	Ener.A.GeV	DEne	Flux	FluxIAS	If·m^2.s	H(g/cm2)	sH(g/cm2)	xPos	yPos	xNeut	yNeu	xGam	yGam	xPos	yPos	xEle	yEle	xMup	yMup	xMun	yMun	xDecM	xESM	EneSum	%Leak	Nphot	sNphN	Nelep	sNelep	Nmuo	sNmu	MuTm	sMuTm	Ner*Fx	sNer*Fx	Nmr*Fx	sNmr*Fx	Nqr*Fx	sNqr*Fx	Ener/A.eV
100K	1.00E+01	1.5E+00	5.0E+00	2.3E+01	1.0E+02	32.6	32.7	0.0	0.0	0.0	0.0	0.0	0.0	0.0	0.0	0.0	0.0	0.0	0.1	0.0	0.1	6.0	1.5	3.17E+01	20.6	0.0	0.0	0.0	0.0	0.0	0.1	0.0	#DIV/0!	7.6E-03	2.0E-01	0.0E+00	7.1E-01	0.0E+00	0.0E+00	1.00E+01
100K	1.33E+01	3.9E+00	3.0E+00	1.0E+01	6.4E+01	32.6	32.6	0.0	0.0	0.0	0.0	0.0	0.1	0.0	0.1	0.0	0.1	0.0	0.2	0.0	0.2	8.6	2.2	4.38E+01	17.7	0.0	0.0	0.0	0.1	0.0	0.3	0.0	#DIV/0!	1.9E-02	2.5E-01	0.0E+00	8.5E-01	0.0E+00	0.0E+00	1.33E+01
100K	1.78E+01	5.2E+00	1.5E+00	4.8E+00	3.9E+01	32.4	32.5	0.0	0.0	0.0	0.0	0.0	0.2	0.0	0.1	0.0	0.1	0.1	0.3	0.1	0.3	12.0	3.1	6.08E+01	14.7	0.0	0.0	0.0	0.1	0.2	0.4	11.7	100.5	2.6E-02	2.1E-01	3.9E-01	9.4E-01	0.0E+00	0.0E+00	1.78E+01
100K	2.37E+01	6.8E+00	1.0E+00	2.2E+00	2.4E+01	32.6	32.7	0.0	0.0	0.0	0.1	0.0	0.3	0.0	0.1	0.0	0.2	0.2	0.5	0.2	0.5	16.2	4.1	8.27E+01	12.8	0.0	0.1	0.0	0.2	0.4	0.7	11.3	70.1	3.5E-02	2.1E-01	4.0E-01	7.1E-01	0.0E+00	0.0E+00	2.37E+01
100K	3.16E+01	9.2E+00	4.0E-01	1.0E+00	1.5E+01	32.7	32.7	0.0	0.0	0.0	0.1	0.1	0.4	0.0	0.2	0.0	0.2	0.5	0.7	0.5	0.7	21.7	5.3	1.15E+02	9.3	0.0	0.1	0.1	0.3	1.0	1.0	14.3	64.5	2.8E-02	1.2E-01	4.0E-01	4.6E-01	0.0E+00	0.0E+00	3.16E+01
100K	4.22E+01	1.2E+01	2.3E-01	4.6E-01	9.0E+00	32.4	32.5	0.0	0.1	0.0	0.1	0.2	0.6	0.1	0.3	0.1	0.3	0.9	0.9	0.8	0.9	28.2	6.7	1.58E+02	5.7	0.0	0.1	0.1	0.4	1.7	1.3	13.4	47.3	2.9E-02	9.9E-02	3.9E-01	2.9E-01	0.0E+00	2.3E-02	4.22E+01
100K	5.62E+01	1.6E+01	1.0E-01	2.1E-01	5.5E+00	32.2	32.4	0.0	0.1	0.0	0.1	0.3	0.8	0.1	0.4	0.1	0.4	1.7	1.2	1.4	1.1	34.4	8.2	2.17E+02	3.6	0.0	0.1	0.2	0.4	2.9	1.6	14.0	319.7	2.1E-02	4.7E-01	2.9E-01	3.1E-01	0.0E+00	1.0E-02	5.62E+01
100K	7.50E+01	2.2E+01	5.0E-02	9.8E-02	3.4E+00	32.3	32.4	0.0	0.1	0.0	0.1	0.4	1.1	0.2	0.5	0.2	0.5	2.3	1.4	2.1	1.4	41.6	9.9	2.93E+02	2.5	0.0	0.1	0.3	0.7	4.4	2.0	14.1	33.5	1.6E-02	3.6E-02	2.2E-01	9.9E-02	0.0E+00	5.0E-03	7.50E+01
100K	1.00E+02	4.7E+01	2.5E-02	4.5E-02	2.8E+00	30.3	30.3	0.0	0.1	0.0	0.1	0.5	1.2	0.2	0.6	0.2	0.6	3.0	1.6	2.9	1.6	48.9	9.8	3.85E+02	3.6	0.0	0.1	0.4	0.8	5.9	2.3	13.9	28.2	1.1E-02	2.1E-02	1.5E-01	5.7E-02	0.0E+00	2.5E-03	1.00E+02
100K	1.78E+02	1.0E+02	4.5E-03	9.5E-03	1.6E+00	30.1	30.3	0.0	0.1	0.0	0.2	1.0	1.9	0.4	0.8	0.4	0.9	5.9	2.3	5.8	2.3	67.3	13.7	6.96E+02	2.3	0.0	0.2	0.8	1.2	11.7	3.3	14.1	21.6	3.7E-03	5.6E-03	5.3E-02	1.5E-02	0.0E+00	4.5E-04	1.78E+02
100K	3.16E+02	1.8E+02	9.0E-04	2.0E-03	6.1E-01	29.5	29.5	0.0	0.2	0.0	0.2	1.9	3.0	0.7	1.3	0.8	1.3	10.5	3.2	10.3	3.1	90.9	19.2	1.24E+03	1.8	0.0	0.3	1.5	1.8	20.8	4.5	14.0	17.5	1.3E-03	1.7E-03	1.9E-02	4.0E-03	0.0E+00	1.8E-04	3.16E+02
1K	5.62E+02	3.3E+02	1.9E-04	4.3E-04	2.3E-01	28.6	27.9	0.0	0.2	0.0	0.3	3.3	4.6	1.2	1.8	1.3	1.9	17.5	4.3	17.2	4.4	123.1	27.3	2.23E+03	0.8	0.0	0.4	2.5	2.6	34.7	6.2	13.9	14.7	4.7E-04	4.9E-04	6.6E-03	1.2E-03	0.0E+00	3.8E-05	5.62E+02
1K	1.00E+03	1.0E+03	6.0E-05	9.0E-05	1.1E-01	28.5	29.8	0.1	0.3	0.1	0.4	5.8	6.1	2.1	2.6	2.2	2.7	28.7	6.3	28.0	6.0	174.9	41.3	3.97E+03	0.7	0.2	0.5	4.4	3.8	56.7	8.7	13.0	11.4	2.6E-04	2.3E-04	3.4E-03	5.2E-04	6.0E-06	1.8E-05	1.00E+03
1K	3.16E+03	3.8E+03	2.5E-06	4.0E-06	2.7E-02	27.3	27.9	0.1	0.5	0.2	0.6	16.6	16.6	6.0	6.1	6.7	6.7	73.9	14.7	72.1	14.1	384.0	103.9	1.25E+04	0.7	0.3	0.8	12.7	9.0	146.9	20.4	11.5	8.3	3.2E-05	2.3E-05	3.7E-04	5.1E-05	2.5E-07	1.3E-06	3.16E+03
1K	1.00E+04	1.2E+04	1.7E-07	1.8E-07	3.8E-03	26.7	27.0	0.5	1.0	0.9	1.6	5.6E+01	6.7E+01	19.9	23.0	21.8	25.0	199.9	38.2	194.8	36.2	956.2	290.9	3.99E+04	0.3	1.4	1.9	40.7	34.0	394.7	52.6	9.5	7.8	7.1E-06	5.8E-06	6.7E-05	8.9E-06	8.5E-08	1.7E-07	1.00E+04
1K	3.16E+04	3.8E+04	6.0E-09	8.0E-09	5.4E-04	21.9	23.0	0.4	0.9	0.8	1.5	9.7E+01	5.6E+01	35.1	19.4	37.9	10.9	443.6	82.9	433.8	79.9	2602.2	704.6	1.26E+05	0.6	1.2	1.7	72.9	22.3	877.4	115.1	12.0	4.0	4.4E-07	1.3E-07	5.3E-06	6.9E-07	2.4E-09	5.4E-09	3.16E+04
1K	1.00E+05	1.2E+05	2.9E-10	3.6E-10	7.7E-05	20.8	20.3

Table XIV: Multiplicity and response function study in the USC for incidence angle ranges of primary He in the atmosphere of [49.4, 58.3]°, [58.3, 69.5]° and [0, 69.5]° (total particle counts for all zenith angle range).

E:z:Z=0.3	Ener:A:GeV	DEne	Flux	Flux1AS	If:m^2.s	H:(g/cm2)	cH:(g/cm2)	nProt	nProt	nNeut	nNeut	nGam	nGam	nPos	nPos	nEle	nEle	nMup	nMup	nMun	nMun	nDecM	nEDM	EneSum	%Lost	Npiks	cSpikN	Nelkp	cNelkp	Nmm	cNmm	Mu/Em	cMu/Em	Nm*Fix	cNm*Fix	Nnm*Fix	cNnm*Fix	Nep*Fix	cNep*Fix	Ener:A:eV
100K	1.00E+01	1.5E+00	5.0E+00	2.8E+01	1.0E+02	27.5	27.6	0.0	0.0	0.0	0.0	0.0	0.0	0.0	0.0	0.0	0.0	0.0	0.0	0.1	0.0	6.1	1.3	3.19E+01	20.3	0.0	0.0	0.0	0.0	0.0	0.1	0.0	#DIV/0!	3.4E-03	1.3E-01	0.0E+00	7.5E-01	0.0E+00	0.0E+00	1.00E+01
100K	1.33E+01	3.9E+00	3.0E+00	1.3E+01	6.4E+01	27.5	27.6	0.0	0.0	0.0	0.0	0.0	0.1	0.0	0.0	0.0	0.4	0.0	0.1	0.0	0.1	8.8	1.9	4.40E+01	17.4	0.0	0.0	0.0	0.4	0.0	0.1	0.0	#DIV/0!	8.2E-03	1.3E+00	0.0E+00	4.2E-01	0.0E+00	0.0E+00	1.33E+01
100K	1.78E+01	5.2E+00	1.5E+00	5.9E+00	3.9E+01	27.4	27.6	0.0	0.0	0.0	0.0	0.0	0.1	0.0	0.1	0.0	0.1	0.1	0.2	0.1	0.2	12.3	2.6	6.09E+01	14.4	0.0	0.0	0.0	0.1	0.2	0.3	20.0	236.9	1.4E-02	1.6E-01	3.0E-01	4.2E-01	0.0E+00	0.0E+00	1.78E+01
100K	2.37E+01	6.8E+00	1.0E+00	2.7E+00	2.4E+01	27.5	27.7	0.0	0.0	0.0	0.0	0.0	0.2	0.0	0.1	0.0	0.1	0.1	0.4	0.1	0.4	16.7	3.4	8.29E+01	12.5	0.0	0.0	0.0	0.2	0.2	0.6	9.8	81.0	2.0E-02	1.6E-01	2.6E-01	5.7E-01	0.0E+00	0.0E+00	2.37E+01
100K	3.16E+01	9.2E+00	4.0E-01	1.3E+00	1.5E+01	27.2	27.4	0.0	0.0	0.0	0.0	0.1	0.3	0.0	0.2	0.0	0.2	0.3	0.6	0.3	0.5	22.5	4.5	1.15E+02	9.0	0.0	0.0	0.0	0.3	0.6	0.8	12.9	73.1	1.9E-02	1.8E-01	2.4E-01	3.1E-01	0.0E+00	0.0E+00	3.16E+01
100K	4.22E+01	1.2E+01	2.3E-01	5.8E-01	9.0E+00	27.3	27.3	0.0	0.0	0.0	0.0	0.1	0.5	0.0	0.3	0.0	0.3	0.6	0.8	0.6	0.7	29.2	5.7	1.58E+02	5.5	0.0	0.0	0.1	0.4	1.2	1.1	13.5	56.7	2.0E-02	8.3E-02	2.8E-01	2.4E-01	0.0E+00	0.0E+00	4.22E+01
100K	5.62E+01	1.6E+01	1.0E-01	2.7E-01	5.5E+00	27.2	27.3	0.0	0.0	0.0	0.0	0.1	0.2	0.7	0.1	0.3	0.1	0.3	1.1	1.0	1.0	1.0	1.0	35.9	7.0	2.17E+02	3.4	0.0	0.1	0.1	0.5	2.1	1.4	14.5	49.2	1.4E-02	4.8E-02	2.1E-01	1.4E-01	0.0E+00	0.0E+00	5.62E+01
100K	7.50E+01	2.2E+01	5.0E-02	1.2E-01	3.4E+00	27.1	27.1	0.0	0.0	0.0	0.0	0.1	0.3	0.9	0.1	0.4	0.1	0.5	1.7	1.2	1.5	1.2	43.5	8.4	2.93E+02	2.4	0.0	0.1	0.2	0.6	3.2	1.7	13.9	39.0	1.1E-02	3.2E-02	1.6E-01	8.5E-02	0.0E+00	0.0E+00	7.50E+01
100K	1.00E+02	4.7E+01	2.5E-02	5.6E-02	2.8E+00	25.5	25.7	0.0	0.0	0.0	0.0	0.1	0.4	1.1	0.1	0.5	0.2	0.5	2.2	1.4	2.1	1.4	51.4	8.2	3.86E+02	3.5	0.0	0.1	0.3	0.7	4.3	2.0	14.2	34.4	7.6E-03	1.8E-02	1.1E-01	4.9E-02	0.0E+00	0.0E+00	1.00E+02
100K	1.78E+02	1.0E+02	4.5E-03	1.2E-02	1.6E+00	25.2	25.4	0.0	0.1	0.0	0.1	0.8	1.7	0.3	0.8	0.3	0.8	4.6	2.1	4.5	2.0	71.0	11.5	6.96E+02	2.2	0.0	0.1	0.6	1.1	9.1	2.9	14.5	25.8	2.8E-03	5.0E-03	4.1E-02	1.3E-02	0.0E+00	4.5E-04	1.78E+02
100K	3.16E+02	1.8E+02	9.0E-04	2.5E-03	6.1E-01	25.0	25.1	0.0	0.1	0.0	0.1	1.5	2.6	0.6	1.1	0.6	1.2	8.4	2.8	8.2	2.8	95.8	16.1	1.24E+03	1.7	0.0	0.1	1.2	1.6	16.6	4.0	14.2	20.1	1.0E-03	1.5E-03	1.5E-02	3.6E-03	0.0E+00	9.0E-05	3.16E+02
1K	5.62E+02	3.3E+02	1.9E-04	5.3E-04	2.3E-01	26.0	27.3	0.0	0.1	0.0	0.1	2.9	4.1	1.0	1.7	1.1	1.7	14.7	4.0	14.4	3.9	130.8	23.5	2.23E+03	0.8	0.0	0.1	2.1	2.4	29.1	5.6	13.6	15.3	4.1E-04	4.5E-04	5.5E-03	1.1E-03	0.0E+00	1.9E-05	5.62E+02
1K	1.00E+03	1.0E+03	6.0E-05	1.1E-04	1.1E-01	24.7	25.0	0.0	0.2	0.0	0.2	4.8	7.1	1.8	2.9	1.9	3.3	23.5	5.6	23.3	5.4	183.0	34.3	3.98E+03	0.6	0.0	0.3	3.7	4.4	46.8	7.8	12.6	15.0	2.2E-04	2.6E-04	2.6E-03	4.7E-04	0.0E+00	1.2E-05	1.00E+03
1K	3.16E+03	3.8E+03	2.5E-06	5.0E-06	2.7E-02	24.1	25.3	0.0	0.2	0.1	0.3	11.4	10.1	4.1	3.9	4.5	4.1	60.6	12.6	59.1	12.4	395.2	83.3	1.26E+04	0.6	0.1	0.4	8.7	5.7	119.7	17.7	13.8	9.2	2.2E-05	1.4E-05	3.0E-04	4.4E-05	0.0E+00	5.0E-07	3.16E+03
1K	1.00E+04	1.2E+04	1.7E-07	2.2E-07	3.8E-03	22.2	21.4	0.1	0.4	0.2	0.7	3.3E+01	2.3E+01	12.1	8.4	13.0	9.3	160.6	31.4	157.0	31.0	973.1	234.7	3.99E+04	0.3	0.3	0.8	25.1	12.5	317.6	44.1	12.6	6.5	4.3E-06	2.1E-06	5.4E-05	7.5E-06	1.7E-08	6.8E-08	1.00E+04
1K	3.16E+04	3.8E+04	6.0E-09	1.0E-08	5.4E-04	21.9	23.0	0.4	0.9	0.8	1.5	9.61E+01	5.56E+01	35.1	19.4	37.9	20.9	443.6	82.9	433.8	79.9	2602.2	704.6	1.26E+05	0.6	1.2	1.7	72.9	28.5	877.4	115.1	12.0	5.0	4.4E-07	1.7E-07	5.9E-06	6.9E-07	2.4E-09	5.4E-09	3.16E+04
1K	1.00E+05	1.2E+05	2.9E-10	4.5E-10	7.7E-05	20.8	20.3	1.5	2.4	3.0	3.6	3.2E+02	2.6E+02	1.1E+02	8.5E+01	1.3E+02	9.3E+01	1261.1	225.7	1231.6	215.5	7120.6	2136.0	3.99E+05	0.2	4.5	4.3	239.5	126.5	2492.7	312.1	10.4	5.6	6.5E-08	3.7E-08	7.2E-07	9.0E-08	4.4E-10	7.0E-10	1.00E+05
1K	3.16E+05	1.4E+05	1.5E-11	2.0E-11	1.1E-05	21.3	22.3	5.3	7.4	11.0	12.6	1.1E+03	1.0E+03	3.7E+02	3.4E+02	4.0E+02	3.7E+02	3578.6	581.8	3493.1	567.5	19745.7	6414.4	1.26E+06	0.5	16.3	14.6	768.1	584.0	7071.7	812.7	9.2	6.1	1.2E-08	7.6E-09	1.1E-07	1.2E-08	8.0E-11	1.3E-10	3.16E+05
E:z:Z=0.4	Ener:A:GeV	DEne	Flux	Flux1AS	If:m^2.s	H:(g/cm2)	cH:(g/cm2)	nProt	nProt	nNeut	nNeut	nGam	nGam	nPos	nPos	nEle	nEle	nMup	nMup	nMun	nMun	nDecM	nEDM	EneSum	%Lost	Npiks	cSpikN	Nelkp	cNelkp	Nmm	cNmm	Mu/Em	cMu/Em	Nm*Fix	cNm*Fix	Nnm*Fix	cNnm*Fix	Nep*Fix	cNep*Fix	Ener:A:eV
100K	1.00E+01	1.5E+00	5.0E+00	3.9E+01	1.0E+02	29.8	21.0	0.0	0.0	0.0	0.0	0.0	0.0	0.0	4.0	0.0	0.0	0.0	0.0	0.0	0.0	6.1	0.9	3.21E+01	19.8	0.0	0.0	0.0	4.0	0.0	0.0	0.0	#DIV/0!	2.2E-02	2.0E-01	0.0E+00	0.0E+00	0.0E+00	0.0E+00	1.00E+01
100K	1.33E+01	3.9E+00	3.0E+00	1.8E+01	6.4E+01	29.7	21.0	0.0	0.0	0.0	0.0	0.0	0.0	0.0	0.0	0.0	0.0	0.0	0.1	0.0	0.1	8.8	1.4	4.42E+01	16.8	0.0	0.0	0.0	0.0	0.0	0.1	0.0	#DIV/0!	2.0E-03	7.8E-02	0.0E+00	4.2E-01	0.0E+00	0.0E+00	1.33E+01
100K	1.78E+01	5.2E+00	1.5E+00	8.3E+00	3.9E+01	28.6	20.8	0.0	0.0	0.0	0.0	0.0	0.1	0.0	0.0	0.0	0.0	0.0	0.1	0.0	0.1	12.5	1.9	6.13E+01	13.9	0.0	0.0	0.0	0.1	0.0	0.1	0.0	#DIV/0!	4.9E-03	9.6E-02	0.0E+00	2.1E-01	0.0E+00	0.0E+00	1.78E+01
100K	2.37E+01	6.8E+00	1.0E+00	3.0E+00	2.4E+01	28.7	20.9	0.0	0.0	0.0	0.0	0.0	0.1	0.0	0.1	0.0	0.1	0.1	0.2	0.1	0.2	16.9	2.6	8.34E+01	12.1	0.0	0.0	0.0	0.1	0.2	0.3	22.7	268.6	8.8E-03	1.8E-01	2.0E-01	2.8E-01	0.0E+00	0.0E+00	2.37E+01
100K	3.16E+01	9.2E+00	4.0E-01	1.8E+00	1.5E+01	28.7	21.1	0.0	0.0	0.0	0.0	0.0	0.2	0.0	0.1	0.0	0.1	0.1	0.4	0.1	0.4	23.0	3.3	1.15E+02	8.6	0.0	0.0	0.0	0.2	0.2	0.6	9.3	78.0	8.6E-03	6.8E-02	8.0E-02	2.3E-01	0.0E+00	0.0E+00	3.16E+01
100K	4.22E+01	1.2E+01	2.3E-01	8.1E-01	9.0E+00	28.5	20.7	0.0	0.0	0.0	0.0	0.1	0.4	0.0	0.2	0.0	0.2	0.3	0.6	0.3	0.5	30.2	4.2	1.60E+02	5.2	0.0	0.0	0.0	0.3	0.6	0.8	13.5	80.1	1.0E-02	5.9E-02	1.4E-01	1.8E-01	0.0E+00	0.0E+00	4.22E+01
100K	5.62E+01	1.6E+01	1.0E-01	3.7E-01	5.5E+00	28.5	20.8	0.0	0.0	0.0	0.0	0.1	0.6	0.0	0.3	0.0	0.3	0.6	0.8	0.5	0.7	37.4	5.1	2.18E+02	3.1	0.0	0.0	0.0	0.3	0.4	1.1	3.1	13.3	60.6	8.3E-03	3.7E-02	1.1E-01	1.3E-01	0.0E+00	0.0E+00	5.62E+01
100K	7.50E+01	2.2E+01	5.0E-02	1.7E-01	3.4E+00	28.4	20.7	0.0	0.0	0.0	0.0	0.2	0.7	0.1	0.3	0.1	0.4	1.0	1.0	0.9	0.9	45.5	6.2	2.94E+02	2.1	0.0	0.0	0.0	0.3	0.5	1.9	1.3	14.3	54.0	6.6E-03	2.5E-02	9.5E-02	6.7E-02	0.0E+00	0.0E+00	7.50E+01
100K	1.00E+02	4.7E+01	2.5E-02	7.9E-02	2.8E+00	19.3	19.5	0.0	0.0	0.0	0.0	0.2	0.9	0.1	0.4	0.1	0.4	1.3	1.1	1.2	1.1	54.0	6.0	3.86E+02	3.4	0.0	0.0	0.0	0.2	0.6	2.5	1.6	13.9	45.1	4.5E-03	1.4E-02	6.3E-02	3.9E-02	0.0E+00	0.0E+00	1.00E+02
100K	1.78E+02	1.0E+02	4.5E-03	1.7E-02	1.6E+00	19.1	19.3	0.0	0.0	0.0	0.0	0.5	1.4	0.2	0.6	0.2	7.0	2.9	1.7	2.8	1.7	75.1	8.4	6.97E+02	2.1	0.0	0.0	0.4	7.0	5.7	2.4	14.1	242.8	1.8E-03	3.1E-02	2.6E-02	1.1E-02	0.0E+00	0.0E+00	1.78E+02
100K	3.16E+02	1.8E+02	9.0E-04	3.5E-03	6.1E-01	18.7	18.9	0.0	0.0	0.0	0.0	1.0	2.3	0.4	0.9	0.4	1.0	5.6	2.4	5.5	2.4	101.8	11.6	1.24E+03	1.6	0.0	0.0	0.8	1.4	11.1	3.4	14.0	25.2	7.1E-04	1.3E-03	1.0E-02	3.1E-03	0.0E+00	0.0E+00	3.16E+02
1K	5.62E+02	3.3E+02	1.9E-04	7.5E-04	2.3E-01	19.3	19.9	0.0	0.0	0.0	0.0	2.0	3.2	0.7	1.4	0.8	1.5	10.1	3.4	9.9	3.2	138.1	16.7	2.23E+03	0.7	0.0	0.0	1.5	2.0	20.0	4.7	13.4	18.5	2.8E-04	3.8E-04	3.8E-03	9.5E-04	0.0E+00	0.0E+00	5.62E+02
1K	1.00E+03	1.0E+03	6.0E-05	1.6E-04	1.1E-01	18.1	19.1	0.0	0.0	0.0	0.1	3.5	5.1	1.3	2.0	1.3	2.1	16.7	4.5	16.7	4.5	192.7	24.2	3.98E+03	0.5	0.0	0.1	2.6	2.9	33.4	6.4	12.8	14.5	1.6E-04	1.7E-04	2.0E-03	3.8E-04	0.0E+00	0.0E+00	1.00E+03
1K	3.16E+03	3.8E+03	2.5E-06	7.0E-06	2.7E-02	18.0	17.3	0.0	0.1	0.0	0.1	8.4	9.9	3.2	3.9	3.4	4.2	43.8	10.2	43.1	9.8	407.8	58.7	1.26E+04	0.5	0.0	0.1	6.6	5.7	86.9	14.1	13.2	11.7	1.6E-05	1.4E-05	2.2E-04	3.5E-05	0.0E+00	2.5E-07	3.16E+03
1K	1.00E+04	1.2E+04	1.7E-07	3.1E-07	3.8E-03	17.0	17.2	0.0	0.1	0.0	0.2	2.3E+01	1.8E+01	8.4	6.4	9.1	7.2	115.3	25.1	112.8	24.3	973.0	159.2	3.99E+04	0.2	0.0	0.2	17.5	3.6	228.1	34.9	13.1	7.5	3.0E-06	1.6E-06	3.9E-05	5.9E-06	0.0E+00	1.7E-08	1.00E+04
1K	3.16E+04	3.8E+04	6.0E-09	1.4E-08	5.4E-04	16.0	16.3	0.0	0.3	0.1	0.4	6.12E+00	3.23E+01	22.5	11.8	24.3	12.9	309.7	65.4	305.1	63.9	2604.2	473.3	1.26E+05	0.5	0.1	0.5	46.9	17.5	614.8	91.4	13.1	5.3	2.8E-07	1.1E-07	3.7E-06	5.5E-07	0.0E+00	1.8E-09	3.16E+04
1K	1.00E+05	1.2E+05	2.9E-10	6.3E-10	7.7E-05	15.5	15.5	2.0	0.6	0.4	1.0	1.7E+02	5.8E+01	6.4E+01	2.2E+01	6.9E+01	2.4E+01	866.9	179.2	853.6	173.5	7193.0	1446.0	3.99E+05	0.2	2.4	1.2	132.7	32.2	1720.5	249.4	13.0	3.7	3.8E-08	9.3E-09	5.0E-07	7.2E-08	5.8E-10	1.7E-10	1.00E+05
1K	3.16E+05	1.4E+05	1.5E-11	2.8E-11	1.1E-05	14.9	14.7	0.5	1.1	1.3	1.8	4.8E+02	1.3E+02	1.8E+02	4.8E+01	1.9E+02	5.2E+01	2435.3	488.0	2385.7	472.0	19987.2	4482.1	1.26E+06	0.5	1.8	2.1	370.4	71.9	4821.0	678.9	13.0	3.1	5.6E-09	1.1E-09	7.2E-08	1.0E-08	7.3E-12	1.7E-11	3.16E+05
E:z:Z=0.4	Ener:A:GeV	DEne	Flux	TFlux	Flux:m^2.s	H:(g/cm2)	cH:(g/cm2)	nProt	nProt	nNeut	nNeut	nGam	nGam	nPos	nPos	nEle	nEle	nMup	nMup	nMun	nMun	nDecM	nEDM	EneSum	%Lost	Npiks	cSpikN	Nelkp	cNelkp	Nmm	cNmm	Mu/Em	cMu/Em	Nm*Fix1e	Nnm*Fix1e	cNnm*Fix1e	Nep*Fix1e	cNep*Fix1e	Ener:A:eV
100K	1.00E+01	1.5E+00	5.0E+00	5.0E+00	8.4E+02			0.0	0.1	0.0	1.3	2.8	0.6	0.0	4.9	0.0	0.3	0.0	1.1	0.1	1.1	47.0	13.3		100.0	0.0	1.3	0.0	5.0	0.100	1.6	2.7	366.8	1.9E-01	6.4E+02	5.0E-01	6.1E+01	0.0E+00	2.5E-01	1.00E+01
100K	1.33E+01	3.9E+00	3.0E+00	3.0E+00	5.1E+02			0.0	0.3	0.0	0.5	0.1	1.0	0.0	0.6	0.1	1.0	0.5	1.9	0.5	2.1	67.0	19.3		100.0	0.0	0.6	0.1	1.2	1.000	2.8	10.4	131.3	2.9E-01	1.4E+03	3.8E+00	7.3E+01	0.0E+00	8.1E-01	1.33E+01
100K	1.78E+01	5.2E+00	1.5E+00	2.2E+00	3.2E+02			0.0	0.4	0.0	0.7	0.3	1.8	0.1	1.0	0.1	1.0	1.4	2.9	1.4	3.1	93.4	26.5		100.0	0.0	0.8	0.2	1.4	2.810	4.2	13.3	91.2	3.2E-01	4.4E+03	4.2E+00	4.1E+01	0.0E+00	4.4E-01	1.78E+01
100K	2.37E+01	6.8E+00	1.0E+00	1.5E+00	1.9E+02			0.0	0.6	0.0	0.9	0.4	2.7	0.2	1.4	0.2	1.5	2.7	4.4	2.7	4.4	125.8	35.1		100.0	0.0	1.1	0.4	2.0	5.400	6.2	12.4	58.5	4.4E-01	4.0E+00	5.4E+00	3.9E+01	0.0E+00	5.6E-01	2.37E+01
100K	3.16E+01	9.2E+00	4.0E-01	5.0E-01	1.2E+02			0.0	0.7	0.3	1.1	1.0	3.9	0.4	2.0	0.4	2.1	4.9	6.1	4.9	6.0	168.4	45.9		100.0	0.3	1.3	0.8	2.9	9.800	8.6	12.1	43.6	5.3E-01	1.3E+00	3.9E+00	1.2E+01	0.0E+00	7.8E-02	3.16E+01
100K	4.22E+01	1.2E+01	2.3E-01	2.7E-01	7.2E+01			0.1	1.0	0.2	1.2	1.8	5.7	0.7	6.9	0.7	2.9	8.9	8.1	8.6	7.7	218.0	57.7		100.0	0.3	1.6	1.4	7.5	17.500	11.2	12.3	65.0	3.3E-01	3.4E+00	4.0E+00	6.6E+00	2.3E-02	5.3E-02	4.22E+01
100K	5.62E+01	1.6E+01	1.0E-01	1.0E-01	4.4E+01			0.2	1.2	0.3	1.7	3.0	8.0	1.1	3.7	1.2	8.2	14.7	10.3	13.8	10.0	265.8	70.4		100.0	0.5	2.1	2.3	9.0	28.500	14.4	12.2	47.0	2.3E-01	9.8E-01	2.9E+00	2.1E+00	2.0E-02	1.4E-02	5.62E+01
100K	7.50E+01	2.2E+01	5.0E-02	5.0E-02	2.7E+01			0.3	1.5	0.5	2.0	4.5	10.5	1.7	4.7	1.8	5.0	21.8	12.4	20.4	12.1	321.3	84.5		100.0	0.8	2.5	3.5	6.9	42.200	17.3	12.1	24.5	1.7E-01	1.2E-01	2.1E+00	7.5E-01	1.5E-02	5.6E-03	7.50E+01
100K	1.00E+02	4.7E+01	2.5E-02	2.8E-02	2.2E+01			0.3	1.5	0.5	1.9	5.9	12.5	2.2	5.5	2.4	5.9	28.7	14.1	27.8	14.1	377.6	83.5		100.0	0.8	2.4	4.6	8.0	56.500	19.8	12.2	21.7	1.2E-01	4.8E-02	1.4E+00	2.5E-01	7.3E-03	1.4E-03	1.00E+02
100K	1.78E+02	1.0E+02	4.5E-03	4.5E-03	1.3E+01			0.5	1.9	0.7	2.5	11.9	20.9	4.4	8.6	4.7	15.6	54.8	20.3	53.6	19.9	518.5	116.8		100.0	1.2	3.1	9.3	17.8	168.400	28.4	11.9	23.4	4.1E-02	7.1E-03	4.9E-01	1.6E-02	2.3E-03	7.3E-05	1.78E+02
100K	3.16E+02	1.8E+02	9.0E-04	1.3E-03	4.8E+00			0.7	2.4	1.1	3.2	22.6	35.5	8.1	13.7	8.8	14.9	95.6	27.9	93.7	27.4	699.7	163.5		100.0	1.8	4.0	16.9	29.3	189.330	39.1	11.2	13.7	1.5E-02	3.3E-04	1.7E-01	1.2E-03	6.3E-04	4.7E-06	3.16E+02
1K	5.62E+02	3.3E+02	1.9E-04	2.1E-04	1.8E+00			1.2	3.0	1.7	4.0	42.4	62.0	14.7	22.7	16.1	24.5	160.0	39.2	156.9	38.6	957.7	237.9		100.0	2.9	5.0	30.8	33.4	316.900	55.0	10.3	10.3	5.8E-03	4.0E-05	6.0E-02	1.5E-04	2.3E-04	3.2E-07	5.62E+02
1K	1.00E+03	1.0E+03	6.0E-05	5.0E-05	8.5E-01			1.8	4.0	2.8	5.4	83.1	117.1	28.5	40.9	31.2	44.7	257.8	57.1	254.6	55.9	1347.6	353.9		100.0	4.6	8.7	59.7	60.6	532.400	79.9	8.6	8.8	3.6E-03	1.3E-05	3.1E-02	2.3E-05	1.1E-04	5.8E-08	1.00E+03
1K	3.16E+03	3.8E+03	2.5E-06	3.8E-06	2.2E-01			4.5	7.5	7.4	10.5	315.3	393.4	103.0	131.7	100.8	143.7	668.4	138.1	651.7	133.6	2950.8	886.3		100.0	13.9	12.9	203.8	194.9	1320.140	192.1	6.5	6.3	5.1E-04	2.4E-07	3.3E-03	2.3E-07	1.1E-05	2.5E-10	3.16E+03
1K	1.00E+04	1.2E+04	1.7E-07	2.3E-07	3.1E-02			14.8	16.8	23.6	23.5	1.4E+03	1.5E+03	4.5E+02	4.9E+02	5.1E+02	5.4E+02	1.8E+03	3.5E+02	1.8E+03	3.4E+02	7.3E+03	2.5E+03		100.0	38.4	28.9	953.3	7.3E+02	3.6E+03	4.9E+02	5.8	2.9	1.6E-04	1.5E-08	6.1E-04	7.0E-09	2.5E-06	8.2E-12	1.00E+04
1K	3.16E+04	3.8E+04	6.0E-09	8.0E-08	4.3E-03			48.6	40.8	78.8	59.6	6.1E+03	5.3E+03	1.5E+03	1.7E+03	2.1E+03	1.9E+03	5.0E+03	9.1E+02	4.8E+03	8.7E+02	1.9E+04	7.1E+03		100.0	127.4	72.2	4026.1	2.5E+03	9.8E+03	1.3E+03	2.4	1.6	2.4E-05	2.3E-10	5.9E-05	5.7E-11	2.9E-07	6.0E-14	3.16E+04
1K	1.00E+05	1.2E+05	2.9E-10	2.0E-10	6.1E-04			175.6	112.7	278.7	165.6	2.8E+04	2.1E+04	8.8E+03	7.0E+03	9.9E+03	7.7E+03	1.4E+04	2.4E+03	1.4E+04	2.3E+03	5.3E+04	#VALUE!		100.0	454.3	2.0E+02	18715.7	1.0E+04	2.8E+04	3.3E+03	1.5	0.9	5.4E-06	9

Table XV: Multiplicity and response function study in the USC for incidence angle ranges of primary C in the atmosphere of [0.12.8]°, [12.8, 22.3]° and [22.3, 29]°.

Tabla de simulaciones de la red CORSAIR. Administrador: Yanis Fontenla (USC), yanis.fontenla@rai.usc.es

USC	Site:	Univ. de Santiago de Compostela. Fisd. de Física, ala norte	G. Coord(°):	42.88	-8.56	MField(nT)	24.2	38.5	Height(m):	235

	Flags:	HADFLG,HADFLG,0 0 0 0 0	Zaxis	H,M,E,(	0.3	0.3	0.06	0.1	GeV	Zangles(°):	0	12.8	22.3	29	34.4	41.4	49.4	58.3	69.5
	TFlux: 1.8*10^4*E^-2.7 /(m^2.s.sr.GeV)				0.79	protons	2pi:	6.3	dCosZA	0.05	dSolangle	0.314			Fo=	1.80E+04	Fo/1.7=	1.06E+04	

nEv=cZ=1	E:A.GeV	DEne	Flux	FluxIAS	E=m^2.s	H(g/cm2)	sH(g/cm2)	nProt	dProt	nNeut	dNeut	nGam	dGam	nPos	dPos	nElec	dElec	nMup	dMup	nMun	dMun	nDecM	nEDM	EneSum	%LostE	NpKe	sNpKN	NeKp	sNeKp	Nemu	sNemu	Mu/Em	sMu/Em	Nm*Fk	sNm*Fk	Nnm*Fk	sNnm*Fk	Nnp*Fk	sNnp*Fk	Ene:A.GeV
100K	1.00E+01	1.5E+00	2.3E-01	4.5E+00	1.0E+02	26.2	26.1	0.0	0.1	0.0	0.2	0.0	0.2	0.0	0.1	0.0	0.1	0.1	0.4	0.1	0.4	17.0	5.9	9.49E+01	21.0	0.0	0.2	0.0	0.2	0.2	0.6	8.2	60.2	5.6E-03	3.8E-02	4.6E-02	1.3E-01	8.0E+00	2.3E-02	1.00E+01
100K	1.33E+01	3.9E+00	1.8E-01	2.1E+00	6.4E+01	26.2	26.2	0.0	0.1	0.0	0.2	0.1	0.3	0.0	0.2	0.0	0.2	0.4	0.6	0.4	0.6	24.4	8.4	1.32E+02	17.4	0.0	0.2	0.1	0.3	0.8	0.8	11.8	50.0	1.2E-02	5.0E-02	1.4E-01	1.5E-01	8.0E+00	1.8E-02	1.33E+01
100K	1.78E+01	5.2E+00	1.2E-01	9.4E-01	3.9E+01	26.3	26.3	0.0	0.2	0.1	0.3	0.2	0.6	0.1	0.3	0.1	0.3	0.9	0.9	0.9	0.9	33.6	11.7	1.82E+02	14.6	0.1	0.4	0.2	0.4	1.8	1.3	11.6	33.4	2.0E-02	5.6E-02	2.3E-01	1.7E-01	8.0E+00	2.5E-02	1.78E+01
100K	2.37E+01	6.8E+00	7.0E-02	4.3E-01	2.4E+01	26.3	26.3	0.1	0.3	0.1	0.4	0.4	0.8	0.1	0.4	0.1	0.4	1.6	1.6	1.6	1.6	45.1	15.5	2.49E+02	12.4	0.2	0.5	0.3	0.6	3.2	2.3	11.3	25.4	2.0E-02	4.2E-02	2.2E-01	1.5E-01	7.0E-03	2.1E-02	2.37E+01
100K	3.16E+01	9.2E+00	5.0E-02	2.0E-01	1.5E+01	26.1	26.2	0.1	0.3	0.2	0.5	0.6	1.2	0.2	0.6	0.3	0.6	2.9	1.7	2.9	1.7	59.8	20.1	3.44E+02	9.3	0.3	0.6	0.5	0.8	5.8	2.4	11.5	19.6	2.5E-02	4.2E-02	2.5E-01	1.2E-01	5.0E-03	1.5E-02	3.16E+01
100K	4.22E+01	1.2E+01	3.0E-02	9.1E-02	9.0E+00	26.3	26.3	0.1	0.4	0.2	0.6	1.1	1.7	0.4	0.8	0.4	0.8	4.9	2.2	4.7	2.2	76.4	25.2	4.75E+02	6.2	0.3	0.7	0.9	1.1	9.6	3.1	11.1	15.1	2.6E-02	3.4E-02	2.9E-01	9.3E-02	3.0E-03	1.2E-02	4.22E+01
100K	5.62E+01	1.6E+01	2.0E-02	4.2E-02	5.5E+00	26.2	26.1	0.2	0.5	0.4	0.7	1.8	2.4	0.7	1.0	0.7	1.1	7.8	2.8	7.4	2.7	92.4	30.8	6.48E+02	3.9	0.6	0.9	1.4	1.5	15.2	3.9	10.8	12.1	2.6E-02	3.1E-02	3.0E-01	7.8E-02	4.0E-03	1.0E-02	5.62E+01
100K	7.50E+01	2.2E+01	1.0E-02	1.9E-02	3.4E+00	26.2	26.2	0.3	0.6	0.5	0.8	2.8	3.2	1.0	1.4	1.1	1.5	11.3	3.4	10.7	3.3	111.1	37.1	8.76E+02	2.7	0.8	1.0	2.1	2.0	22.0	4.7	10.4	10.1	2.1E-02	2.9E-02	2.2E-01	4.7E-02	3.0E-03	6.9E-03	7.50E+01
100K	1.00E+02	4.7E+01	5.0E-03	8.9E-03	2.8E+00	26.2	26.2	0.3	0.6	0.5	0.8	3.8	4.0	1.4	1.7	1.5	1.8	15.5	4.0	15.2	4.0	126.2	38.2	1.16E+03	3.7	0.8	1.0	2.9	2.4	30.7	5.7	10.7	9.3	1.4E-02	1.2E-02	1.5E-01	2.8E-02	1.5E-03	3.3E-03	1.00E+02
100K	1.78E+02	1.0E+02	8.5E-04	1.9E-03	1.6E+00	25.9	25.9	0.8	0.7	1.0	1.1	7.1	2.7	2.8	3.0	3.0	28.4	28.4	5.6	27.8	5.6	172.2	53.3	2.09E+03	2.2	1.8	1.3	5.7	28.6	56.2	7.9	9.8	49.0	4.9E-03	2.4E-02	4.8E-02	6.7E-03	6.8E-04	6.0E-04	1.78E+02
100K	3.16E+02	1.8E+02	2.0E-04	4.0E-04	6.1E-01	25.6	25.6	0.7	1.0	1.1	1.3	15.0	13.2	5.1	4.8	5.6	5.2	48.1	7.9	47.1	7.8	232.4	74.6	3.73E+03	1.6	1.8	1.6	10.8	7.1	95.2	10.1	8.8	5.9	2.2E-03	1.4E-03	1.9E-02	2.2E-03	1.4E-04	2.9E-04	3.16E+02
1K	5.62E+02	3.3E+02	4.5E-05	8.4E-05	2.3E-01	25.1	25.2	1.1	1.4	1.8	1.7	28.9	24.6	9.7	8.6	10.7	9.5	78.9	11.8	77.3	11.4	319.9	108.2	6.67E+03	1.1	2.9	2.2	20.4	12.8	156.2	16.4	7.7	4.9	9.2E-04	5.8E-04	7.0E-03	7.4E-04	5.0E-05	6.3E-05	5.62E+02
1K	1.00E+03	1.0E+03	1.0E-05	1.8E-05	1.1E-01	25.4	25.4	1.7	1.8	2.6	2.2	58.7	48.3	19.1	15.8	21.3	17.7	126.0	17.4	122.8	16.9	452.3	162.1	1.19E+04	0.8	4.3	2.8	40.4	23.8	248.8	24.3	6.2	3.7	4.0E-04	2.4E-04	2.5E-03	2.4E-04	1.7E-05	1.8E-05	1.00E+03
1K	3.16E+03	3.8E+03	4.5E-07	7.9E-07	2.7E-02	24.8	24.0	4.4	3.3	6.8	4.6	268.8	201.5	85.4	66.1	94.8	72.3	327.1	46.1	319.2	45.0	1012.3	409.6	3.77E+04	0.6	11.2	5.7	180.2	97.9	646.3	64.4	3.6	2.0	8.1E-05	4.4E-05	2.9E-04	2.9E-05	2.0E-06	1.5E-06	3.16E+03
1K	1.00E+04	1.2E+04	2.0E-08	3.5E-08	3.8E-03	23.3	23.7	13.3	7.8	21.1	11.1	1.3E+03	8.3E+02	401.4	268.8	444.4	296.3	896.9	120.4	872.8	118.0	2515.3	1140.5	1.19E+05	0.4	34.4	13.6	845.8	400.0	1769.7	1.7E+2	2.1	1.0	1.7E-05	8.0E-06	3.5E-05	3.4E-06	2.7E-07	1.6E-07	1.00E+04
1K	3.16E+04	3.8E+04	9.0E-10	1.6E-09	5.4E-04	24.2	24.2	47.2	21.0	74.3	31.4	6.4E+03	3.3E+03	1977.5	1067.4	2093.6	1181.0	2562.5	316.9	2494.0	306.0	6583.1	3323.2	3.78E+05	0.4	121.3	37.8	4171.0	1.6E+03	5056.5	4.4E+2	1.2	0.5	3.8E-06	1.4E-06	4.6E-06	4.0E-07	4.2E-06	1.9E-08	3.16E+04
1K	1.00E+05	1.2E+05	5.0E-11	7.1E-11	7.7E-05	23.6	23.9	162.4	57.6	254.9	85.0	2.8E+04	1.2E+04	8.8E+03	3.9E+03	9.8E+03	4.3E+03	7372.4	889.7	7171.1	786.0	17525.7	9635.2	1.20E+06	0.3	417.3	102.7	18540.6	5.8E+03	14543.5	1.1E+3	0.8	0.3	9.3E-07	2.9E-07	7.3E-07	5.6E-08	8.1E-09	2.9E-09	1.00E+05
1K	3.16E+05	1.4E+05	2.1E-12	3.2E-12	1.1E-05	22.6	23.1	536.9	162.9	840.3	240.3	1.2E+05	4.4E+04	3.7E+04	1.4E+04	4.1E+04	1.6E+04	23057.1	2032.6	26481.0	1984.1	47146.4	27690.5	3.78E+06	0.3	1377.2	290.3	77258.6	2.1E+04	41538.1	2.8E+3	0.5	0.2	1.6E-07	4.4E-08	8.7E-08	6.0E-09	1.1E-09	3.4E-10	3.16E+05

cZ=0.9	E:A.GeV	DEne	Flux	FluxIAS	E=m^2.s	H(g/cm2)	sH(g/cm2)	nProt	dProt	nNeut	dNeut	nGam	dGam	nPos	dPos	nElec	dElec	nMup	dMup	nMun	dMun	nDecM	nEDM	EneSum	%LostE	NpKe	sNpKN	NeKp	sNeKp	Nemu	sNemu	Mu/Em	sMu/Em	Nm*Fk	sNm*Fk	Nnm*Fk	sNnm*Fk	Nnp*Fk	sNnp*Fk	Ene:A.eV
100K	1.00E+01	1.5E+00	2.3E-01	8.9E+00	1.0E+02	25.4	25.3	0.0	0.1	0.0	0.1	0.0	0.2	0.0	0.1	0.0	0.1	0.1	0.3	0.1	0.3	17.2	5.7	9.49E+01	20.9	0.0	0.1	0.0	0.15	0.2	0.4	9.9	75.2	4.7E-03	3.4E-02	4.6E-02	9.8E-02	8.0E+00	2.3E-02	1.00E+01
100K	1.33E+01	3.9E+00	1.8E-01	4.1E+00	6.4E+01	25.3	25.4	0.0	0.1	0.0	0.2	0.1	0.3	0.0	0.2	0.0	0.2	0.3	0.6	0.4	0.6	24.6	8.2	1.32E+02	17.4	0.0	0.2	0.1	0.26	0.7	0.8	11.6	52.5	1.1E-02	4.7E-02	1.3E-01	1.5E-01	8.0E+00	1.8E-02	1.33E+01
100K	1.78E+01	5.2E+00	1.3E-01	1.9E+00	3.9E+01	25.2	25.2	0.0	0.2	0.1	0.2	0.2	0.5	0.1	0.3	0.1	0.3	0.8	0.9	0.8	0.9	34.0	11.3	1.83E+02	14.5	0.1	0.3	0.1	0.40	1.6	1.3	11.9	36.5	1.8E-02	5.2E-02	2.1E-01	1.7E-01	8.0E+00	2.6E-02	1.78E+01
100K	2.37E+01	6.8E+00	7.0E-02	8.7E-01	2.4E+01	25.1	25.1	0.0	0.2	0.1	0.3	0.3	0.8	0.1	0.4	0.1	0.4	1.5	1.2	1.5	1.2	45.7	15.0	2.49E+02	12.4	0.1	0.4	0.2	0.56	3.0	1.7	12.1	28.1	1.7E-02	3.9E-02	2.1E-01	1.2E-01	8.0E+00	1.4E-02	2.37E+01
100K	3.16E+01	9.2E+00	5.0E-02	4.0E-01	1.5E+01	25.2	25.2	0.1	0.3	0.1	0.4	0.6	1.1	0.2	0.5	0.2	0.6	2.7	1.6	2.7	1.6	60.6	19.6	3.44E+02	9.3	0.2	0.5	0.4	0.78	5.4	2.3	12.2	22.0	2.2E-02	3.9E-02	2.7E-01	1.1E-01	5.0E-03	1.5E-02	3.16E+01
100K	4.22E+01	1.2E+01	3.0E-02	1.8E-01	9.0E+00	25.1	25.1	0.1	0.4	0.2	0.5	1.0	1.5	0.4	0.7	0.4	0.8	4.6	2.1	4.4	2.1	77.6	24.6	4.75E+02	6.2	0.3	0.6	0.8	1.06	9.0	3.0	11.8	17.0	2.3E-02	3.2E-02	2.7E-01	8.9E-02	3.0E-03	1.2E-02	4.22E+01
100K	5.62E+01	1.6E+01	2.0E-02	8.4E-02	5.5E+00	25.2	25.1	0.2	0.5	0.3	0.6	1.6	2.2	0.6	1.0	0.6	1.0	7.3	2.7	6.9	2.6	93.9	30.1	6.48E+02	3.9	0.5	0.8	1.2	1.42	14.2	3.7	11.4	13.4	2.5E-02	2.8E-02	2.9E-01	7.5E-02	4.0E-03	1.0E-02	5.62E+01
100K	7.50E+01	2.2E+01	1.0E-02	3.9E-02	3.4E+00	25.1	25.1	0.2	0.6	0.4	0.7	2.5	2.9	0.9	1.3	1.0	1.3	10.7	3.2	10.1	3.2	113.0	36.2	8.76E+02	2.7	0.6	0.9	1.9	1.84	20.8	4.5	11.1	11.1	1.9E-02	1.8E-02	2.1E-01	4.5E-02	2.0E-03	6.0E-03	7.50E+01
100K	1.00E+02	4.7E+01	5.0E-03	1.8E-02	2.8E+00	25.3	25.1	0.2	0.5	0.4	0.7	3.3	3.6	1.2	1.5	1.3	1.6	14.6	3.9	14.3	3.8	128.6	37.3	1.16E+03	3.7	0.6	0.9	2.5	2.23	28.9	5.4	11.3	10.2	1.3E-02	1.1E-02	1.4E-01	2.7E-02	1.9E-03	2.5E-03	1.00E+02
100K	1.78E+02	1.0E+02	8.5E-04	3.7E-03	1.6E+00	25.0	25.0	0.4	0.7	0.6	0.9	6.8	6.4	2.4	2.5	2.6	2.7	27.0	5.5	26.5	5.4	175.6	52.1	2.09E+03	2.2	1.8	1.1	5.0	3.70	53.5	7.7	10.6	7.9	4.3E-03	3.1E-03	4.5E-02	6.6E-03	3.4E-04	6.6E-04	1.78E+02
100K	3.16E+02	1.8E+02	2.0E-04	8.0E-04	6.1E-01	24.5	24.5	0.6	0.9	0.9	1.2	0.1	11.4	4.5	4.2	4.9	4.6	45.9	7.7	45.0	7.5	237.1	72.9	3.73E+03	1.6	1.5	1.5	9.3	6.20	90.9	10.7	9.7	6.6	1.9E-03	1.2E-03	1.8E-02	2.1E-03	1.2E-04	1.8E-04	3.16E+02
1K	5.62E+02	3.3E+02	4.5E-05	1.7E-04	2.3E-01	22.9	23.0	1.0	1.2	1.4	1.5	24.9	214.0	8.5	7.3	9.1	8.3	74.7	10.7	73.4	10.9	326.0	105.4	6.67E+03	1.1	2.4	1.9	17.6	11.07	148.1	15.3	8.4	5.4	7.9E-04	5.0E-04	6.7E-03	6.9E-04	4.5E-05	5.4E-05	5.62E+02
1K	1.00E+03	1.0E+03	1.0E-05	3.5E-05	1.1E-01	25.8	25.2	1.4	1.5	2.0	2.0	49.2	43.4	16.3	14.3	17.9	15.8	120.8	17.0	118.0	16.8	458.9	158.3	1.19E+04	0.8	3.4	2.5	34.2	21.29	238.8	23.9	7.0	4.4	3.4E-04	2.1E-04	2.4E-03	2.4E-04	1.4E-05	1.5E-05	1.00E+03
1K	3.16E+03	3.8E+03	4.5E-07	1.6E-06	2.7E-02	22.4	22.9	3.5	2.9	5.5	3.9	210.6	171.9	67.9	57.1	75.2	63.3	311.6	41.6	303.5	41.0	1023.9	396.8	3.77E+04	0.6	9.0	4.9	143.2	85.22	615.1	58.4	4.3	2.6	6.4E-05	3.8E-05	2.0E-04	2.6E-05	1.6E-06	1.3E-06	3.16E+03
1K	1.00E+04	1.2E+04	2.0E-08	7.1E-08	3.8E-03	23.3	24.1	11.0	7.1	17.8	10.0	1.0E+03	6.5E+02	317.4	211.0	352.3	232.9	858.0	117.2	816.5	112.4	2561.2	1119.2	1.20E+05	0.4	28.8	12.3	669.7	314.22	1675.5	162.4	2.5	1.2	1.3E-05	6.3E-06	3.4E-05	3.2E-06	2.2E-07	1.4E-07	1.00E+04
1K	3.16E+04	3.8E+04	9.0E-10	3.2E-09	5.4E-04	22.2	22.5	38.0	17.4	60.1	25.3	4.8E+03	2.6E+03	1500.7	855.1	1662.8	941.1	2426.8	295.4	2362.1	286.3	6704.4	3231.3	3.78E+05	0.4	98.1	30.7	3353.4	1271.50	4788.9	4.1E+02	1.5	0.6	2.8E-06	1.1E-06	4.3E-06	3.7E-07	3.4E-08	1.6E-08	3.16E+04
1K	1.00E+05	1.2E+05	5.0E-11	1.4E-10	7.7E-05	21.7	21.2	129.3	46.8	296.8	70.2	21421.1	9966.5	6643.2	3214.7	7369.4	3554.9	6968.1	723.5	6779.3	701.5	17977.9	9421.6	1.20E+06	0.3	336.1	84.4	1.4E+04	4.8E+03	13747.4	1.0E+03	1.0	0.3	7.0E-07	2.4E-07	6.9E-07	5.0E-08	6.5E-09	2.3E-09	1.00E+05
1K	3.16E+05	1.4E+05	2.1E-12	6.3E-12	1.1E-05	21.2	20.7	451.3	142.5	711.0	213.7	9.4E+04	3.8E+04	2.9E+04	1.2E+04	3.2E+04	1.3E+04	20175.9	1971.5	19625.7	1913.2	48408.2	27477.4	3.78E+06	0.3	1162.3	256.9	6.2E+04	1.8E+04	39801.6	2.7E+03	0.6	0.2	1.3E-07	3.8E-08	8.4E-08	5.8E-09	9.5E-10	3.0E-10	3.16E+05

cZ=0.5	Ene:A.GeV	DEne	Flux	FluxIAS	E=m^2.s	H(g/cm2)	sH(g/cm2)	nProt	dProt	nNeut	dNeut	nGam	dGam	nPos	dPos	nElec	dElec	nMup	dMup	nMun	dMun	nDecM	nEDM	EneSum	%LostE	NpKe	sNpKN	NeKp	sNeKp	Nemu	sNemu	Mu/Em	sMu/Em	Nm*Fk	sNm*Fk	Nnm*Fk	sNnm*Fk	Nnp*Fk	sNnp*Fk	Ene:A.eV
100K	1.00E+01	1.5E+00	2.3E-01	8.9E+00	1.0E+02	24.0	24.0	0.0	0.1	0.0	0.1	0.0	0.2	0.0	0.1	0.0	0.1	0.1	0.3	0.1	0.3	17.5	5.4	9.50E+01	20.8	0.0	0.1	0.0	0.1	0.20	0.4	13.1	113.6	3.5E-03	2.9E-02	4.6E-02	9.0E-02	8.0E+00	2.3E-02	1.00E+01
100K	1.33E+01	3.9E+00	1.8E-01	4.1E+00	6.4E+01	24.1	24.0	0.0	0.1	0.0	0.2	0.1	0.3	0.0	0.2	0.0	0.2	0.3	0.5	0.3	0.5	25.0	7.8	1.32E+02	17.3	0.0	0.2	0.0	0.2	0.60	0.7	12.7	64.1	8.5E-03	4.2E-02	1.1E-01	1.3E-01	8.0E+00	1.8E-02	1.33E+01
100K	1.78E+01	5.2E+00	1.3E-01	1.9E+00	3.9E+01	24.0	23.9	0.0	0.1	0.0	0.2	0.1	0.5	0.1	0.2	0.1	0.3	0.7	0.8	0.7	0.8	34.6	10.8	1.83E+02	14.5	0.0	0.2	0.1	0.4	1.40	1.1	12.7	43.1	1.4E-02	4.7E-02	1.8E-01	1.5E-01	8.0E+00	1.3E-02	1.78E+01
100K	2.37E+01	6.8E+00	7.0E-02	8.7E-01	2.4E+01	23.9	24.0	0.0	0.2	0.1	0.3	0.3	0.7	0.1	0.4	0.1	0.4	1.3	1.1	1.3	1.1	46.5	14.4	2.49E+02	12.3	0.1	0.4	0.2	0.5	2.60	1.6	12.3	31.0	1.5E-02	3.6E-02	1.8E-01	1.1E-01	8.0E+00	1.4E-02	2.37E+01
100K	3.16E+01	9.2E+00	5.0E-02	4.0E-01	1.5E+01	23.9	23.8	0.0	0.2	0.1	0.3	0.5	1.0	0.2	0.5	0.2	0.5	2.4	1.5	2.4	1.5	61.7	18.8	3.44E+02	9.2	0.1	0.4	0.4	0.7	4.80	2.1	12.6	24.6	1.9E-02	3.6E-02	2.4E-01	1.1E-01	8.0E+00	1.8E-02	3.16E+01
100K	4.22E+01	1.2E+01	3.0E-02	1.8E-01	9.0E+00	23.9	24.0	0.1	0.3	0.1	0.4	0.8	1.4	0.3	0.7	0.3	0.7	4.2	2.0	4.0	2.0	79.2	23.6	4.75E+02	6.1	0.2	0.5	0.6	1.0	8.20	2.8	13.0	20.7	1.9E-02	2.9E-02	2.5E-01	8.5E-02	3.0E-03	9.9E-03	4.22E+01
100K	5.62E+01	1.6E+01	2.0E-02	8.4E-02	5.5E+00	23.8	23.7	0.1	0.4	0.2	0.5	1.4	1.9	0.5	0.9	0.6	0.9	6.7	2.5	6.3	2.5	95.9	29.0	6.48E+02	3.9	0.3	0.6	1.1	1.3	13.00	3.5	12.2	15.2	2.1E-02	2.6E-02	2.6E-01	7.1E-02	2.0E-03	8.9E-03	5.62E+01
100K	7.50E+01	2.2E+01	1.0E-02	3.9E-02	3.4E+00	23.8	23.8	0.2	0.4	0.3	0.6	2.1	2.6	0.8	1.5	0.8	1.2	9.8	3.1	9.3	3.1	115.6	34.9	8.76E+02	2.7	0.5	0.7	1.6	1.9	19.10	4.4	11.9	14.5	1.6E-02	1.9E-02	1.9E-01	4.4E-02	2.0E-03	4.0E-03	7.50E+01
100K	1.00E+02	4.7E+01	5.0E-03	1.8E-02	2.8E+00	23.8	23.8	0.2	0.4	0.3	0.6	2.8	3.2	1.0	1.4	1.1	1.5	13.4	3.7	13.2	3.6	130.8	35.9	1.16E+03	3.7	0.5	0.7	2.2	2.0	26.60	5.2	12.1	11.4	1.1E-02	1.0E-02	1.3E-01	2.6E-02	1.9E-03	2.9E-03	1.00E+02
100K	1.78E+02	1.0E+02	8.5E-04	3.7E-03	1.6E+00	23.6	23.7	0.3	0.6	0.4	0.8	5.6	5.4	2.0	2.2	2.2	2.3	25.1	5.2	24.6	5.1	180.3	50.3	2.09E+03	2.2	0.7	1.0	4.3	3.2	49.70	7.3	11.6	8.9	3.6E-03	2.7E-03	4.2E-02	6.2E-03	2.6E-04	5.1E-04	1.78E+02
100K	3.16E+02	1.8E+02	2.0E-04	8.0E-04	6.1E-01	23.4	23.4	0.4	0.8	0.7	1.0	10.6	9.4	3.8	3.6	4.1	3.9	43.1	7.3	42.2	7.2	243.3	70.4	3.73E+03	1.6	1.1	1.3	7.9	5.3	85.30	10.3	10.8	7.3	1.6E-03	1.1E-03	1.7E-02	2.1E-03	8.0E-05	1.6E-04	3.16E+02
1K	5.62E+02	3.3E+02	4.5E-05	1.7E-04	2.3E-01	22.4	22.5	0.6	0.9	1.0	1.3	19.4	17.8	6.8	6.5	7.3	6.8	70.2	10.4	68.9	10.4	334.3	101.0	6.67E+03	1.1	1.6	1.6	14.1	9.3	139.10	14.7	9.9	6.6	6.4E-04	4.2E-04	6.3E-03	6.6E-04	2.7E-05	4.3E-05	5.62E+02
1K	1.00E+03	1.0E+03	1.0E-05	3.5E-05	1.1E-01	22.0	22.3	1.0	1.3	1.5	1.6	36.0	29.1	12.1	10.2	13.3	11.3	113.2	16.4	110.9	15.7	470.7	153.3	1.19E+04	0.8	2.5	2.1	25.4	15.3	224.10	22.7	8.8	5.4	2.5E-04	1.5E-04	2.2E-03	2.3E-04	1.0E-05	1.3E-05	1.00E+03
1K	3.16E+03	3.8E+03	4.5E-07	1.6E-06	2.7E-02	21.8	20.2	2.7	2.5	4.3	3.4	156.6	128.9	50.9	42.6	56.2	47.4	295.2	38.9	287.7	38.5	1053.9	385.9	3.77E+04	0.5	7.0	4.2	107.1	63.7	582.90	54.7	5.4	3.3	4.8E-05	2.9E-05	2.6E-04

Table XVI: Multiplicity and response function study in the USC for incidence angle ranges of primary C in the atmosphere of [29,34.4]°, [34.4, 41.4]° and [41.4, 49.4]°.

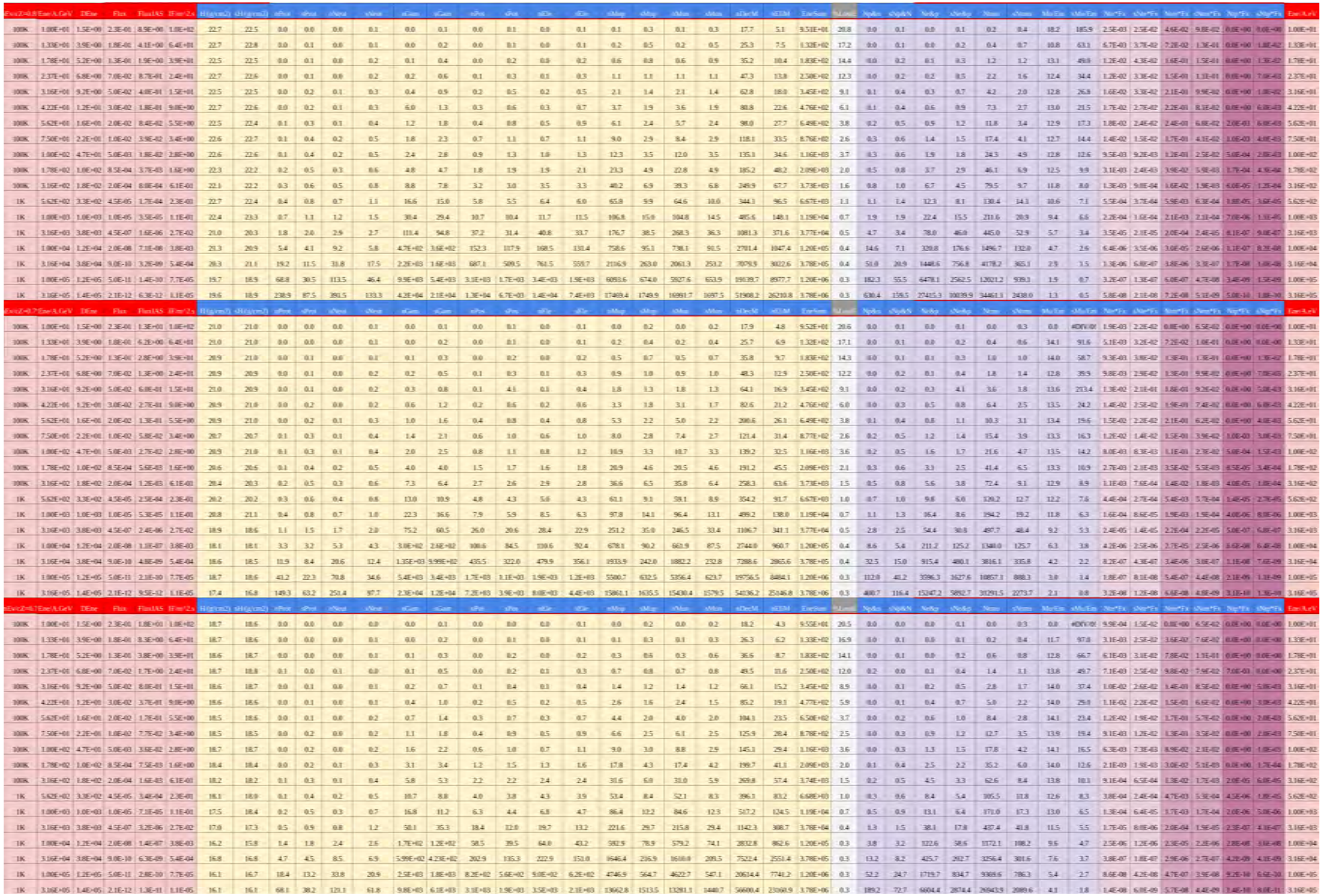

Table XVII: **Multiplicity and response function study in the USC for incidence angle ranges of primary C in the atmosphere of [49.4, 58.3]°, [58.3, 69.5]°.**

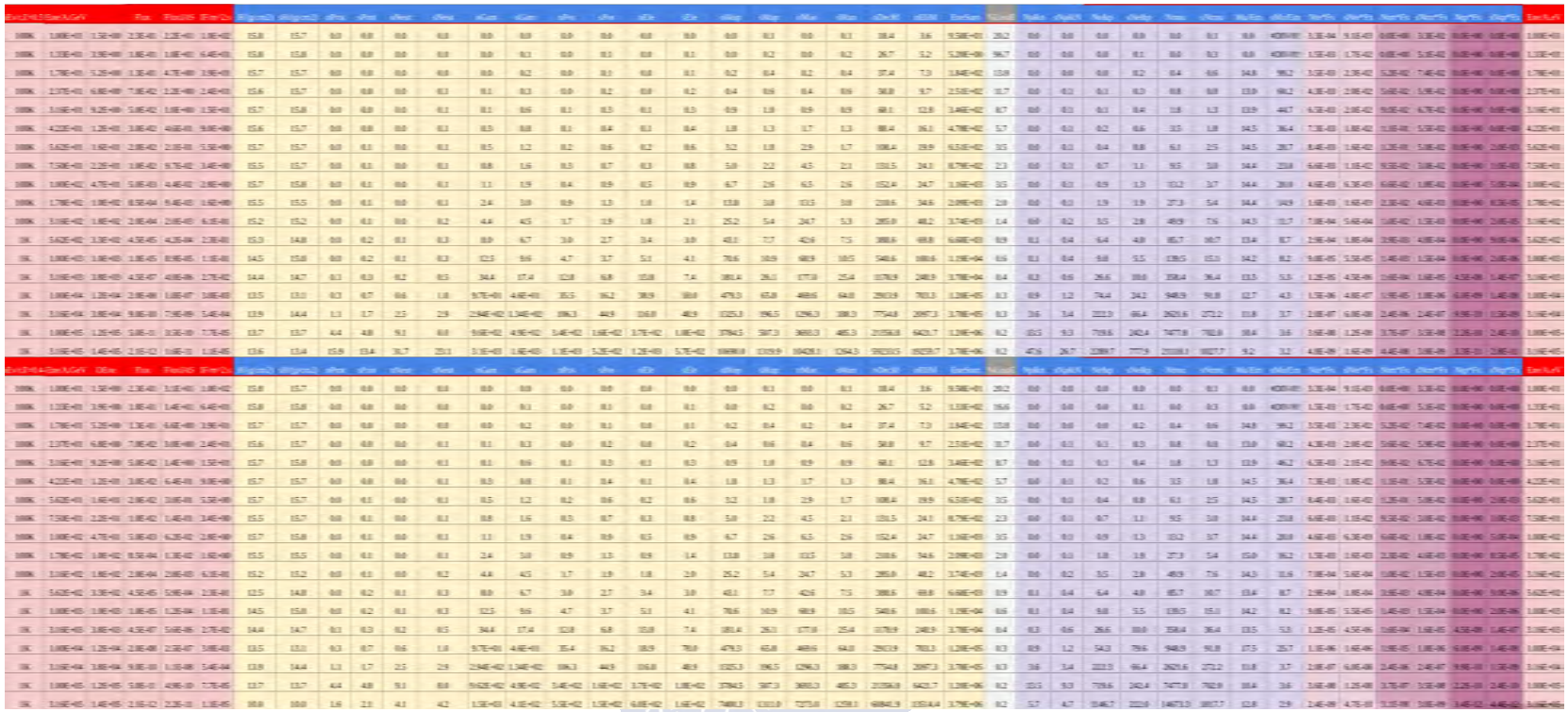

Source codes

```
//%%%%%%%%%%%%%%%%%%%%%%%%%%%%%%%%%%%%%%%%%%%%=== Y. Fontenla ===%%%%%%%%%%%%%%%%%%%%%%%%%%%%%%%%%%%%%%%%%%%%%%%//
//%%%%%%%%%%%%%%%%%%%%%%%%%%%%%%%%%%%%%%%%%%%%%%%%%%%%%%%%%%%%%%%%%%%%%%%%%%%%%%%%%%%%%%%%%%%%%%%%%%%%%%%%%%%%%%//
//% Program for the study of the systematic effects from the EAS generated by CORSIKA through cluster analysis.%//
//% Identification of particles of a radius of action of 1 meter and cutoff of 0.5 meters by recursive method.%//
//%%%%%%%%%%%%%%%%%%%%%%%%%%%%%%%%%%%%%%%%%%%%%%%%%%%%%%%%%%%%%%%%%%%%%%%%%%%%%%%%%%%%%%%%%%%%%%%%%%%%%%%%%%%%%%//
//%%%%%%%%%%%%%%%%%%%%%%%%%%%%%%%%%%%%%%%%%%%%%%%%%%%%%%%%%%%%%%%%%%%%%%%%%%%%%%%%%%%%%%%%%%%%%%%%%%%%%%%%%%%%%%//


#define c000100_cxx
#include "c000100.h"
#include <TH2.h>
#include <TStyle.h>
#include <TCanvas.h>
#include <iostream>
#include <fstream>
#include <stdlib.h>
#define mele 0.000511 // GeV
#define mmuo 0.10566 // GeV
#define mgam 0.0 // GeV
#define mother 0.5 // GeV. If we assume that the other particles are protons
#define mpi 0.1396
#define mp 0.5
#define mn 0.9396
#define sep 2 // Radio a la primera interaccion. distancia de separación entre partículas [m]
#define limite 0.5// limite de separacion entre interacciones

void c000100::Loop()
{

        // Analisis de cascadas atmosfericas de rayos cosmicos de distinta energÃa con incidencia vertical.
        // Nota: Generados por Ricardo Vazquez (AIRES)
        /*
         *  Intervalos de Energia.c
         *
         *  /anaRadialShowers_100 : 100 showers
         *
         *  Created by R. Vazquez & J.A. Garzon on 23/01/13.
         *  Copyright 2013 Facultad de Fisica USC. All rights reserved.
         *  Modified by G.Kornakov on  11/03/2013
         *  Modified by JAGarzon on 29/04/2013
         *  Modified by Yanis Fontenla Barba on 23/05/2017 for Corsika
         *  Modified by Yanis Fontenla Barba on 20/03/2019 for study of cluster with Corsika
         *
         */
        //   In a ROOT session, you can do:
        //      root> .L clase.C
        //      root> clase t
        //      root> t.GetEntry(12); // Fill t data members with entry number 12
        //      root> t.Show();       // Show values of entry 12
        //      root> t.Show(16);     // Read and show values of entry 16
        //      root> t.Loop();       // Loop on all entries
        //
        //    This is the loop skeleton w/    jentry is the global entry number in the chain
        //    ientry is the entry number in the current Tree
        //    Note that the argument to GetEntry must be:
        //    jentry for TChain::GetEntry
        //    ientry for TTree::GetEntry and TBranch::GetEntry
        //
        //    To read only selected branches, Insert statements like:
        //    METHOD1:
        //    fChain->SetBranchStatus("*",0);  // disable all branches
        //    fChain->SetBranchStatus("branchname",1);  // activate branchname
```

```
//    METHOD2: replace line
//    fChain->GetEntry(jentry);       //read all branches
//    by  b_branchname->GetEntry(ientry); //read only this branch

if (fChain == 0) return;

Long64_t nentries = fChain->GetEntriesFast();
Long64_t nbytes
, nb = 0;
Long64_t fbytes = 0, fb = 0;
Long64_t pbytes = 0, pb = 0;
Long64_t hbytes = 0, hb = 0;
Long64_t tbytes = 0, tb = 0;

// Identificadores de particulas en Corsika:
//  1              gammas
//  2 3      e- e+
//  5 6      mu- mu+
//  7 8 9  pi0 pi+ pi-
//  11 12     K+ K-
//  13 14      n p
// ======================================

Float_t id, x, y, x1, x2, y1, y2, e, r, r1, r2, t ; //

Int_t cuentas=0;
Int_t n=0;
Int_t cuenta=0, contar=0;
Float_t theta=0., theta1=0., phi=0, phi1=0, phi2=0, theta_tan=0, theta_tan1=0, theta2=0.;
Float_t thetamean=0., tttheta=0., sigmatheta=0.;
Int_t pid=0, pidmin=1000000000, pidmax=0, pid1=0, pid2=0;
Long64_t id1=.0, id2=.0, idclus=.0;
Int_t label=-1, cmult=0, cuentmas=0;
Float_t time1=0., time2=0., tmax=0., tminmin=1000000000, tmin = 1000000000, rmin = 1000000000, rmax = 0.;
Float_t thetamax=0, phimax=0, thetamin=1000000000, phimin=1000000000;
Float_t h = 0, ThE=0, PhI=0, pt=0;
Float_t px, py, pz, px1, py1, pz1, px2, py2, pz2, p_sq, p_sq1, p_sq2; // momenta particles
Float_t d_sq, d_sq2, dx_sq, dy_sq, delta_r;
Float_t energy1, energy2, kinetic1, kinetic2, kmax, kmin=1000000000, kkmax, kkmin=1000000000;

Float_t xmean=0, ymean=0, tmean=0, xmax=0, xmin=0, ymax=0, ymin=0, Kmean=0;


Float_t prev_xmean=0, xsigma_sq=0;
Float_t prev_ymean=0, ysigma_sq=0;
Float_t prev_tmean=0, tsigma_sq=0;
Float_t resc_prev_tmean=0, resc_tmean=0, resc_time2=0;

Float_t prev_Kmean=0, Ksigma_sq=0;

// Definimos las energias en intervalos logaritmos de 0.25

/* SE COMENTA POR FALTA DE ESPACIO
fstream archivo;
archivo.open("C_P_1E11_10.txt", fstream::out);
<<archivo << "N shower" << "\t" << "FirstHeight [m]" << "\t" << "ZenithAng [°]" << "\t"
<<"AzimuthalAng [°]" << "\t" << "NumClust" << "\t" << "TamClust." << "\t" << "IdClust"  << "\t"
<< "DistCore [m]" << "\t" << "Id_{Ti}" << "\t" << "x_{Ti} [m]" << "\t" << "y_{Ti} [m]"  << "\t"
<< "Tiempo_{i}" << "\t" << "ZenithAng_{Ti} [°]" << "\t" << "AzimuthalAng_{Ti} [°]" << "\t"
<< "Kinetic_{Ti} [GeV]" << "\t" << "Id_{Tf}" << "\t" << "x_{Tf} [m]" << "\t" << "y_{Tf} [m]" << "\t"
<< "Tiempo_{f}" << "\t" << "ZenithAng_{Tf} [°]" << "\t" << "AzimuthalAng [°]" << "\t"
<< "Kinetic_{Tf} [GeV]" << "\t" << "XCentralClust [m]" << "\t" << "SigXClust [m]" << "\t"
<< "YCentralClust [m]"  << "\t" << "SigYClust [m]"  << "\t" << "T_{Averg} [ns]"  << "\t" << "SigT [ns]"
<< "\t" <<" KCluster_{Max} [GeV]" << "\t" << "KCluster_{Min} [GeV]" << "\t" <<  "K_{Averg} [GeV]" << "\t"
```

```
<< "SigK_{Averg} [GeV]" << endl;
*/

nentries=10;

for (Long64_t jentry=0; jentry < nentries;jentry++) {

        Long64_t ientry = LoadTree(jentry);

        if (ientry < 0) break;

        nb  = b_particle__->GetEntry(ientry);   nbytes += nb;
        fb  = b_shower_FirstHeight->GetEntry(ientry);   fbytes += fb;
        hb  = b_shower_Theta->GetEntry(ientry);   hbytes += hb;
        tb  = b_shower_Phi->GetEntry(ientry);   tbytes += tb;

        h   = shower_FirstHeight/100; // de cm a metros
        ThE = shower_Theta*(180/TMath::Pi());;
        PhI = shower_Phi*(180/TMath::Pi());;

        Float_t arr[9][particle__];
        Float_t ilabel[300000] = { [0 ... 299999] = -1.0 };

        for(Int_t nparticles=0; nparticles<particle__; nparticles++){

                id = particle__ParticleID[nparticles];
                if(id==1) continue;//Whithout gammas
                if(id){
                        cuenta++;
                        cuentas++;
                }

                x       = particle__x[nparticles];
                y       = particle__y[nparticles];
                r       = sqrt(x*x + y*y);
                px      = particle__Px[nparticles];
                py      = particle__Py[nparticles];
                pz      = particle__Pz[nparticles];
                p_sq    = px*px + py*py + pz*pz;
                pt      = ((px*y)-(py*x))/(r*p_sq);
                theta   = acos(pz/sqrt(p_sq))*(180/TMath::Pi());
                phi     = atan(px/py)*(180/TMath::Pi());
                //      theta_tan = atan(y/x)*(180/TMath::Pi());

                arr[0][nparticles] = id;
                arr[1][nparticles] = x/100; //cm a metros
                arr[2][nparticles] = y/100; //cm a metros
                arr[3][nparticles] = particle__Time[nparticles];
                arr[4][nparticles] = px;
                arr[5][nparticles] = py;
                arr[6][nparticles] = pz;
                arr[7][nparticles] = theta;
                arr[8][nparticles] = phi;
        }
        //    cout << cuenta << endl;

        //Multiplicidad
        for(Int_t i=0; i < particle__; i++){
                //      cout << ilabel[i] << endl;

                if(ilabel[i]!=-1) continue;

                px1     = arr[4][i];
                py1     = arr[5][i];
```

```
pz1        = arr[6][i];
time1      = arr[3][i];
pid        = arr[0][i];
x1         = arr[1][i];
y1         = arr[2][i];
theta1     = arr[7][i];
phi1       = arr[8][i];
r1         = sqrt(x1*x1 + y1*y1);
p_sq1      = px1*px1 + py1*py1 + pz1*pz1;

if(pid==1){
        id1      = 1; // Codigo de contaje para fotones. Hasta 999 fotones
        energy1  = sqrt(p_sq1 + mgam*mgam);
        kinetic1 = energy1 - mgam;
}
else if((pid==2)||(pid==3)){
        id1      = 1000; // Codigo de contaje para electrones. Hasta 99 electrones
        energy1  = sqrt(p_sq1 + mele*mele);
        kinetic1 = energy1 - mele;
}
else if((pid==5)||(pid==6)){
        id1      = 1000000; // Codigo de contaje para muones.
        energy1  = sqrt(p_sq1 + mmuo*mmuo);
        kinetic1 = energy1 - mmuo;
}
else if((pid==14)||(pid==15)){
        id1      = 100000000; // Codigo de contaje para protones.
        energy1  = sqrt(p_sq1 + mp*mp);
        kinetic1 = energy1 - mp;
}
else if((pid==25)||(pid==13)){
        id1      = 1000000000; // Codigo de contaje para neutrones.
        energy1  = sqrt(p_sq1 + mn*mn);
        kinetic1 = energy1 - mn;
}
else{
        id1      = 10000000000; // Contage para otros.
        energy1  = sqrt(p_sq1 + mother*mother);
        kinetic1 = energy1 - mother;
}

if((pid==1) && (kinetic1<0.2)) continue; // Ecut = 200 MeV to gammas
if((pid==2) && (pid==3)){
        if(kinetic1<0.1) continue;// Ecut = 100 MeV to electrons
}

idclus     = id1;
xmean      = x1;
ymean      = y1;
tmean      = time1;

Kmean=kinetic1;

for(Int_t j=i+1; j < particle__; j++){

        if(ilabel[j]!=-1) continue;

        contar++;

        dx_sq   = (arr[1][j]-xmean)*(arr[1][j]-xmean);
        dy_sq   = (arr[2][j]-ymean)*(arr[2][j]-ymean);// imponer como $

        d_sq2   = dx_sq + dy_sq;
        delta_r = ( sqrt(dx_sq)*xsigma_sq+sqrt(dy_sq)*ysigma_sq )/( sqrt(d_sq2) );
```

```
if( (sqrt(d_sq2)<=sep) && (delta_r<=limite) ){

        label++;
        cmult++;

        pid2       = arr[0][j];
        time2      = arr[3][j];
        x2         = arr[1][j];
        y2         = arr[2][j];
        r2         = sqrt(x2*x2 + y2*y2);
        theta2     = arr[7][j];
        phi2       = arr[8][j];
        px2        = arr[4][j];
        py2        = arr[5][j];
        pz2        = arr[6][j];

        //Cuidado con la forma recursiva Hay que sumarle 1 al conteo de
        // multiplicidad ya que falta contar la 1° interaccion

        prev_xmean = xmean;
        prev_ymean = ymean;
        prev_tmean = tmean;

        xmean      = xmean*(cmult)/(cmult+1) + x2/(cmult+1);
        ymean      = ymean*(cmult)/(cmult+1) + y2/(cmult+1);
        tmean      = tmean*(cmult)/(cmult+1) + time2/(cmult+1);

        //rescala de los valores temporales sino aparecen incoherencias
        //en el resultado debido a la precision

        resc_prev_tmean = prev_tmean-tmean;
        resc_tmean      = tmean-tmean;
        resc_time2      = time2-tmean;

        /* SE COMENTA POR FALTA DE ESPACIO
        xsigma_sq  = xsigma_sq + prev_xmean*prev_xmean - xmean*xmean +
        ((x2*x2-xsigma_sq-prev_xmean*prev_xmean)/(cmult+1));
        ysigma_sq  = ysigma_sq + prev_ymean*prev_ymean - ymean*ymean +
        ((y2*y2-ysigma_sq-prev_ymean*prev_ymean)/(cmult+1));
        tsigma_sq  = tsigma_sq + resc_prev_tmean*resc_prev_tmean -
        resc_tmean*resc_tmean + ((resc_time2*resc_time2-tsigma_sq -
        resc_prev_tmean*resc_prev_tmean)/(cmult+1));
        */


        p_sq2      = px2*px2 + py2*py2 + pz2*pz2;

        if(pid2==1){
                id2      = 1; // Codigo de contaje para fotones
                energy2  = sqrt(p_sq2 + mgam*mgam);
                kinetic2 = energy2 - mgam;
        }
        else if((pid2==2)||(pid2==3)){
                id2      = 1000; // Codigo de contaje para electrones
                energy2  = sqrt(p_sq2 + mele*mele);
                kinetic2 = energy2 - mele;
        }
        else if((pid2==5)||(pid2==6)){
                id2      = 1000000; // Codigo de contaje para muones
                energy2  = sqrt(p_sq2 + mmuo*mmuo);
                kinetic2 = energy2 - mmuo;
        }
        else if((pid2==14)||(pid2==15)){
```

```
                        id2      = 100000000; // Codigo de contaje para protones
                        energy2  = sqrt(p_sq2 + mp*mp);
                        kinetic2 = energy2 - mp;
                }
                else if((pid2==25)||(pid2==13)){
                        id2      = 1000000000; // Codigo de contaje para neutrones
                        energy2  = sqrt(p_sq2 + mn*mn);
                        kinetic2 = energy2 -mn;
                }
                else{
                        id2      = 10000000000; // Contage para otros
                        energy2  = sqrt(p_sq2 + mother*mother);
                        kinetic2 = energy2 - mother;
                }

                prev_Kmean = Kmean;
                Kmean      = Kmean*(cmult)/(cmult+1) + kinetic2/(cmult+1);

                /* SE COMENTA POR FALTA DE ESPACIO
                Ksigma_sq  = Ksigma_sq + prev_Kmean*prev_Kmean - Kmean*Kmean +
                 ((kinetic2*kinetic2-Ksigma_sq-prev_Kmean*prev_Kmean)/(cmult+1));
                 */

                if(time2 > tmax){
                        tmax     = time2;
                        xmax     = x2;
                        ymax     = y2;
                        pidmax   = id2;
                        kmax     = kinetic2;
                        thetamax = theta2;
                        phimax   = phi2;
                }

                if(time2 < tmin){
                        tmin     = time2;
                        xmin     = x2;
                        ymin     = y2;
                        pidmin   = id2;
                        kmin     = kinetic2;
                        thetamin = theta2;
                        phimin   = phi2;
                }

                if(kinetic2 > kkmax){
                        kkmax     = kinetic2;
                }

                if(kinetic2 < kkmin){
                        kkmin     = kinetic2;
                }


                idclus = idclus+id2;
        }

        ilabel[j] = label;
        label     = -1;
}

if(kinetic1 > kkmax){
        kkmax     = kinetic1;
}

if(kinetic1 < kkmin){
```

```
        kkmin     = kinetic1;
}

if(time1 > tmax){
        tmax     = time1;
        xmax     = x1;
        ymax     = y1;
        pidmax   = id1;
        kmax     = kinetic1;
        thetamax = theta1;
        phimax   = phi1;
}

if(time1 < tmin){
        tmin     = time1;
        xmin     = x1;
        ymin     = y1;
        pidmin   = id1;
        kmin     = kinetic1;
        thetamin = theta1;
        phimin   = phi1;
}

xsigma_sq = sqrt(xsigma_sq);
ysigma_sq = sqrt(ysigma_sq);
tsigma_sq = sqrt(tsigma_sq);
Ksigma_sq = sqrt(Ksigma_sq);

/* SE COMENTA POR FALTA DE ESPACIO
archivo << jentry+1 << "\t" << h << "\t" << ThE << "\t" << PhI << "\t" << contar+1 << "\t"
<< cmult+1 << "\t" << idclus  << "\t" << r1  << "\t" << pidmin << "\t" << xmin << "\t"
<< ymin << "\t" << tmin  << "\t" << thetamin << "\t" << phimin << "\t" << kmin << "\t"
<< pidmax << "\t" << xmax << "\t" << ymax << "\t" << tmax  << "\t" << thetamax << "\t"
<< phimax << "\t" << kmax << "\t" << xmean  << "\t" << xsigma_sq  << "\t" << ymean  << "\t"
<< ysigma_sq  << "\t" << tmean << "\t" << tsigma_sq << "\t" <<  kkmax << "\t"
<< kkmin << "\t" << "\t" << Kmean << "\t" << Ksigma_sq << endl;
*/

contar     = 0.;
idclus     = 0.;
x1         = 0.;
y1         = 0.;
x2         = 0.;
y2         = 0.;
id1        = 0.;
id2        = 0.;
pid1       = 0.;
pid2       = 0.;
label      = -1;
cmult      = 0.;
tmax       = 0.;
tmin       = 1000000000.;
time2      = 0.;
time1      = 0.;

xmax       = 0.;
xmin       = 1000000000.;
xmean      = 0.;
xsigma_sq  = 0.;
prev_xmean = 0.;

ymax       = 0.;
ymin       = 1000000000.;
ymean      = 0.;
```

```
                        ysigma_sq  = 0.;
                        prev_ymean = 0.;

                        pidmax     = 0.;
                        pidmin     = 1000000000.;
                        kmin       = 1000000000.;
                        phimin     = 1000000000.;
                        thetamin   = 1000000000.;
                        thetamax   = 0.;
                        phimax     = 0.;
                        kmax       = 0.;

                        tmean      = 0.;
                        tsigma_sq  = 0.;
                        prev_tmean = 0.;

                        Kmean      = 0.;
                        Ksigma_sq  = 0.;
                        prev_Kmean = 0.;
                        kkmax      = 0.;
                        kkmin      = 1000000000.;

                        resc_prev_tmean = 0.;
                        resc_tmean      = 0.;
                        resc_time2      = 0.;

                        dx_sq      = 0.;
                        dy_sq      = 0.;
                        d_sq2      = 0.;
                        delta_r    = 0.;
                        p_sq2      = 0.;
                        r1         = 0.;

                }

                for(Int_t i=0; i < 300000; i++){
                        ilabel[i]=-1;
                }


                for(Int_t i=0; i < 8; i++){
                        for(Int_t j=0; j < particle__; j++){
                                arr[i][j]=0.;
                        }
                }

        }

        /* SE COMENTA
        printf("Proceso completado");
        archivo.close();
        */

        cout << endl;
        cout << "Numero de cascadas : " << nentries << endl;
        cout << endl;
        cout << "Total de secundarios :" << cuenta << endl;
        cout << endl;

        // Estimamos densidades de particulas y sigmas correspondientes

}
```

Illustrations

Illustrations are implemented in this section to clarify the concepts and increase knowledge of the reader.

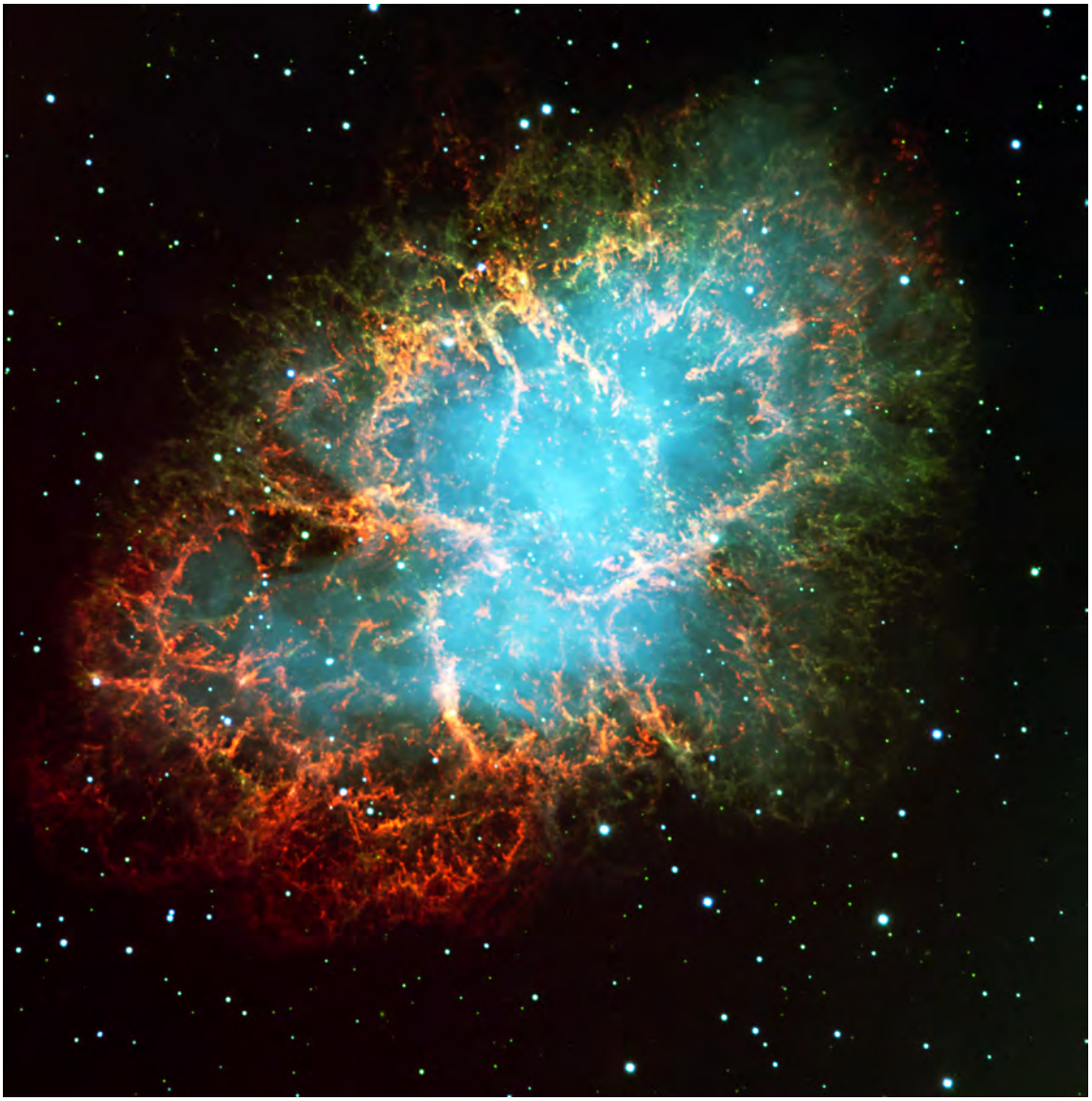

Illustration I: Remnant of a supernova explosion (Crab Nebula), as observed with the FORS2 instrument of european space observatory (ESO) in imaging mode in the morning of November 10, 1999.

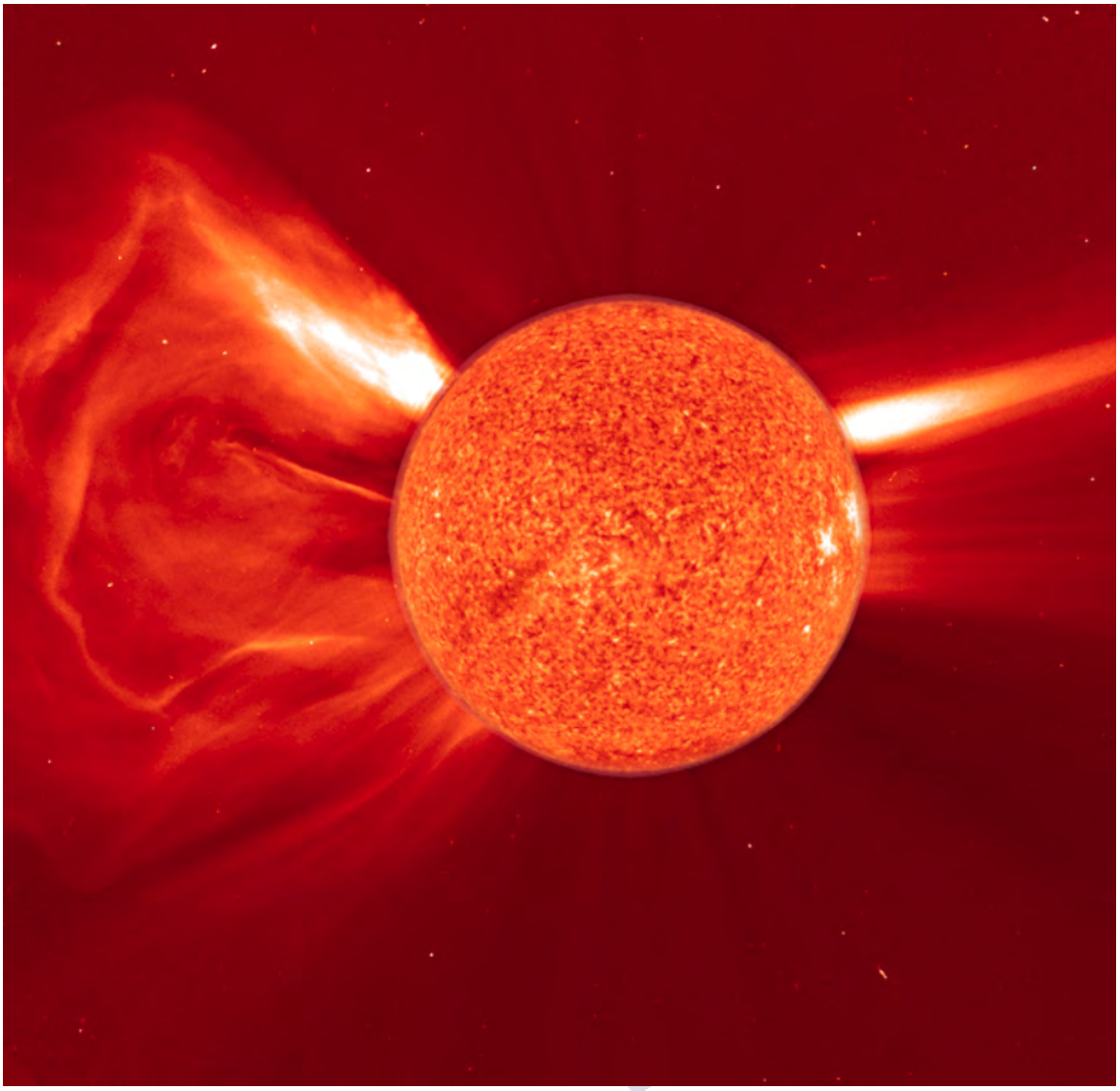

Illustration II: Image of the Sun obtained by the SOHO space observatory on January 24, 2007. A brilliant and expansive coronal mass ejection (*CME*).

Illustration III: Radio source Cygnus A is produced in a galaxy some 600 million light-years away. The National Radio Astronomy Observatory (2009).

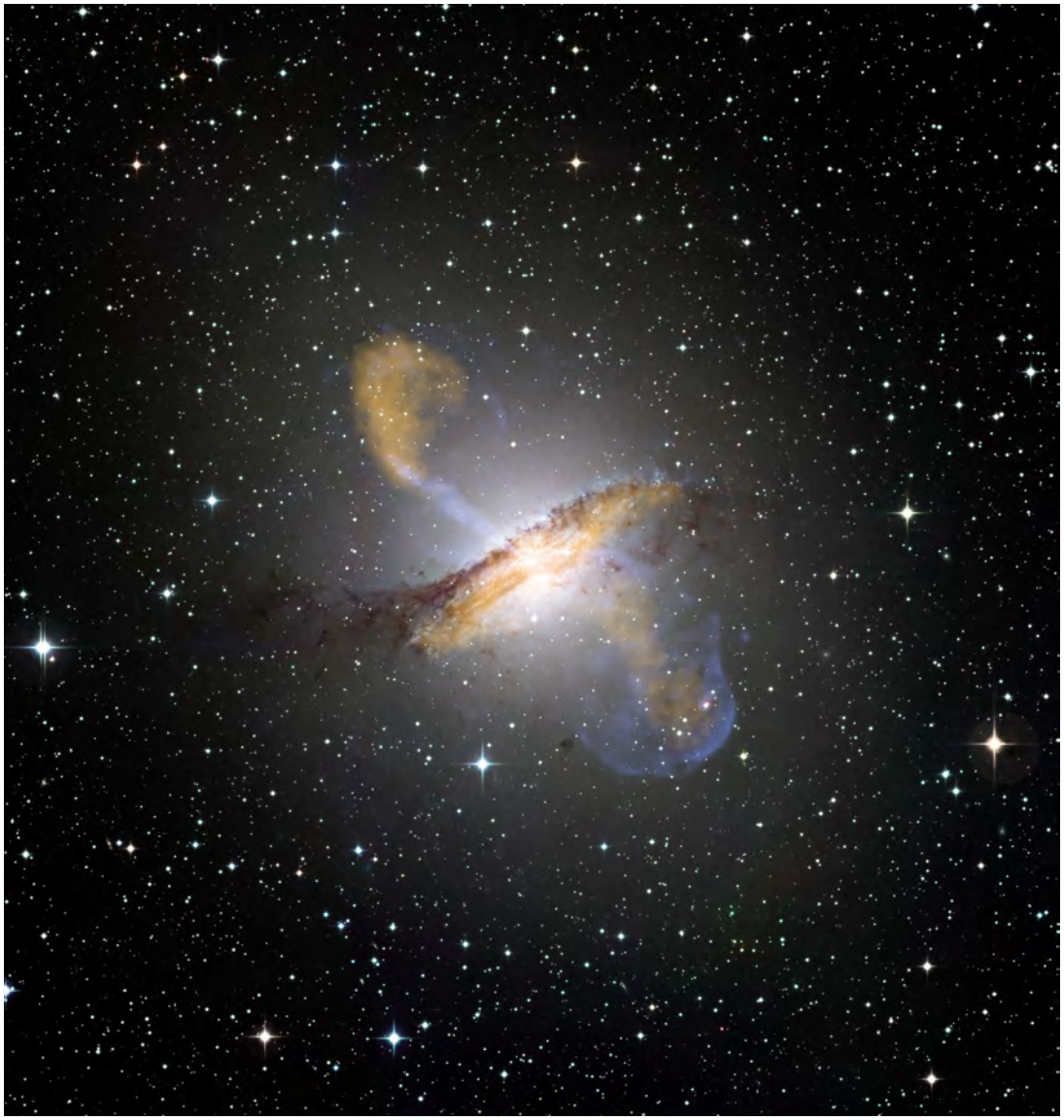

Illustration IV: Centaurus A revealing the lobes and jets emanating from the active galaxy's central black hole. Image from LABOCA on APEX (orange colours), Chandra X-ray Observatory (blue colours) and MPG/ESO 2.2 m telescope located at La Silla, Chile.

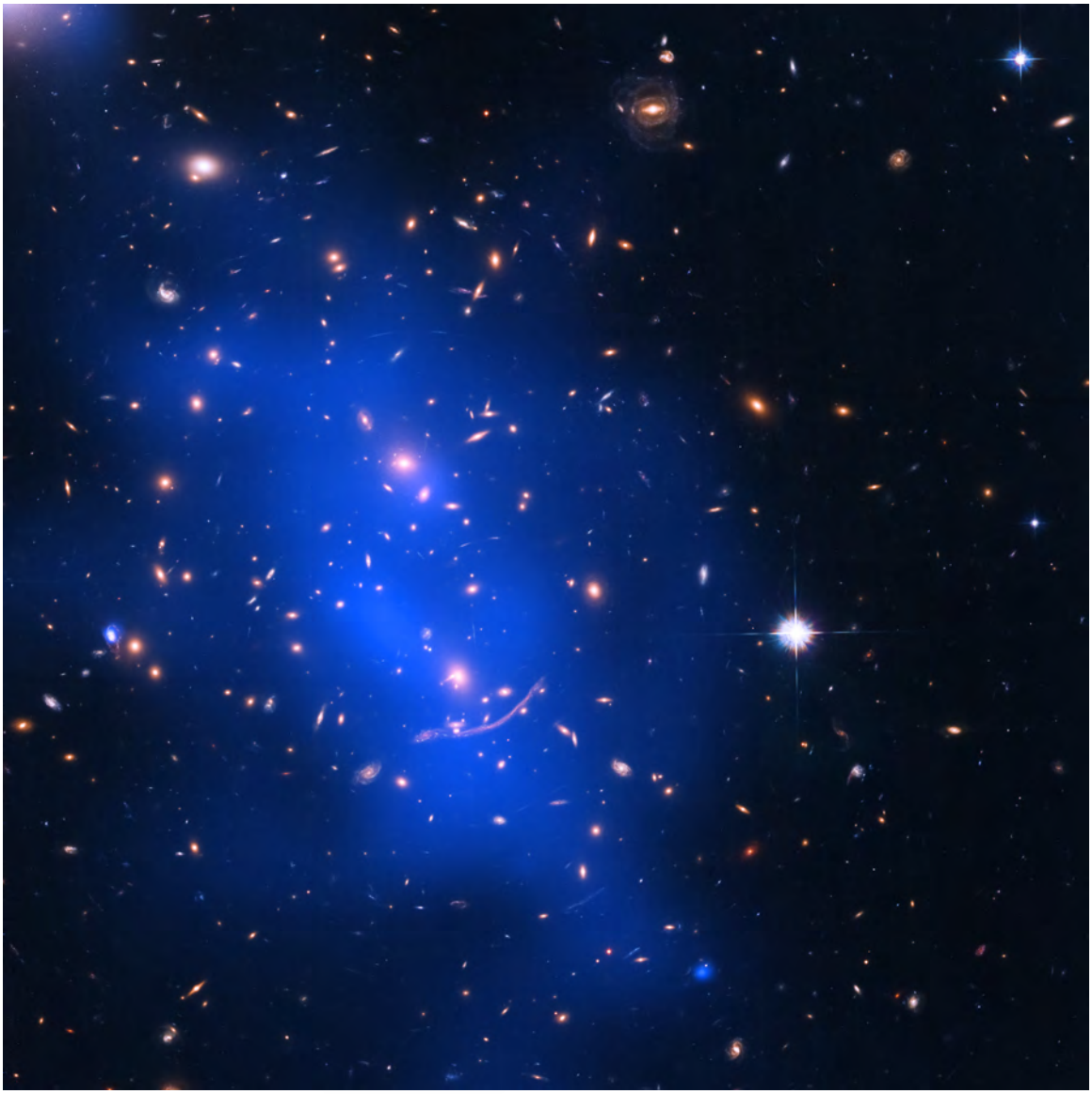

Illustration V: Abell 370 is a galaxy cluster located about 4 billion light years from Earth. Image from Chandra, NASA and ESO.

USC
UNIVERSIDADE
DE SANTIAGO
DE COMPOSTELA